EXPLORING VIBRATION ISOLATION OF A SUPERELASTIC SHAPE MEMORY ALLOY CANTILEVER BEAM

By

Md. Mahbubur Rahman

0417102042

A Thesis submitted for partial fulfillment of the requirements for the degree of
MASTER OF SCIENCE IN MECHANICAL ENGINEERING

Under the Supervision of

Dr. M. Ashiqur Rahman

Professor

Department of Mechanical Engineering

Bangladesh University of Engineering and Technology

DEPARTMENT OF MECHNANICAL ENGINEERING

BANGLADESH UNIVERSITY OF ENGINEERING AND TECHNOLOGY

DHAKA-1000, BANGLADESH

September 2022

The thesis titled "**EXPLORING VIBRATION ISOLATION OF A SUPERELASTIC SHAPE MEMORY ALLOY CANTILEVER BEAM**", submitted by Md. Mahbubur Rahman, Roll No.: 0417102042-P, Session: April 2017, has been accepted as satisfactory in partial fulfillment of the requirement for the degree of MASTER OF SCIENCE IN MECHANICAL ENGINEERING on 07 September, 2022.

BOARD OF EXAMINERS

Dr. Muhammad Ashiqur Rahman Professor Department of Mechanical Engineering BUET, Dhaka-1000	Chairman (Supervisor & Ex-oficio)
Dr. Md. Afsar Ali Professor Department of Mechanical Engineering BUET, Dhaka-1000	Member
Dr. Md. Abdus Salam Akanda Professor Department of Mechanical Engineering BUET, Dhaka-1000	Member
Dr. Raquib Ahsan Professor Department of Civil Engineering BUET, Dhaka-1000	Member (External)

CANDIDATE'S DECLARATION

It is hereby declared that this thesis or any part of it has not been submitted elsewhere for the award of any degree or diploma.

Md. Mahbubur Rahman

DEDICATION

I dedicate this thesis to my beloved sister (Maya).

CONTENTS

LIST OF FIGURES

LIST OF TABLES

LIST OF SYMBOLS & ABBREVIATIONS

x	=	Displacement (m)
$\dot{x}$	=	Velocity (m/s)
$\ddot{x}$	=	Acceleration (m/s^2)
t	=	Time (s)
c	=	Coefficient of damping (Ns/m)
c_c	=	Coefficient of Critical damping (Ns/m)
d	=	Diameter of the beam (mm)
E	=	Modulus of elasticity (MPa)
E_r	=	Reduced modulus of elasticity (GPa)
h_1, h_2	=	Positions of the farthest fibers measured w.r.t neutral axis (mm)
TR	=	Transmissibility
I	=	Moment of inertia (mm^4)
F_t	=	Transmitted force (N)
P	=	Applied static load (N)
F_0	=	Amplitude of the applied load (N)
k	=	Linearly elastic bending stiffness of the beam material (N/m)
M	=	Bending moment (Nm)
m	=	Mass of the applied (kg)
A	=	Cross –sectional area of the beam (mm^2)
ω	=	Forcing frequency, forcing frequency (rad/s)
ω_n	=	Natural frequency, (rad/s)
β	=	Speed ratio $\left(\frac{\omega}{\omega_n}\right)$
ξ	=	Damping ratio $\left(\frac{c}{c_c}\right)$
σ	=	Stress (MPa)
ε	=	Strain
ε_1	=	Tensile strain
ε_2	=	Compressive strain

ρ	=	Radius of curvature (mm)
$\varDelta, \varepsilon_1 + \varepsilon_2$	=	Sum of absolute values of the maximum elongation and the maximum contraction of beam's lengthwise fibers.
r	=	Radius of the beam (mm)
b	=	Width of the beam (mm)
h	=	Height of the beam (mm)
L	=	Length of the beam (mm)
SDOFS	=	Single degree of freedom system
SMA	=	Shape Memory Alloy

ACKNOWLEDGEMENT

The author would like to express his deep gratitude and indebtedness to his supervisor Dr. M. Ashiqur Rahman, Professor, Department of Mechanical Engineering, Bangladesh University of Engineering and Technology (BUET), Dhaka-1000, for his continuous inspirations, great interest, constructive criticism, super guidance, remarkable advice and invaluable supports during this research. The author would also like to thank him for his careful reading and correction of this thesis.

Very special thanks are due for all the teachers of the Department of Mechanical Engineering, BUET for their help to the author during the whole period of his M.Sc. Engineering course.

The author is also indebted to Mr. Md. Jahangir Alam and Mr. Md. Shariful Alam Emon, Faculty, Department of Mechanical Engineering, DUET, Gazipur-1707 for their co-operation during this journey.

ABSTRACT

Vibration of a superelastic Shape Memory Alloy (SMA) cantilever beam has been analyzed comprehensively considering end-shortening effect, geometric non-linearity and effect of material non-linearity (that is, the beam material has a non-linear stress-strain relation and Hook's law cannot be applied) for different forcing frequency and damping ratio. Difference between vibration for two equivalent cross-sections (circular and equivalent rectangular) has also been analyzed. Soundness of the developed mathematical scheme and computer code has been amply demonstrated in the present study.

The Euler-Bernoulli's geometrically non-linear governing equation and equation of classical theory for beam are solved numerically to generate the load-deflection relations. From these load-deflection relations, the restoring forces are chosen as best fit non-linear curves. Then this best fit non-linear curves of restoring forces are inserted into the equation of vibration that converts the equation into non-linear form which is solved numerically by the Runge-Kutta (R-K) 4^{th} order method of integration since exact solution is not possible. Material non-linearity issue is handled in terms of a mathematical model that has been developed to solve pure bending of a beam. It should be noted here that, SMA inherently has highly non-linear stress-strain curves in tension and compression. Thus, bending moment-curvature and reduced modulus-curvature relations are obtained for a superelastic SMA circular and equivalent rectangular beams. Results are used to predict effect of material non-linearity on the response of vibration of the beam.

Some interesting results can be observed from this thesis that the amplitude of the undamped vibration considering end-shortening effect is not going to be infinite over time at resonance ($\beta = \frac{\omega}{\omega_n} = 1$) which is predicted by classical theory. It is also found that increased damping greatly reduces the vibration amplitude for both the classical theory with and without end-shortening effect.

As material non-linearity is taken into account some portion of the beam is found to experience stresses (different magnitude in tension and compression) beyond proportional limit. Effect of material non-linearity becomes prominent as vibration

amplitude starts to become large. Moreover, the maximum deflection of the beam is found to be much larger when material non-linearity is considered in comparison to the case of linearly elastic beam material.

The amplitude of the vibration considering material non-linearity and geometric non-linearity with end-shortening effect is largely lower than that predicted by classical theory when the damping is low. Increased damping greatly reduces the vibration.

The amplitude of the undamped vibration for circular beam is slightly higher than that of equivalent rectangular beam at resonance (β = 1) considering material non-linearity with end-shortening effect. When the geometric non-linearity issue is incorporated to the material non-linearity with end-shortening effect the discrepancy between the vibrations is reduced.

The isolation of the vibration begins when the speed ratio (β) exceeds 1.414 for classical theory with any amount of damping but it requires higher speed ratio to start the vibration isolation when end-shortening effect is included. A very interesting result is found that the speed ratio (β) varies with the damping ratio to isolate the vibration considering material non-linearity and geometric non-linearity with end-shortening effect. A higher damping ratio requires a smaller speed ratio to begin the isolation.

Key words: Cantilever Beam, End-Shortening, Equivalent Cross-section, Vibration Isolation, Transmissibility.

CHAPTER 1

INTRODUCTION

1.1 Vibration and Isolation of Vibration

Vibration is a mechanical phenomenon in which oscillations take place around a point of equilibrium. The term is derived from Latin vibrationem ("shaking, brandishing"). This may be a periodic or random oscillation.

Vibration may be desired, as in a tuning fork, woodwind or harmonica reed, mobile phone, or loudspeaker cone. Vibrations from engines, electric motors, or other mechanical devices are undesired. It wastes energy and creates unwanted noises. Unbalanced spinning components, unequal friction, or gear teeth meshing may create vibrations. Careful design reduces vibration. Mechanical waves convey vibrations, and certain mechanical couplings are more effective than others at transmitting vibrations. Avoiding or isolating vibration in undesirable domains is crucial for system maintenance.

Vibration isolation is the process of separating an object, such as a piece of equipment, from the source of vibrations. Active vibration isolation comprises of sensors and actuators that create disruptive interference in order to negate incoming vibration. Passive vibration isolation makes use of materials and mechanical connections that absorb and dampen vibrations. A wide variety of passive vibration isolators are employed in a wide variety of applications, making passive vibration isolation a broad topic. This technology may be used to protect delicate laboratory equipment, and high-end audio systems from damage caused by earthquakes, including pumps, motors, HVAC systems, and even washing machines. There are common passive isolators i.e. Pneumatic or air isolators, Mechanical springs and spring-dampers, Pads or sheets of flexible materials such as elastomers, rubber, cork, dense foam and laminate materials, Molded and bonded rubber and elastomeric isolators and mounts, Negative-stiffness isolators, Wire rope isolators, Base isolators for seismic isolation of buildings, bridges, Tuned mass dampers etc.

A passive isolation system, such as a shock mount, consists of mass, spring, and damping components and oscillates in a harmonic manner. The mass and spring stiffness determine the system's natural frequency. The dissipation of energy caused by damping has a secondary influence on natural frequency. Every item supported by a flexible surface has a basic natural frequency. When vibration is applied, energy transmission is most effective at the natural frequency, moderately efficiently below the natural frequency, and with diminishing efficiency beyond the natural frequency. This may be shown in the transmissibility curve, which represents the relationship between transmissibility and frequency.

Vibrations cannot be avoided entirely; however, they may be significantly decreased. In general, an isolator with a lower natural frequency will exhibit stronger isolation for any frequency above the natural frequency than one with a higher natural frequency. The optimal isolation system for a specific circumstance relies on the frequency, direction, and amplitude of the vibrations present, as well as the required amount of frequency attenuation. In the actual world, all mechanical systems contain some level of damping. The dissipation of energy in the system through damping minimizes the degree of vibration transmitted at the natural frequency. The fluid in vehicle shock absorbers and the inherent damping in elastomeric (rubber) engine mounts are both types of dampers.

In passive isolators, damping is employed to limit the amount of natural frequency amplification. Increasing damping, however, tends to diminish isolation at higher frequencies. As damping is increased, roll-off in transmissibility diminishes.

1.1.1 Vibration Isolation Theory

Vibratory forces generated by machines and other causes are often unavoidable; however, their disturbing effects (measured in terms of forces transmitted through springs and dampers) on a dynamical system can be minimized by proper isolator design. An isolation system attempts either to protect a delicate object from excessive vibration transmitted to it from its supporting structure or to prevent vibratory forces generated by machines from being transmitted to its surroundings**.** The basic problem is the same for these two objectives that of reducing the transmitted force [1].

The transmissibility *TR,* defined as the ratio of the transmitted force to that of the disturbing force, is then from Thomson [1],

$$TR = \left|\frac{F_t}{F_0}\right| = \sqrt{\frac{1 + (2\zeta\omega/\omega_n)^2}{[1 - (\omega/\omega_n)^2]^2 + [\frac{2\zeta\omega}{\omega_n}]^2}}$$

$$TR = \left|\frac{F_t}{F_0}\right| = \sqrt{\frac{1+(2\zeta\beta)^2}{[1-(\beta)^2]^2+[2\zeta\beta]^2}}$$

Where, F_t = Resultant of spring force and damping force.

$$F_t = \sqrt{(kx)^2 + (c\omega x)^2}$$

$$F_t = kx\sqrt{1 + (2\zeta\beta)^2}$$

When the damping is negligible, the transmissibility equation reduces to

$$TR = \frac{1}{[1 - (\beta)^2]^2}$$

The force to be isolated is transmitted through the spring and damper, as shown in Figure 1.1.1 [1]. Figure 1.1.2 shows that the motion transmitted from the supporting structure to the machine element or payload is less than 1 when the speed ratio, $\beta = \frac{\omega}{\omega_n}$ is greater than $\sqrt{2}$. This indicates that the natural frequency ω_n of the supported system must be small compared to that of the disturbing frequency ω. This requirement can be met by using a soft spring. The other problem of reducing the force transmitted by the machine to the supporting structure has the same requirement.

1.2 Introduction to Smart/Functional Materials

Modern material science and information science have been brought together to create the new emerging system of materials called intelligent materials. Intelligent systems have subsystems that detect, process and actuate as well as self-diagnose and self-recover. An extraordinary performance is achieved by the use of functional features of advanced materials, such as identification, discrimination, and environmental adaption. In order to accomplish a self-controlled smart activity, comparable to that of a biological system with the ability to think, judge, and act, every component of this system must be functioning. Designing a smart system may be seen as emphasizing predictability, adaptability, and repeatability[2].

A smart system is characterized as a nonbiological physical structure that has a specific goal, means and requirements to fulfil it, and biological patterns of functioning. Today's leading smart materials include the following:

(i) Piezoelectric Pb (Zr, Ti)O_3 (PZT)

(ii) Magnetostrictive (Tb, Dy) Fe_2

(iii) Electrostrictive Pb (Mg Nb)O_3 and

(iv) Shape Memory Alloy NiTi.

1.3 The Concept of Shape Memory Effect

The shape-memory effect is a unique thermomechanical property of some metal alloys. The shape memory effect is the capacity of an alloy to revert to its original shape upon re-heating after being deformed. In a similar manner, when tested under varying circumstances, shape recovery may occur spontaneously following removal of the stress that caused the deformation. The term for this is "pseudoelasticity." These alloys are called shape memory alloys (SMAs). Figure 1.3.1 [3] depicts an illustration of the two distinct behaviours of shape-memory alloys. Figure 1.3.1(a) depicts the shape memory effect (SME), which occurs when a straight shape memory alloy rod is deformed in a non-elastic way and retains its bent shape after the external force is removed. Subsequent heating over a threshold temperature leads the bent rod to regain its original form. The pseudoelastic behaviour seen in Figure 1.3.1 (b) occurs when deformation is undertaken at temperatures above the critical temperature. Upon unloading, the bent rod spontaneously returns to its straight shape in this instance. This phenomenon is also occasionally referred to in the literature as "superelasticity." "Superelastic" and "pseudoelastic" are the terms used to describe this behaviour since the deformation may take place under tension, compression, torsion, or flexion. Alloys do mechanical work against the environment by "remembering" and "restoring" the original shape. Alloys with this property have been dubbed "smart materials" or "magic metals" and are set apart from all other types of metal alloys.

1.4 Shape Memory Alloy (SMA)

These alloys are referred to as shape memory alloys (SMAs) because they show shape memory characteristics. Au-Cd alloys described by Olander in 1932 [4] were the first shape memory alloys known. After the discovery of NiTi in 1963 by Buehler in their quest for heat-shielding materials [5], this family of metal alloys received significant attention. SMAs exhibit distinctive properties such as pseudoelasticity and shape memory effect, in which an alloy distorted by a significant strain restores its original shape upon unloading or heating, as seen schematically in Figure 1.4.1. These features result from the martensite transition, a diffusionless phase change in solids.

Typically, the parent phase (austenite phase) stable at higher temperature and lower shear stress is cubic, but the martensite phase, stable at lower temperature and greater shear stress, is asymmetric, and several variations with various orientations are generated from the same parent phase.

The deformation behaviour of SMA is shown in Figure 1.4.1 using a two-dimensional, two-variable model. At higher temperatures, shear stress transforms the austenite phase into martensite, which has a greater strain than the austenite phase. By removing the tension, martensite is converted into austenite and the shape is restored to its former state. The term for this is pseudoelasticity. By cooling, austenite is also converted into martensite. In this instance, variations are produced such that there is no overall strain. At this temperature, an alloy with a considerable strain does not return its previous form by unloading alone; rather, it recovers through the austenite phase by heating and cooling. This diagram demonstrates that both cycles contain a significant hysteresis loop. SMAs are anticipated to be used as passive damping materials as well as actuators or sensors owing to the fact that their area is proportional to the amount of energy lost due to internal friction between phases, etc.

NiTi's superior technical and functional features compared to its predecessor, such as stronger mechanical strength, more cheap cost, outstanding workability, and good property stability, made it an instant contender for creative applications. Since then, several form memory alloys have been identified. On the basis of their metallurgical characteristics, the many shape memory alloys now available may be categorized into five major groups, namely NiTi-based, Cu-based, Fe-based, ferromagnetic shape memory alloys, and "other" shape memory alloys. Table 1.4.1 provides some examples of these alloys. From the perspective of the application profile, these alloys may be categorized into four distinct classes: thermomechanical, high temperature, biomedical, and ferromagnetic actuation.

Table 1.4.1 Examples of the principal types of shape-memory alloys.

<table>
<tr><th>Alloy type</th><th>Alloys</th><th colspan="2">Application profile</th></tr>
<tr><td>NiTi-based</td><td>NiTi, NiTiCu, NiTiFe, NiTiAl, NiTiCo, NiTiPd, NiTiMn, NiTiHf, NiTiZr, NiTiPt.</td><td rowspan="3">Thermo-mechanical</td><td rowspan="6">High temperature (bolded)</td></tr>
<tr><td>Cu-based</td><td>CuZn, CuAl, CuSn, CuZnAl, CuZnSi, CuAlFe, CuAlNi, CuMnSi.</td></tr>
<tr><td>Fe-based</td><td>FeNiCoTi, FeMnSi, FePt, FePd, FeNiC, FeMnSi, FeCrNi, FeMnCoNiSi, FeMnSiCoNi.</td></tr>
<tr><td>Ni-free</td><td>Ni-free Ti-based, TiNb, TiNbZr, TiNbTa, TiNbO, TiMoTa, TiZr, TiAu, TiPt, TiPd, TiAu.</td><td>Biomedical application</td></tr>
<tr><td>Ferromagnetic</td><td>NiMnGa, NiFeGa, MnAs, CoNbSn, CoNi, CoNiAl, CoNiGa, FeMnCo, FeNi, FePt, FePd, FeRh.</td><td>Magnetic actuation</td></tr>
<tr><td>Others and precious metals</td><td>AuCd, InTl, InPb, NiAl, NiMn, ZrCu,ZrRh.</td><td></td></tr>
</table>

All three classes of NiTi-based, Cu-based, and Fe-based shape memory alloys are commercially accessible for thermomechanical applications. Despite the fact that Cu- and Fe-based alloys are less expensive than NiTi, their relatively low property stability, high brittleness, and poor thermomechanical performance [6]–[9] make NiTi-based alloys the most popular option for applications.

The unique features of SMAs make them a very desirable option for novel applications. Numerous applications have been developed over the last several decades, including consumer items and industrial applications [10], structures and composites [11], automotive [12], aerospace [13], tiny actuators and microelectromechanical systems (MEMS) [14] and biomedical devices[15].

Experiments with repeated tension-compression show that all materials exhibit some hysteresis characteristics so that instead of a straight line *AA* (Figure 1.4.2), representing Hooke's law, we usually obtain a loop of which the width depends on the limiting values of stresses applied in the experiment. If the loading and unloading is repeated several hundred times, the shape of the loop is finally stabilized and the area of the loop gives the amount of energy dissipated per cycle due to hysteresis [16].

Upon unloading SMA can recover large strain (Figure 1.4.3) by virtue of superelasticity (SE) or pseudo elasticity (PE) through a hysteresis [17] However, conventional engineering material like steel invariably shows large inelastic/ plastic strain upon unloading due to material non-linearity effect.

Modern adaptive structural element analysis is complex because it often involves nonlinear (geometric and material etc.) analysis. This is due to the fact that such components (for instance beams and columns, particularly in adaptable constructions) often experience extremely substantial deflections throughout their uses. The response of such a cantilever beam made of SMA with variable cross-sectional area under a tip load was studied by Kowser [18]. This research on the superelastic SMA beams was particularly noteworthy since SMA is one of the most often utilized functional materials in adaptive structures. When unloaded, superelastic SMAs may recover incredibly enormous stresses. However, they exhibit "extremely nonlinear stress-strain relations, with intrinsic asymmetry in tension and compression," as observed by Rahman [17]. Rahman [17] stated that the average Young's Modulus during the parent phase was 65 GPa. With this value of Young's Modulus, simulations will be run on a superelastic shape-memory alloy cantilever beam. Machado [19] examined the use of SMAs for vibration isolation and dampening in mechanical systems.

1.5 Motivation for the Present Study

The vibration isolation of a SMA cantilever beam remains unexplored, especially considering the combined effects of geometrical nonlinearity, material-nonlinearity, end-shortening, and different cross-sections, despite the fact that SMA-based vibration control has been in use for a long time [19]. This thesis is likely to yield a realistic method to predict the vibration isolation of the cantilever beam made of superelastic SMA with a time varying tip load. This work also may be useful for any conventional engineering material (having variable stiffness and self-damping property) other than superelastic SMA to determine the vibration isolation conditions of structures.

1.6 Objectives

The specific aim of this study is to focus on the vibration isolation characteristics of a superelastic SMA cantilever beam due to a fluctuating tip load when stiffness cannot be considered to be constant. Influence of factors (for example, end-shortening, self-damping property of SMA and equivalent cross-sectional area) on vibration isolation will also be studied. In short, following points will be considered:

1) To numerically generate load-deflection (P-δ) curves of superelastic SMA cantilever beam including geometric non-linearity, material non-linearity and end-shortening.
2) To determine the conditions of vibration isolation of a superelastic SMA beam vibrating due to a fluctuating tip load for different types of load-deflection (P-δ) relations. Also, to investigate the effect of self-damping on vibration isolation.
3) To examine the change of vibration isolation conditions for different equivalent cross-sections.

1.7 Outline of Methodology

Results, in terms of the force versus tip deflection (P-δ) curve will be obtained numerically in Matlab program to solve the nonlinear differential equations by the integration method as used by Rahman and Kowser [18]. At first, validation of the code will be established by comparing the results obtained by the code with the exact solutions available by classical theory. Once relation is known, equations of dynamics will be used and relevant results will be obtained and analyzed to find the conditions of vibration isolation of a cantilever SMA beam for different changing parameters (frequency ratio, damping ratio, shape of cross-section etc.).

Briefly the steps will be as follows:

(i) At first, the experimentally found non-linear stress-strain curve of SMA obtained [17] will be used to evaluate the moment-curvature and reduced modulus- curvature relations.

(ii) Using the relations of step (i) and equilibrium equation, the P-δ curve will be traced for a particular SMA beam considering geometric linearity and linearly elastic material. The restoring force will be determined from the P-δ curve and will be used in equations of vibration isolation. To simulate the classical theory of vibration isolation, end-shortening effect will be excluded at first. Next, end shortening effect will be included and again P-δ curve will be traced. Thus, change in conditions of vibration isolation can be evaluated for a particular SMA beam when shortening effect will be considered.

(iii) Geometric non-linearity effect will be included in the previous step and again P-δ curve will be determined to be used in equations of vibration isolation.

(iv) Material non-linearity effect will be included in the immediate previous step by using the relations as mentioned in step (i) and P-δ curve will be traced to be used in equations of vibration isolation.

(v) Change of vibration isolation conditions will be examined for different cross-sections (rectangular and equivalent circular) and damping ratio.

CHAPTER 2

LITERATURE REVIEW

Forced vibration on precise equipment, machines, structures, buildings are often unavoidable. It weakens the performance of precise equipment and machines and is detrimental to the health of buildings and structures [20]. Isolation of the precision equipment from the adverse effect of forced vibration on structures is essential for ensuring its proper operation. Forced vibration can be isolated or minimized through properly designed springs and dampers[21], [1]. There are two types of isolating vibration i.e. active and passive ways. Passive isolation systems lessen vibration using the natural features of spring and damper i.e. stiffness and damping properties whereas active vibration isolation systems use a control system with integrated sensors and actuators, hence enhancing low-frequency performance. In many instances, active isolation from vibration is costly and unreliable [22]. In this situation, the passive isolation system performs quite well and is very cost efficient [23]. To analyze the isolation of vibration, transmissibility is the crucial element. There are two types of transmissibility i.e. force transmissibility and displacement transmissibility. The force transmissibility of a linear vibration isolation system under harmonic stimulation is determined by the ratio between the force transmitted to the host structure and the excitation force amplitude [24]. And the displacement Transmissibility is the ratio of the payload displacement amplitude to the base displacement amplitude [24]. When the value of transmissibility is less than one and decreases with frequency ratio or speed ratio, then the system is vibrationally isolated. Numerous engineers and scientists have been interested in nonlinear vibration isolation [25], since it may achieve a low dynamic stiffness and therefore a low natural frequency, while also having lower static deflection [26], [27]. Consequently, nonlinear vibration isolation involves the expense of complexity, nonlinearity, which is deemed desirable in some applications, such as vibration management of the integrated satellite system [28]–[30]. In the work, vibration isolation of a superelastic shape memory alloy cantilever beam is explored.

Beams are frequent structural components in a variety of architectural, civil, and mechanical engineering projects [31], and the study of the bending of straight beams is an important and fundamental aspect of the broader science of mechanics of materials and structural mechanics. In engineering applications, cantilever beams are regarded as one of the most vital components. These applications include the usage of cantilevers in mechanical and aeronautical models such as fixed-wing aircraft, rotor blades for helicopters, and solar arrays. Moreover, the civil engineering sector use these structures for cantilever bridges and balconies [32]. Cantilever beams are often subjected to significant deflection and vibrational loads in real-world applications. Again, cantilever beams are often made lighter by reducing excess components, mostly for economic and spatial reasons. In addition, Rahman state that slots/openings are produced by removing material from it [33].

Usually, beam bending is analyzed considering only small beam deflections to make it simple [34]. In this instance, the differential equation that controls the beam's behavior is linear and straightforward to solve. In this cases, small deflection of the beam is considered. However, the practical issue involves a situation with a significant amount of deflection of the beam, the differential equation must be solved using a nonlinear term [35].

Bele'ndez performed a numerical simulation using the Runge–Kutta–Felhberg technique to determine the tip deflection of an extremely thin beam subjected to a combined stress [36]. The authors analyzed the massive deflections of a uniform cantilever beam under a combined load consisting of an external vertical concentrated force at the free end and a uniformly distributed load and compared the numerical findings with the experimental ones.

When the load is linearly proportional to the magnitude of the displacement, this is referred to as a linear analysis, however when the relationship is nonlinear, this is referred to as a nonlinear analysis. Because of this phenomenon, the stiffness of the system does not remain constant for the system, and as a consequence, the force exerted on it is a nonlinear function of its degree of deformation. It would be a polynomial or nonlinear function of deformation. In the actual field applications of cantilever beams, there are a number of nonlinearities, such as the end shortening effect, geometric nonlinearity, and material nonlinearity etc. [18], [34].

When a cantilever is subjected to an excessive amount of deflection, the overall horizontal length becomes shorter than it was initially during the buckling concave shape, resulting in a drop in moment value. This phenomenon is known as the end shortening effect. The impact of end shortening on tip deflections is substantial. For instance, it is observed that the load-deflection curves are initially straight, but begin to vary nonlinearly as the load increases. If end shortening is included, the load-deflection curves are concave upward [18], [37].

Due to the substantial movement of the cantilever beam, the neutral fiber is nonlinearly displaced from its initial location, causing a change in the specimen's cross section throughout its length. This study is formulated using nonlinear bending theory. The phenomenon is referred to as geometric nonlinearity. Consequently, the precise curvature expression is used in the moment-curvature connection. The bending of a cantilever beam was used to show the notion of geometric nonlinearity in the work [31] and the mathematical study of this system's equilibrium was not very challenging. The resultant nonlinear second-order differential equation was numerically solved utilizing the Runge-Kutta technique of the fourth order [38]. However, unless small deflections are considered, there is no analytical solution, since significant deflections require the solution of a differential equation with a nonlinear factor. According to [34], [39], the issue involves geometric nonlinearity. Then, The work[31] provides the better understanding of geometric nonlinearity.

Another one i.e. material nonlinearity is often connected with the material's plasticity or hyperelasticity/superelasticity when the Young's Modulus does not remain constant throughout deformation. Shape Memory Alloys show the material nonlinearity effect due to the fact that its stress versus strain curve is not conventional and has a nonlinear relationship.

Adaptive structures capable of sensing, diagnosing, and acting have been developed in response to the increased need for smart materials to enhance structural performance. Smart materials may alter their rigidity, shape, natural frequency, damping, and other mechanical properties in response to changes in temperature, electric field, or magnetic field. Shape memory alloys (SMAs), one of the most prevalent smart materials, have shown considerable benefits in the areas of structural response control [40], structural shape control[41] and damping improvement[42]. Due to their capacity to withstand and recover huge amounts of strain, dissipate high levels of energy, and provide a restoring force for the system, pseudoelastic characteristics of SMAs are particularly desirable for passive vibration isolation. Consequently, SMAs have become more prevalent in the passive vibration isolation of the host building.

Shape memory alloy (SMA) being a smart material is extensively used in structures to carry quasi-static load. Under quasi-static load, the response of a cantilever SMA beams with reducing cross section was investigated [18]. When the specimen of SMA is unloaded, the superelastic SMAs may recover incredibly enormous stresses as well as to dampen vibration [17]. However, they exhibit extremely nonlinear stress-strain relations, with intrinsic asymmetry in tension and compression [17]. The average Young's Modulus during the parent phase was 65 GPa [17]. The use of SMAs for vibration isolation and damping of mechanical systems was investigated [19]. The free and forced vibration of a free-standing bridge of superelastic SMA (TiNiCuCo) film with applications was investigated [43]. During the load-induced martensitic phase change, the evolution of the martensitic phase fraction was predicted using a thermodynamics-based finite element model there. The effects of pre-strain, strain rate, and excitation load on the hysteresis of stress-strain characteristics were explored in order to calculate damping energies. The analysis was carried out under non-isothermal settings, taking into account heat transport and the rate-dependence of latent heat release and absorption. They demonstrated that damping energy might be optimized by using an optimal pre-strain. Use of shape memory alloys in seismic resistant design and retrofit was reviewed in [44]. The hysteretic behaviour of pseudoelastic SMAs results in a high dissipation capacity that can be used to attenuate undesired vibrations of a mechanical system or structure [19]. Various SMA dampers were developed to reduce structural vibration responses [45]. Vibration characteristics of shafts made of superelastic shape memory alloy has been analyzed emphasizing following points during whirling: mass eccentricity ratio, whirl speed ratio, spin ratio, damping ratio, synchronous & asynchronous modes, and, the effect of material nonlinearity [46], [47]. The response of beams depends on the shape of cross-section. Unlike the linearly elastic structures, response of superelastic SMA beams depends on the shape of cross-section[46], [47]. Therefore, vibration characteristics of the SMA beams will be different for different shapes of cross section.

Despite the fact that SMA has been used for vibration control for a long time[23], the vibration isolation of a SMA cantilever beam itself has not yet been investigated. This is especially the case when taking into consideration the combined effects of geometrical nonlinearity, material-nonlinearity, and end-shortening. This aspect is brought forth further in the aforementioned work.

CHAPTER 3

GOVERNING EQUATIONS

3.1 General

In this chapter governing differential equations and the other additional equations necessary to obtain the tip deflections, vibration amplitude, bending moment and reduced modulus of the beam are discussed.

Rearranging and employing necessary transformations, 2nd order differential equations are converted to first order differential equations. Runge-Kutta 4th order method of numerical integration is applied to solve those first order differential equations. For steady-state vibration of the beam, exact and numerical solutions are obtained from linear and non-linear governing equations, respectively. However, these numerical solutions are time dependent and cover both transient (initially) and steady-state (finally) vibration.

3.2 Governing Differential Equations for the Cantilever Beam for Deriving Load Deflection Relation

The basic equations for the analysis of beam can be derived by considering the beam subjected to a tip load *P* (Figure 3.2.1). The Euler-Bernoulli's governing equations are:

$$EI\frac{d^2y}{dx^2} - PL + Px = 0 \qquad (3.2.1)$$

$$EI\frac{\dfrac{d^2y}{dx^2}}{[1+(\dfrac{dy}{dx})^2]^{3/2}} - PL + Px = 0 \qquad (3.2.2)$$

The symbols used here indicate;

E = modulus of elasticity (MPa)

I = moment of inertia (mm^4)

P = amplitude of the applied load (N)

L = length of the beam (mm)

Equations (3.2.1) and (3.2.2) are linear and nonlinear Bernoulli-Euler's equation, respectively. Boundary conditions are:

$$y = 0 \qquad \text{at } x = 0$$

$$\frac{dy}{dx} = 0 \qquad \text{at } x = 0$$

Though the boundary conditions remain the same, the governing equation itself has become much more complicated than that obtained from the linear theory. Therefore, numerical techniques should be used to get the deflection. The design is based on the inelastic properties of structural materials. The shearing effects have been neglected because it is a slender beam.

The load versus tip deflection curve for linear beam is obtained by solving the second order linear governing equation (3.2.1). The deflections are determined for non-linear governing equation (3.2.2) with the numerical procedure.

3.3 Large Deflection Analysis of the Cantilever Beam

A cantilever beam of circular or rectangular cross-sectional area (Figures 3.2.1 and 3.3.1) was simulated. Since the beams are slender (slenderness ratio, $\frac{L}{r} = 200$) for the present case, only pure bending is taken into account ignoring the effect of shearing stresses. When bending is large with respect to the span of the beam, the governing equation of the elastic curve for a cantilever beam with a point load P (Figures 3.2.1 and 3.3.1), in terms of large deflection formulation is given in equation (3.2.2).

Equation (3.2.2) neglects the effect of end-shortening of the tip (δ_H). If this end-shortening is considered, only the second term of equation (3.2.2), is to be changed as P(L-δ_H). The above equation is highly nonlinear (geometrically) and has been solved numerically in the present study.

For calculating this end-shortening, δ_H, let us consider a cantilever beam having length L acted upon by a load P. On the elastic curve, an infinitesimal segment length *ds* is given by

$$ds = \sqrt{dx^2 + dy^2}$$

Therefore, the total length of the elastic curve is given by

$$s = \int_0^{X_H} \sqrt{dx^2 + dy^2}$$

$$= \int_0^{X_H} \sqrt{1 + (\frac{dy}{dx})^2}\, dx \text{ ………………………………………………………..…....(3.3.1)}$$

Where $X_H = L - \delta_H$

With the assumption of inextensible elastic curve, δ_H is calculated numerically by trial. At first the elastic curve is evaluated from the equation (3.2.2) without considering δ_H. Next, assuming the value of $X_H = L - \delta_H$, in such a way that the value of integration of equation (3.3.1) becomes $s \approx L$, it can be said that end-shortening is, $\delta_H = L - X_H$. In this thesis, δ_H was calculated with the following convergence criteria, $L \geq s \geq 0.995L$. Then putting the value of δ_H in the equation (3.2.2) of the elastic curve, deflections at corresponding loads can be found. Alternately, at first a small value of δ_H is assumed and equation (3.2.2) is solved. Once the elastic curve is known, equation (3.3.1) is integrated numerically by Simpson's 3/8th rule to check whether the assumed value of δ_H is accurate or, needs to be improved by the next step. Therefore, in order to take into account, the end-shortening, equations (3.2.2) and (3.3.1) have to be solved simultaneously.

3.4 Beam Deflection Analysis for Geometric Non-linearity

Let, $\frac{dy}{dx} = z$ ……………………………………………………...…………..…(3.4.1)

Equation (3.2.2) becomes

$$\frac{EI\frac{dz}{dx}}{(1+z^2)^{3/2}} = P(L-x) \quad \text{(3.4.2)}$$

Rearranging equation (3.4.2)

$$\frac{dz}{(1+z^2)^{3/2}} = \frac{P(L-x)}{EI}dx \quad \text{(3.4.3)}$$

Let, $z = \tan\theta$ ……………………………………………………………….……(3.4.4)

Differentiating equation (3.4.4)

$$dz = \sec^2\theta d\theta \quad \text{(3.4.5)}$$

From equation (3.4.3)

$$\frac{\sec^2\theta d\theta}{(1+\tan^2\theta)^{3/2}} = \frac{P(L-x)}{EI}dx$$

$$\frac{\sec^2\theta d\theta}{\sec^3\theta} = \frac{P(L-x)}{EI}dx$$

$$\cos\theta d\theta = \frac{P(L-x)}{EI}dx \quad \text{(3.4.6)}$$

Integrating equation (3.4.6)

$$\sin\theta = \frac{P}{EI}(Lx - \frac{x^2}{2}) + C_1$$

$$\sin\tan^{-1} z = \frac{P}{EI}(Lx - \frac{x^2}{2}) + C_1$$

$$\frac{z}{\sqrt{1+z^2}} = \frac{PL}{EI}x - \frac{P}{2EI}x^2 + C_1 \quad \text{(3.4.7)}$$

Let,

$$Q = \frac{PL}{EI}$$

$$R = \frac{P}{2EI}$$

From equation (3.4.7)

$$\frac{z}{\sqrt{1+z^2}} = Qx - Rx^2 + C_1$$

$$\frac{1+z^2}{z^2} = \frac{1}{(Qx - Rx^2 + C_1)^2}$$

$$\frac{1}{z^2} = \frac{1}{(Qx - Rx^2 + C_1)^2} - 1$$

$$z^2 = \frac{(Qx - Rx^2 + C_1)^2}{1-(Qx - Rx^2 + C_1)^2}$$

$$z = \frac{(Qx - Rx^2 + C_1)}{\sqrt{1-(Qx - Rx^2 + C_1)^2}}$$

$$\frac{dy}{dx} = \frac{(Qx - Rx^2 + C_1)}{\sqrt{1-(Qx - Rx^2 + C_1)^2}} \quad \text{...(3.4.8)}$$

At $x = 0, \frac{dy}{dx} = 0, z = 0$

From equation (3.4.8)

$$C_1 = 0$$

$$\frac{dy}{dx} = \frac{(Qx - Rx^2)}{\sqrt{1-(Qx - Rx^2)^2}}$$

$$dy = \frac{(Qx - Rx^2)}{\sqrt{1-(Qx - Rx^2)^2}}\,dx$$

$$dy = \frac{(\frac{PL}{EI}x - \frac{P}{2EI}x^2)}{\sqrt{1-(\frac{PL}{EI}x - \frac{P}{2EI}x^2)^2}}\,dx \quad \text{...(3.4.9)}$$

Integrating equation (3.4.9), tip deflection for different loads can be found numerically to plot the *P-δ* curve.

3.5 Inclusion of Vibration in the Governing Equation

A cantilever beam (Figure 3.5.1) subjected to a time varying tip load can be modeled as the spring mass system with damper (Figure 3.5.2).

The governing equation of vibration is;

$$m\ddot{x} + c\dot{x} + kx = F_0 sin(\omega t) \quad \text{(3.5.1)}$$

$$\ddot{x} + \frac{c}{m}\dot{x} + \frac{k}{m}x = \frac{F_0}{m}\, sin(\omega t) \quad \text{(3.5.2)}$$

The symbols used here indicate;

m = mass of the applied force

$\ddot{x}$ = acceleration of the beam

$\dot{x}$ = velocity of the beam

k = stiffness of the system

kx = restoring force of the system

F_0 = amplitude of the applied force which is equal to mg

ω = forcing/exciting frequency

c = damping coefficient

t = time

From equation (3.5.2), the damping coefficient (c) can be replaced with the critical damping coefficient times damping ratio. That is, damping ratio (ζ) = $\frac{c}{c_c}$ = $\frac{c}{2m\omega_n}$, where ω_n is the natural frequency of the superelastic SMA cantilever beam. And the speed ratio, $\beta = \frac{\omega}{\omega_n}$.

In the present study the restoring force, kx in equation 3.5.1 will be replaced by the following non-linear form:

$$Restoring\ Force = k_1x^3 + k_2x^2 + k_3x + k_4 \ldots\ldots\ldots\ldots\ldots\ldots(3.5.3)$$

Equation (3.5.2) is solved numerically by Runge-Kutta 4th order method of numerical integration since it contains a non-linear equation (3.5.3) of restoring force.

The detailed Runge-Kutta 4th order method of numerical integration is given in **APPENDIX-A**.

3.6 Inclusion of Material Non-linearity in the Governing Equations

3.6.1 Cantilever Beam of Circular Cross-Section

For materials having non-linear stress-strain relations Timoshenko [16] derived the $M - \Delta$ and $E_r - \Delta$ relations for a rectangular beam section. He first defined the term reduced modulus, E_r for inelastic bending of beams.

Following Timoshenko [16], it is assumed that the cross-section of the beam remains plane during pure bending; hence elongations and contractions of longitudinal fibers are proportional to their distances from the neutral surface. Further assuming that during bending there exists the same relation between stress and strain as in the case of simple tension and compression, the stresses produced can be found out by a bending moment of a given magnitude. Considering the beam of circular cross-section in Figures 3.6.1.1 and 3.6.1.2, it is assumed that the radius of curvature of the neutral surface produced by the moments M is equal to ρ. In such a case the unit elongation of a fiber at a distance y from the neutral surface is

$$\varepsilon = \frac{y}{\rho} \ldots\ldots\ldots\ldots\ldots\ldots(3.6.1.1)$$

Denoting h_1 and h_2 (Figure 3.6.1.2) the distances from the lower and the upper surfaces of the beam respectively to the neutral axis, we find that the elongation in the outermost fibers are

$$\varepsilon_1 = \frac{h_1}{\rho},\ \varepsilon_2 = -\frac{h_2}{\rho} \ldots\ldots\ldots\ldots\ldots\ldots(3.6.1.2)$$

It is seen that the elongation or contraction of any fiber is readily obtained provided we know the position of the neutral axis, say ratio $\frac{h_1}{h_2}$, and the radius of curvature ρ. These two quantities can be found from the two equations of static equilibrium:

$$\int \sigma dA = \int_{-h_2}^{h_1} \sigma dA = 0 \text{..(3.6.1.3)}$$

$$\int \sigma y dA = \int_{-h_2}^{h_1} \sigma y dy = M \text{.....................................(3.6.1.4)}$$

The first of these equations states that the sum of normal forces acting on a cross-section of the beam vanishes, since those forces represent a couple. The second equation states that the moment of the same forces with respect to the neutral axis is equal to the bending moment *M*.

Equation (3.6.1.3) is now used for determining the position of the neutral axis. For finding the area *dA* at first (Figure 3.6.1.2), we consider equation of the circle

$$x^2 + y^2 = r^2, (r = \text{radius of the circle}) \text{...........................(3.6.1.5)}$$

$$x = \sqrt{r^2 - y^2} \text{...(3.6.1.6)}$$

Here, $$dA = bdy \text{..(3.6.1.7)}$$

$$b = 2x = 2\sqrt{r^2 - y^2} \text{...(3.6.1.8)}$$

Again $$dA = bdy = 2\sqrt{r^2 - y^2}\, dy \text{....................................(3.6.1.9)}$$

Now, employing dA in equation (3.6.1.3), we get

$$\int \sigma dA = 2\int_{-h_2}^{h_1} \sigma \sqrt{r^2 - y^2}\, dy = 0 \text{...............................(3.6.1.10)}$$

From equation (3.6.1.1)

$$y = \rho \mathcal{E} \text{..(3.6.1.11)}$$

$$dy = \rho d\mathcal{E} \text{..(3.6.1.12)}$$

Therefore, equation (3.6.1.9) becomes

$$dA = 2\sqrt{r^2 - \rho^2 \varepsilon^2}\rho d\mathcal{E} \text{...(3.6.1.13)}$$

Employing equation (3.6.1.13) in (3.6.1.10), we get,

$$\int \sigma dA = 2\int_{-h_2}^{h_1} \sigma \sqrt{r^2 - y^2}\, dy = 2\rho^2 \int_{\varepsilon_2}^{\varepsilon_1} \sigma \sqrt{(\frac{r}{\rho})^2 - \varepsilon^2}\, d\varepsilon = 0 \text{............(3.6.1.14)}$$

Hence the position of the neutral axis is such that the integral $\int_{\varepsilon_2}^{\varepsilon_1} \sigma \sqrt{(\frac{r}{\rho})^2 - \varepsilon^2}\, d\varepsilon$ vanishes.

Therefore, $$\int_{\varepsilon_2}^{\varepsilon_1} \sigma \sqrt{(\frac{r}{\rho})^2 - \varepsilon^2}\, d\varepsilon = 0 \text{...............................(3.6.1.15)}$$

Equation (3.6.1.15) is rewritten as

$$\int_{\varepsilon_2}^{0} \sigma \sqrt{(\frac{r}{\rho})^2 - \varepsilon^2}\, d\varepsilon = \int_{0}^{\varepsilon_1} \sigma \sqrt{(\frac{r}{\rho})^2 - \varepsilon^2}\, d\varepsilon \text{.....................(3.6.1.16)}$$

Integral on the left hand side of the equation (3.6.1.16) represents normal forces acting on the compression region of the beam and right hand side of the equation represents normal forces acting on the tension region of the beam.

To determine the neutral axis position, we use the curve AOB (Figure 3.6.1.3a) which represents the ($\sigma - \varepsilon$) diagrams in tension and compression for the material of the beam, and we denote $\varDelta$, the sum of the absolute values of the maximum elongation and the maximum contraction, which is

$$\varDelta = |\varepsilon_1| + |\varepsilon_2| = \left|\frac{h_1}{\rho}\right| + \left|\frac{h_2}{\rho}\right| = \frac{h}{\rho} = \frac{d}{\rho} \text{...........................(3.6.1.17)}$$

$$\rho = \frac{d}{\varDelta} \text{..(3.6.1.18)}$$

$$\rho = \frac{d}{|\varepsilon_1| + |\varepsilon_2|} \text{...(3.6.1.19)}$$

Using equation (3.6.1.19) in equation (3.5.1.15), we get

$$\int_{\varepsilon_2}^{\varepsilon_1} \sigma \sqrt{\left(\frac{r}{\frac{d}{|\varepsilon_1| + |\varepsilon_2|}}\right)^2 - \varepsilon^2}\; d\varepsilon = 0 \text{..................................(3.6.1.20)}$$

Or, $$\int_{\varepsilon_2}^{\varepsilon_1} \sigma \sqrt{\left(\frac{|\varepsilon_1|+|\varepsilon_2|}{2}\right)^2 - \varepsilon^2}\, d\varepsilon = 0 \quad \text{.......................................(3.6.1.21)}$$

Since, integral of equation (3.6.1.21) has no closed form solution, numerical solution technique has been used. As stress-strain curve of superelastic SMA is asymmetric in tension and compression beyond proportional limit,

Therefore, $$|\varepsilon_1| \neq |\varepsilon_2|$$

Therefore, from the stress-strain curve $|\varepsilon_2|$ is chosen. And for any chosen values of $|\varepsilon_2|$, by applying numerical integration method, $|\varepsilon_1|$ is found out which can make the integral zero. In this manner we obtain strain ε_2 and ε_1 in the outermost fibers; equation (3.6.1.2) then gives

$$\frac{h_1}{h_2} = \left|\frac{\varepsilon_1}{\varepsilon_2}\right| \quad \text{...(3.6.1.22)}$$

This determines the position of neutral axis. Observing that elongations ε are proportional to the distance from the neutral axis, we conclude that the curve AOB (Figure 3.6.1.3a) also represents the distribution of bending stresses along the depth of the beam, if h is substituted for Δ.

Therefore, the equation of moment at any of the point on the beam is,

$$M = \int \sigma y dA = 2\rho^3 \int_{\varepsilon_2}^{\varepsilon_1} \sigma\varepsilon \sqrt{\left(\frac{r}{\rho}\right)^2 - \varepsilon^2}\, d\varepsilon \quad \text{...........................(3.6.1.23)}$$

Applying numerical integration method to equation (3.6.1.23), moments are known. Value of stress in equation (3.6.1.23) is taken from corresponding value of strain from stress-strain curve.

If the stress-strain curve is known for a specific material, then considering the value of strain (piece-wise linear) from the diagram, value of corresponding stress can be found out.

Equation of straight line for $(x - y)$ coordinate,

$$y = vx + z \text{ ………….…...………………………….…..}(3.6.1.24)$$

Here, v is the gradient of the straight line.
Similarly for $(\sigma - \varepsilon)$ curve,

$$\sigma_{i+1} = v\mathcal{E}_{i+1} + \sigma_i \text{....……………………………..…...}(3.6.1.25)$$

Equations (3.6.1.23) and (3.6.1.25) give,

$$M = 2\rho^3 \int_{\mathcal{E}_2}^{\mathcal{E}_1} \left[(v\mathcal{E}_{i+1} + \sigma_i) \sqrt{\left(\frac{r}{\rho}\right)^2 - \mathcal{E}^2} \right] \mathcal{E} d\mathcal{E} \text{………………..}(3.6.1.26)$$

Incorporating moment of inertia (*I*) in equation (3.6.1.26), we get,

$$M = \frac{I}{\rho} \times \frac{128\mathrm{p}}{\pi d\Delta^3} \int_{\mathcal{E}_2}^{\mathcal{E}_1} \left[(v\mathcal{E}_{i+1} + \sigma_i) \sqrt{\left(\frac{r}{\rho}\right)^2 - \mathcal{E}^2} \right] \mathcal{E}\, d\mathcal{E} \text{………..………………...}(3.6.1.27)$$

Let, moment of inertia,

$$I = \frac{\pi d^4}{64} \text{ ……………..……..…….……………….....}(3.6.1.28)$$

Linear moment-curvature relation,

$$M = \frac{EI}{\rho} \text{………….………………..……...……….}(3.6.1.29)$$

If equations (3.6.1.27) and (3.6.1.29) are compared, then for bending of beam following , we conclude that beyond the proportional limit, the curvature produced by a moment *M* can be calculated from the equation,

$$M = \frac{E_r I}{\rho} \text{………………….......……….….……..}(3.6.1.30)$$

Here E_r is the reduced modulus. Now comparing equations (3.6.1.27) and (3.6.1.30), the value of E_r (reduced value) can be obtained as follows.

$$E_r = \frac{128\rho}{\pi d\Delta^3}\int_{\varepsilon_2}^{\varepsilon_1}\left[(v+\sigma_i)\sqrt{\left(\frac{r}{\rho}\right)^2 - \varepsilon^2}\right]\varepsilon\, d\varepsilon \ldots\ldots\ldots\ldots\ldots\ldots(3.6.1.31)$$

The integral in this expression represents the moment with respect to the vertical (σ) axis through the origin O of the shaded area shown in Figure 3.6.1.3a. Since the ordinate of the curve in the figure represents stresses, and the abscissas, strain, the integral and also E_r have the dimension of GPa, i.e., the same dimension as the modulus E. The magnitude of E_r for a given material is a function of Δ or of h/ρ. Taking several values of Δ and using each time the curve in Figure 3.6.1.3a as was previously explained, we determine for each value of Δ the corresponding outermost elongations ε_1 and ε_2, and from equation (3.6.1.31) the corresponding value of E_r as a function of ($\Delta = h/\rho$) is obtained.

Equations (3.6.1.26) and (3.6.1.31) can be solved by applying numerical method to obtain values of bending moment and reduced modulus for different values of Δ.

From the actual true stress-strain diagram (Figure 3.6.1.3b) random values of strain ε_2 from the compression region is chosen like that from Figure 3.6.1.3a and by using equation (3.6.1.21) and by applying trial and error method, values of strain ε_1 at tension region is found out for which result of the integral of equation (3.6.1.21) becomes zero each time. This determines the position of neutral axis and, value of total strain Δ as well. Numerical method is used to solve this problem in Matlab.

Using values of ε_1 and ε_2 in equation (3.6.1.17), value of Δ and corresponding ρ is found out from equation (3.6.1.18) as well. Now, taking several values of Δ and using equations (3.6.1.26) and (3.6.1.31), values of corresponding bending moment and reduced modulus are obtained. Again numerical method is used in Matlab to solve equations (3.6.1.26) and (3.6.1.31). Finally, Figures of $E_r - \Delta$ and M – are obtained for superelastic SMA beam.

3.6.2 Cantilever Beam of Equivalent Rectangular Cross-Section

For materials having non-linear stress-strain relations Timoshenko [16] derived the $M - \Delta$ and $E_r - \Delta$ relations for a rectangular beam section. He first defined the term reduced modulus, E_r for inelastic bending of beams.

The $M - \Delta$ and $E_r - \Delta$ relations are given by the following equations.

$$M = \frac{I}{\rho} \times \frac{12}{\Delta^3} \int_{\varepsilon_2}^{\varepsilon_1} [(v\varepsilon_{i+1} + \sigma_i)]\varepsilon \, d\varepsilon \qquad (3.6.2.1)$$

$$E_r = \frac{12}{\Delta^3} \int_{\varepsilon_2}^{\varepsilon_1} [(v + \sigma_i)]\varepsilon \, d\varepsilon \qquad (3.6.2.2)$$

The details of the derivation of equations (3.6.2.1) and (3.6.2.2) are given in the **APPENDIX-B**.

3.7 Solution Procedures

The load vs tip-deflection curve for classical theory without end-shortening effect is plotted by solving the equation (3.2.1) and end-shortening effect is included into the classical theory with the help of equation (3.3.1). Equation (3.4.9) is used to plot the load vs tip-deflection curve considering geometric non-linearity without end-shortening effect. End-shortening effect is added to the geometric non-linearity by simultaneously solving the equations (3.4.9) and (3.3.1). Material non-linearity issue is incorporated with the help of equations (3.6.1.27) and (3.6.1.31) for circular beam and equations (3.6.2.1) and (3.6.2.2) for equivalent rectangular beam. The detailed solution procedures for equations (3.6.1.27) and (3.6.1.31) are given in section 3.6.1. The details of the derivation of equations (3.6.2.1) and (3.6.2.2) are given in the **APPENDIX-B**. The load vs tip-deflection curve for material non-linearity and geometric non-linearity with end-shortening effect is plotted by solving equation (3.3.1), (3.4.9), (3.6.1.27), (3.6.1.31), (3.6.2.1) and (3.6.2.2).

From these load-deflection relations, the restoring forces are chosen as best fit non-linear curves. Then this best fit non-linear curves of restoring forces are inserted into the equation of vibration that converts the equation into non-linear mode which is solved numerically by the R-K 4^{th} order method of numerical integration (**APPENDIX-A**) since exact solution is not possible. Theses solution provides the transient (initially) and steady-state (finally) vibrations of superelastic SMA cantilever beam.

CHAPTER 4

RESULTS AND DISCUSSION

4.1 General Discussion

Vibrations of superelastic SMA cantilever beam considering different conditions (end-shortening, geometric non-linearity, material non-linearity, speed ratio, damping ratio and equivalent cross-section etc.) are extensively analyzed in terms of numerical solutions. Soundness of the mathematical scheme is proven in section 4.2. Section 4.3 analyzes the vibration for classical theory. In sections 4.4, 4.5 and 4.6, effects of considering end-shortening and geometric non-linearity are analyzed. Sections 4.7 and 4.8 discuss the effect of material non-linearity (w.r.t. Figures 3.6.1.3b, 4.7.1, 4.7.2) on the SMA beam's vibrations. Analysis of vibration considering material non-linearity and geometric non-linearity with end-shortening effect are studied through sections 4.9 to 4.13. Transmissibility of the vibration is discussed in section 4.14. In all cases viscous damping of different intensity is considered. It is assumed damping ratio (ξ) will be quite low (0.1) when the beam vibrates through air. However, if the beam's vibration is in liquid (water or, oil) other values of damping ratio of 0.1 to 1 might be more realistic.

In this dissertation the terms 'Transient' and 'Unsteady-state' are interchangeably used to indicate time dependent solutions. The term vibration or amplitude of the vibration are also interchangeably used to indicate magnitude of the vibration. In similar fashion, words 'Superelastic SMA' and 'SMA' are used interchangeably to indicate a smart material that can regain original size and shape from an apparently plastically deformed state. The term 'linear case' and 'classical theory' are also interchangeably used to indicate solutions obtained by solving the Euler-Bernoulli's linear governing equations (3.2.1) for beam.

Mathematical model that is developed in section 3.7 is used to obtain bending moment (M) vs. Δ and reduced modulus (E_r) vs. Δ curves. In this research, actual stress-strain curve of superelastic shape memory alloy (SMA) beam of diameter of 2 mm (Figure 3.6.1.3b) obtained by Rahman [17], is used to find the $M - \Delta$ (Figure 4.7.1) and $E_r - \Delta$

(Figure 4.7.2) relations. These relations are used to include material non-linearity issue in the analysis of the vibration isolation of the cantilever beam in Section 4.9.

Section 4.3 deals with linearly elastic beam material of the cantilever beam subjected to a time varying tip load that vibrates as a single degree of freedom system (SDOFS). Equation (3.2.1) is solved to obtain load-deflection curve. Using this load-deflection relation in equation (3.5.2), vibrations over time of the beam are found out by changing different parameters such as speed ratio (β), damping ratio, (ξ) etc.

4.1.1 The Beam Specifications for Section 4.3:

Beam length (L) = 200 mm, beam dia (d) = 2 mm, modulus of elasticity (E) = 65 GPa, linearly elastic bending stiffness of the beam ($k = 3EI/L^3$) = 19.14 N/m, natural frequency (ω_n) = 9.69 rad/s, critical damping of the beam (c_c) = 3.9535 Ns/m, Area (A) = 3.1416×10^{-6} m^2 and the area moment of inertia (I) = 7.854×10^{-13} m^4.

4.1.2 The Beam Specifications for Section 4.11:

Beam length (L) = 200 mm, beam width (b) = 1.8138 mm, beam height (h) = 1.7321 mm, modulus of elasticity (E) = 65 GPa, linearly elastic bending stiffness of the beam ($k = 3EI/L^3$) = 19.14 N/m, natural frequency (ω_n) = 9.69 rad/s, critical damping of the beam (c_c) = 3.9535 Ns/m, Area (A) = 3.1416×10^{-6} m^2 and the area moment of inertia (I) = 7.854×10^{-13} m^4.

The calculations of equivalent cross-sections are given in **APPENDIX-C**.

4.2 Code Validation

For classical theory, it's known to all of us that the isolation begins when the speed ratio β exceeds 1.414 with a certain level of damping, it doesn't matter how small or big the F_0 or ζ is. When speed ratio, β reaches to 1.414, the Transmissibility (TR) becomes 1. Further increase of speed ratio decrease the amplitude of the vibration and corresponding TR becomes less than 1. That is vibration isolated. Following table shows the value of TR for different damping ratios when β = 1.414. The numerical solutions provide a good agreement with the exact solution. The code used to solve the governing equation of vibration is further extended to solve the non-linear governing equation of vibration for different cases that are discussed from section 4.3 to section 4.14. The soundness of the following results can also be checked by Figure 4.14.1.1.

Table 4.2.1: Validation of the numerical scheme.

Speed Ratio $\beta = \frac{\omega}{\omega_n}$	Damping Ratio $\zeta = \frac{c}{c_c}$	$\text{TR} = \frac{F_t}{F_0}$		% Deviation
		Numerical Solution	Exact Solution	
1.44	0.05	1.0072	1	0.72
1.44	0.1	0.9900	1	1.00
1.44	0.5	1.0001	1	0.01
1.44	1.0	0.9808	1	1.92

4.3. Analysis of Vibration of the Superelastic SMA Cantilever Beam according to Classical Theory

Figure 4.3.1 shows the tip deflection against the applied load. The maximum tip deflection found is 0.104 m at 2 N load which is the maximum load chosen for the present study. This load vs tip deflection curve is plotted by solving the Euler-Bernoulli's linear governing equations (3.2.1) for beam.

Figure 4.3.2 shows the ever increasing amplitude of the vibration which is termed as resonance that indicates the speed ratio, $\beta = 1$ or the exciting frequency coincides with the natural frequency of the beam without damping. This is going to be infinite with time that also indicates the proof of numerical code since it is the expected scenario for the linear analysis.

Figures 4.3.3 to 4.3.4 show the effect of damping on the vibration. Here three damping ratios are chosen for each figure that are 0 (undamped), 0.05, 0.1 (underdamped) (Figure 4.3.3) and 0.1, 0.5 (underdamped) and 1 (critically damped) (Figure 4.3.4) for speed ratio, $\beta = 1$ to check the influence of the damping effect on the vibration. Increase of damping greatly reduces the vibration amplitude which is desired phenomena for the linear analysis. It can notably be observed that the amplitude of the vibration is significantly reduced when the beam is critically damped.

Figure 4.3.5 shows the effect of exciting frequency on the vibration with a damping ratio of $\zeta = 0.1$. Here three speed ratios are chosen that are 1, 1.414 and 2 to check the influence of speed ratio on the vibration. The amplitude of vibration is maximum at resonance (β =1) and the isolation begins when speed ratio exceeds 1.414 and then gradually decreases for the further increase of exciting frequency which is desired phenomena for the linear analysis.

Figure 4.3.6 shows the effect of exciting frequency on the vibration with a damping ratio of $\zeta = 0.1$. Here three speed ratios are chosen that are 3, 4 and 5 to check the influence of exciting frequency on the vibration. The amplitude of vibration is gradually decreasing with the increase of speed ratio since the speed ratios are above 1.414 which is the critical value after which the isolation of the vibration begins. These phenomena are expected in case of linear analysis.

4.4 Analysis of Vibration of the Beam Considering End-Shortening Effect

Figure 4.4.1 shows the load-deflection curve considering end-shortening effect. This load vs tip deflection curve is plotted by solving simultaneously the Euler-Bernoulli's linear governing equations (3.2.1) and equation (3.3.1). It indicates that the end-shortening effect becomes prominent above 0.2 N load. The maximum tip deflection considering end-shortening is approximately 0.066 m and without end-shortening (linear) is 0.104 m. The tip deflection is approximately 36.54% lower considering end-shortening than predicted by linear case at maximum load. This is due to the issue that considering end-shortening means the effective length of the beam is reducing that affects to reduce bending moment. That's why less tip deflection is observed considering end-shortening than classical theory.

Figure 4.4.2 indicates the amplitude of the vibration at resonance (β = 1) or the exciting frequency coincides with the natural frequency of the beam without damping considering end-shortening effect only. Interestingly, it can be noticed that the amplitude of the vibration is not going to be infinite over time as predicted by classical theory rather it is sufficiently suppressed below the amplitude when compared to the classical theory. The maximum amplitude found from Figure 4.3.2 is 0.1170 m.

Figure 4.4.3 shows a very interesting feature of the present study. It can be noticed that the amplitude of vibration is significantly lower when end-shortening is accounted. For linear case, the vibration is going to be infinite over time at resonance but it is too low to compare when end-shortening effect is considered.

Figures 4.4.4 to 4.4.6 are to compare the amplitudes of the vibrations for classical theory and considering end-shortening effect. Here speed ratio is kept constant that is, β = 1 and damping ratios are varied from ζ = 0.1 (Figure 4.4.4), ζ = 0.5 (Figure 4.4.5) to ζ = 1 (Figure 4.4.6). The vibrations are almost steady from very beginning of the commencement of the vibration when the end-shortening effect is considered. The amplitude of the vibration is largely lower considering end-shortening effect than that predicted by classical theory when the damping is low (Figure 4.4.4). Increased damping greatly reduces the vibrations for both the cases but the larger damping has more influence on the vibration when it is linear case. That's why the difference between the amplitude of the vibrations is gradually disappearing when the beam is going to be critically damped.

Figures 4.4.7 to 4.4.8 show the comparison for β = 3 (Figure 4.4.7) and β = 5 (Figure 4.4.8) between the amplitudes of the vibrations for linear case and considering end-shortening effect. Here damping ratio is kept constant that is ζ = 0.1 (underdamped). The difference between the two vibrations is significant initially (Figure 4.4.7). Increased speed ratio greatly reduces the vibrations for both the cases. The differences between the amplitudes of the vibration disappear when they become steady and coincide each other.

Figures 4.4.9 to 4.4.10 show the effect of damping on the vibration solely considering end-shortening effect. Here three damping ratios are chosen for each figure that are 0 (undamped), 0.1, 0.2 (underdamped) (Figure 4.4.9) and 0.3, 0.5 (underdamped) and 1 (critically damped) (Figure 4.4.10) for speed ratio, β = 1 to check the influence of the damping effect on the vibration when end-shortening effect is considered. The increase of damping slightly decreases the vibration amplitude when it is below critical damping. The amplitude of the vibration is somewhat significantly reduced when the beam is critically damped. After all, it can remarkably be observed that the impact of damping on the vibration is not so much significant when end-shortening effect is accounted.

Figure 4.4.11 shows the effect of exciting frequency on the vibration with a damping ratio of $\zeta = 0.1$. Here three forcing frequencies are chosen that are 1, 1.414 and 2 to check the influence of speed ratio on the vibration. Interestingly, it is seen that the maximum vibration amplitude is not found at resonance ($\beta = 1$). At the end of this chapter a section 4.13 will be discussed to find out where the maximum vibration amplitude is occurred when end-shortening effect with material non-linearity and geometric non-linearity is considered.

Figure 4.4.12 shows the effect of exciting frequency on the vibration with a damping ratio of $\zeta = 0.1$. Here three speed ratios are chosen that are 3, 4 and 5 to check the influence of exciting frequency on the vibration. The amplitude of vibration is gradually decreasing with the increase of speed ratio. It follows the similar trend to the classical theory.

4.5 Analysis of Vibration of the Beam Considering End-Shortening Effect with Geometric Non-linearity

Figure 4.5.1 shows the different load-deflection curves for different cases that are classical theory with and without end-shortening, geometrically non-linearity with and without end-shortening. The load-deflection curve for geometrically non-linear with end-shortening effect is plotted by solving simultaneously the Euler-Bernoulli's non-linear governing equation (3.2.2) for beam and equation (3.3.1). From the figure it can be seen that the maximum and minimum tip-deflections are found for geometrically non-linear without end-shortening and solely considering end-shortening effect, respectively.

Figure 4.5.2 shows a very interesting feature of the present study. It can be noticed that the amplitude of vibration is significantly lower at resonance ($\beta = 1$) without damping when geometrical non-linearity with end-shortening effect is considered. This is likely to match with the Figure 4.5.3. The maximum amplitude found from Figure 4.5.2 is 0.1251 m which is slightly higher than considering end-shortening effect only (0.1170 m). For classical theory, the vibration is ever increasing at resonance without damping but it is too low to compare when geometrical non-linearity with end-shortening effect is considered. It would be better to say that the effect of end-shortening on the vibration of the beam is more dominating than geometrical non-linearity.

Figures 4.5.3 to 4.5.5 compare the amplitudes of the vibrations for classical theory and considering geometric non-linearity with end-shortening effect. Here speed ratio is kept constant that is, β = 1 and damping ratios are varied from ζ = 0.1 (Figure 4.5.3), ζ = 0.5 (Figure 4.5.4) to ζ = 1 (Figure 4.5.5). The vibrations are almost steady from very beginning of the commencement of the vibration when geometric non-linearity with end-shortening effect is considered. The amplitude of the vibration is largely lower considering geometric non-linearity with end-shortening effect than that of classical theory when the damping is low (Figure 4.5.3). Increased damping greatly reduces the vibrations for both the cases but the amplitude of the vibration considering geometric non-linearity with end-shortening effect is lower and slightly higher than that predicted by classical theory (Figure 4.5.4 and Figure 4.5.5), respectively.

Figures 4.5.6 to 4.5.7 show the comparison for β = 3 (Figure 4.5.6) and β = 5 (Figure 4.5.7) between the amplitudes of the vibrations for linear case and considering geometric non-linearity with end-shortening effect. Here damping ratio is kept constant that is ζ = 0.1 (underdamped). The vibrations are highly transient in nature at the beginning. The difference between the two vibrations is significant initially (Figure 4.5.6). Increased speed ratio greatly reduces the vibrations for both the cases. The differences between the amplitudes of the vibration disappear when they become steady and coincide each other.

Figure 4.5.8 shows the effect of damping ratio on the vibration for geometrically non-linear beam with end-shortening effect. Here three damping ratios are chosen that are 0.3, 0.5 (underdamped) and 1 (critically damped) for β =1 to check the influence of the damping effect on the vibration. Increase of damping decreases the vibration amplitude. The amplitude of the vibration is significantly reduced when the beam is critically damped. The trend is similar when it is compared to the linear analysis.

Figure 4.5.9 shows the effect of exciting frequency on the vibration with a damping ratio of $\zeta = 0.1$. Here three forcing frequencies are chosen that are 1, 1.414 and 2 to check the influence of speed ratio on the vibration. Interestingly, it is seen that the maximum vibration amplitude is not found at resonance ($\beta = 1$) when geometric non-linearity with end-shortening effect is considered. At the end of this chapter a section 4.13 will be discussed to find out where the maximum vibration amplitude is occurred when end-shortening effect with material non-linearity and geometric non-linearity is considered.

Figure 4.5.10 shows the effect of exciting frequency on the vibration with a damping ratio of $\zeta = 0.1$ considering the beam is geometrically non-linear with end-shortening effect. Here three speed ratios are chosen that are 3, 4 and 5 to check the influence of exciting frequency on the vibration. The amplitude of vibration is greatly reduced with the increase of speed ratio. It follows the similar trend to the classical theory.

4.6 Comparisons among Vibrations of the Beam Considering Classical Theory with and without End-Shortening Effect and Geometric Non-linearity with End-Shortening Effect

Figures 4.6.1 to 4.6.5 compare the amplitudes of the vibrations considering classical theory with and without end-shortening effect and geometric non-linearity with end-shortening effect. Here speed ratio is kept constant that is, $\beta = 1$ and damping ratios are varied from $\zeta = 0.1$ (Figure 4.6.1), $\zeta = 0.5$ (Figure 4.6.2) to $\zeta = 1$ (Figure 4.6.3). Again the damping ratio is kept constant that is $\zeta = 0.1$ (underdamped) for $\beta = 3$ (Figure 4.6.4) and $\beta = 5$ (Figure 4.6.5). The analysis of these similar type of results are performed in the sections 4.4 to 4.5. This section is designed to observe that is there any significant discrepancy between the amplitudes of the vibration considering end-shortening effect and geometric non-linearity with end-shortening. It can be notably observed that there is no remarkable discrepancy between them. The vibrations almost overlap each other. So it would not be more to say that the vibration is mostly dominated by the end-shortening issue.

4.7 Analysis of Material Non-linearity Effect on the Cantilever Beam

As mentioned material non-linearity issue has been conveniently incorporated in terms of $\sigma - \varepsilon$ (Figure 3.6.1.3b), $M - \Delta$ (Figure 4.7.1) and $E_r - \Delta$ (Figure 4.7.2) relations for the beam material.

If $M - \Delta$ curve (Figure 4.7.1) of shape memory alloy is analyzed, it can also be seen that, up to Δ = 0.01 bending moment curve is a straight line but after that it is increasing with a decreasing slope. And, bending moments are 0.28 Nm and 0.30 Nm for circular and equivalent rectangular beam, respectively, corresponding to Δ = 0.01. So, if the bending moment is more than 0.28 Nm and 0.30 Nm for circular and equivalent rectangular beam, respectively, then beam will exhibit material non-linearity effect. For this research, M = 0.28 Nm and 0.30 Nm for circular and equivalent rectangular beam, respectively, are termed as the *threshold bending moments* (bending moment after which beam exhibits material non-linearity). This is because, if the value of Δ is more than 0.01, beam undergoes strain which is no more proportional to stress.

In Figure 4.7.1, the maximum bending moment is M_f = 1.768 Nm and 1.8277 Nm for circular and equivalent rectangular beam, respectively. According to linearly elastic model for the same bending moment corresponding elastic strain (Δ_l) will be only 0.0346 and 0.0358 for circular and equivalent rectangular beam, respectively. But by considering material non-linearity effect, for the same intensity bending moment of M_f = 1.768 Nm and 1.8277 Nm for circular and equivalent rectangular beam, respectively, actual total strain is Δ_f = 0.285 as seen from Figure 4.6.1. This shows actual strain is much larger than assumed by linear elastic model. In turn, this point proves the necessity of taking into account the material non-linearity effect.

Modulus of elasticity (E) of shape memory alloy material that is considered for this simulation is 65 GPa [17]. From Figure 4.7.2, it is observed that $E_r = E$ = 65 GPa up to Δ = 0.01. Therefore, superelastic SMA beam will exhibit linearly elastic behavior up to Δ = 0.01. For $\Delta > 0.01$, E_r starts decreasing as material non-linearity effect starts and the stress applied on the beam material exceeds elastic limit of the stress-strain curve (Figure 3.6.1.3b). So, material non-linearity effect indicates that the beam undergoes strain which is no more proportional to stress. The lowest values of E_r that is calculated are 16 GPa and 14 GPa for a total strain of 0.285 for circular and equivalent rectangular beam, respectively. In such a case the beam will show less bending stiffness (as, $E_r << E$). The *Er* vs Δ curves for both the circular and equivalent rectangular beam follow the similar pattern but it is slightly lower for rectangular beam than that of circular beam when both the beams are non-linearly elastic.

It should be mentioned here that upon unloading, SMA can recover large strain by virtue of super/pseudo elasticity through a hysteresis [17]. Therefore, large deformation for SMA can be termed as non-linearly elastic deformation. However, conventional engineering material like stainless steel (SS) invariably shows large inelastic/plastic strain upon unloading due to material non-linearity effect [17].

4.8 Effect of Reduced Modulus (E_r) on the Cantilever Beam's Natural Frequency (ω_n)

Bending moments will be different at different points on the beam for a specific load when it is vibrating. When bending moment at any point along the beam length exceeds the threshold bending moment, corresponding Young's modulus will be lower than that for initial linearly elastic model (Figure 4.7.1 and Figure 4.7.2). As a whole, the resultant bending stiffness (k) will decrease. But, natural frequency depends on k as explained below,

$$\delta \text{ (Beam's tip deflection)} = \frac{PL^3}{3EI}$$

$$\text{Therefore, } k = \frac{P}{\delta} = \frac{3EI}{L^3} \text{ and, } \omega_n = \sqrt{\frac{k}{m}} = \sqrt{\frac{3EI}{mL^3}}$$

Resonance occurs when $\omega = \omega_n$. As E reduces to E_r, therefore ω_n will also reduce to $\sqrt{\frac{3E_rI}{mL^3}}$. Obviously, resonance will occur at a lower speed than that expected by linearly elastic model.

4.9 Analysis of Vibration of the Beam Considering Material Non-linearity with End-Shortening Effect

Figures 4.9.1 to 4.9.4 compare the amplitudes of the vibrations for classical theory and considering material non-linearity with end-shortening effect. Here speed ratio is kept constant that is, β = 1 and damping ratios are varied from ζ = 0 (undamped, Figure 4.9.1), ζ = 0.1 (Figure 4.9.2), ζ = 0.5 (Figure 4.9.3) to ζ = 1 (Figure 4.9.4). The vibrations are almost steady from very beginning of the commencement of the vibration when material non-linearity with end-shortening effect is considered at resonance (β = 1) with a certain level of damping. The maximum amplitude found from Figure 4.9.1 is 0.230 m considering material non-linearity with end-shortening effect at resonance (β = 1) without damping. The amplitude of the vibration is largely lower considering material non-linearity with end-shortening effect than that predicted by classical theory when the damping is low (Figure 4.9.1 and Figure 4.9.2). Increased damping greatly reduces the vibrations for both the cases but the amplitude of the vibration considering material non-linearity with end-shortening effect is slightly lower than that predicted by classical theory (Figure 4.9.3 and Figure 4.9.4), when large damping is applied to the beam.

Figures 4.9.5 to 4.9.6 show the comparison for β = 3 (Figure 4.9.5) to β = 5 (Figure 4.9.6) between the amplitudes of the vibrations for linear case and considering material non-linearity with end-shortening effect. Here damping ratio is kept constant that is ζ = 0.1 (underdamped). The vibrations are highly transient in nature at the beginning. Increased speed ratio greatly reduces the vibrations for both the cases. The differences between the amplitudes of the vibration disappear when they approach steady-state and coincide each other.

4.10 Analysis of Vibration of the Beam Considering Material Non-linearity and Geometric Non-linearity with End-Shortening Effect

Figures 4.10.1 to 4.10.4 show the comparison for β = 1 between the amplitudes of the vibrations for classical theory and considering material non-linearity and geometric non-linearity with end-shortening effect where damping ratios are varied from ζ = 0 (undamped, Figure 4.10.1), ζ = 0.1 (Figure 4.10.2), ζ = 0.5 (Figure 4.10.3) to ζ = 1 (Figure

4.10.4). The vibrations are almost steady from very beginning of the commencement of the vibration when material non-linearity and geometric non-linearity with end-shortening effect is considered at resonance (β = 1) with a certain level of damping. The maximum amplitude found from Figure 4.10.1 is 0.1648 m considering material non-linearity and geometric non-linearity with end-shortening effect at resonance (β = 1) without damping. The amplitude of the vibration is largely lower considering material non-linearity and geometric non-linearity with end-shortening effect than that predicted by classical theory when the damping is low (Figure 4.10.1 and Figure 4.10.2). Increased damping greatly reduces the vibrations for both the cases but the amplitude of the vibration considering material non-linearity and geometric non-linearity with end-shortening effect is slightly lower than that predicted by classical theory (Figure 4.10.3) and they almost overlap when critically damped (Figure 4.10.4).

Figures 4.10.5 to 4.10.6 show the comparison for β = 3 (Figure 4.10.5) to β = 5 (Figure 4.10.6) between the amplitudes of the vibrations for linear case and considering material non-linearity and geometric non-linearity with end-shortening effect. Here damping ratio is kept constant that is ζ = 0.1 (underdamped). The vibrations are highly transient in nature at the beginning. Increased speed ratio greatly reduces the vibrations for both the cases. The differences between the amplitudes of the vibration disappear when they approach steady-state and coincide each other.

Figure 4.10.7 shows the comparison between the amplitudes of the vibrations considering classical theory with end-shortening, geometric non-linearity with end-shortening, and material non-linearity and geometric non-linearity with end-shortening. Here speed ratio is chosen, β = 1 without damping. The vibrations for all the above-mentioned cases are not likely to go infinity as classical theory predicts. From the figure, maximum amplitude of the vibration is found 0.1648 m considering material non-linearity and geometric non-linearity with end-shortening effect followed by geometric non-linearity with end-shortening (0.1251 m) and considering end-shortening only (0.1170 m).

Of course, the effect of material non-linearity would be significant for a shorter beam while the effect geometrical non-linearity would be significant for a more slender beam.

4.11 Comparison of Vibration of the Circular and Equivalent Rectangular Beam (APPENDIX-C) Considering Material Non-linearity with End-Shortening Effect

Figure 4.11.1 compares the amplitudes of the vibrations for circular and equivalent rectangular beam considering material non-linearity with end-shortening effect without damping at resonance (β = 1). The amplitude of the vibration for circular beam is somewhat higher than that of rectangular beam. Though the vibration amplitude is higher but transmissibility (Figures 4.14.2.16 to 4.14.2.19) is slightly lower for circular beam than that of rectangular beam. This is due to the issue of material non-linearity. From Figure 4.7.2, it can be seen that for a maximum strain of 0.285, the reduced modulus for equivalent rectangular beam is 14 GPa where it is 16 GPa for the circular beam and corresponding bending moments are 1.8277 Nm and 1.768 Nm. respectively. The lower reduced modulus enhances the tip deflection ($\delta = \frac{PL^3}{3E_r I}$).

Figures 4.11.2 to 4.11.4 compare the amplitudes of the vibrations for circular and equivalent rectangular beam considering material non-linearity with end-shortening effect. Here speed ratio is kept constant that is, β = 1 and damping ratios are varied from ζ = 0.1 (Figure 4.11.2), ζ = 0.5 (Figure 4.11.3) to ζ = 1 (Figure 4.11.4). Increased damping greatly reduces the vibrations for both the beams but the amplitude of the vibration for circular beam is higher when the damping is low (Figure 4.11.2). On the contrary, the amplitude of the vibration for circular beam is slightly lower when the damping is high (Figure 4.11.3 and Figure 4.11.4). So, it can be said that the circular beam is more responsive on the increased damping.

Figure 4.11.5 compares the amplitudes of the vibrations for circular and equivalent rectangular beam considering material non-linearity with end-shortening effect. Here chosen speed and damping ratio are, β = 1.414 and ζ = 0.1, respectively. The vibration for rectangular beam becomes steady prior to the circular beam and also possesses a smaller vibration compared to it.

Figures 4.11.6 to 4.11.7 show the comparison for β = 3 (Figure 4.11.6) to β = 5 (Figure 4.11.7) between the amplitudes of the vibrations for circular and equivalent rectangular beam considering material non-linearity with end-shortening effect. Here damping ratio is kept constant that is $\zeta = 0.1$ (underdamped). The vibrations are highly transient in nature at the beginning. Increased speed ratio greatly reduces the vibrations for both the cases. The difference between the amplitudes of the vibration disappear when they become steady and coincide each other.

4.12 Comparison of Vibration of the Circular and Equivalent Rectangular Beam (APPENDIX-C) Considering Material Non-linearity and Geometric Non-linearity with End-Shortening Effect

Figure 4.12.1 compares the amplitudes of the vibrations for circular and equivalent rectangular beam considering material non-linearity and geometric non-linearity with end-shortening effect without damping at resonance ($\beta = 1$). Comparing with Figure 4.11.1, it can be noticed that the discrepancy between the vibrations is reduced when geometric non-linearity issue is incorporated to the material non-linearity with end-shortening effect.

Figures 4.12.2 to 4.12.4 compare the amplitudes of the vibrations for circular and equivalent rectangular beam considering material non-linearity and geometric non-linearity with end-shortening effect. Here speed ratio is kept constant that is, $\beta = 1$ and damping ratios are varied from $\zeta = 0.1$ (Figure 4.12.2), $\zeta = 0.5$ (Figure 4.12.3) to $\zeta = 1$ (Figure 4.12.4). Increased damping greatly reduces the vibrations. There is no significant discrepancy between the amplitudes of the vibrations for all the cases.

Figure 4.12.5 compares between the amplitudes of the vibrations for circular and rectangular beam considering material non-linearity and geometric non-linearity with end-shortening effect. Here chosen speed and damping ratio are, $\beta = 1.414$ and $\zeta = 0.1$, respectively. The vibration for circular beam is insignificantly higher than that of rectangular beam. They almost overlap each other.

Figures 4.12.6 to 4.12.7 show the comparison for $\beta = 3$ (Figure 4.12.6) to $\beta = 5$ (Figure 4.12.7) between the amplitudes of the vibrations for circular and equivalent rectangular beam considering material non-linearity and geometric non-linearity with end-shortening effect for a damping ratio of $\zeta = 0.1$ (underdamped). The vibrations are highly transient in nature at the beginning. Increased speed ratio greatly reduces the vibrations for both the cases. The difference between the amplitudes of the vibration disappear when they approach steady-state and coincide each other.

4.13 Finding the Speed Ratio for Maximum Undamped Vibration of a Circular Beam Considering Material Non-linearity and Geometric Non-linearity with End-Shortening Effect

This section is designed to check where the maximum vibration is found or at what speed ratio the amplitude of vibration is maximum when considering material non-linearity and geometric non-linearity with end-shortening effect for a circular beam. The Figures 4.13.1 to 4.13.5 show the amplitudes of the vibrations for different speed ratios without damping. Here speed ratios are chosen as, β = 0.5, 0.6, and 0.7 (Figure 4.13.1), β = 0.8, 0.9, and 1 (Figure 4.13.2), β = 1.1, 1.2, and 1.3 (Figure 4.13.3), β = 1.414, 1.5 and 1.6 (Figure 4.13.4), β = 1.7, 1.8 and 2 (Figure 4.13.5). The amplitude of the vibration is increasing with the increase of speed ratio (Figure 4.13.1 to Figure 4.13.3) and peaks between β = 1.7 to 1.8 approximately and then starts to decrease with the further increase of speed ratio. The maximum amplitude found from these results is 0.2791 m at β = 1.8. This can also be rechecked with the help of the next section where Transmissibility (TR) will be discussed.

4.14 Analysis of Transmissibility (TR) of the Vibration through Damper and Spring Considering Different Cases for Superelastic SMA Cantilever Beam

Transmissibility (TR) is defined as the ratio of the force transmitted (F_t) to the force applied (F_0) or can mathematically be expressed as $TR = \frac{F_t}{F_0}$. Where F_t and F_0 are transmitted and applied force, respectively.

4.14.1 Transmissibility Analysis for Classical Theory

From classical theory it can be known that the restoring force or spring force varies linearly with displacement. The transmitted force (F_t) can be expressed with the following relations:

$$F_t = \sqrt{(kx)^2 + (c\omega x)^2}$$

$$F_t = kx\sqrt{1 + (2\zeta\beta)^2}$$

Figure 4.14.1.1 indicates steady-state *TR* against speed ratio, β for different damping ratio. Here four damping ratios are chosen as ζ=0.05, 0.1, 0.5 and 1. Increased damping greatly reduces the *TR*. For any damping ratio, isolation begins at β = 1.414 that justifies the classical theory. **This phenomena validates the numerical scheme that is developed in the present study has elaborately been discussed in the section 4.2 as code validation**.

4.14.2 Transmissibility Analysis Comparison for Different Cases

The non-linear restoring force (*RF*) can be obtained from the best fit load-deflection curves considering different issues for example, end-shortening effect, geometric non-linearity, material non-linearity, different speed ratio (β), different damping ratio (ζ) and equivalent cross-section etc. This non-linear restoring force (*RF*) or spring force varies non-linearly with displacement. This restoring force (*RF*) can be expressed as the following ways:

$$RF = k_1x^3 + k_2x^2 + k_3x + k_4$$

In this case, transmitted force (F_t) can be expressed with the following relations:

$$F_t = \sqrt{(RF)^2 + (c\omega x)^2}$$

$$F_t = \sqrt{(k_1x^3 + k_2x^2 + k_3x + k_4)^2 + (c\omega x)^2}$$

Figure 4.14.2.1, Figure 4.13.2.6 and Figure 4.14.2.11 compare the undamped steady-state *TR* against speed ratio (β) for classical theory with and without end-shortening effect, considering geometric non-linearity with end-shortening and material non-linearity and geometric non-linearity with end-shortening, respectively. *TR* becomes maximum at resonance (β = 1) for classical theory which also validates the numerical procedures adopted in this thesis. It peaks approximately at $\beta = 1.8$ considering material non-linearity and geometric non-linearity with end-shortening. It can be interestingly noticed that the *TR* is sufficiently smaller considering all the above-mentioned cases than that predicted by classical theory at resonance when undamped.

Figures 4.14.2.2 to 4.14.2.4 discuss the steady-state *TR* for classical theory with and without end-shortening effect. When $\zeta = 0.3$ (Figure 4.14.2.2), $\zeta = 0.5$ (Figure 4.14.2.3), $\zeta = 1$ (Figure 4.14.2.4), steady-state *TR* peaks to 3.63, (1.99 for classical theory), 2.00, (1.46 for classical theory) and 1.31, (1.15 for classical theory) at $\beta = 1.66$, 1.33, 0.89 and isolation begins at $\beta = 1.8$, 1.75, 1.78, respectively. Steady-state *TR* is found maximum at a decreasing speed with the increase of damping ratio but isolation begins almost at a constant speed ratio (Figure 4.14.2.5).

Figures 4.14.2.7 to 4.14.2.9 discuss the steady-state *TR* for classical theory and considering geometric non-linearity with end-shortening effect. When $\zeta = 0.3$ (Figure 4.14.2.7), $\zeta = 0.5$ (Figure 4.14.2.8), $\zeta = 1$ (Figure 4.14.2.9), *TR* peaks to 3.55 (1.99 for classical theory), 1.97 (1.46 for classical theory) and 1.31 (1.15 for classical theory) at $\beta =$ 1.63, 1.31, 0.93 and isolation begins at $\beta = 1.78$, 1.74, 1.79, respectively. *TR* is found maximum at a decreasing speed with the increase of damping ratio but isolation begins almost at a constant speed ratio (Figure 4.14.2.10).

Figures 4.14.2.12 to 4.14.2.14 discuss the steady-state *TR* for classical theory and considering material non-linearity and geometric non-linearity with end-shortening effect. When $\zeta = 0.3$ (Figure 4.14.2.12), $\zeta = 0.5$ (Figure 4.14.2.13), $\zeta = 1$ (Figure 4.14.2.14), *TR* peaks to 3.05, (1.99 for classical theory), 1.81 (1.46 for classical theory) and 1.23 (1.15 for classical theory) at $\beta = 1.40$, 1.07, 0.73 and isolation begins at $\beta = 1.62$, 1.58, 1.50, respectively. *TR* is found maximum at a decreasing speed with the increase of damping ratio but isolation begins at lower speed ratio compared to the other cases (Figure 4.14.2.15).

Figure 4.14.2.16 compares the undamped steady-state *TR* against speed ratio (β) for circular and equivalent rectangular beam considering material non-linearity and geometric non-linearity with end-shortening. The *TR* is insignificantly higher for rectangular beam than that of circular beam.

Figures 4.14.2.17 to 4.14.2.19 compares the steady-state *TR* for circular and equivalent rectangular beam considering material non-linearity and geometric non-linearity with end-shortening effect. Here three damping ratios are chosen as ζ = 0.3 (Figure 4.14.2.17), ζ = 0.5 (Figure 4.14.2.18), ζ = 1 (Figure 4.14.2.19). *TR* is insignificantly greater and isolation begins at slightly higher speed ratio for rectangular beam than that of circular beam.

4.14.3 Transmissibility Analysis for Slenderness Ratio of 100

Figures 4.14.3.1 to 4.14.3.6 discuss the steady-state *TR* for classical theory and considering material non-linearity and geometric non-linearity with end-shortening effect. The maximum value of *TR* is sufficiently below considering material non-linearity and geometric non-linearity with end-shortening effect than predicted by classical theory at resonance when undamped (Figure 4.14.3.1). When ζ = 0.05 (Figure 4.14.3.2), ζ = 0.1 (Figure 4.14.3.3), ζ = 0.3 (Figure 4.14.3.4), *TR* peaks to 11.33, (10 for classical theory), 7.47 (5.09 for classical theory) and 2.12 (2.0 for classical theory) at β = 1.33, 1.27, 1.03, respectively. With the increase of damping *TR* coincides each other and isolation begins approximately at β = 1.414 for classical theory and considering material non-linearity and geometric non-linearity with end-shortening effect (Figures 4.14.3.5 to 4.14.3.6).

4.14.4 Transmissibility Analysis for Slenderness Ratio of 50

Figures 4.14.4.1 to 4.14.4.6 discuss the steady-state *TR* for classical theory and considering material non-linearity and geometric non-linearity with end-shortening effect. The maximum value of *TR* is sufficiently below considering material non-linearity and geometric non-linearity with end-shortening effect than predicted by classical theory at resonance when undamped (Figure 4.14.4.1). With the increase of damping *TR* coincides each other and isolation begins approximately at β = 1.414 for classical theory and considering material non-linearity and geometric non-linearity with end-shortening effect (Figures 4.14.4.2 to 4.14.4.6).

4.14.5 Comparison of Transmissibility for Different Slenderness Ratio

Figures 4.14.5.1 to 4.14.5.6 compares the steady-state *TR* for different slenderness ratio considering material non-linearity and geometric non-linearity with end-shortening effect. *TR* peaks near resonance for slenderness ratio of 50 but for higher slenderness ratio (100 and 200), it peaks beyond resonance for different damping ratios (Figures 4.14.5.1 to 4.14.5.6). Isolation begins approximately at β = 1.414 for slenderness ratio of 50. When the slenderness ratio is higher (100 and 200), isolation begins at a larger value of β than 1.414.

CHAPTER 5

CONCLUSIONS AND RECOMMENDATIONS

Vibration of a cantilever beam has been analyzed comprehensively considering end-shortening effect, geometric non-linearity and effect of material non-linearity for different forcing frequency and damping ratio. Difference between vibration for two equivalent cross-section (circular and rectangular) has also been analyzed. Soundness of the developed mathematical scheme and computer code has been amply demonstrated. Chapter wise, following salient conclusions can be drawn at the end of research.

5.1 Analysis of Vibration of the Superelastic SMA Cantilever Beam according to Classical Theory

It is found that the ever increasing amplitude of the vibration at β = 1without damping due to the resonance. It is also found that increased damping greatly reduces vibration amplitude. The isolation of the vibration begins when β exceeds 1.414 and further increase of speed ratio greatly reduces the vibration amplitude.

5.2 Analysis of Vibration of the Cantilever Beam Considering End-Shortening Effect

It is found that the maximum tip deflection considering end-shortening is approximately 0.066 m and without end-shortening (classical theory) is 0.104 m. This is due to the issue that considering end-shortening effect means the effective length of the beam is reducing that affects to reduce the bending moment.

Interestingly, it can be noticed that the undamped vibration is not going to be infinite over time at resonance (β = 1) that predicted by classical theory rather it is sufficiently suppressed below the amplitude when compared to the classical theory. The maximum amplitude found considering end-shortening without damping is 0.1170 m.

It is also found that increased damping greatly reduces vibration amplitude. The isolation of the vibration begins approximately from β = 1.7 to 1.8 considering end-shortening effect and further increase of speed ratio greatly reduces the vibration amplitude.

5.3 Analysis of Vibration of the Beam Considering Geometric Non-linearity with End-Shortening

It is found that the maximum vibration amplitude found considering geometric non-linearity with end-shortening without damping is 0.1251 m which is slightly higher than considering end-shortening only (0.1170 m). For classical theory, the vibration is ever increasing at resonance but it is too low to compare when geometrical non-linearity with end-shortening effect is considered. It would be better to say that the effect of end-shortening on the vibration of the beam is more dominating than geometrical non-linearity.

5.4 Analysis of Material Non-linearity Effect on the Superelastic SMA Cantilever Beam

Material non-linearity issue is incorporated in terms of $\sigma - \varepsilon$, $M - \Delta$ and $E_r - \Delta$ relations for the beam material. It is found that when vibration amplitude is large enough actual strain is much larger than assumed by linear elastic model. Also modulus of elasticity decreases significantly as strain increases.

As material non-linearity is taken into account, some portion of the beam is found to experience stresses (different magnitude in tension and compression) beyond proportional limit. For a particular SMA beam, the maximum deflection at tip considering the material as linearly elastic is 0.104 mm but it is 0.121 mm when material non-linearity effect is considered.

5.5 Analysis of Vibration of the Cantilever Beam Considering Material Non-linearity with End-Shortening

It is found that the vibration is almost steady from very beginning of the vibration when material non-linearity with end-shortening effect is considered with a certain level of damping. The maximum amplitude found is 0.2300 m considering material non-linearity with end-shortening effect when undamped. The amplitude of the vibration is largely lower considering material non-linearity with end-shortening effect than predicted by classical theory when the damping is low. Increased damping greatly reduces the vibration amplitude.

5.6 Analysis of Vibration of the Cantilever Beam Considering Material Non-linearity and Geometric Non-linearity with End-Shortening

The maximum amplitude found is 0.1648 m considering material and geometric non-linearity with end-shortening effect without damping. The amplitude of the vibration is largely lower than predicted by classical theory when the damping is low. Increased damping greatly reduces the vibration.

5.7 Comparison of Vibration for the Circular and Equivalent Rectangular Beam

The amplitude of the vibration for circular beam is slightly higher than that of equivalent rectangular beam at resonance (β = 1) with no damping considering material non-linearity with end-shortening effect.

When geometric non-linearity issue is incorporated to the material non-linearity with end-shortening effect the discrepancy between the vibrations is reduced.

5.8 Finding the Speed Ratio for Maximum Vibration of a Circular Considering Material and Geometric Non-linearity with End-Shortening Effect

The amplitude of the vibration is increasing with the increase of speed ratio and peaks between β = 1.7 to 1.8 approximately and then starts to decrease with the further increase of speed ratio. The maximum amplitude found from these results is 0.2791 m at β = 1.8 without damping.

5.9 Analysis of Transmissibility (TR) of the Vibration Considering Different Cases for Superelastic SMA Cantilever Beam

It is found that isolation begins when β exceeds 1.414 for classical theory with any amount of damping which validates the numerical scheme. It is also found that isolation begins at about β = 1.8 for considering classical theory with end-shortening effect and geometric non-linearity with end-shortening effect. But it is significantly reduced (β = 1.62, 1.58, 1.50) for different damping ratio when material non-linearity and geometric non-linearity with end-shortening is considered.

5.10 Analysis of Transmissibility (TR) for Different Slenderness Ratio

When the slenderness ratio (50) is low *TR* peaks at resonance and isolation begins approximately at β = 1.414 for both the classical theory and considering material non-linearity and geometric non-linearity with end-shortening effect. But for higher slenderness ratio (100 and 200), it peaks beyond resonance for different damping ratios and isolation begins at a larger value of β than 1.414.

5.11 Recommendations for Future Works

The following recommendations can be made for future works based on the experience gained while achieving the set objectives of this thesis.

(1) Only rectangular and circular beam have been selected as equivalent cross-section in the present research. Other cross-section for example square or elliptical cross-section can be chosen for future studies.

(2) Experimental studies with sophisticated instrumentation can be carried out to verify the results obtained from numerical analysis from this thesis.

(3) The load chosen for the analysis of the vibrations considering material non-linearity was not significant enough to incorporate the non-linearly elastic behavior of the beam. It can be taken into consideration for future studies.

(4) Here damping force is considered to vary linearly with velocity. Non-linear damping force can be taken into consideration for future studies.

(5) The studies performed in this thesis is only for Superelastic SMA. Other types of engineering materials can be considered for future studies.

(6) In this research, the beam is chosen as cantilever beam. Same study can be performed for other types of ends for beams and columns.

(7) Because of unavailability of proper instrument, the stress-strain ($\sigma - \varepsilon$) curve and hence the $M - \Delta$ and $E_r - \Delta$ relations could not be obtained experimentally for the rectangular beam. It can be taken into consideration for future studies.

REFERENCES

[1] M. D. Thomson, W. T., Dahleh, *Theory of Vibration with Applications*, 5th ed. Pearson Education, Inc., Dorling Kindersley (India) Pvt. Ltd., 1998.

[2] Z. C. Wang, Z. L., & Kang, *Functional and smart materials: structural evolution and structure analysis*. Springer Science & Business Media, 2012.

[3] S. Bakhtiari, "NiTi-based Shape Memory Alloys beyond The Shape Memory Effect and Superelasticity," The University of Western Australia, 2019.

[4] C. M. (Eds.). Otsuka, K., & Wayman, *Shape memory materials*. Cambridge university press, 1999.

[5] W. Buehler, J. Gilfrich, R. W.-J. of applied physics, and undefined 1963, "Effect of low-temperature phase changes on the mechanical properties of alloys near composition TiNi," *aip.scitation.org*, vol. 34, no. 5, p. 1475, 1963, doi: 10.1063/1.1729603.

[6] K. E. Wilkes and P. K. Liaw, "Fatigue behavior of shape-memory alloys," *JOM*, vol. 52, no. 10, pp. 45–51, 2000, doi: 10.1007/S11837-000-0083-3.

[7] J. Cederström, J. V. H.-L. J. de, and undefined 1995, "Relationship between shape memory material properties and applications," *jp4.journaldephysique.org*, vol. 111, 1995, doi: 10.1051/jp4:1995251.

[8] R. J. Hodgson, D. E., Ming, W. H., & Biermann, *Hodgson, D. E., Ming, W. H., & Biermann, R. J. (1990). Shape memory alloys. ASM International, Metals Handbook, Tenth Edition, 2, 897-902.*, ASM Intern. 1990.

[9] W. H.-M. & design and undefined 2002, "On the selection of shape memory alloys for actuators," *Elsevier*,

[10] M. Wu, … L. S. conference on shape memory, and U. 2000, "Industrial applications for shape memory alloys," in *the international conference on shape memory and superelastic technologies*, 2000, pp. 171–182,

[11] Y. Furuya, "Design and material evaluation of shape memory composites," *J. Intell. Mater. Syst. Struct.*, vol. 7, no. 3, pp. 321–330, 1996, doi: 10.1177/1045389X9600700313.

[12] S. G. S. F. Butera, A. Coda, G. Vergani, "Shape memory actuators for automotive applications," Nanotec IT newsletter. Roma: AIRI/nanotec IT (2007) 12-6., 2007.

[13] C. Bil, K. Massey, and E. J. Abdullah, “Wing morphing control with shape memory alloy actuators,” *J. Intell. Mater. Syst. Struct.*, vol. 24, no. 7, pp. 879–898, May 2013, doi: 10.1177/1045389X12471866.

[14] M. Kohl, *Shape memory microactuators*. Springer Science & Business Media, 2004.

[15] L. Petrini, F. M.-J. of Metallurgy, and undefined 2011, “Biomedical applications of shape memory alloys,” *downloads.hindawi.com*, vol. 2011, p. 15, 2011, doi: 10.1155/2011/501483.

[16] Timoshenko S., (1955), “Vibration Problem in Engineering”, Third edition.

[17] M. A. Rahman, “Behavior of Superelastic SMA Columns under Compression and Torsion,” Ph. D. Thesis, School of Engineering, Mechatronics & Precision Engineering, Tohoku University Japan, 2001.

[18] M. A. Rahman and M. A. Kowser, “Nonlinear analysis of cantilever shape memory alloy beams of variable cross section,” *Smart Mater. Struct.*, vol. 16, no. 2, pp. 531–540, 2007, doi: 10.1088/0964-1726/16/2/035.

[19] L. G. Machado, “Shape Memory Alloys for Vibration Isolation and Damping,” Ph. D. Thesis, Department of Aerospace Engineering, Texas A&M University., 2007.

[20] K. Yang, R. L. Harne, K. W. Wang, and H. Huang, “Investigation of a bistable dual-stage vibration isolator under harmonic excitation,” *Smart Mater. Struct*, vol. 23, no. 4, 2014, doi: 10.1088/0964-1726/23/4/045033.

[21] S. S. Rao, *Mechanical Vibrations*, 5th ed. Pearson Education, Inc., Publishing as Prentice Hall, 1 Lake Street, Upper Saddle River, New Jersey, the USA, 2011.

[22] E. I. Rivin, “Vibration isolation of precision equipment,” *Precis. Eng.*, vol. 17, no. 1, pp. 41–56, 1995, doi: 10.1016/0141-6359(94)00006-L.

[23] M. Dolce, D. Cardone, and R. Marnetto, “Implementation and testing of passive control devices based on shape memory alloys,” *Earthq. Eng. Struct. Dyn.*, vol. 29, no. 7, pp. 945–968, 2000, doi: 10.1002/1096-9845(200007)29:7<945::aid-eqe958>3.0.co;2-%23.

[24] Z. Lu, M. J. Brennan, and L. Q. Chen, “On the transmissibilities of nonlinear vibration isolation system,” *J. Sound Vib.*, vol. 375, pp. 28–37, 2016, doi: 10.1016/j.jsv.2016.04.032.

[25] R. A. Ibrahim, “Recent advances in nonlinear passive vibration isolators,” *J. Sound Vib.*, vol. 314, no. 3–5, pp. 371–452, 2008, doi: 10.1016/j.jsv.2008.01.014.

[26] A. Carrella, M. J. Brennan, and T. P. Waters, “Static analysis of a passive vibration isolator with quasi-zero-stiffness characteristic,” *J. Sound Vib.*, vol. 301, no. 3–5, pp. 678–689, 2007, doi: 10.1016/j.jsv.2006.10.011.

[27] A. Carrella, M. J. Brennan, T. P. Waters, and V. Lopes, “Force and displacement transmissibility of a nonlinear isolator with high-static-low-dynamic-stiffness,” *Int. J. Mech. Sci.*, vol. 55, no. 1, pp. 22–29, 2012, doi: 10.1016/j.ijmecsci.2011.11.012.

[28] Y. Zhang, Z. Guo, H. He, J. Zhang, M. Liu, and Z. Zhou, “A novel vibration isolation system for reaction wheel on space telescopes,” *Acta Astronaut.*, vol. 102, pp. 1–13, 2014, doi: 10.1016/j.actaastro.2014.05.014.

[29] J. Zhang, Z. Guo, Y. Zhang, L. Tang, and X. Guan, “Inner structural vibration isolation method for a single control moment gyroscope,” *J. Sound Vib.*, vol. 361, pp. 78–98, 2016, doi: 10.1016/j.jsv.2015.09.027.

[30] Z. Yao, Z. Jingrui, and X. Shijie, “Parameters design of vibration isolation platform for control moment gyroscopes,” *Acta Astronaut.*, vol. 81, no. 2, pp. 645–659, 2012, doi: 10.1016/j.actaastro.2012.08.031.

[31] T. Beléndez, C. Neipp, and A. Beléndez, “Numerical and Experimental Analysis of a Cantilever Beam: A Laboratory Project to Introduce Geometric Nonlinearity in Mechanics of Materials,” *Int. J. Eng. Educ.*, vol. 19, no. 6, pp. 885–892, 2003.

[32] Z. A. Jassim, N. N. Ali, F. Mustapha, and N. A. Abdul Jalil, “A review on the vibration analysis for a damage occurrence of a cantilever beam,” *Eng. Fail. Anal.*, vol. 31, pp. 442–461, 2013, doi: 10.1016/j.engfailanal.2013.02.016.

[33] M. Rahman, M. Rahman, and A. H. Applied, “Large deflection analysis of cantilever beams with an opening,” *Int. J. Appl. Mech. Eng.*, pp. 12(1), 169–181, 2007.

[34] T. Beléndez, C. Neipp, and A. Beléndez, “Large and small deflections of a cantilever beam,” *Eur. J. Phys.*, vol. 23, no. 3, pp. 371–379, 2002, doi: 10.1088/0143-0807/23/3/317.

[35] M. Rahman, M. Rahman, A. H.-I. J. of Applied, and undefined 2007, “Large deflection analysis of cantilever beams with an opening,” *infona.pl*,

[36] T. Beléndez, M. Pérez-Polo, C. Neipp, and A. Beléndez, “Numerical and experimental analysis of large deflections of cantilever beams under a combined load,” *Phys. Scr. T*, vol. T118, no. T118, pp. 61–65, Jan. 2005, doi: 10.1238/PHYSICA.TOPICAL.118A00061/XML.

[37] M. A. K. and M. T. S. M. A. Rahman, "Effect of end-shortening on the response of a steel cantilever beam with an opening," *Int. J. Appl. Mech. Eng.*, vol. 13, no. 3, pp. 735–751, 2008.

[38] G. Lewis and F. Monasa, "Large deflections of cantilever beams of non-linear materials of the Ludwick type subjected to an end moment," *Int. J. Non. Linear. Mech.*, vol. 17, no. 1, pp. 1–6, 1982, doi: 10.1016/0020-7462(82)90032-4.

[39] K. Lee, "Large deflections of cantilever beams of non-linear elastic material under a combined loading," *Int. J. Non. Linear. Mech.*, vol. 37, no. 3, pp. 439–443, 2002, doi: 10.1016/S0020-7462(01)00019-1.

[40] J. Roh, I. Oh, S. Yang, … J. H.-S. materials and, and undefined 2004, "Thermal post-buckling analysis of shape memory alloy hybrid composite shell panels," *iopscience.iop.org*, vol. 13, p. 1337, 2004, doi: 10.1088/0964-1726/13/6/006.

[41] J.-H. Roh, J.-H. Han, I. Lee, J. Roh, and J. Han, "Nonlinear finite element simulation of shape adaptive structures with SMA strip actuator," *journals.sagepub.com*, vol. 17, no. 11, pp. 1007–1022, Nov. 2011, doi: 10.1177/1045389X06063084.

[42] Y. Matsuzaki, T. Ikeda, and C. Boller, "New technological development of passive and active vibration control: Analysis and test," *Smart Mater. Struct.*, vol. 14, no. 2, pp. 343–348, 2005, doi: 10.1088/0964-1726/14/2/007.

[43] S. Ahmadi, K. Jacob, F. Wendler, and M. Kohl, "Shape memory alloy film damping for smart miniature systems," *Int. J. Smart Nano Mater.*, vol. 9, no. 3, pp. 199–215, 2018, doi: 10.1080/19475411.2018.1496953.

[44] R. Desroches and B. Smith, "Shape memory alloys in seismic resistant design and retrofit: A critical review of their potential and limitations," *J. Earthq. Eng.*, vol. 8, no. 3, pp. 415–429, 2004, doi: 10.1080/13632460409350495.

[45] Y. Jia, L. Li, C. Wang, Z. Lu, and R. Zhang, "A novel shape memory alloy damping inerter for vibration mitigation," *Smart Mater. Struct.*, vol. 28, no. 11, 2019, doi: 10.1088/1361-665X/ab3dc8.

[46] S. M. M. Siddique, "Analysis of Synchronous and Asynchronous Whirl of Jeffcott Rotor Considering Material Non-linearity," M.Sc. Engg. Thesis, Mechanical Engineering, Bangladesh University of Engineering and Technology, 2018.

[47] M. A. Rahman, S. M. M. Siddique, and M. M. Rahman, "Whirling of a Jeffcott rotor on a superelastic SMA shaft," *AIP Conf. Proc.*, vol. 2324, no. 2017, pp. 1–10, 2021, doi:

FIGURES

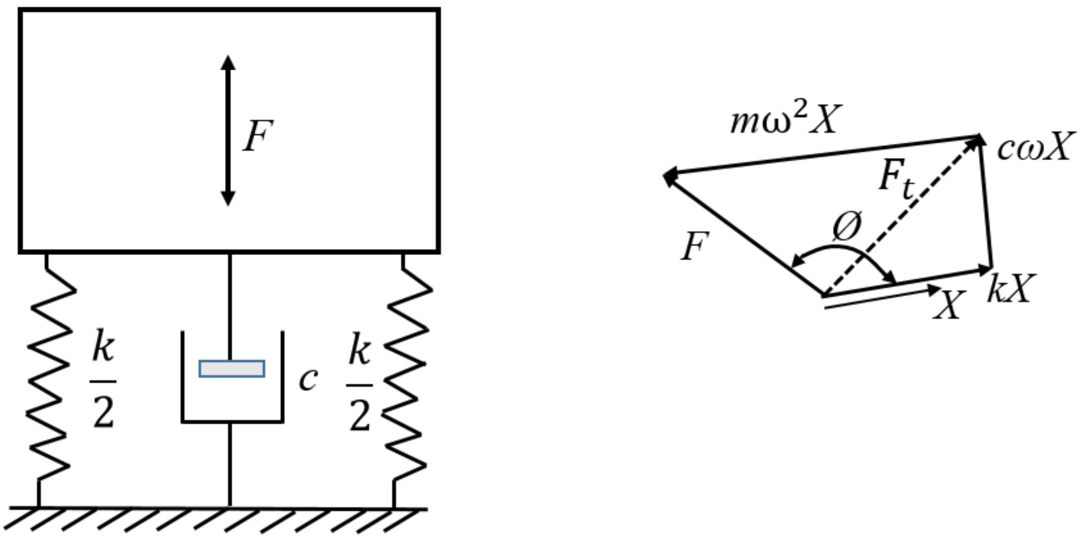

Figure 1.1.1 Disturbing force (F_t) transmitted through springs and damper [1].

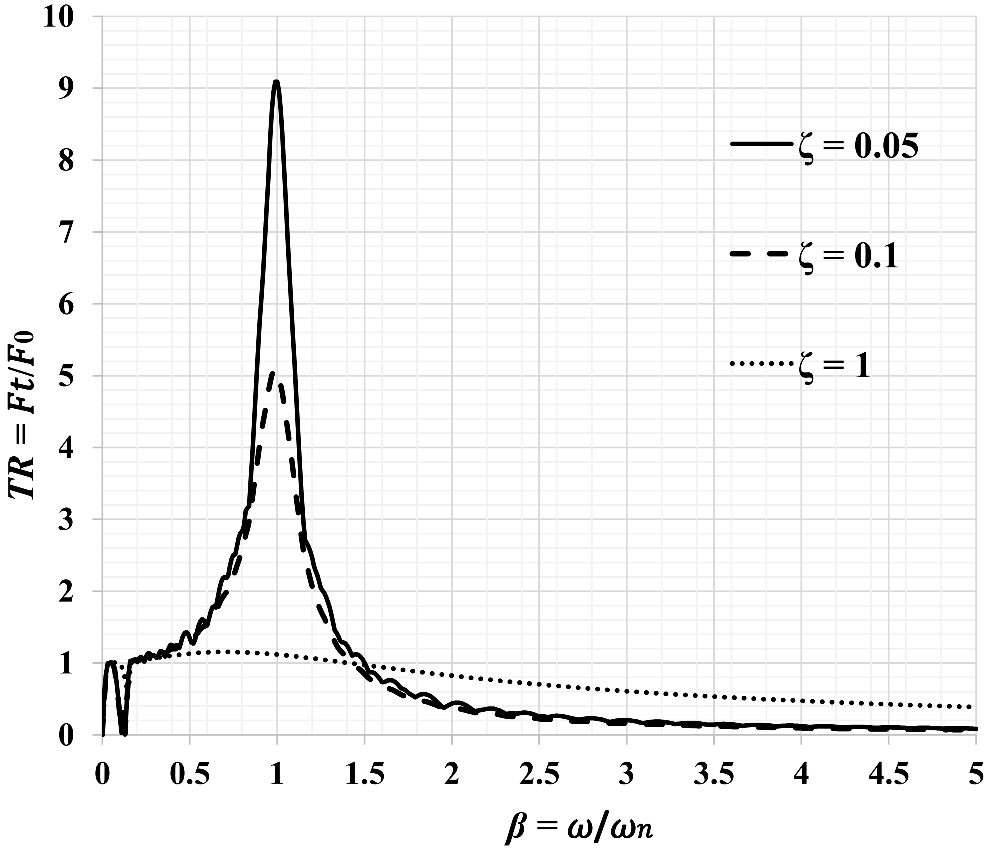

Figure 1.1.2: Steady-state TR vs speed ratio ($\beta = \frac{\omega}{\omega_n}$).

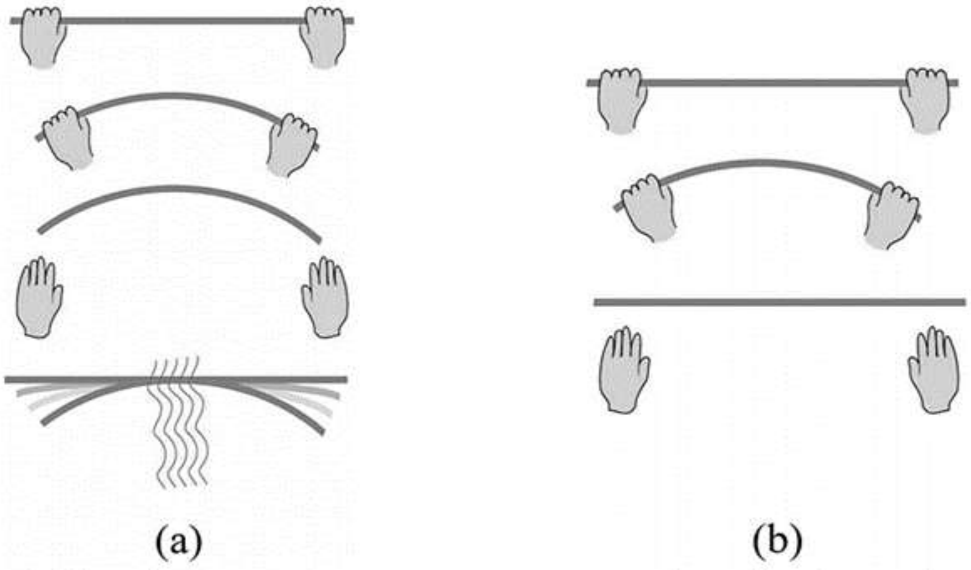

Figure 1.3.1: Illustration of (a) shape memory effect and (b) pseudoelasticity in shape memory alloys [3].

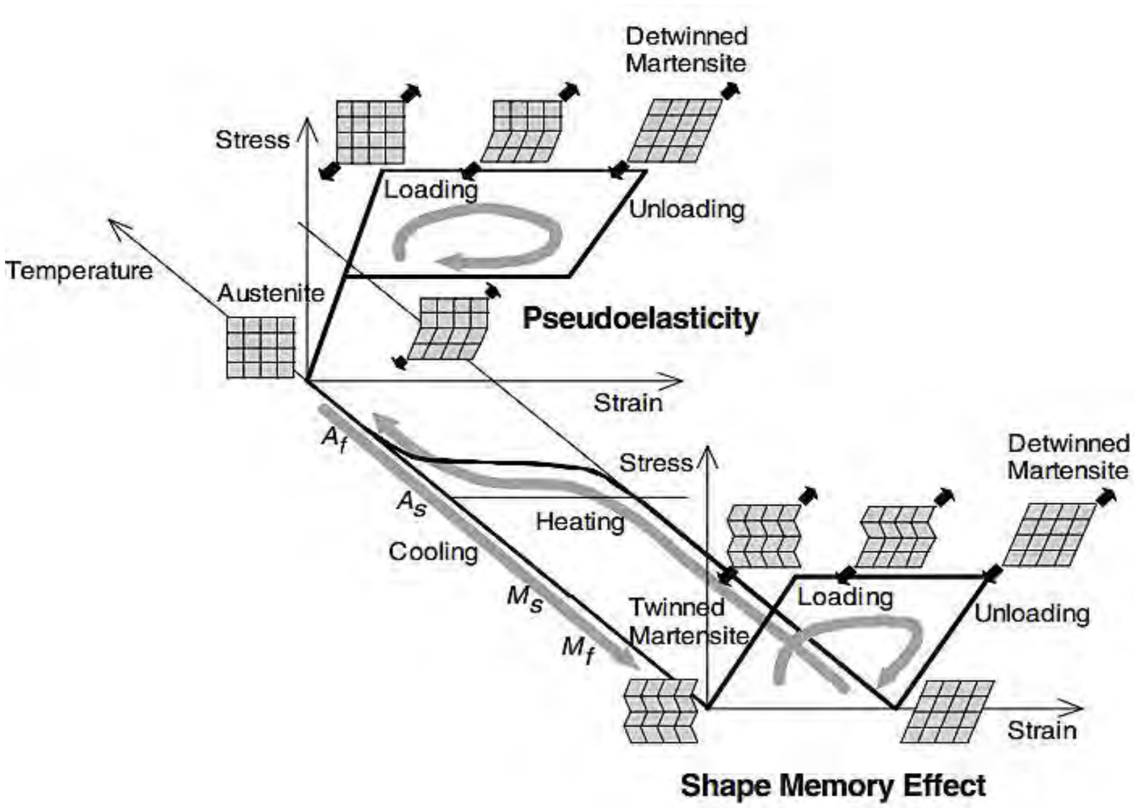

Figure 1.4.1**:** Schematic illustration of the relation between stress and strain for SMA and crystal structures at typical temperatures [3].

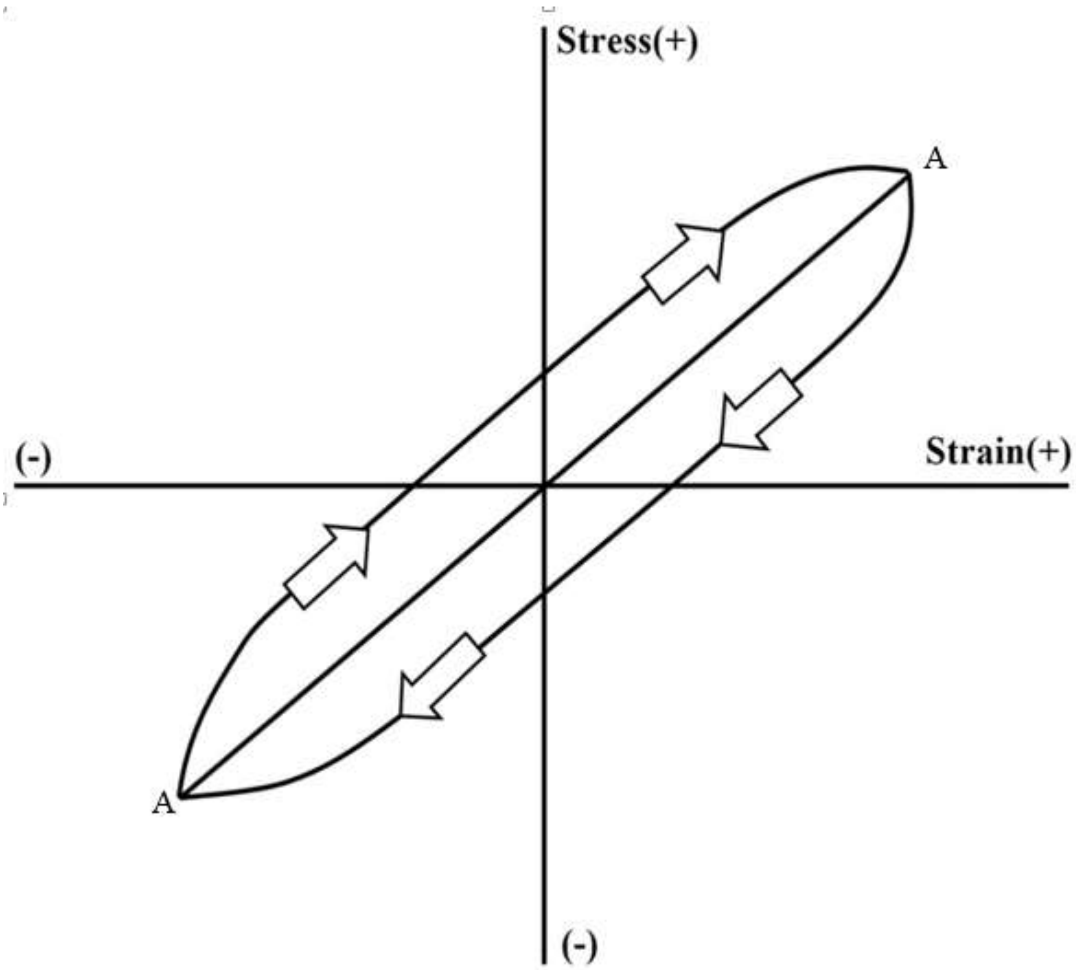

Figure 1.4.2: Stress-strain diagram for material possessing elastic hysteresis characteristics.

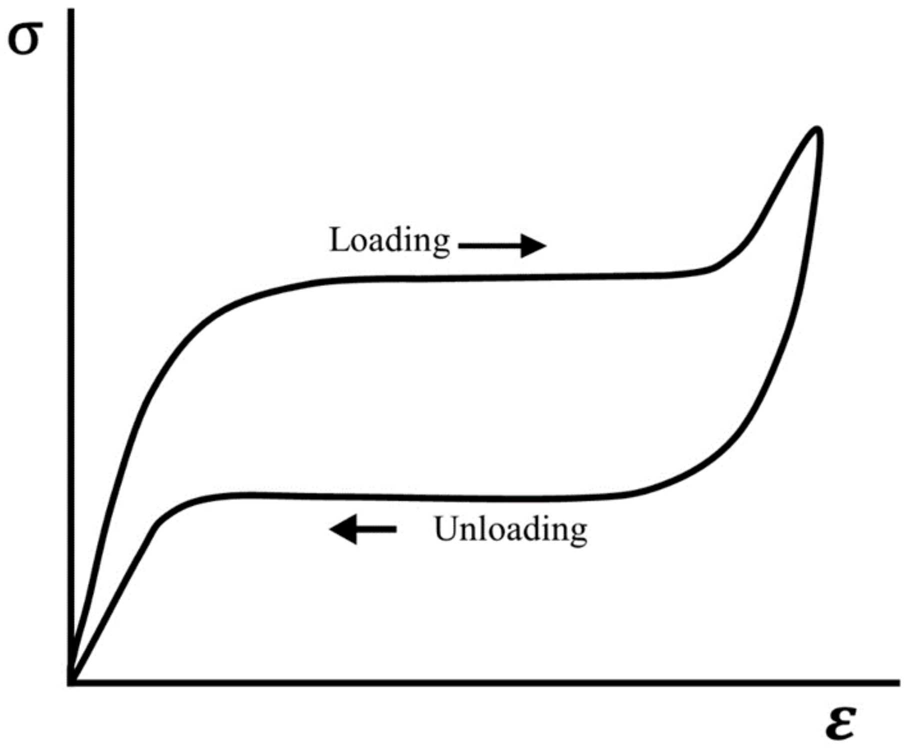

Figure 1.4.3: Fictitious stress-strain curve showing superelastic SMA's shape and size recovery through a nonlinear hysteresis.

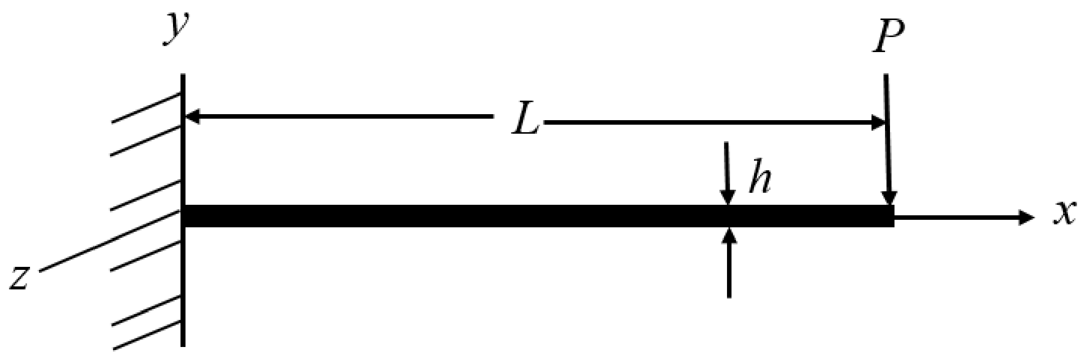

Figure 3.2.1: Cantilever beam subjected to a tip load P.

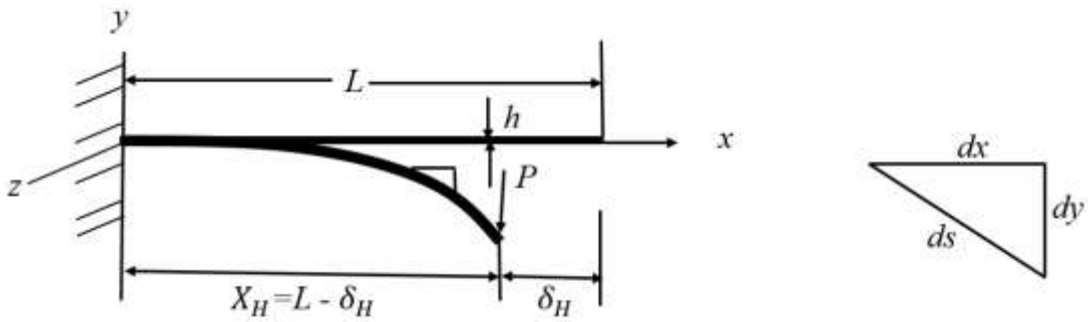

Figure 3.3.1: Cantilever beam subjected to a tip load P considering end-shortening.

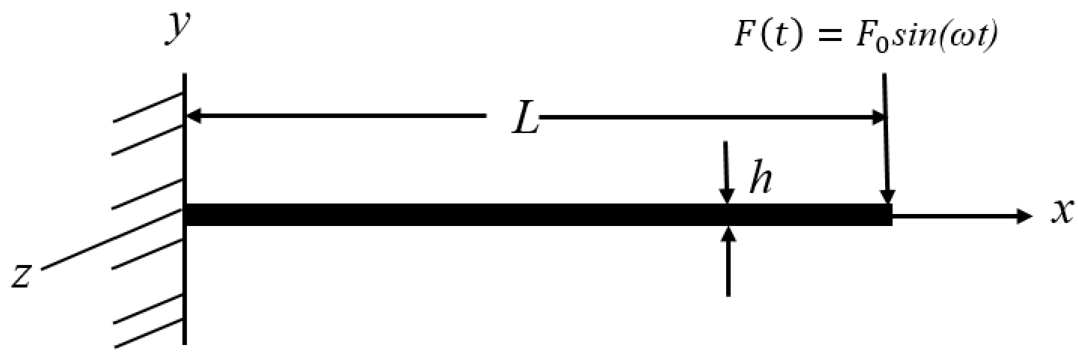

Figure 3.5.1: Cantilever beam subjected to a time varying tip load.

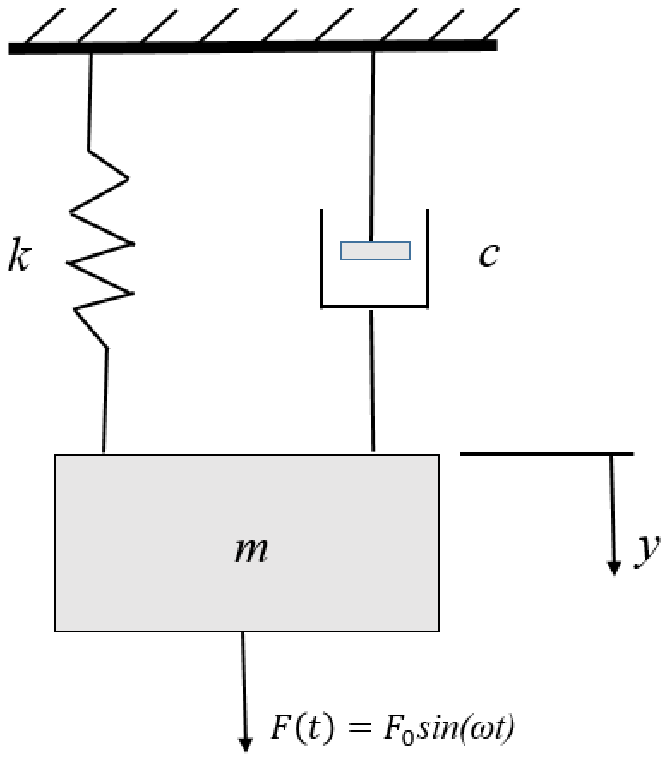

Figure 3.5.2: Equivalent model of Figure 3.5.1.

(Mass of the beam is ignored while $m = \frac{F_0}{g}$)

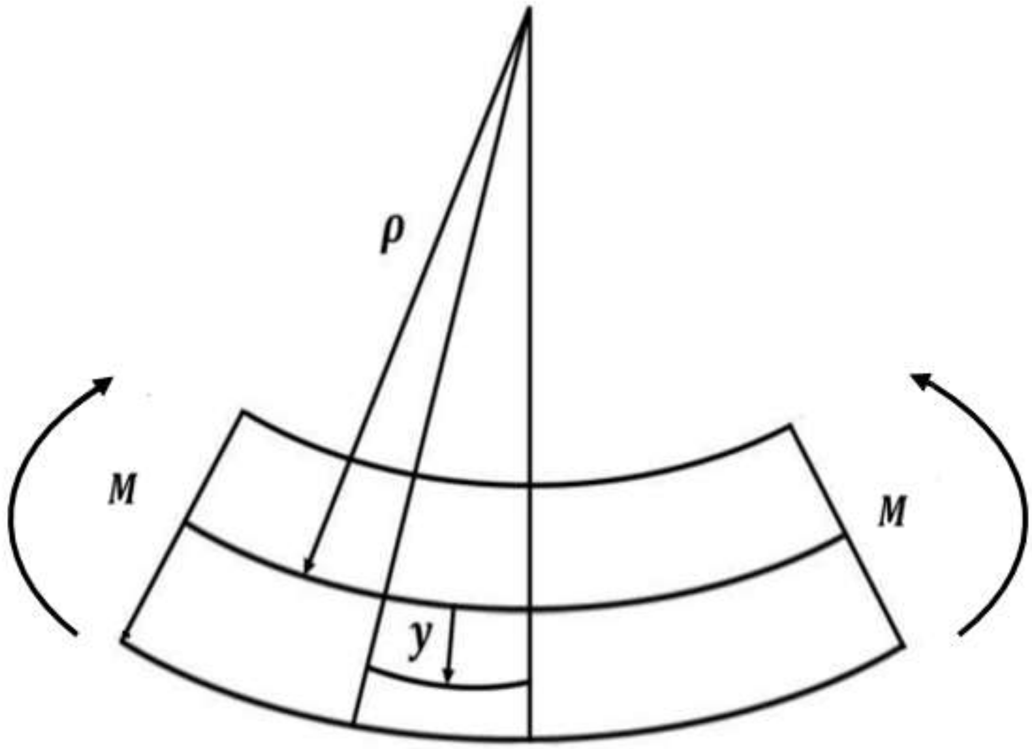

Figure 3.6.1.1: Bending of the beam.

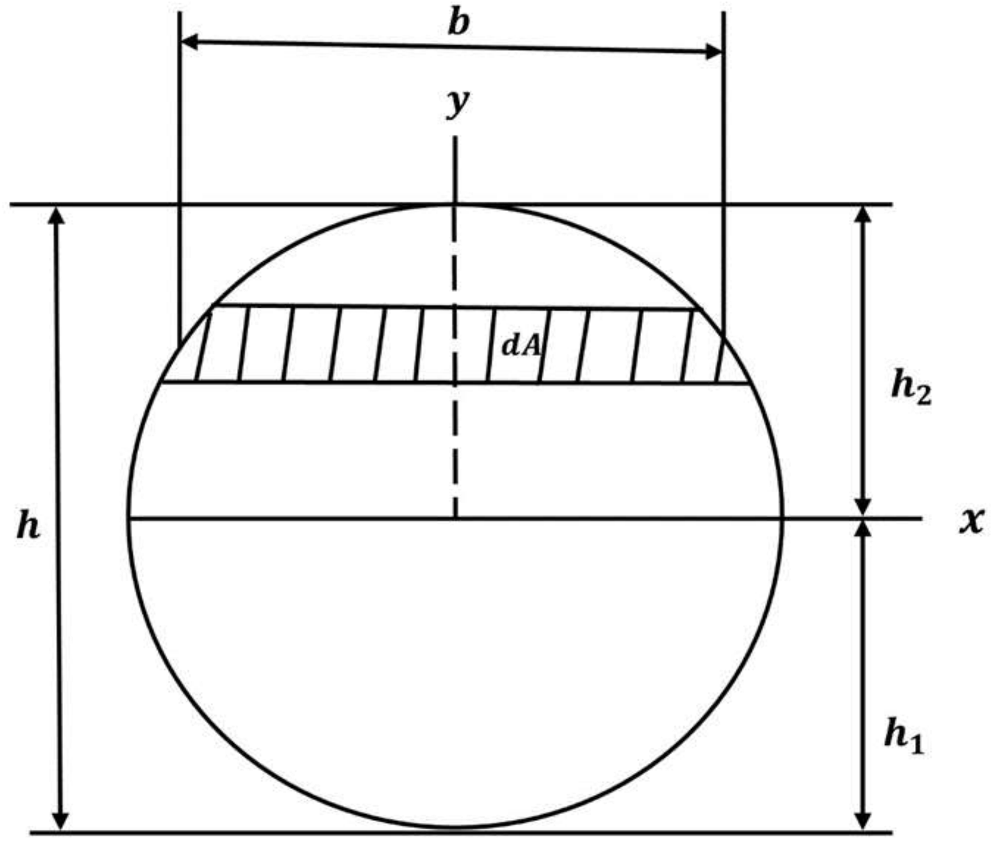

Figure 3.6.1.2**:** Circular cross-section of the beam.

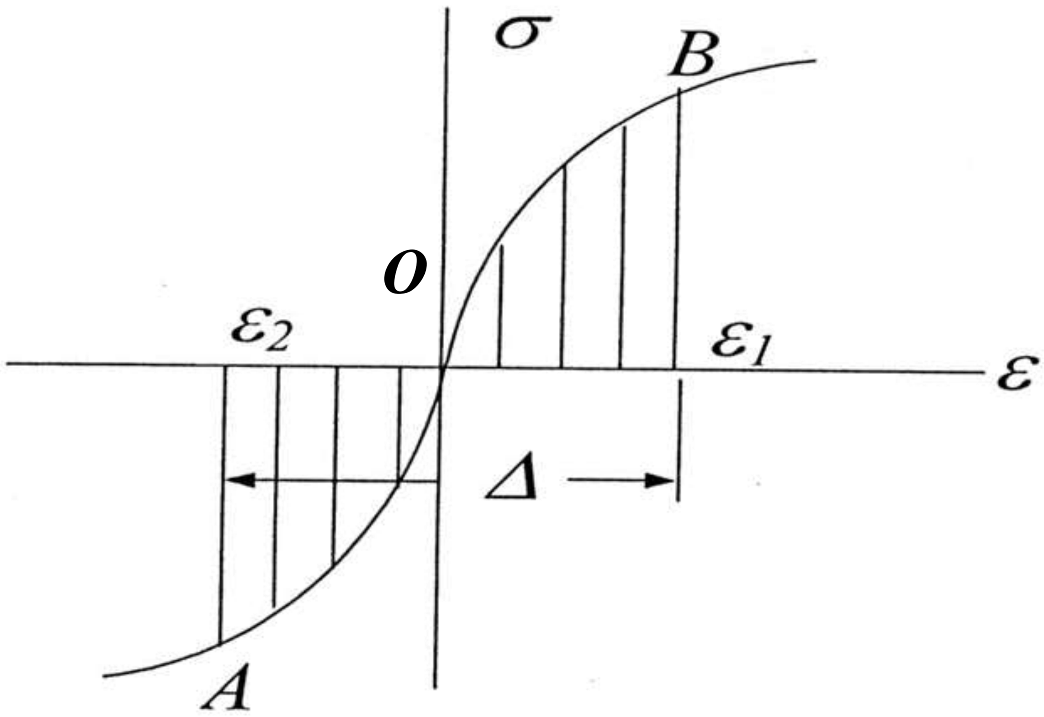

Figure 3.6.1.3a: Fictitious non-linear $\sigma - \varepsilon$ curve under tension & compression showing material non-linearity.

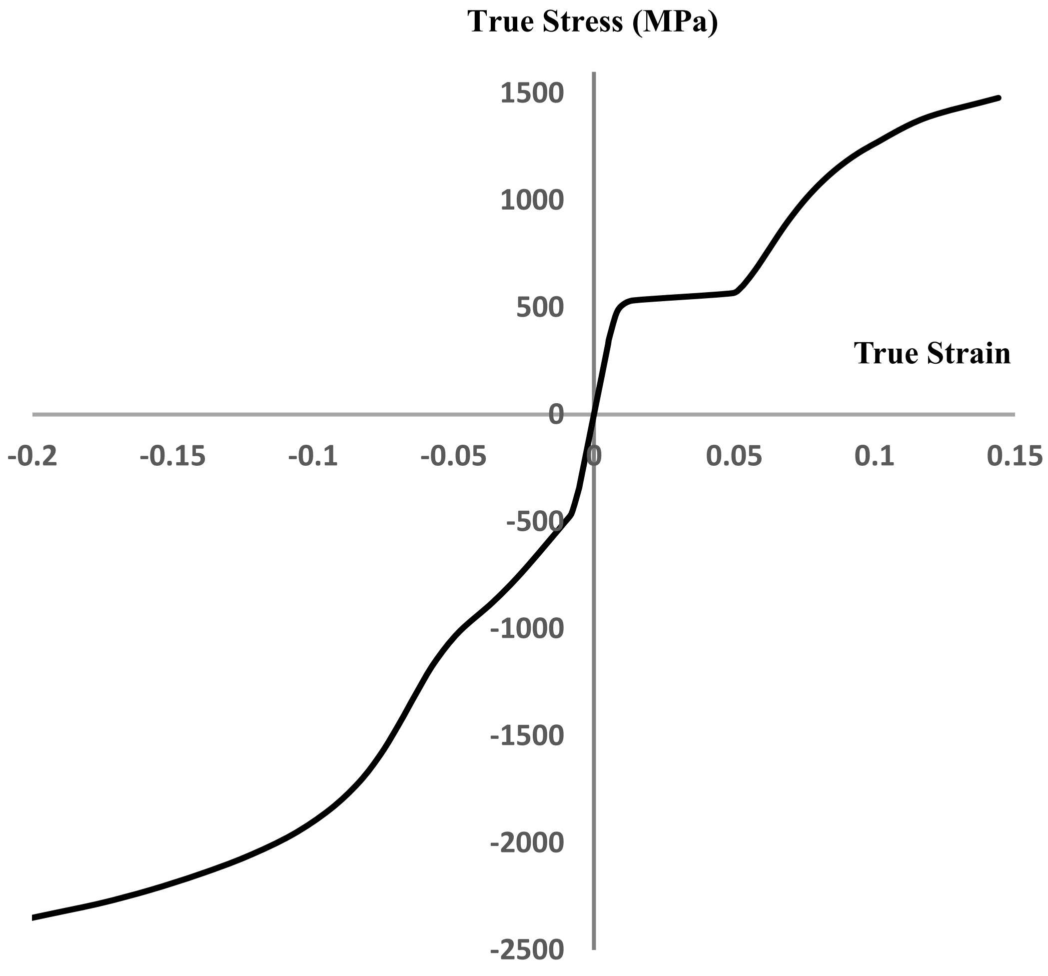

Figure 3.6.1.3b**:** Actual stress-strain curve of superelastic SMA (dia = 2 mm), showing asymmetric behavior in tension and compression [16].

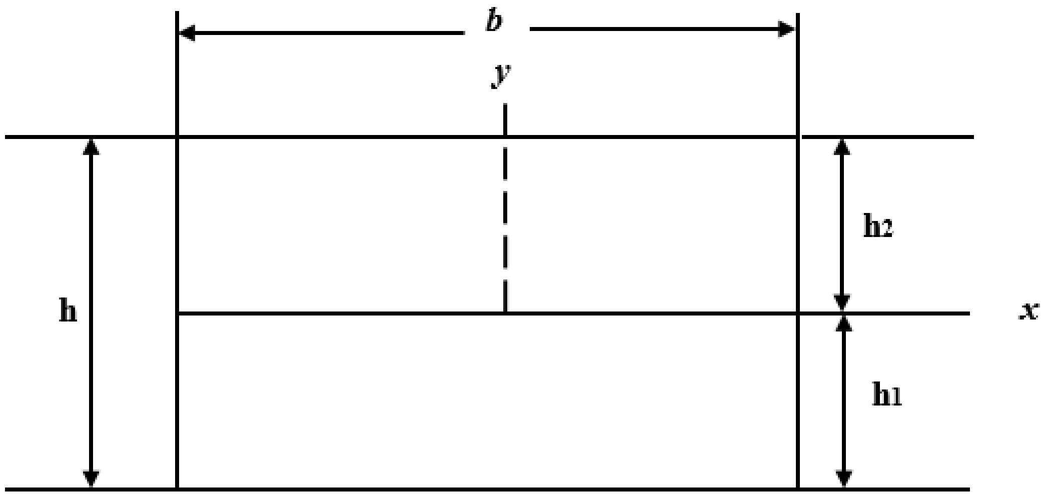

Figure 3.6.2.1**:** Equivalent rectangular cross-section of the beam.

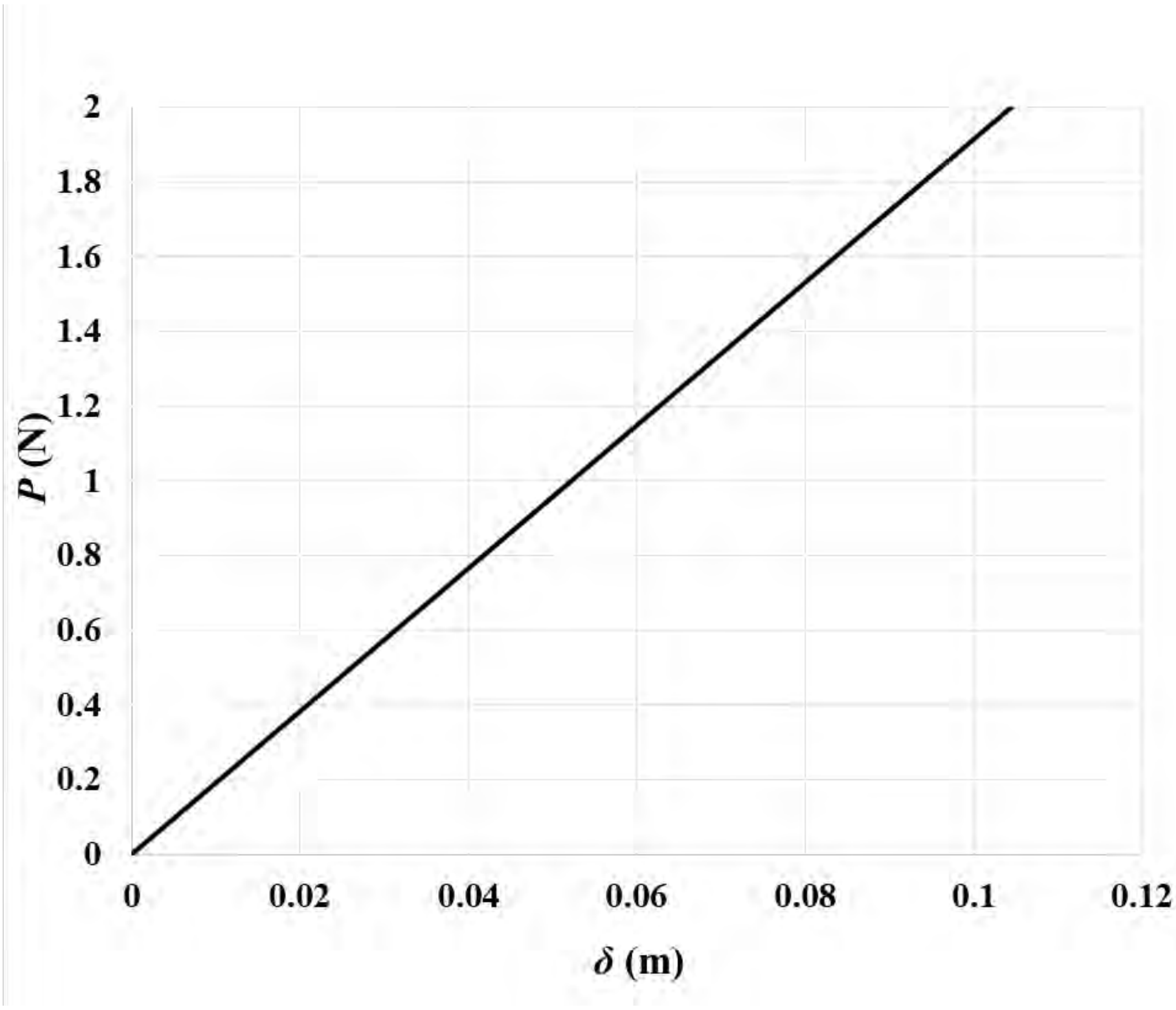

Figure 4.3.1: Load (N) vs tip deflection (m) curve for classical theory.

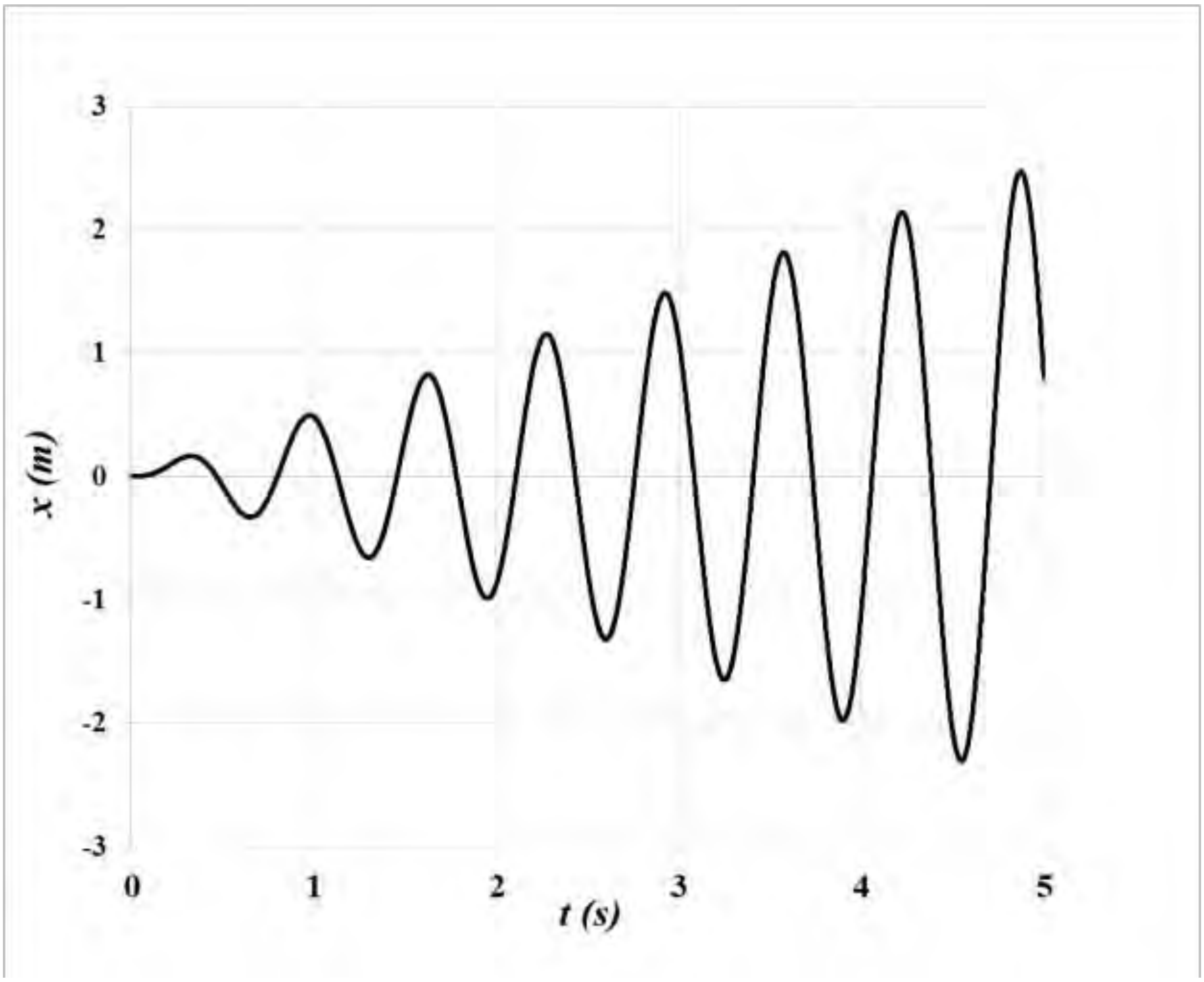

Figure 4.3.2: Displacement (m) vs time (s) curve at resonance (β = 1) when undamped (ζ = 0) for classical theory.

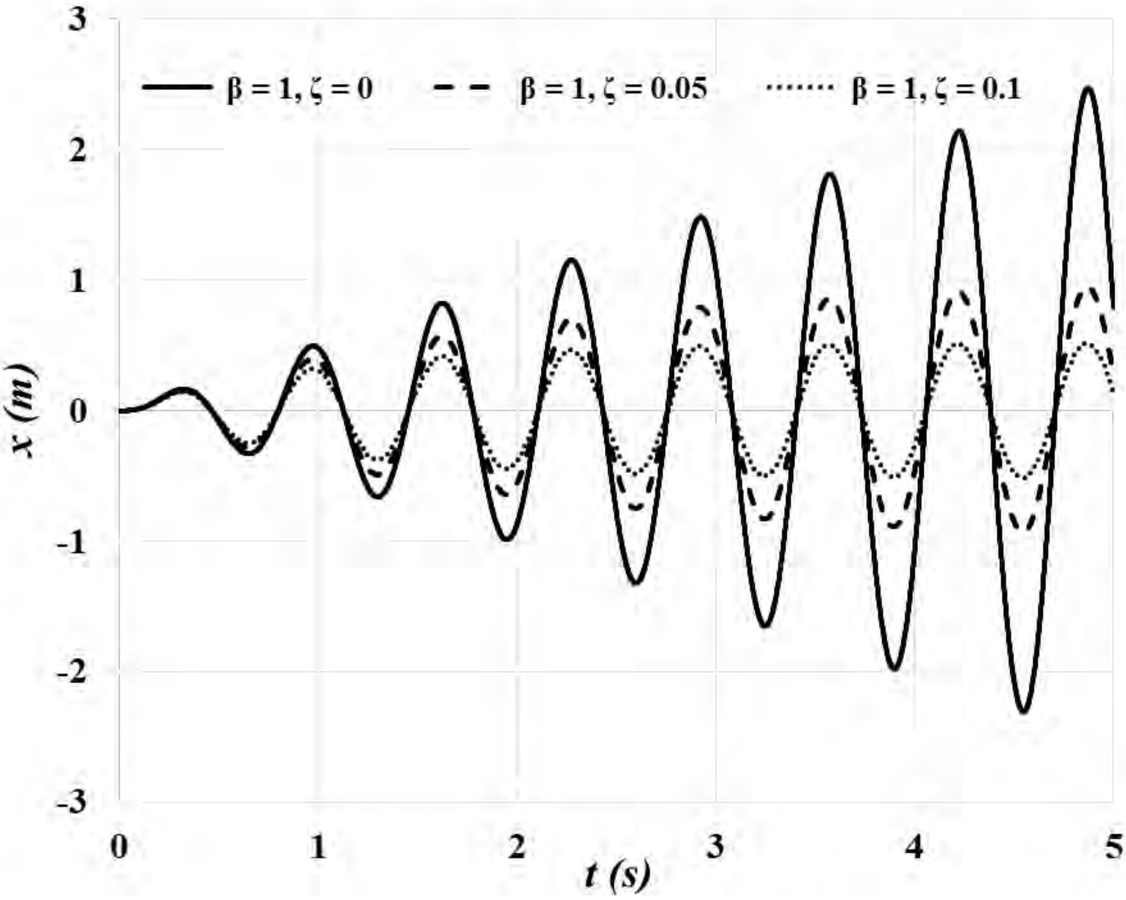

Figure 4.3.3: Displacement (m) vs time (s) curve for speed ratio, β = 1 and different damping ratio, ζ for linear analysis.

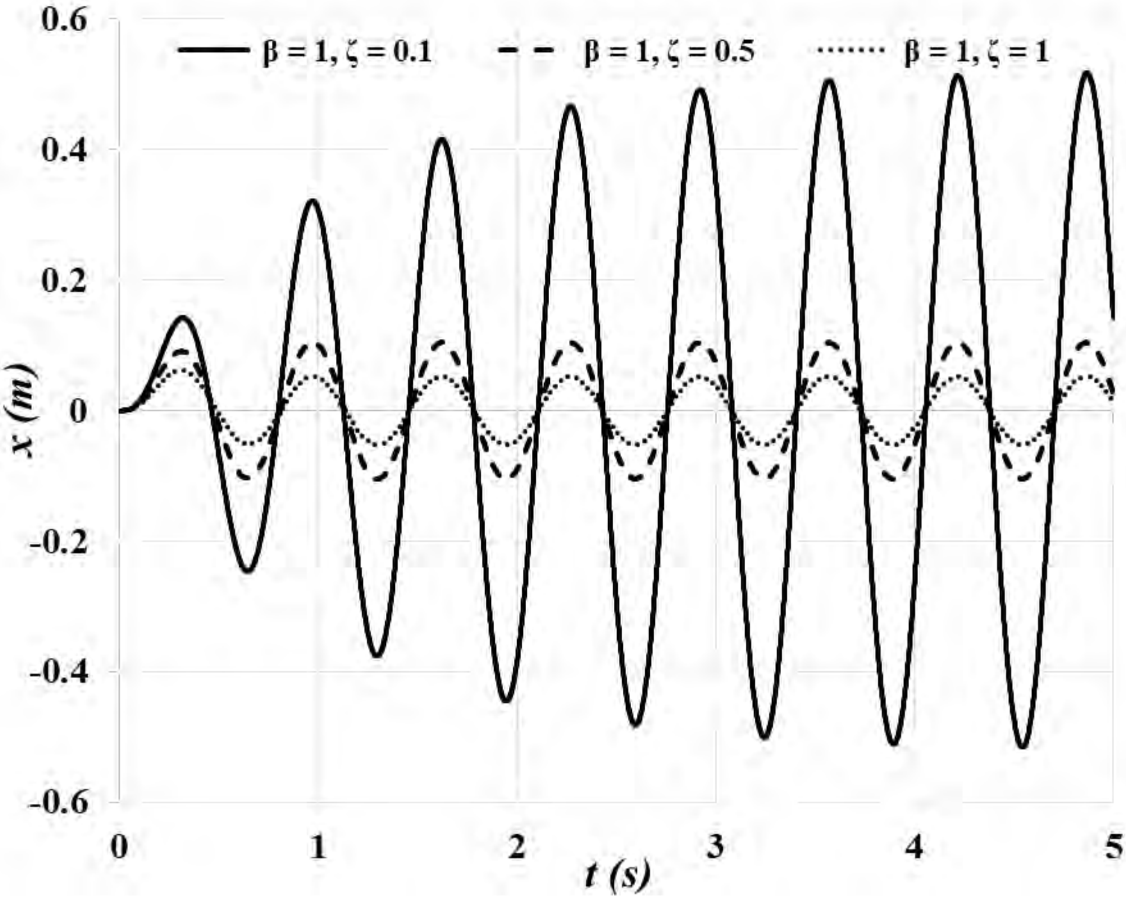

Figure 4.3.4: Displacement (m) vs time (s) curve for speed ratio, $\beta = 1$ and different damping ratio, ζ for linear analysis.

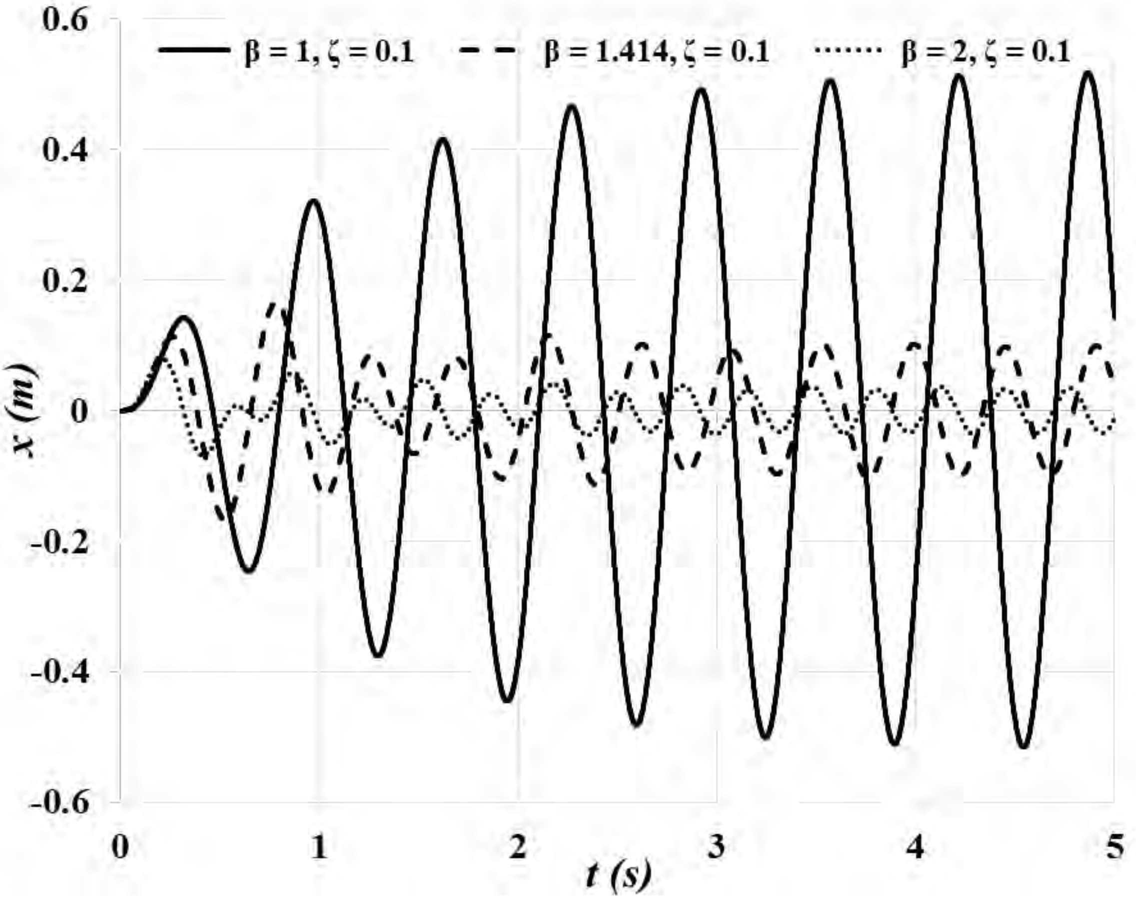

Figure 4.3.5: Displacement (m) vs time (s) curve for different speed ratio, β and damping ratio, $\zeta = 0.1$ for linear analysis.

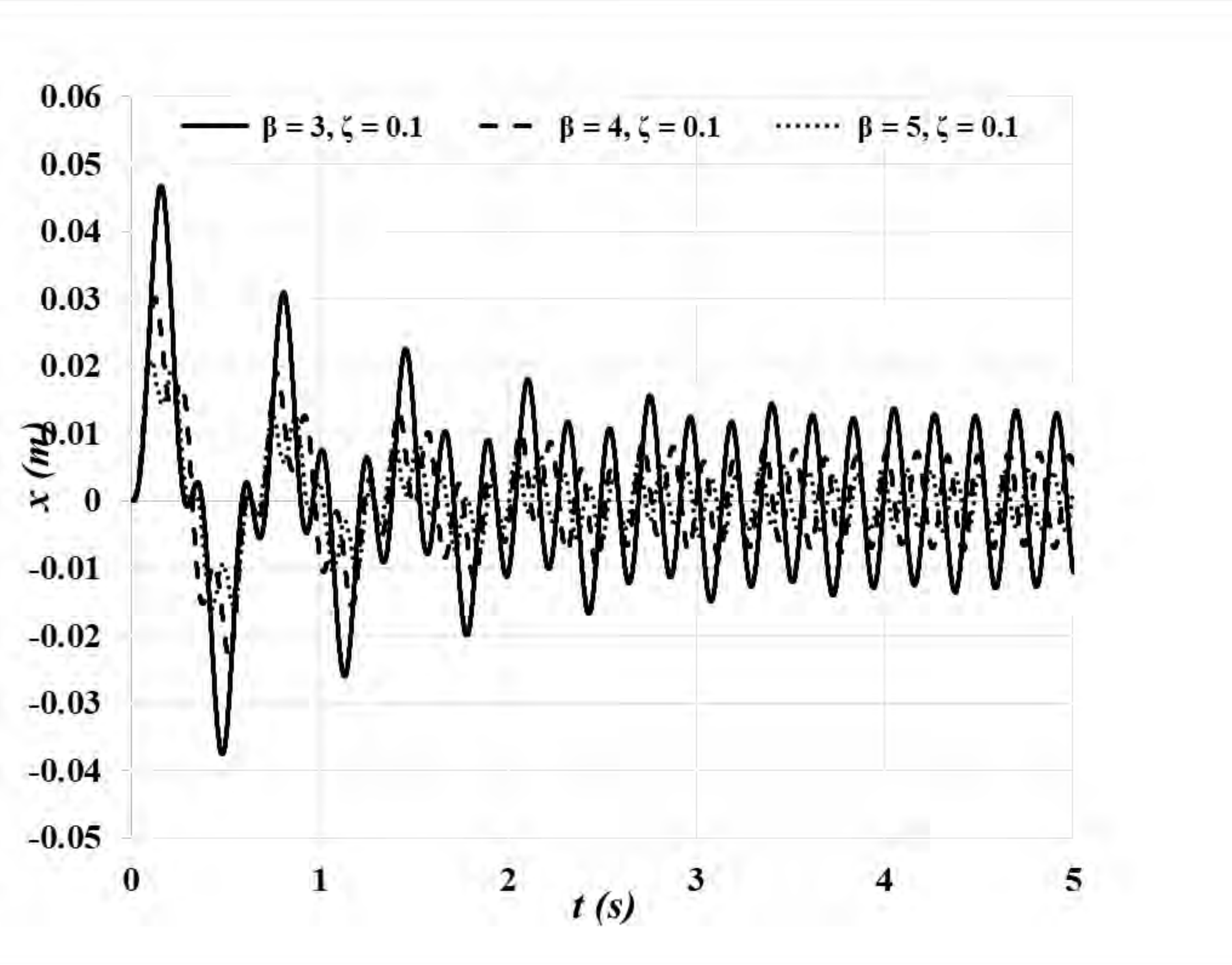

Figure 4.3.6: Displacement (m) vs time (s) curve for different speed ratio, β and damping ratio, $\zeta = 0.1$ for linear analysis.

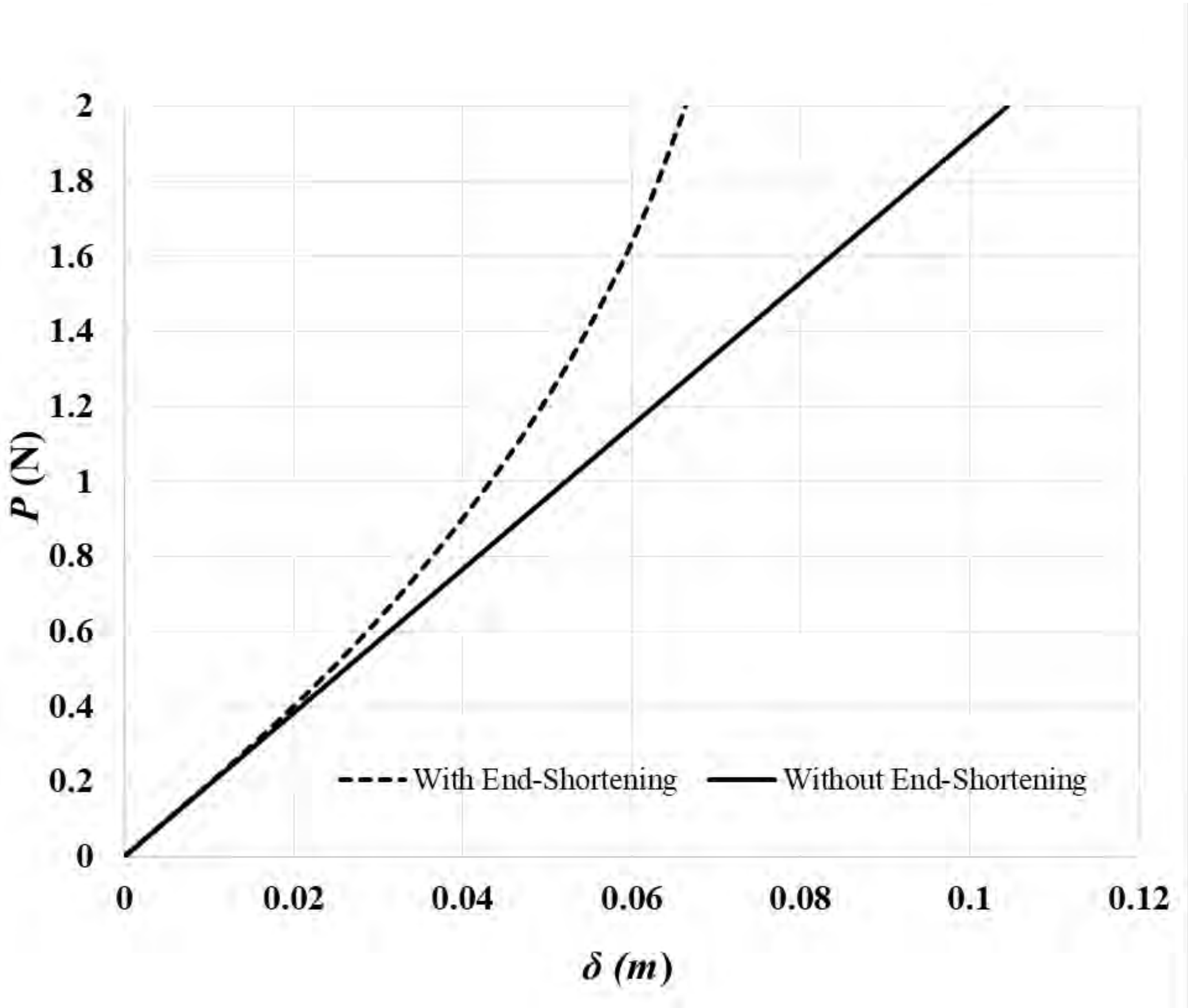

Figure 4.4.1: Load (N) vs tip deflection (m) curve for classical theory with and without end-shortening.

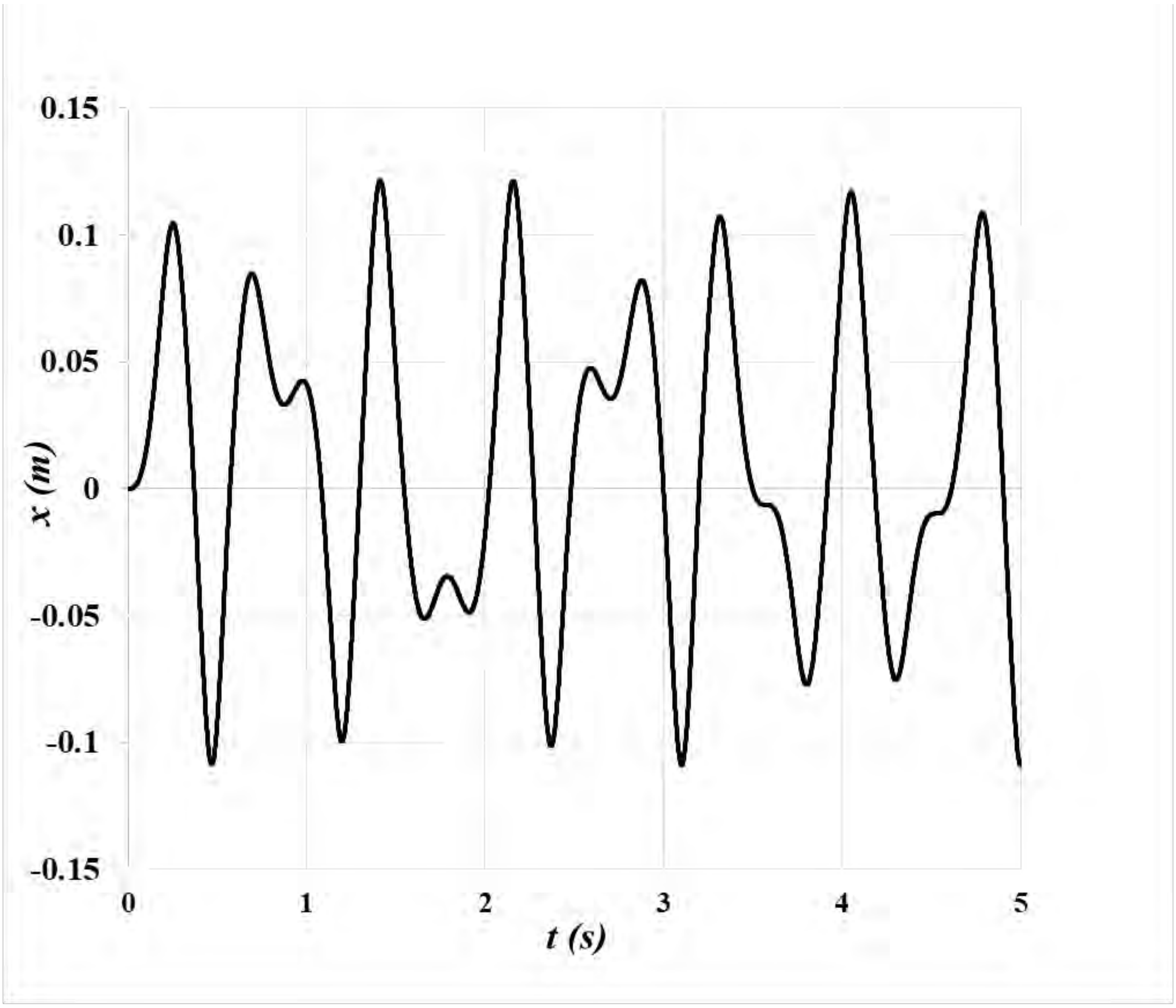

Figure 4.4.2: Displacement (m) vs time (s) curve at resonance (β = 1) when undamped (ζ = 0) considering end-shortening.

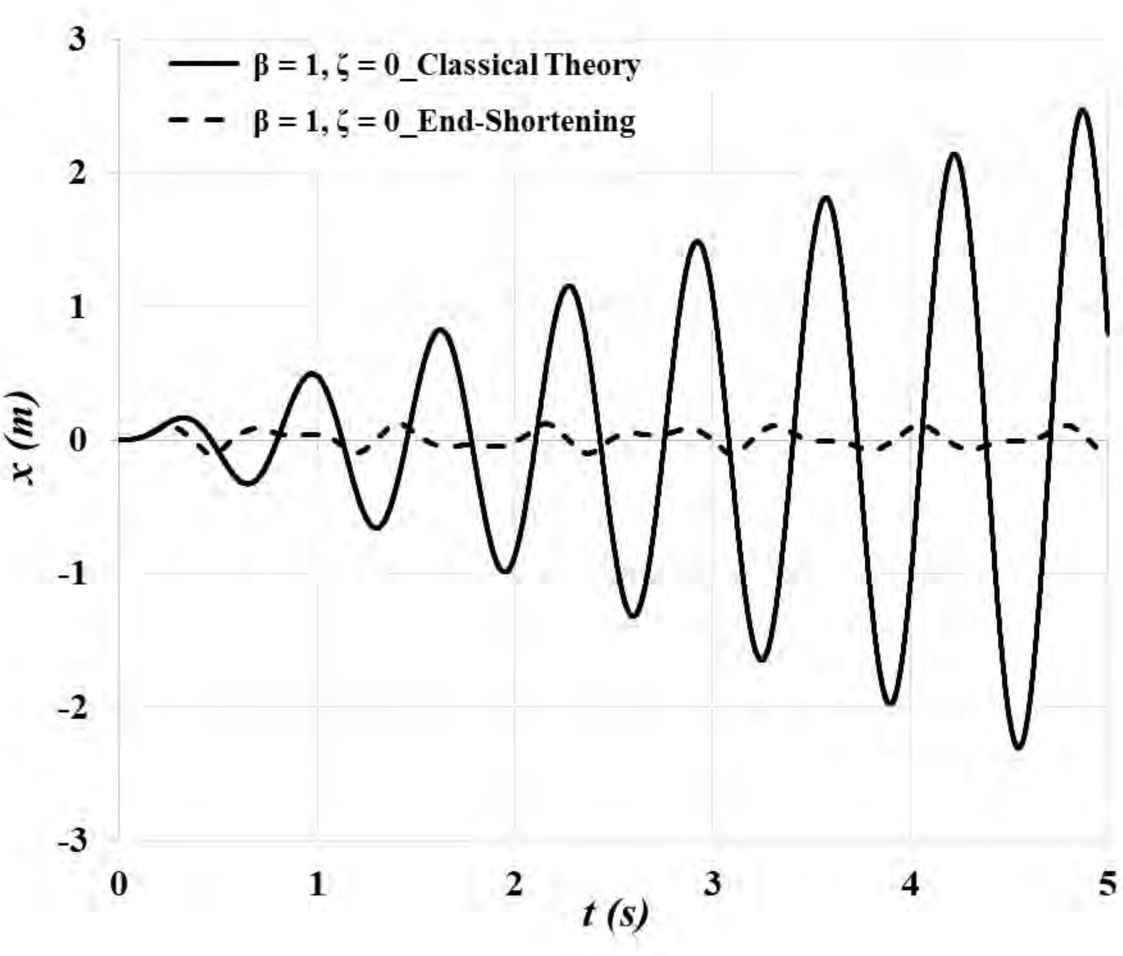

Figure 4.4.3: Displacement (m) vs time (s) curve at resonance ($\beta = 1$) when undamped ($\zeta = 0$) considering end-shortening and without end-shortening effect.

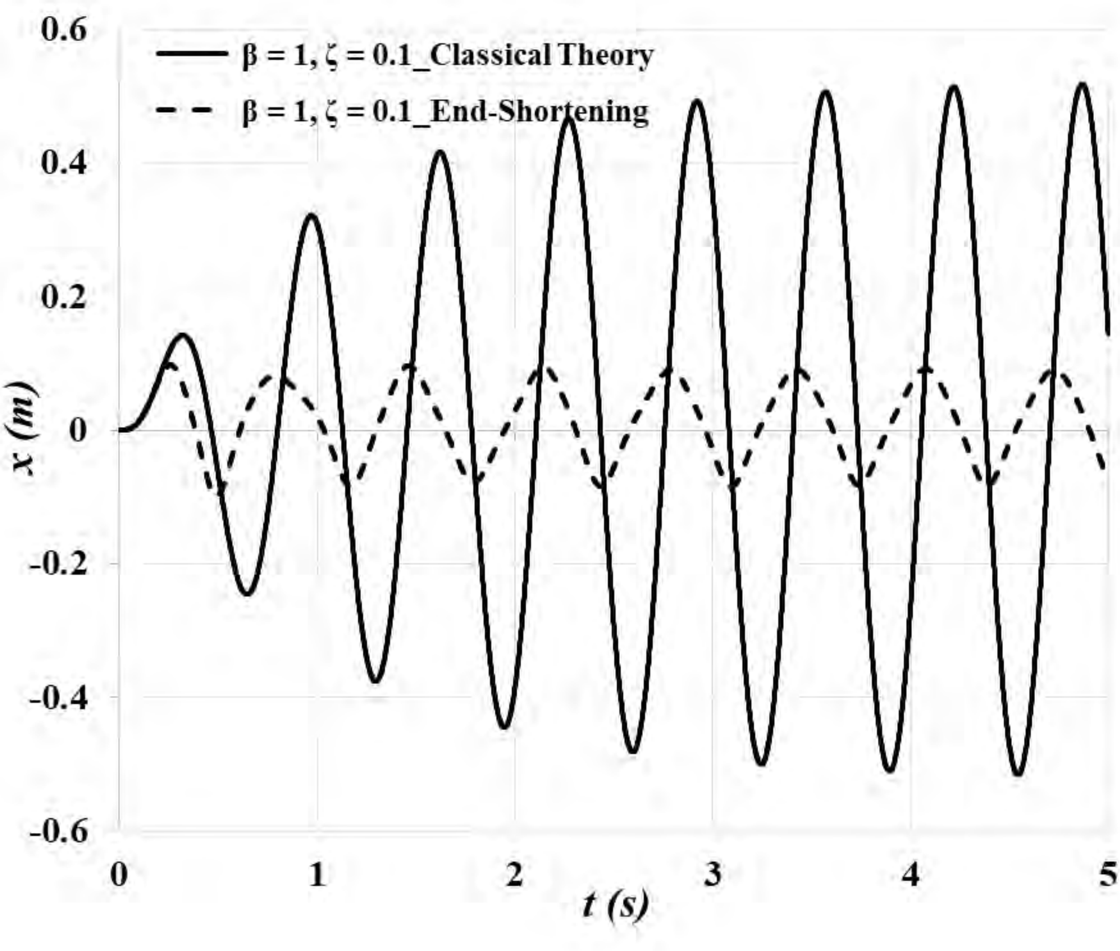

Figure 4.4.4: Displacement (m) vs time (s) curve at resonance (β = 1) and damping ratio, ζ = 0.1 considering end-shortening and without end-shortening effect.

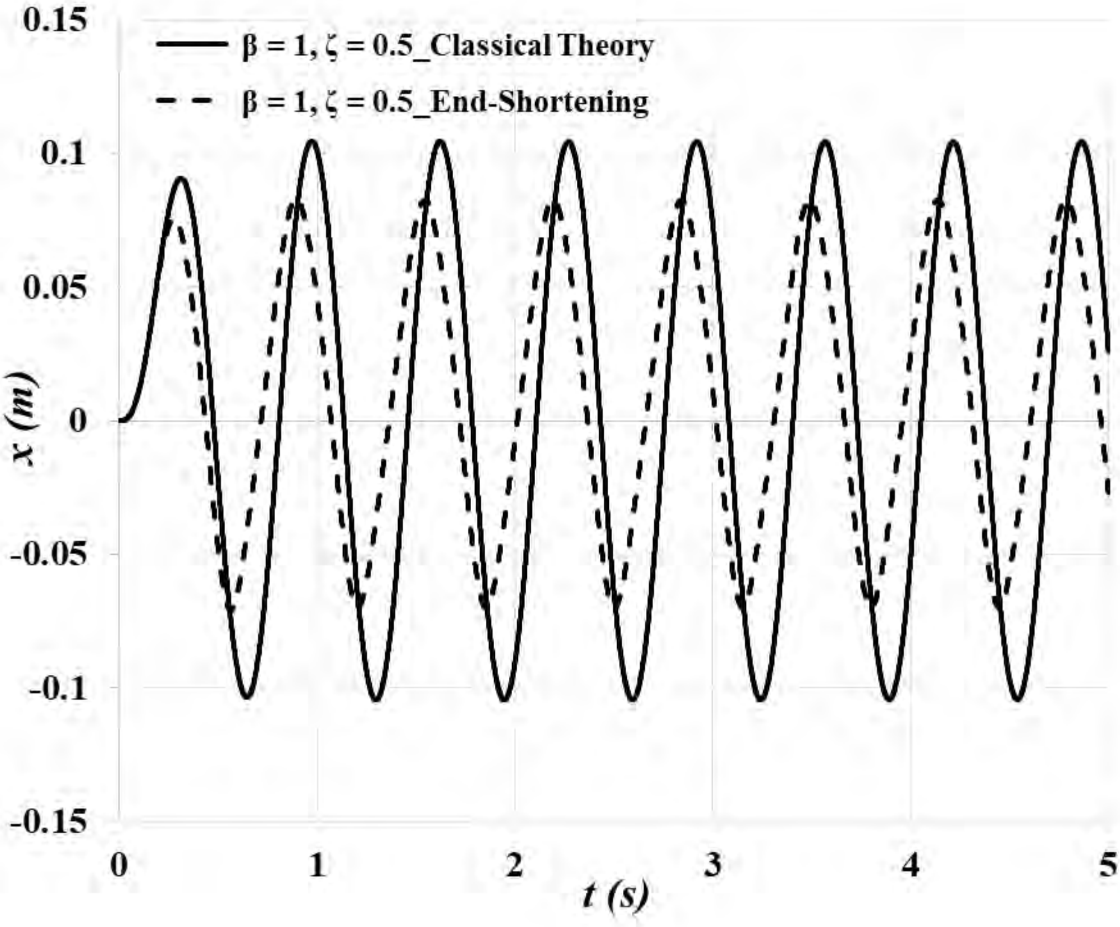

Figure 4.4.5: Displacement (m) vs time (s) curve at resonance (β = 1) and damping ratio, ζ = 0.5 considering end-shortening and without end-shortening effect.

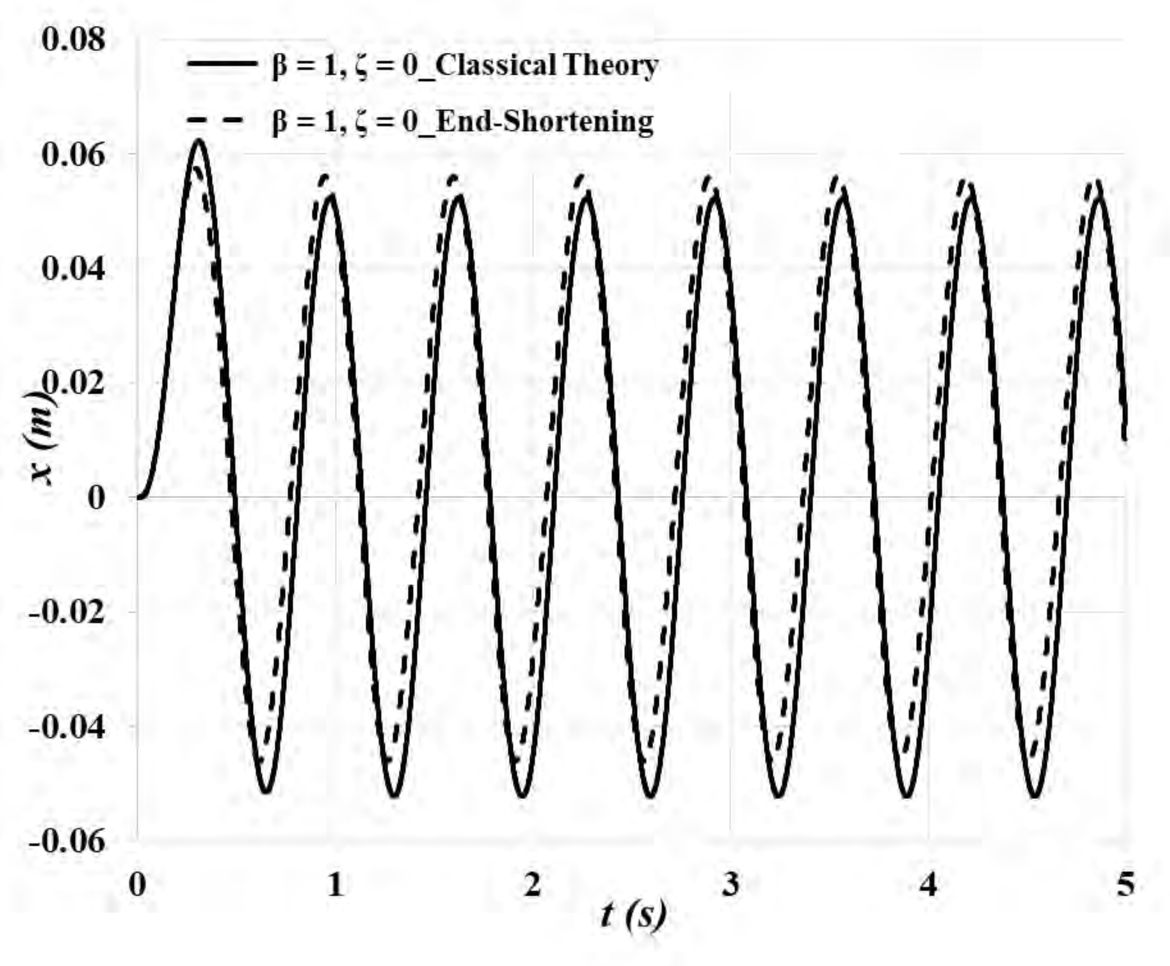

Figure 4.4.6: Displacement (m) vs time (s) curve at resonance (β = 1) and damping ratio, ζ = 1 considering end-shortening and without end-shortening effect.

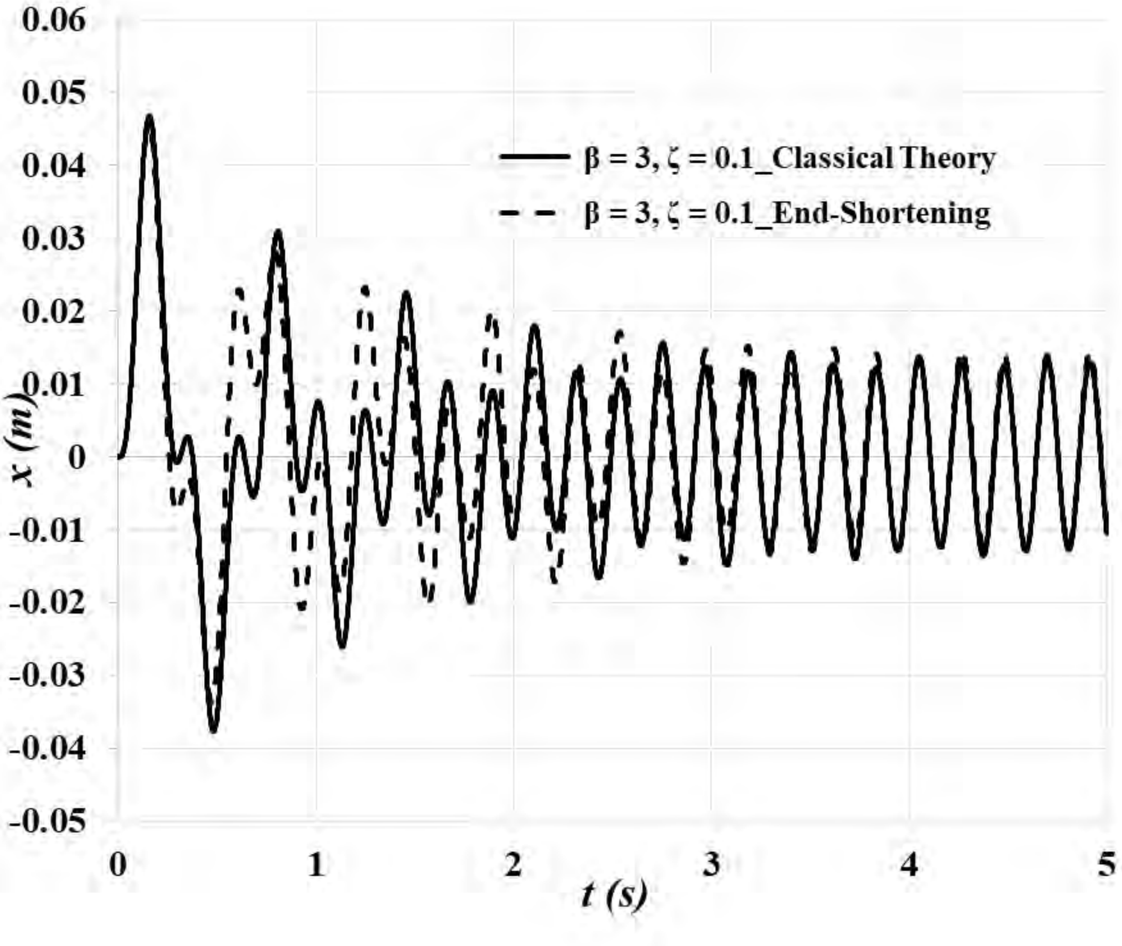

Figure 4.4.7: Displacement (m) vs time (s) curve for speed ratio, β = 3 and damping ratio, ζ = 0.1 considering end-shortening and without end-shortening effect.

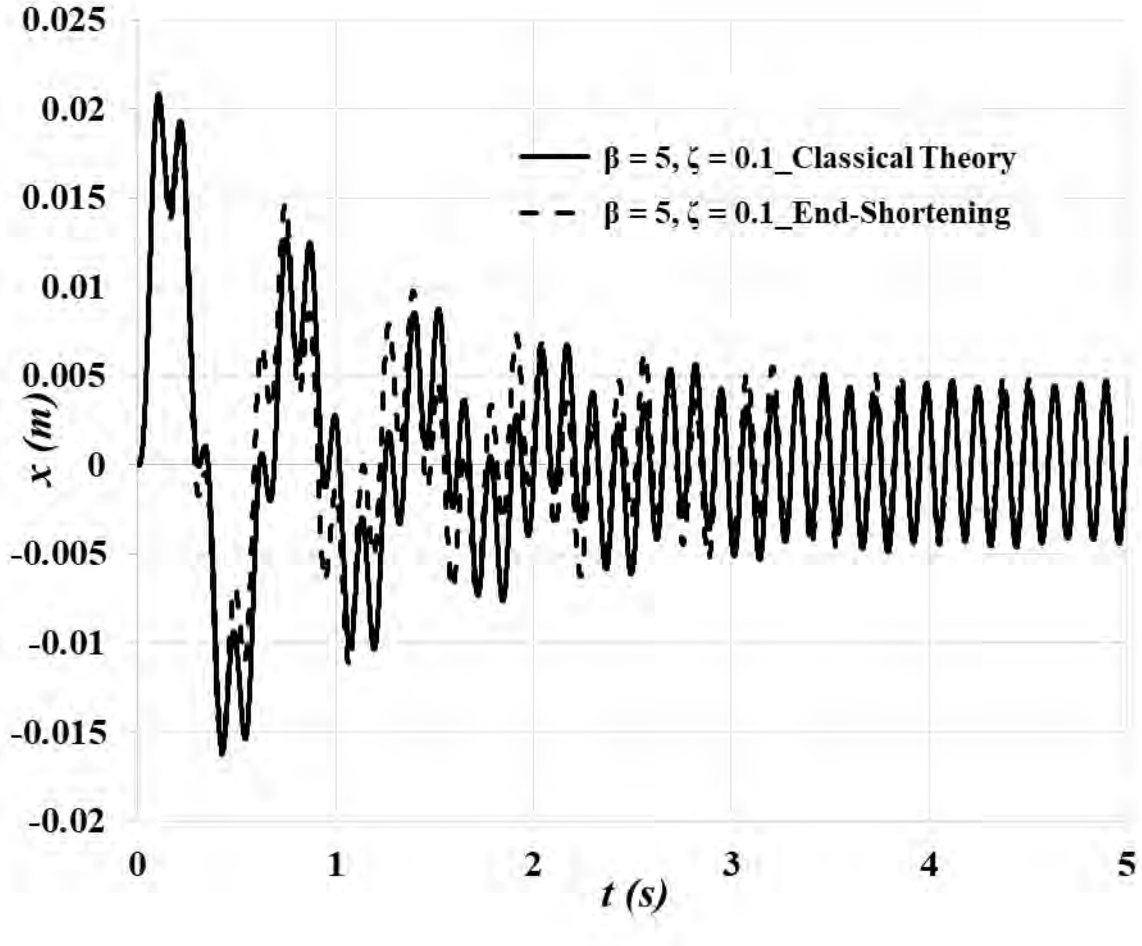

Figure 4.4.8: Displacement (m) vs time (s) curve for speed ratio, β = 5 and damping ratio, ζ = 0.1 considering end-shortening and without end-shortening effect.

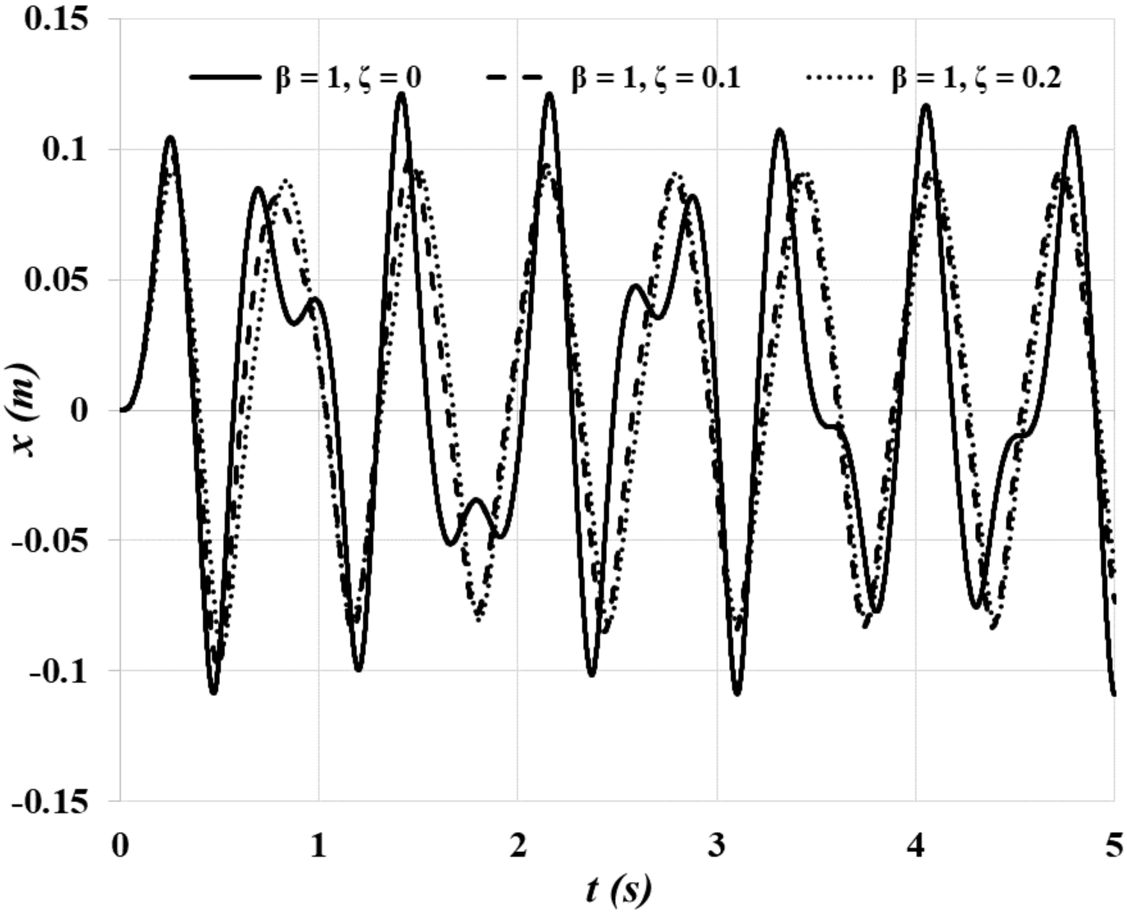

Figure 4.4.9: Displacement (m) vs time (s) curve at resonance (β = 1) for different damping ratio, ζ with end-shortening.

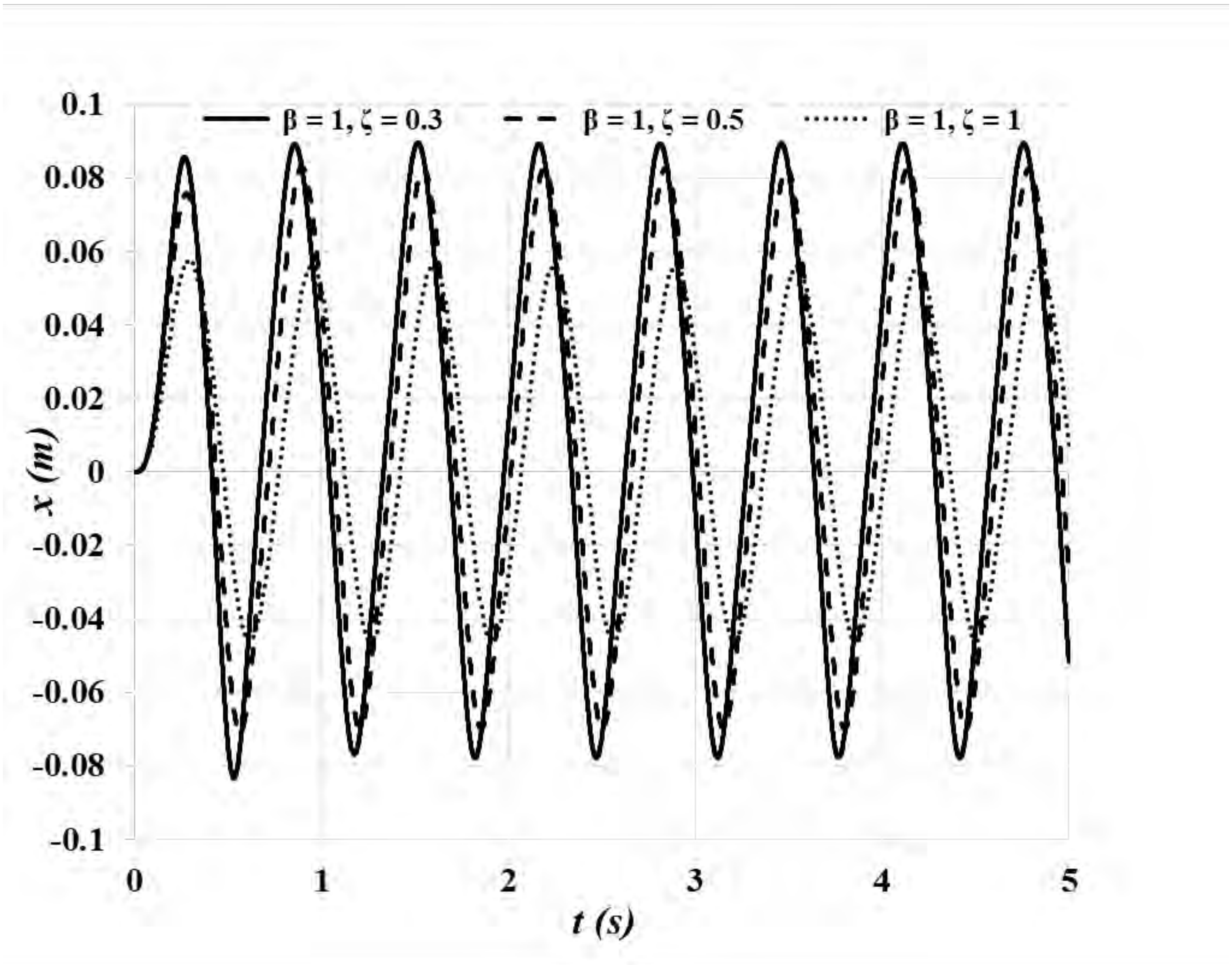

Figure 4.4.10: Displacement (m) vs time (s) curve at resonance (β = 1) for different damping ratio, ζ with end-shortening.

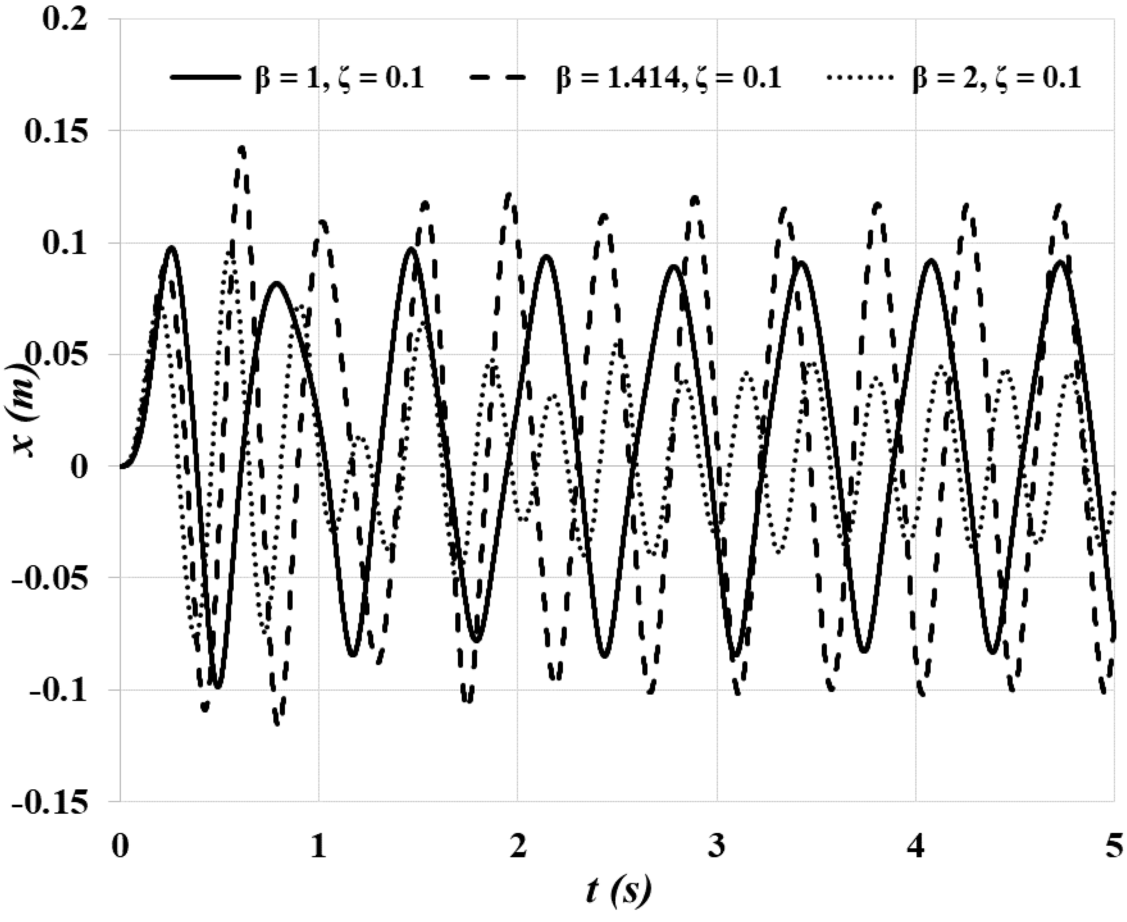

Figure 4.4.11: Displacement (m) vs time (s) curve for different speed ratio, β and damping ratio, $\zeta = 0.1$ with end-shortening.

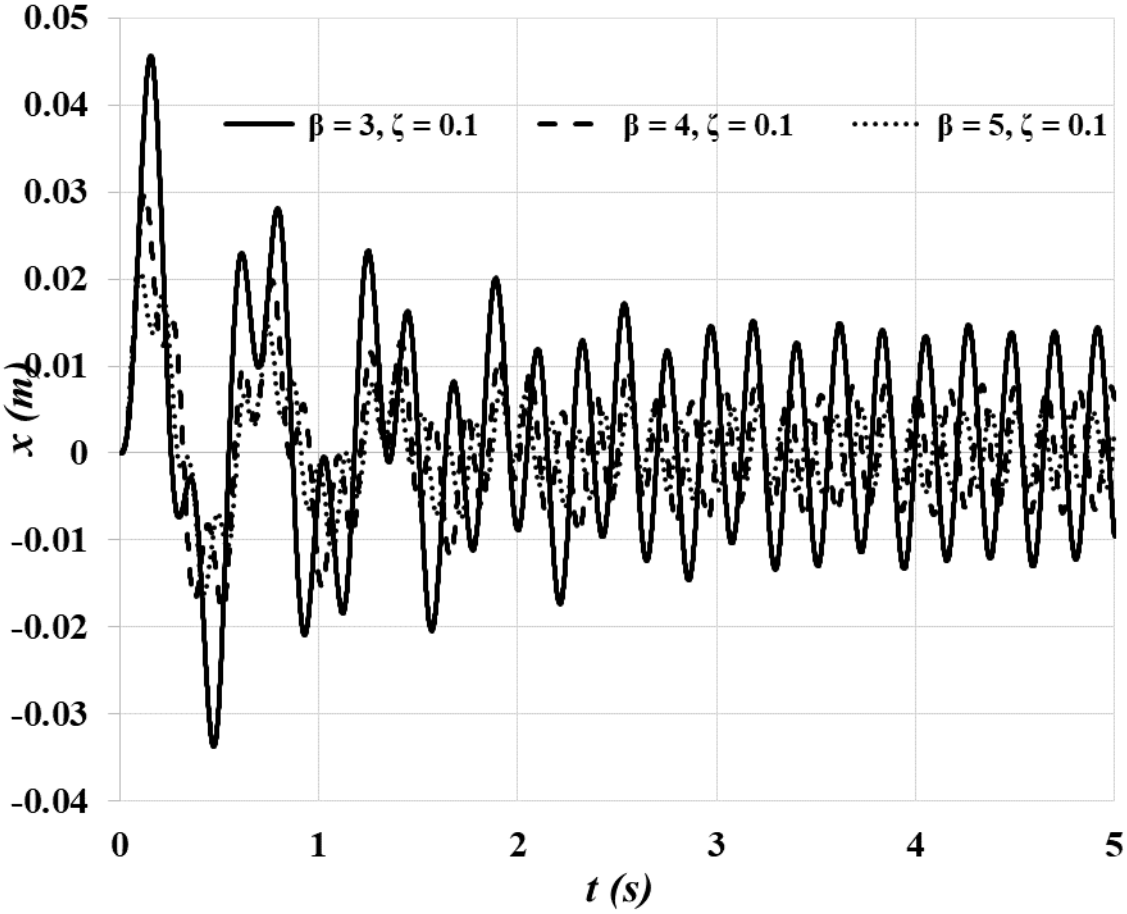

Figure 4.4.12: Displacement (m) vs time (s) curve for different speed ratio, β and damping ratio, $\zeta = 0.1$ with end-shortening.

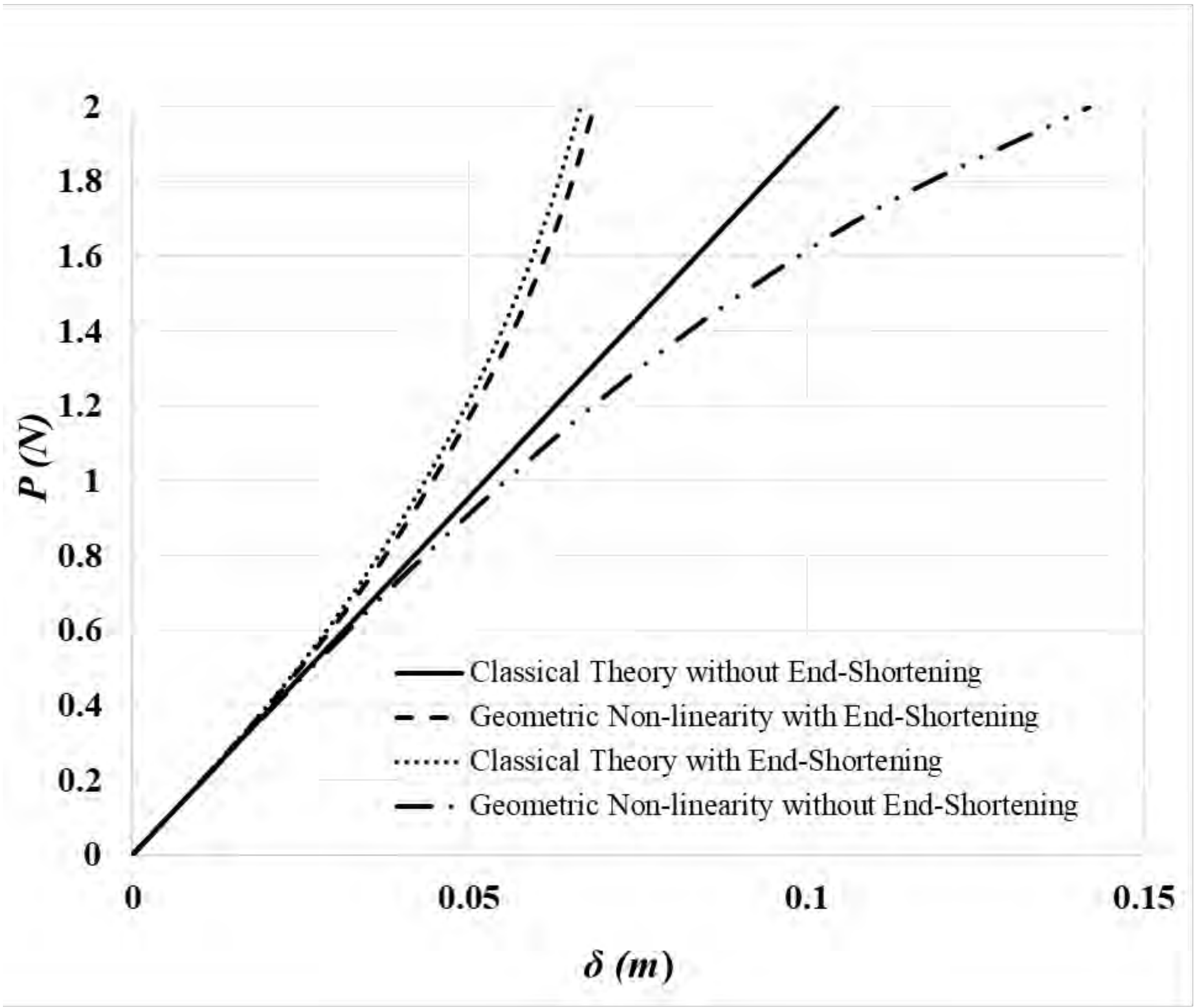

Figure 4.5.1: Load (N) vs tip deflection (m) curve for geometrically non-linear analysis considering end-shortening and without end-shortening.

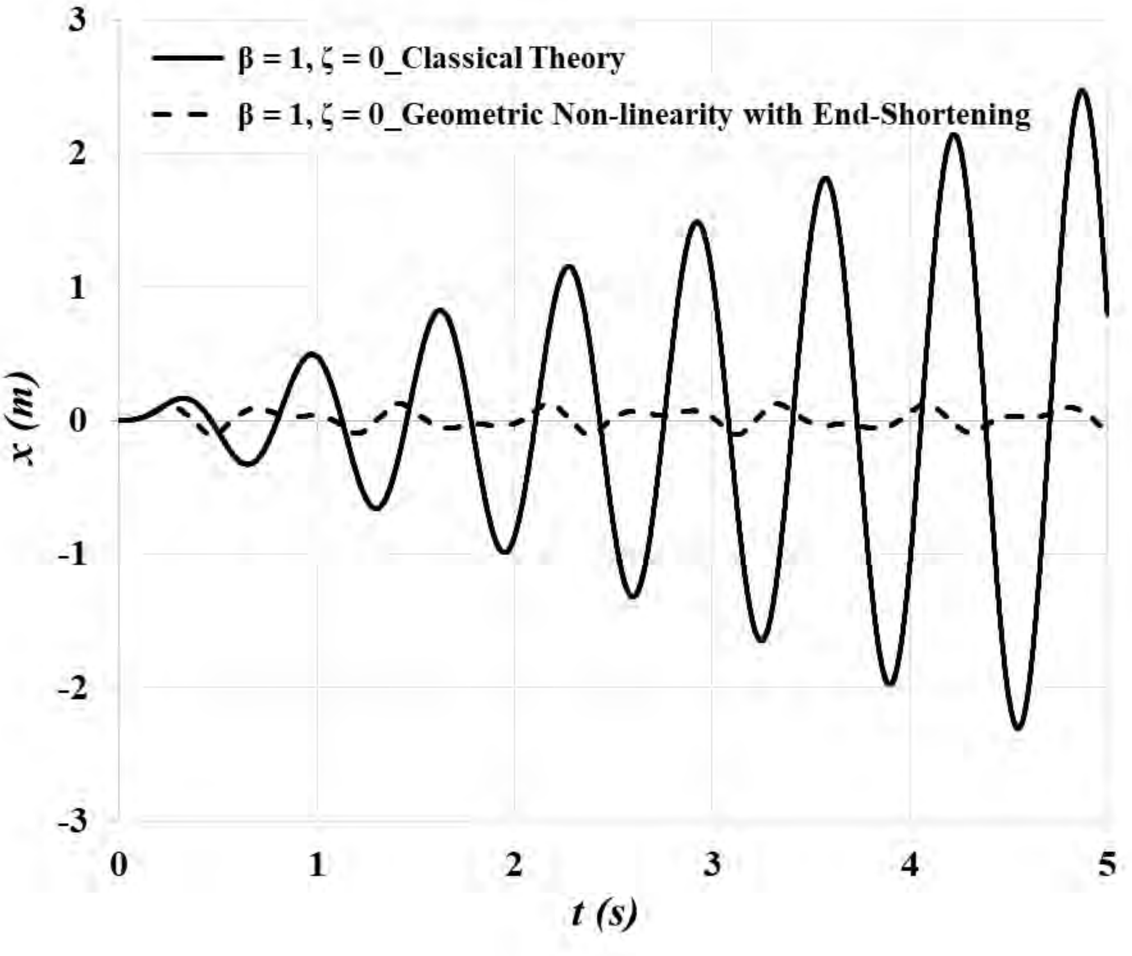

Figure 4.5.2: Displacement (m) vs time (s) curve at resonance (β = 1) when undamped (ζ = 0) for classical theory and considering geometric non-linearity with end-shortening.

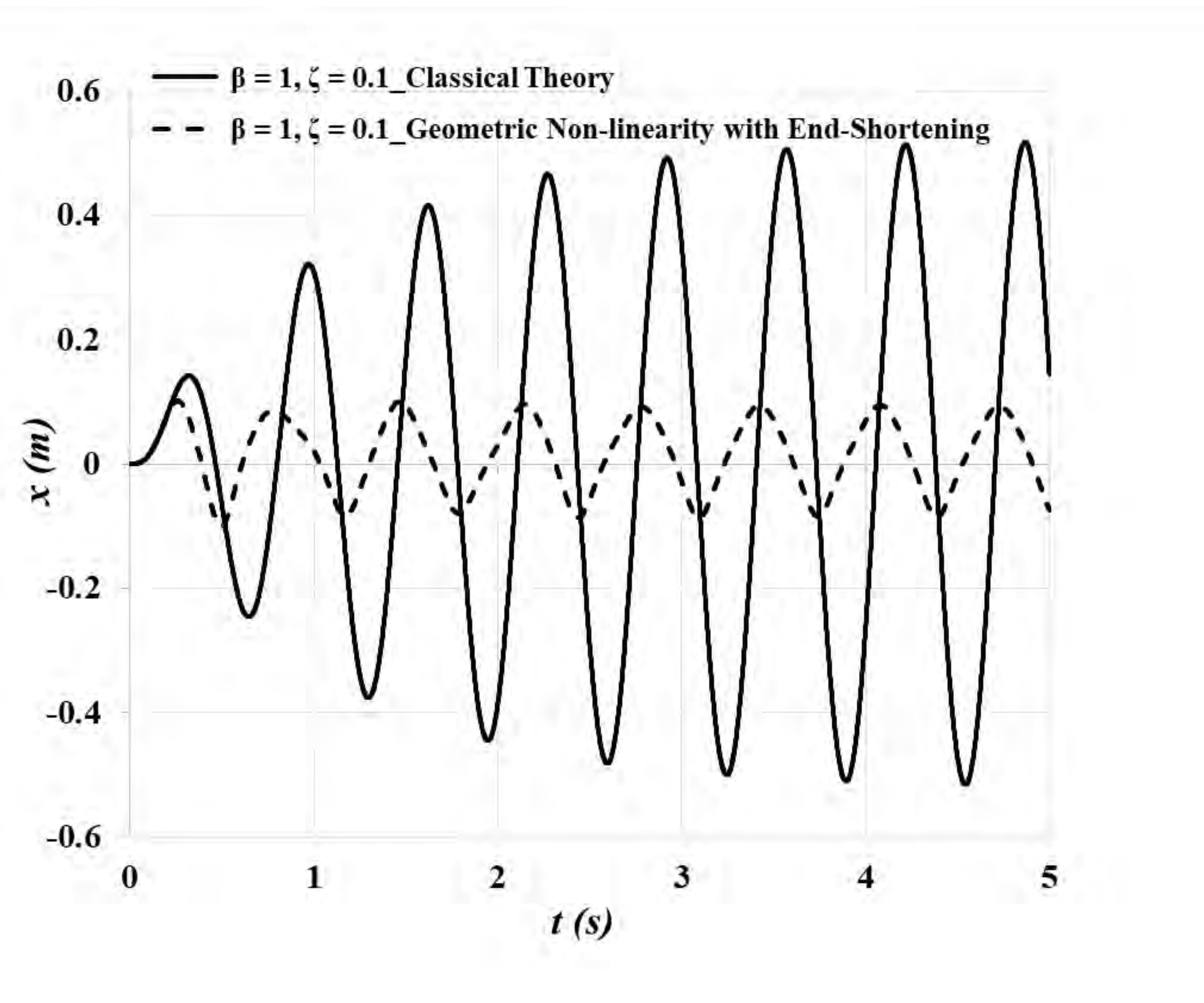

Figure 4.5.3: Displacement (m) vs time (s) curve at resonance (β = 1) for damping ratio, ζ = 0.1 for classical theory and considering geometric non-linearity with end-shortening.

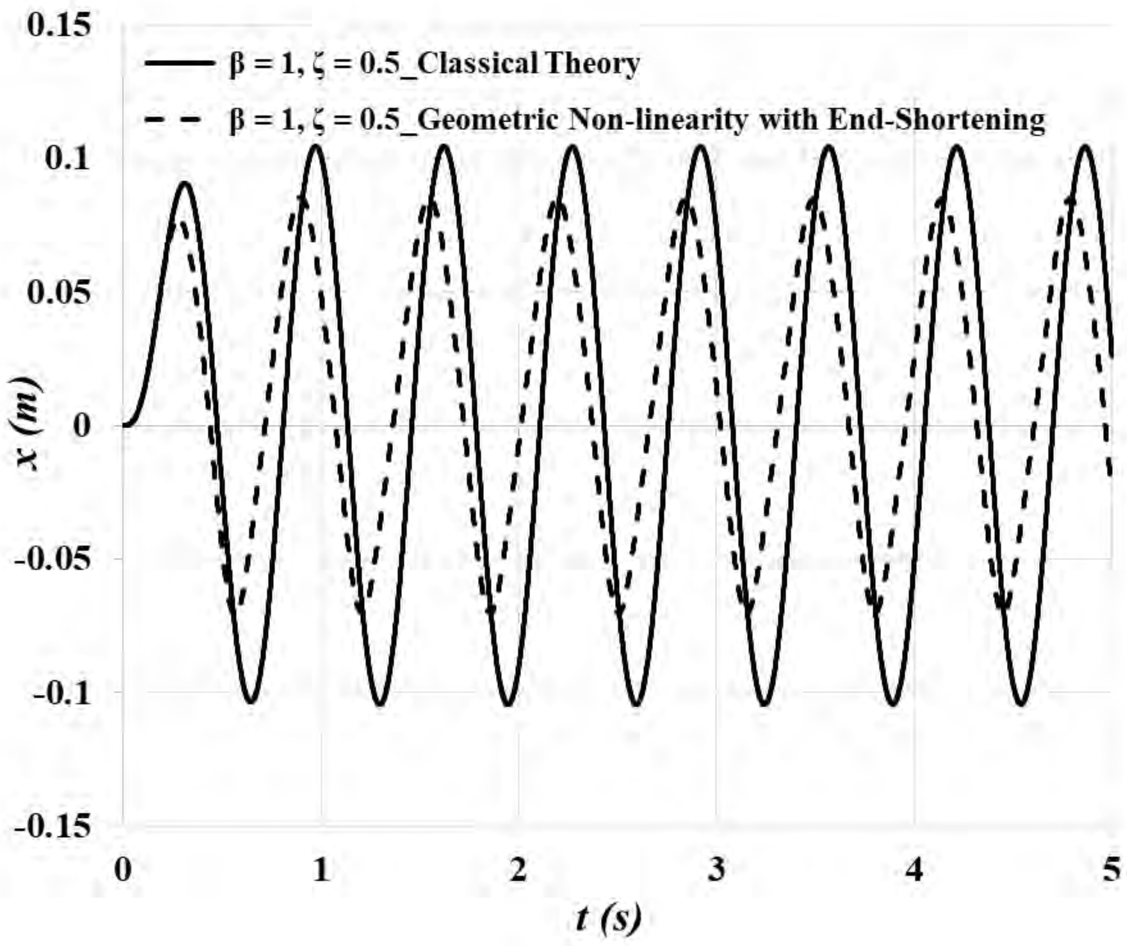

Figure 4.5.4: Displacement (m) vs time (s) curve at resonance (β = 1) for damping ratio, ζ = 0.5 for classical theory and considering geometric non-linearity with end-shortening.

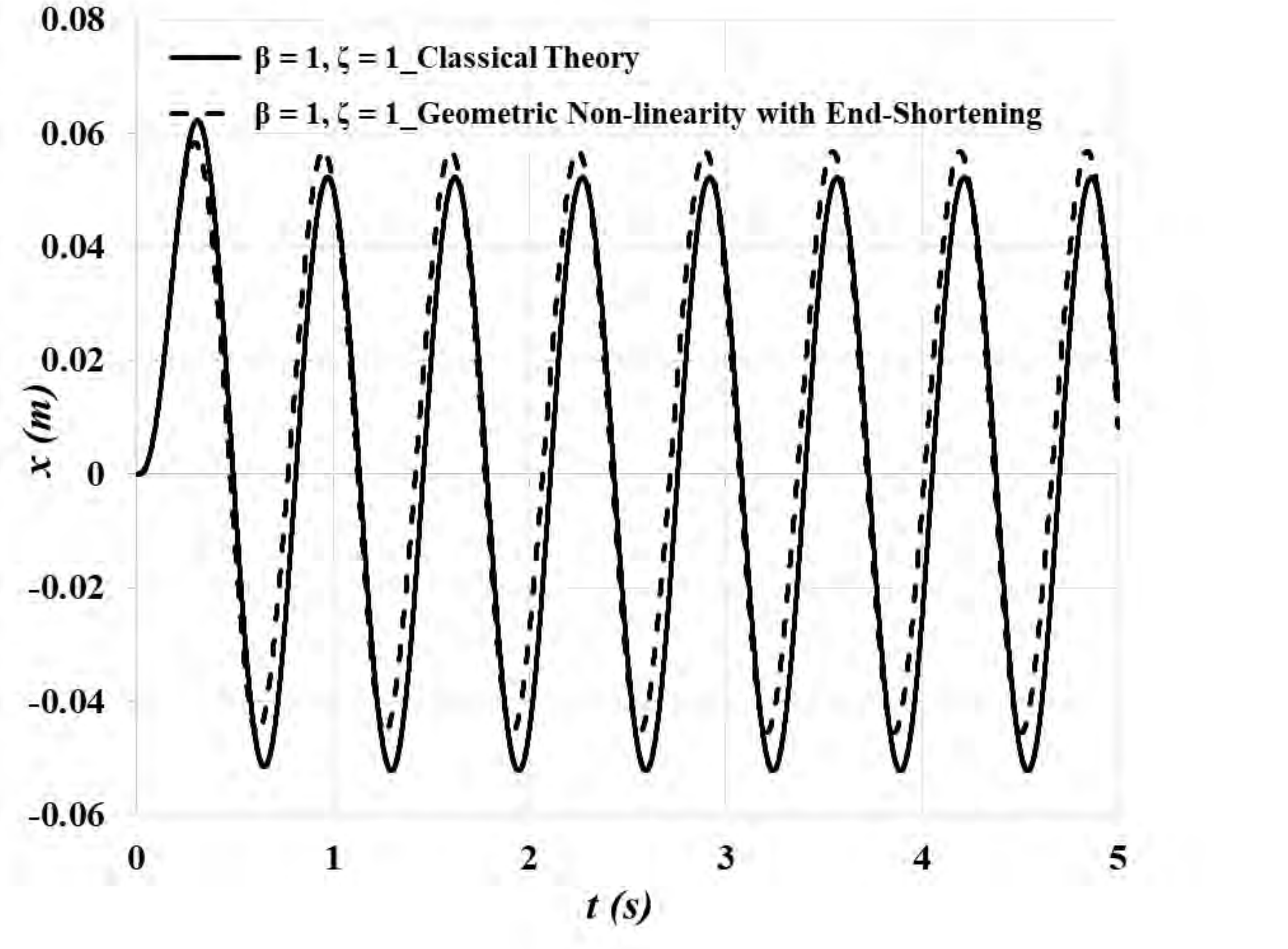

Figure 4.5.5: Displacement (m) vs time (s) curve at resonance ($\beta = 1$) for damping ratio, $\zeta = 1$ for classical theory and considering geometric non-linearity with end-shortening.

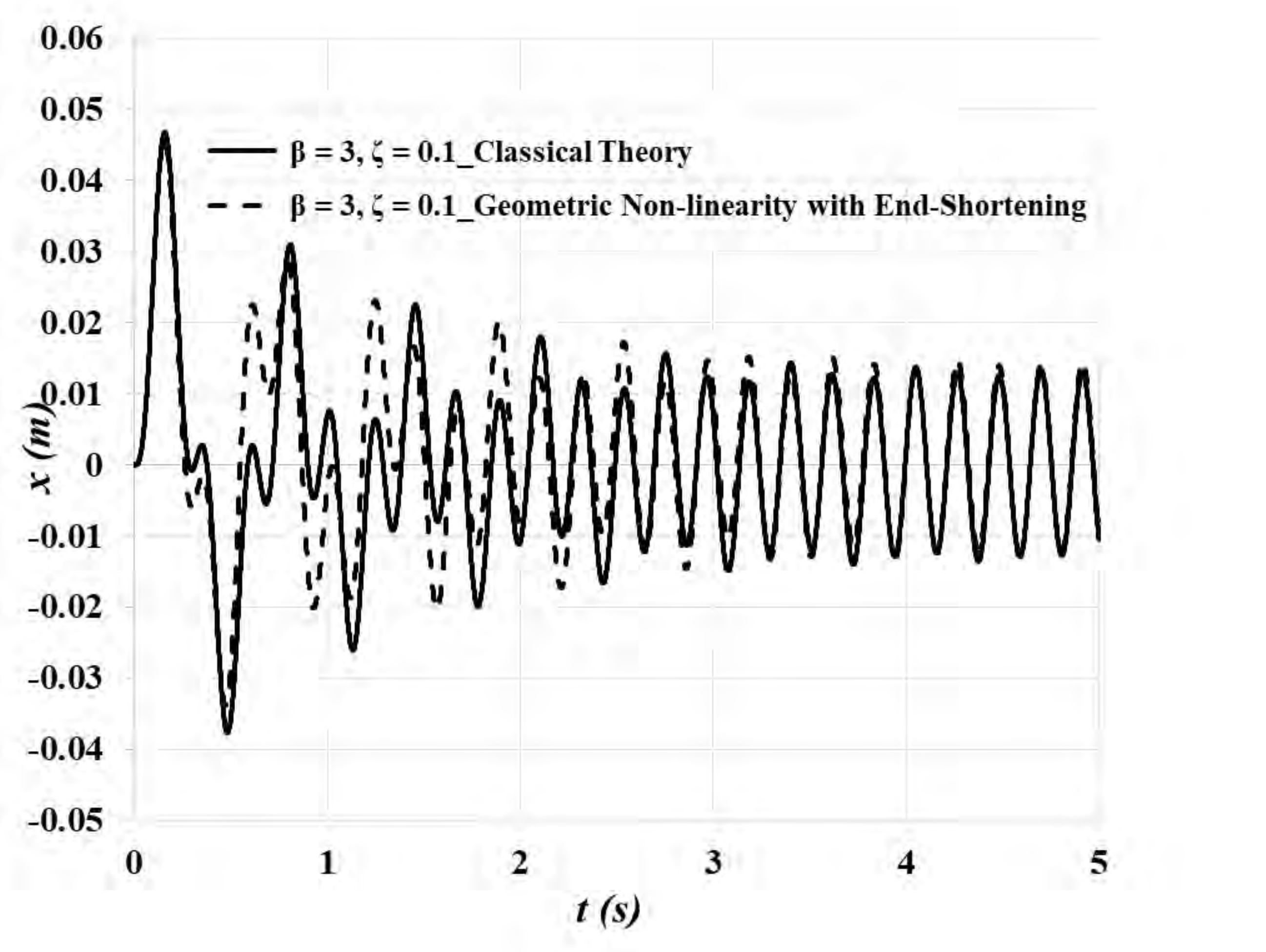

Figure 4.5.6: Displacement (m) vs time (s) curve for speed ratio, $\beta = 3$ and damping ratio, $\zeta = 0.1$ for classical theory and considering geometric non-linearity with end-shortening.

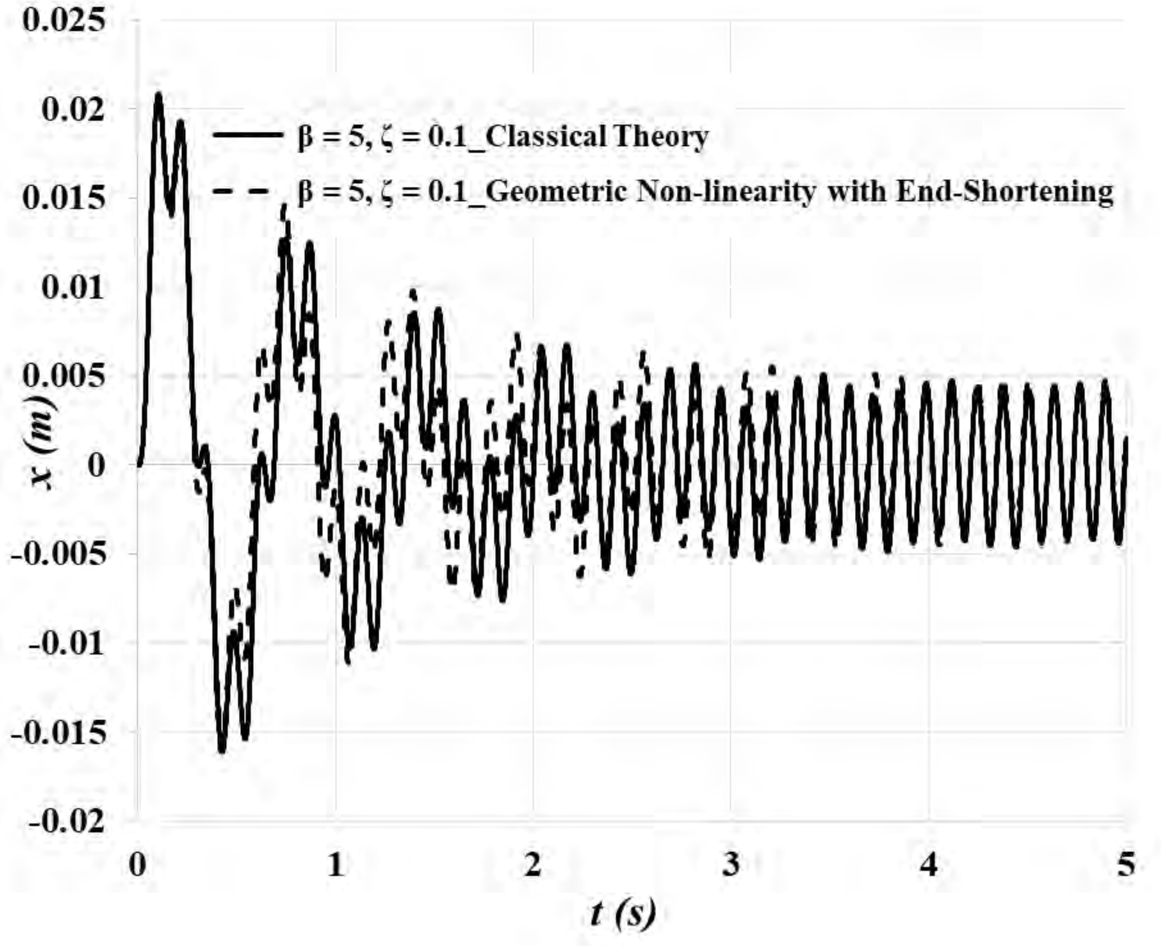

Figure 4.5.7: Displacement (m) vs time (s) curve for speed ratio, β = 5 and damping ratio, ζ = 0.1 for classical theory and considering geometric non-linearity with end-shortening.

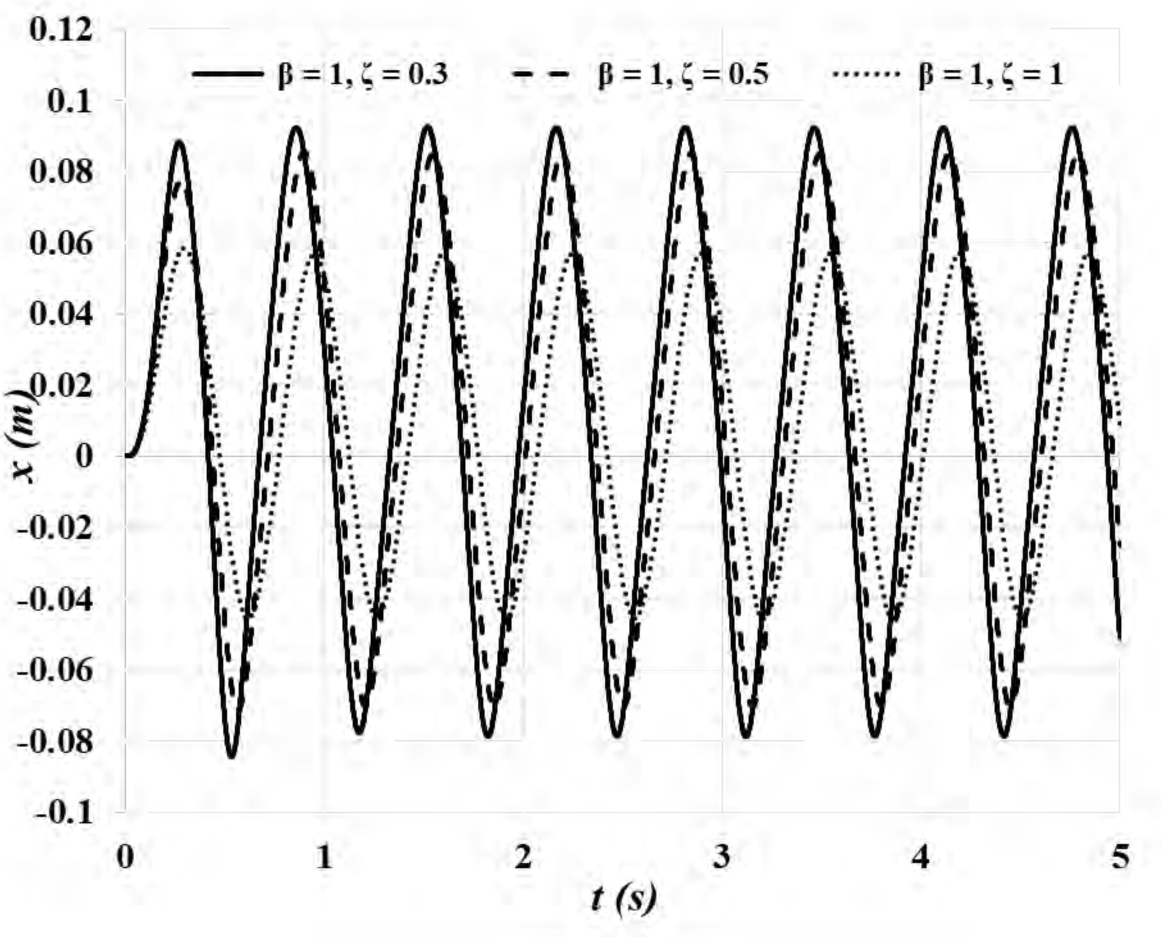

Figure 4.5.8: Displacement (m) vs time (s) curve at resonance (β = 1) for different damping ratio, ζ considering geometric non-linearity with end-shortening.

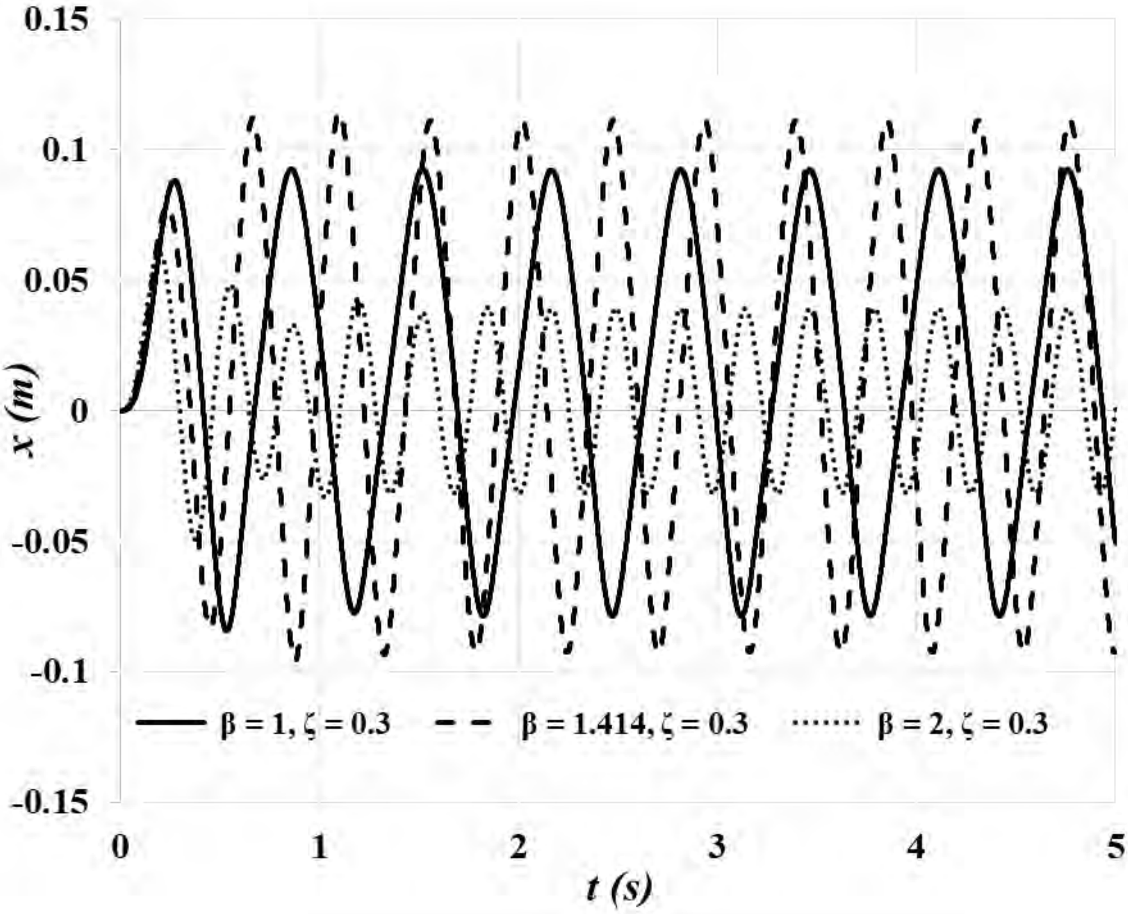

Figure 4.5.9: Displacement (m) vs time (s) curve for different speed ratio, β and for damping ratio, $\zeta = 0.3$ considering geometric non-linearity with end-shortening.

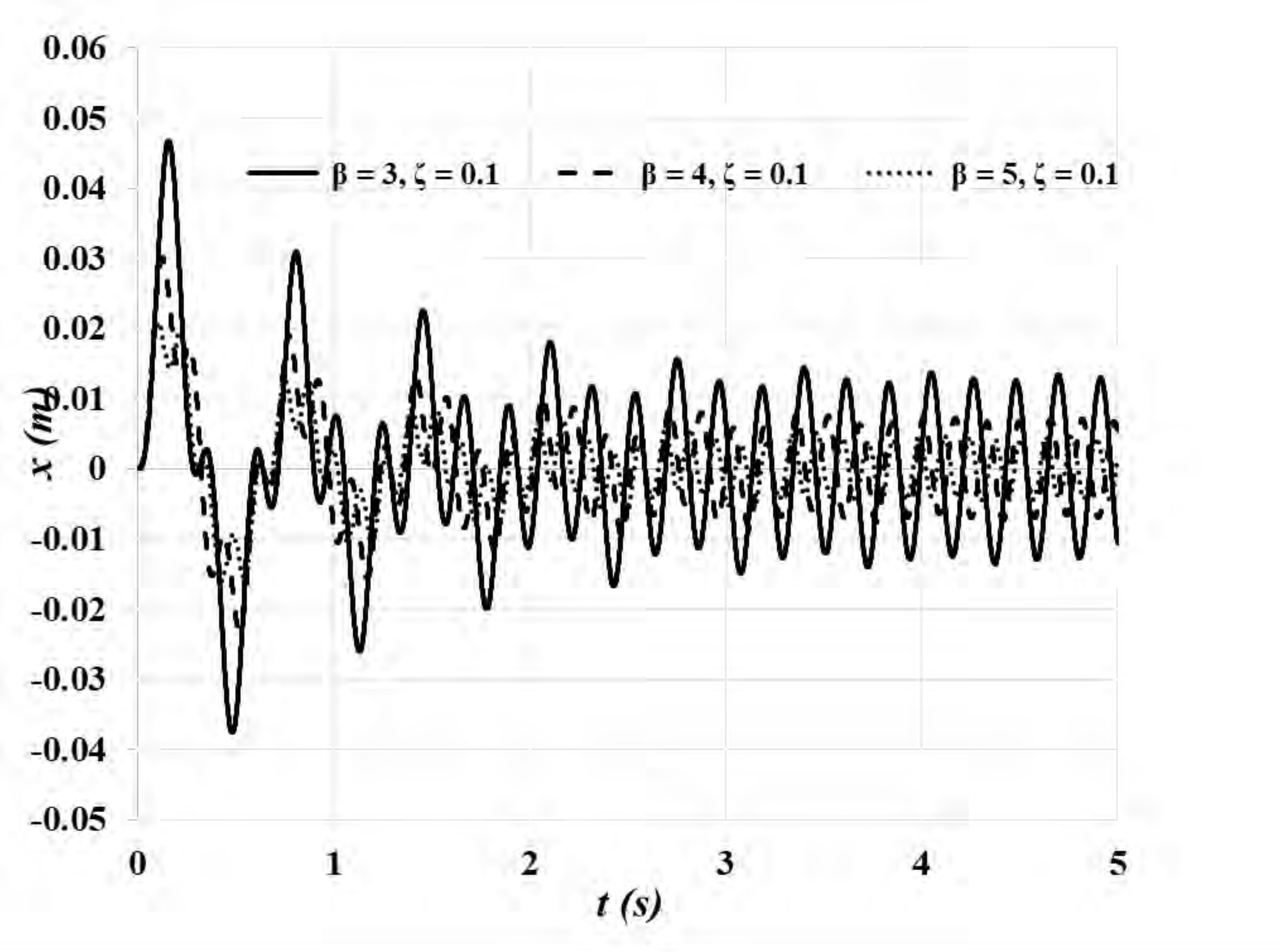

Figure 4.5.10: Displacement (m) vs time (s) curve for different speed ratio, β and for damping ratio, $\zeta = 0.1$ considering geometric non-linearity with end-shortening.

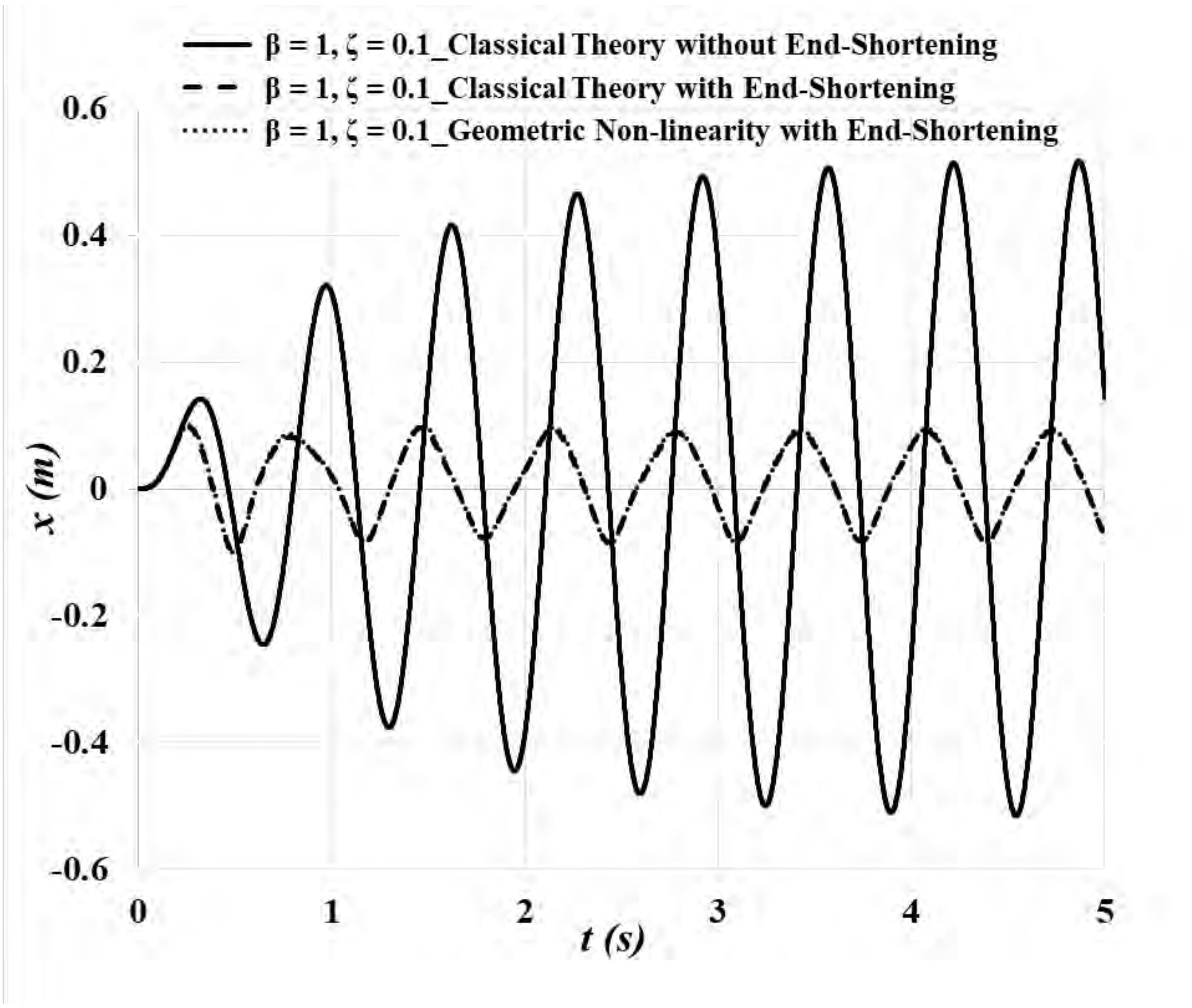

Figure 4.6.1: Displacement (m) vs time (s) curve at resonance ($\beta = 1$) for damping ratio, $\zeta = 0.1$ for classical theory with and without end-shortening and geometric non-linearity with end-shortening.

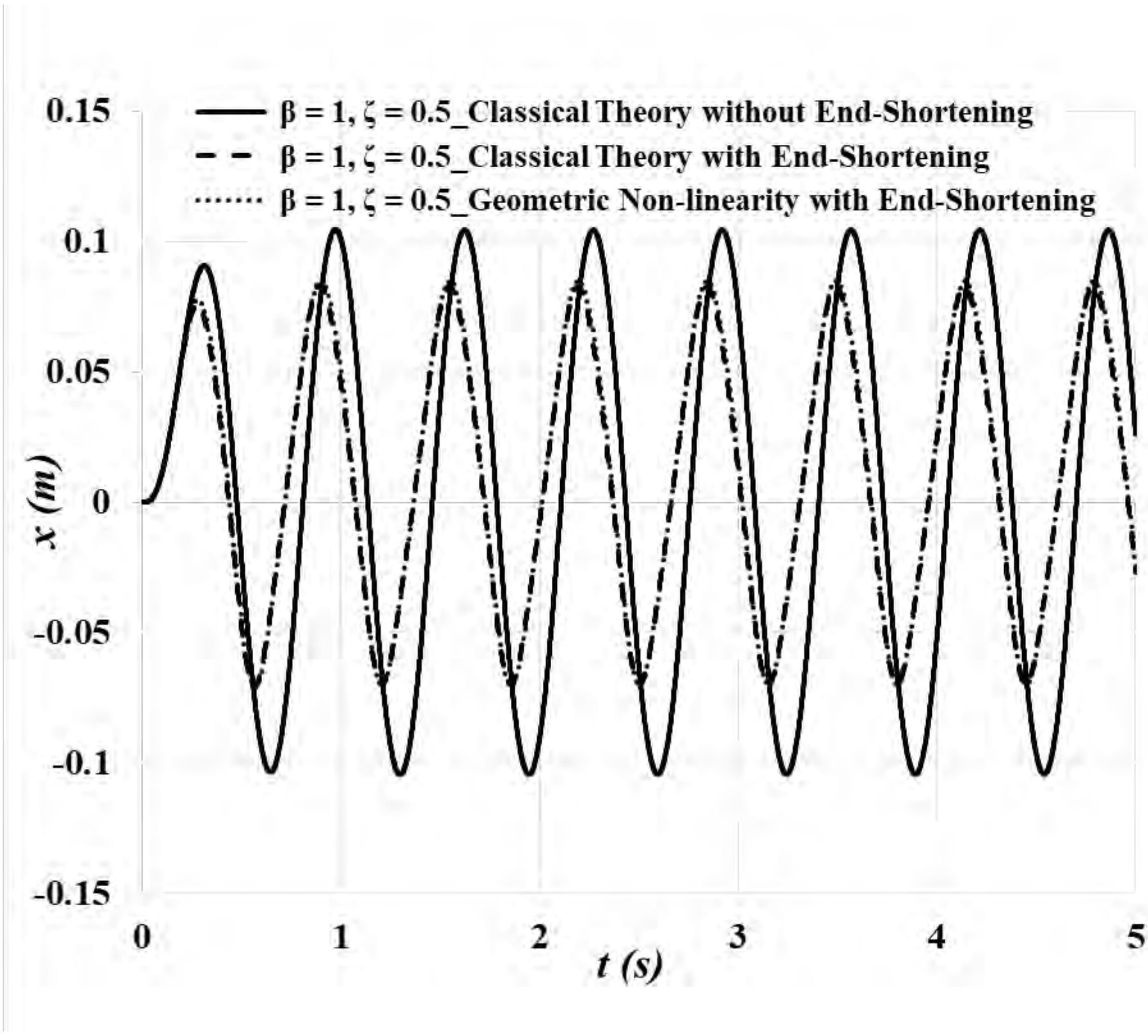

Figure 4.6.2: Displacement (m) vs time (s) curve at resonance ($\beta = 1$) for damping ratio, $\zeta = 0.5$ for classical theory with and without end-shortening and geometric non-linearity with end-shortening.

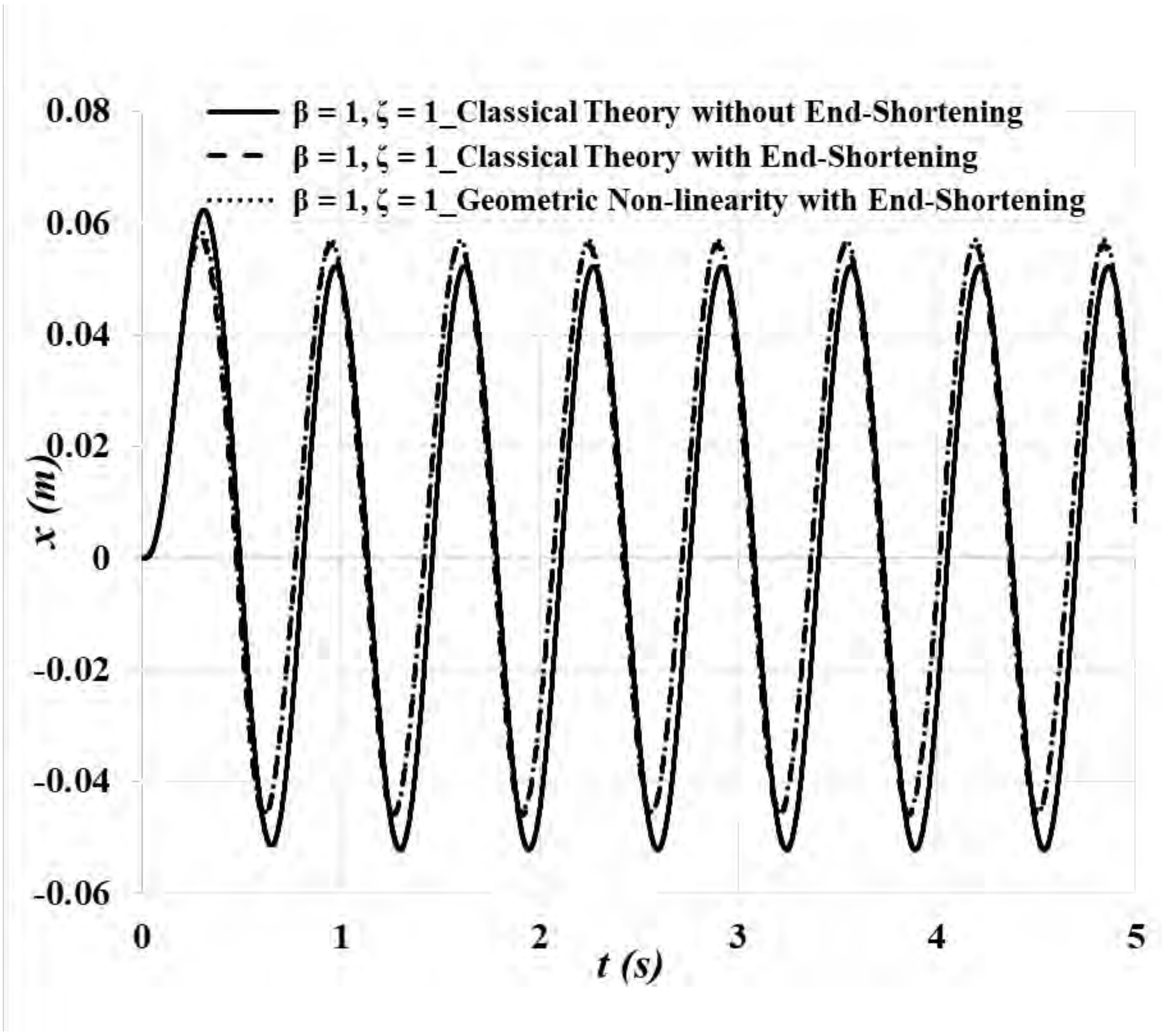

Figure 4.6.3: Displacement (m) vs time (s) curve at resonance (β = 1) for damping ratio, ζ = 1 for classical theory with and without end-shortening and geometric non-linearity with end-shortening.

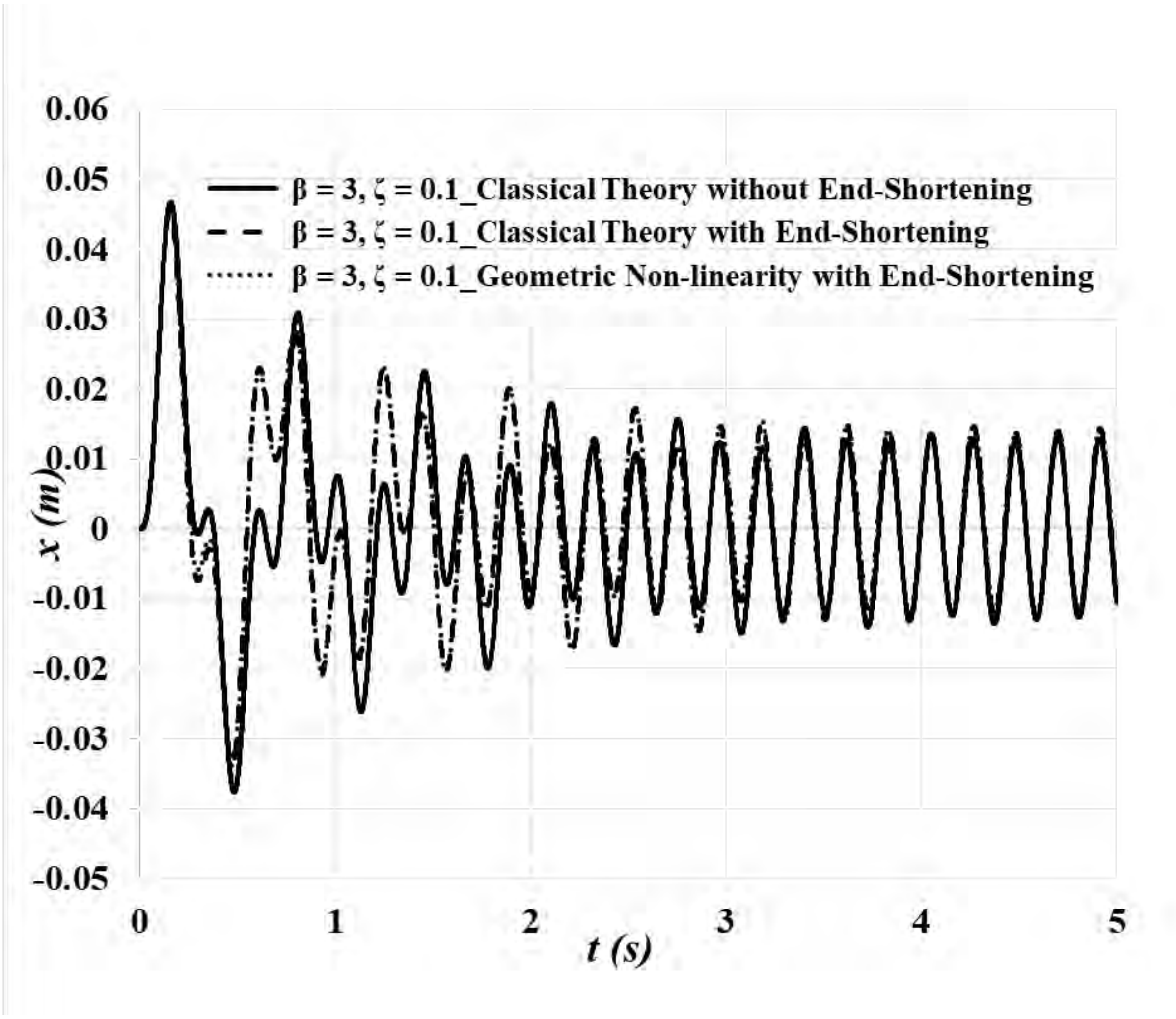

Figure 4.6.4: Displacement (m) vs time (s) curve for speed ratio, β = 3 and damping ratio, ζ = 0.1 for classical theory with and without end-shortening and geometric non-linearity with end-shortening.

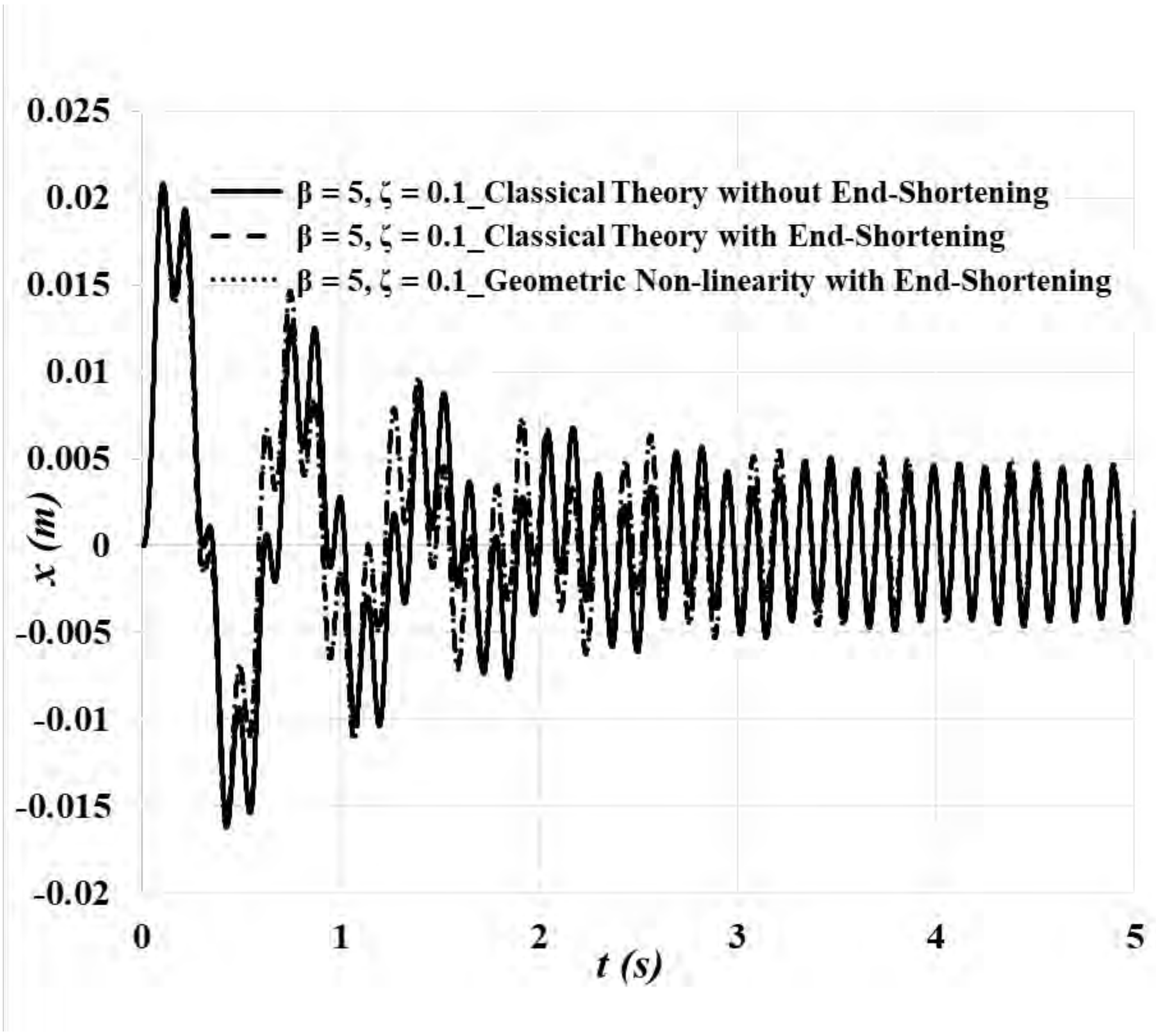

Figure 4.6.5: Displacement (m) vs time (s) curve for speed ratio, $\beta = 5$ and damping ratio, $\zeta = 0.1$ for classical theory with and without end-shortening and geometric non-linearity with end-shortening.

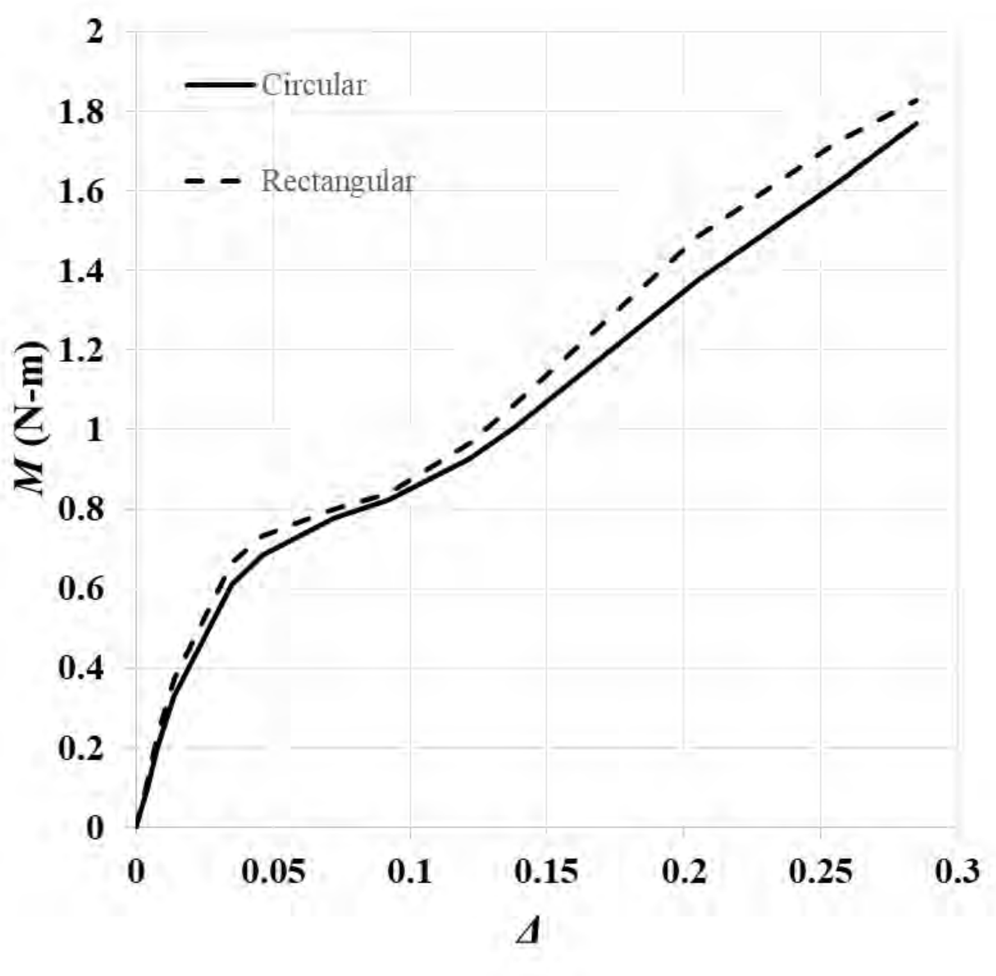

Figure 4.7.1: Bending moment vs Δ curve for superelastic SMA circular and equivalent rectangular beam (APPENDIX-C).

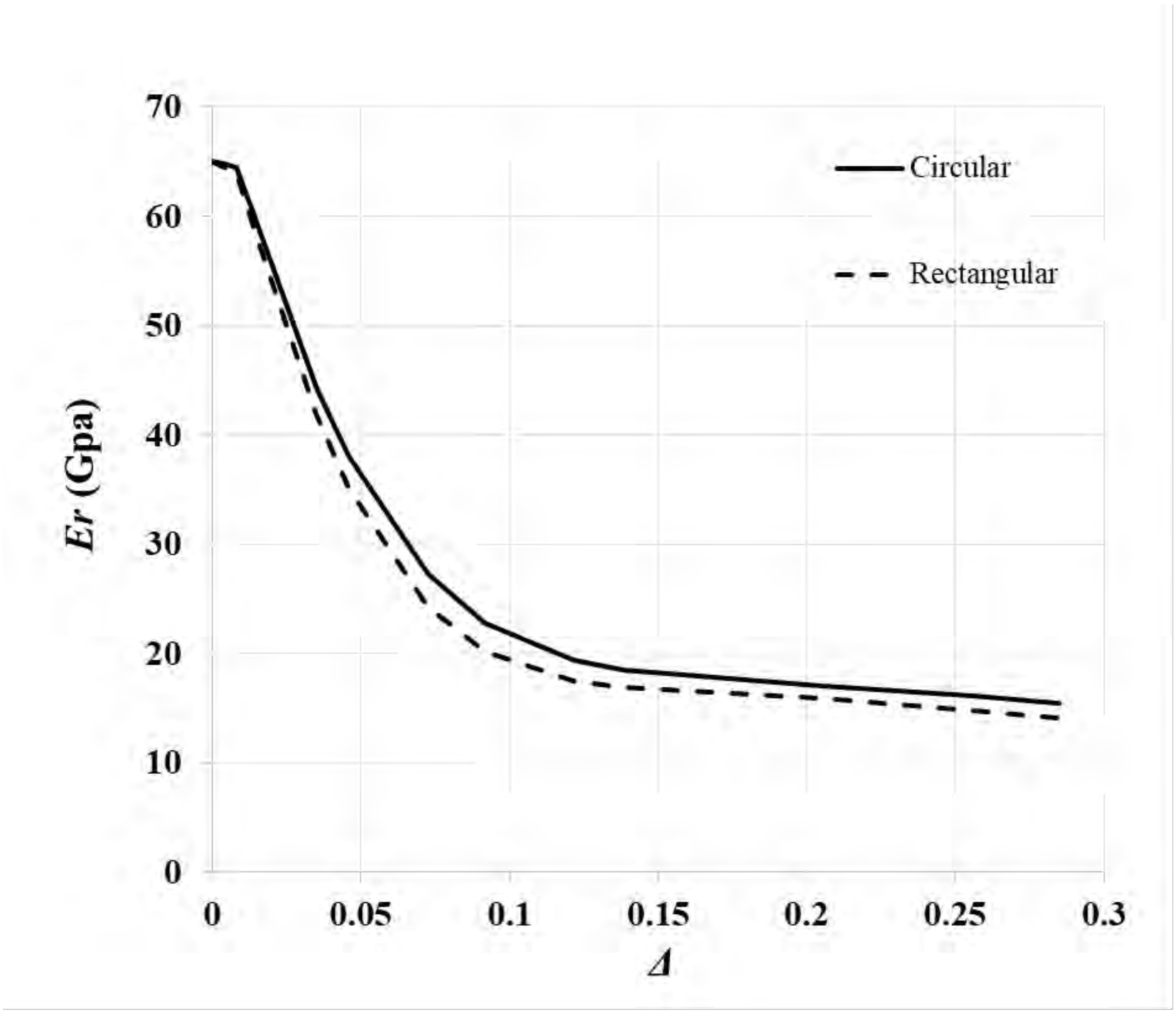

Figure 4.7.2: Reduced modulus vs *Δ* curve for superelastic SMA circular and equivalent rectangular beam (APPENDIX-C).

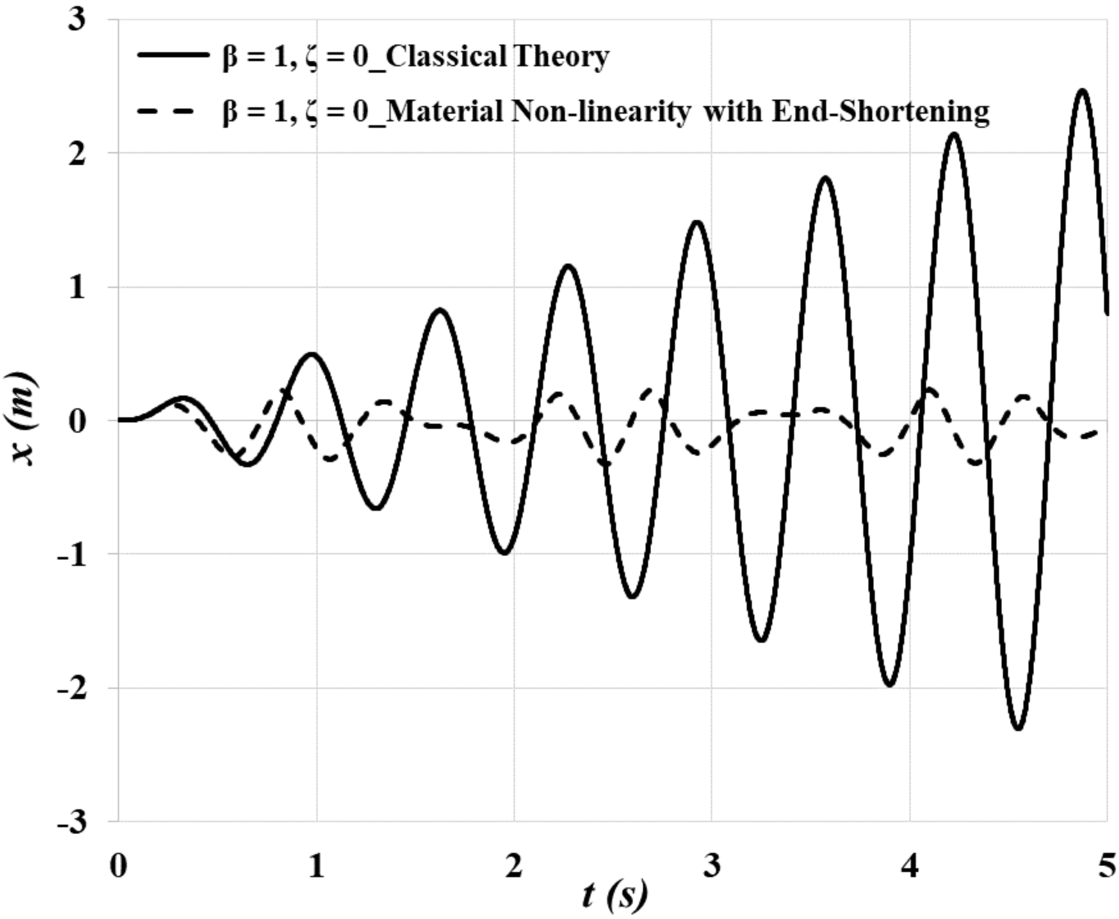

Figure 4.9.1: Displacement (m) vs time (s) curve at resonance (β = 1) when undamped (ζ = 0) for classical theory and considering material non-linearity with end-shortening.

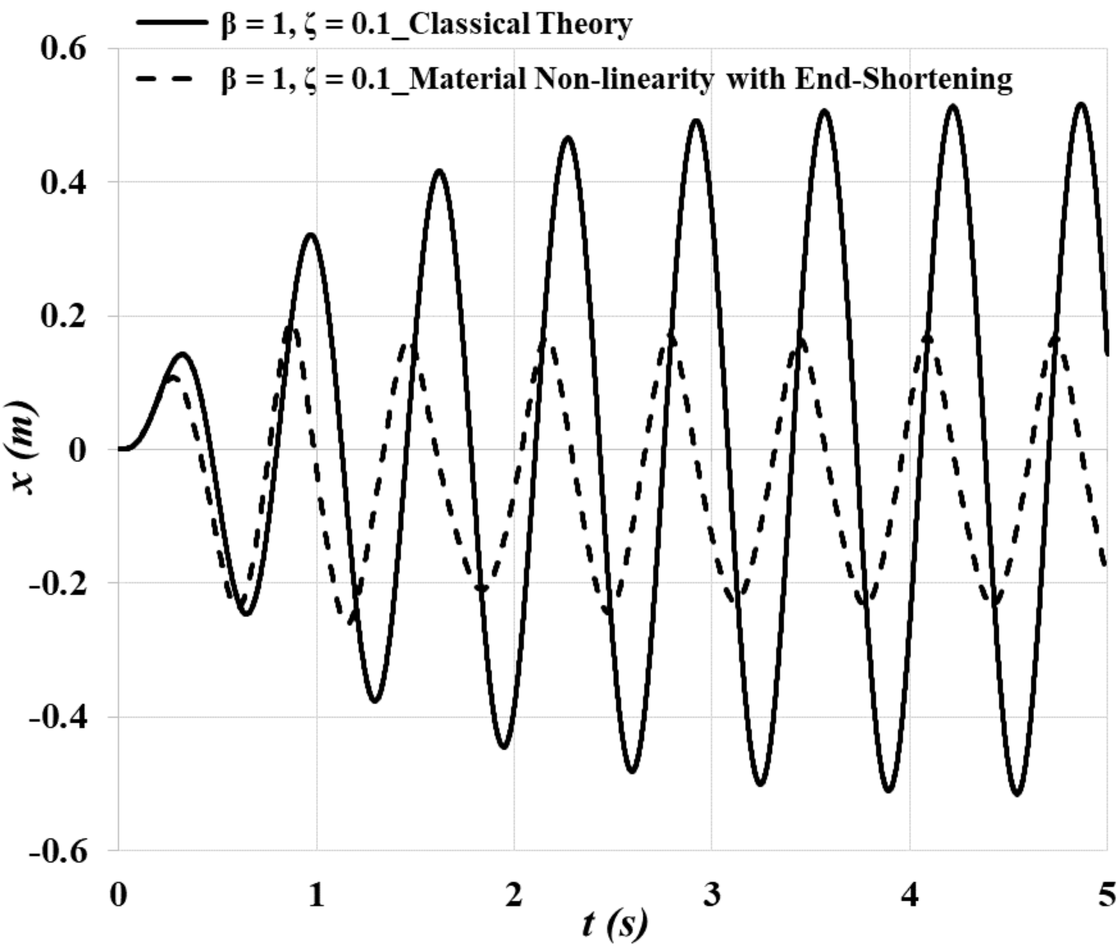

Figure 4.9.2: Displacement (m) vs time (s) curve at resonance (β = 1) for damping ratio, ζ = 0.1 for classical theory and considering material non-linearity with end-shortening.

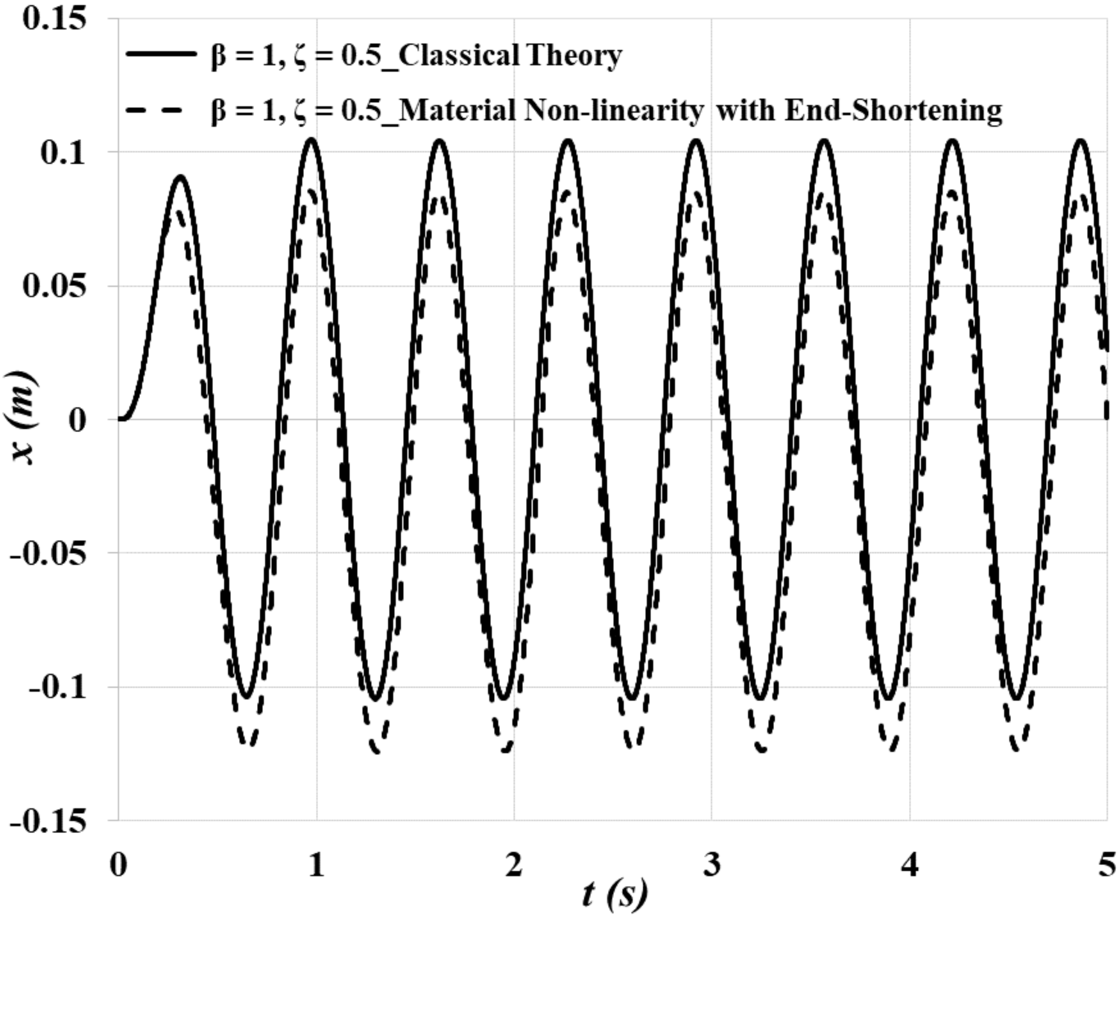

Figure 4.9.3: Displacement (m) vs time (s) curve at resonance ($\beta = 1$) for damping ratio, $\zeta = 0.5$ for classical theory and considering material non-linearity with end-shortening.

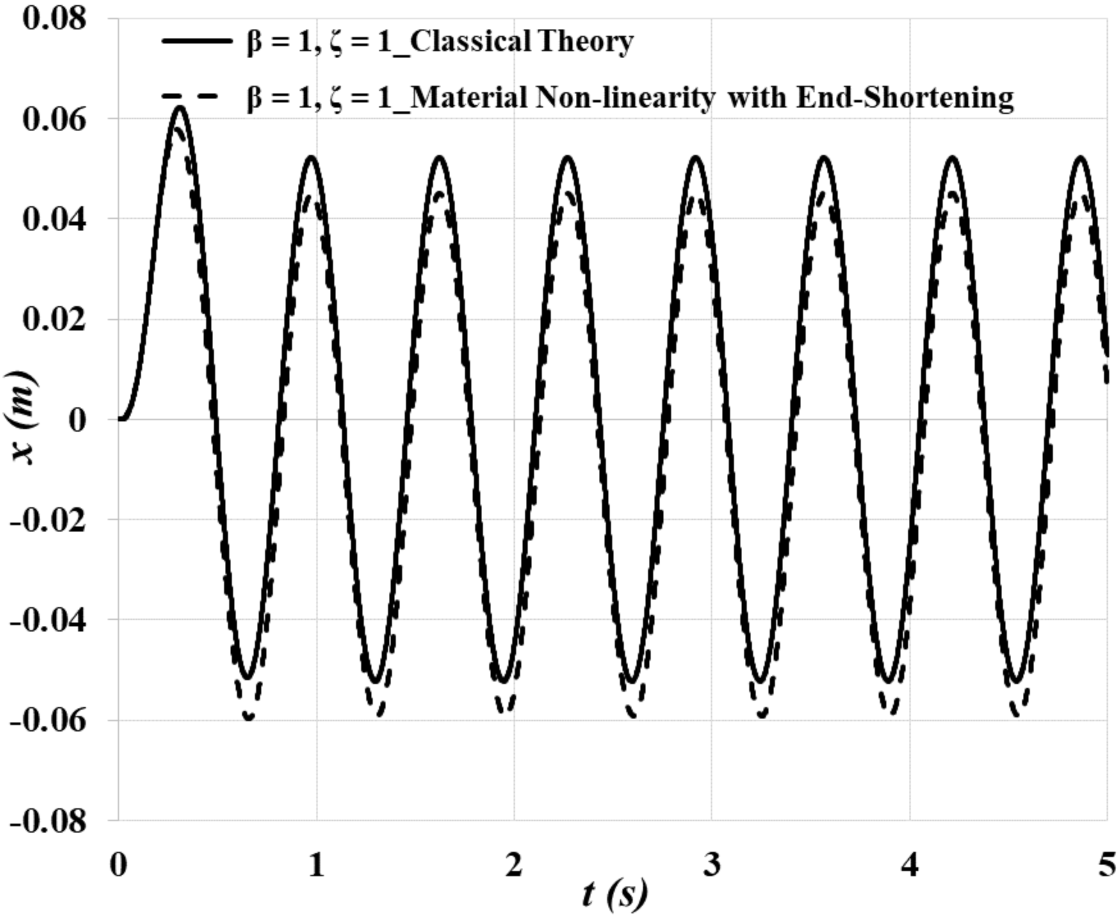

Figure 4.9.4: Displacement (m) vs time (s) curve at resonance (β = 1) for damping ratio, ζ = 1 for classical theory and considering material non-linearity with end-shortening.

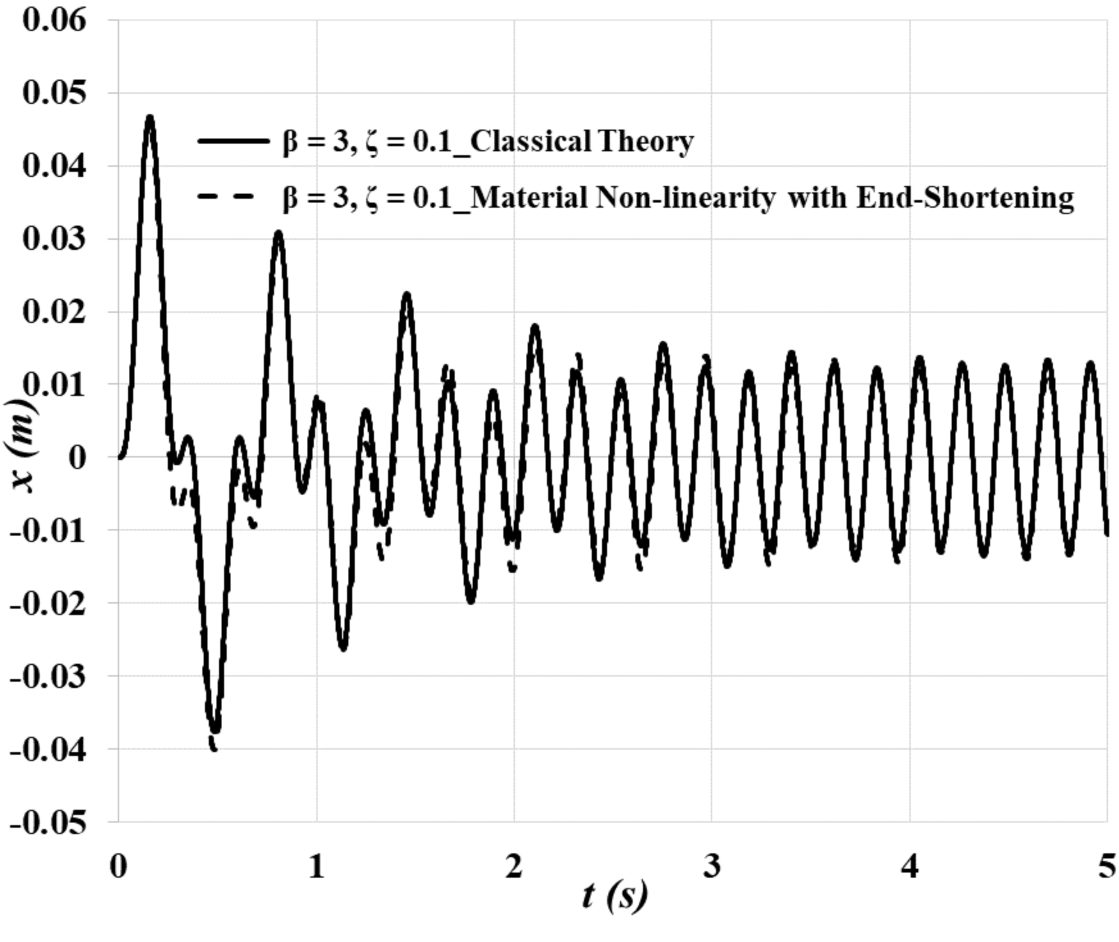

Figure 4.9.5: Displacement (m) vs time (s) curve for speed ratio, $\beta = 3$ and damping ratio, $\zeta = 0.1$ for classical theory and considering material non-linearity with end-shortening.

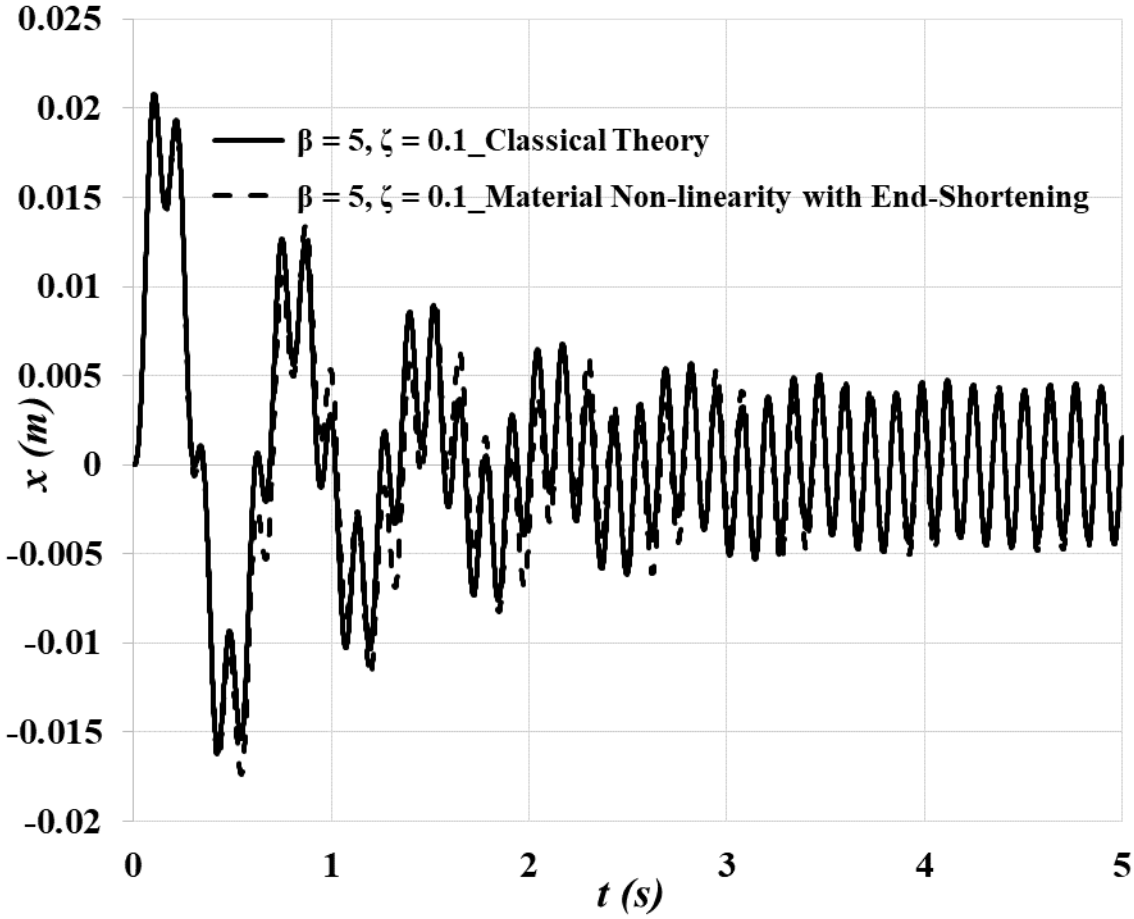

Figure 4.9.6: Displacement (m) vs time (s) curve for speed ratio, $\beta = 5$ and damping ratio, $\zeta = 0.1$ for classical theory and considering material non-linearity with end-shortening.

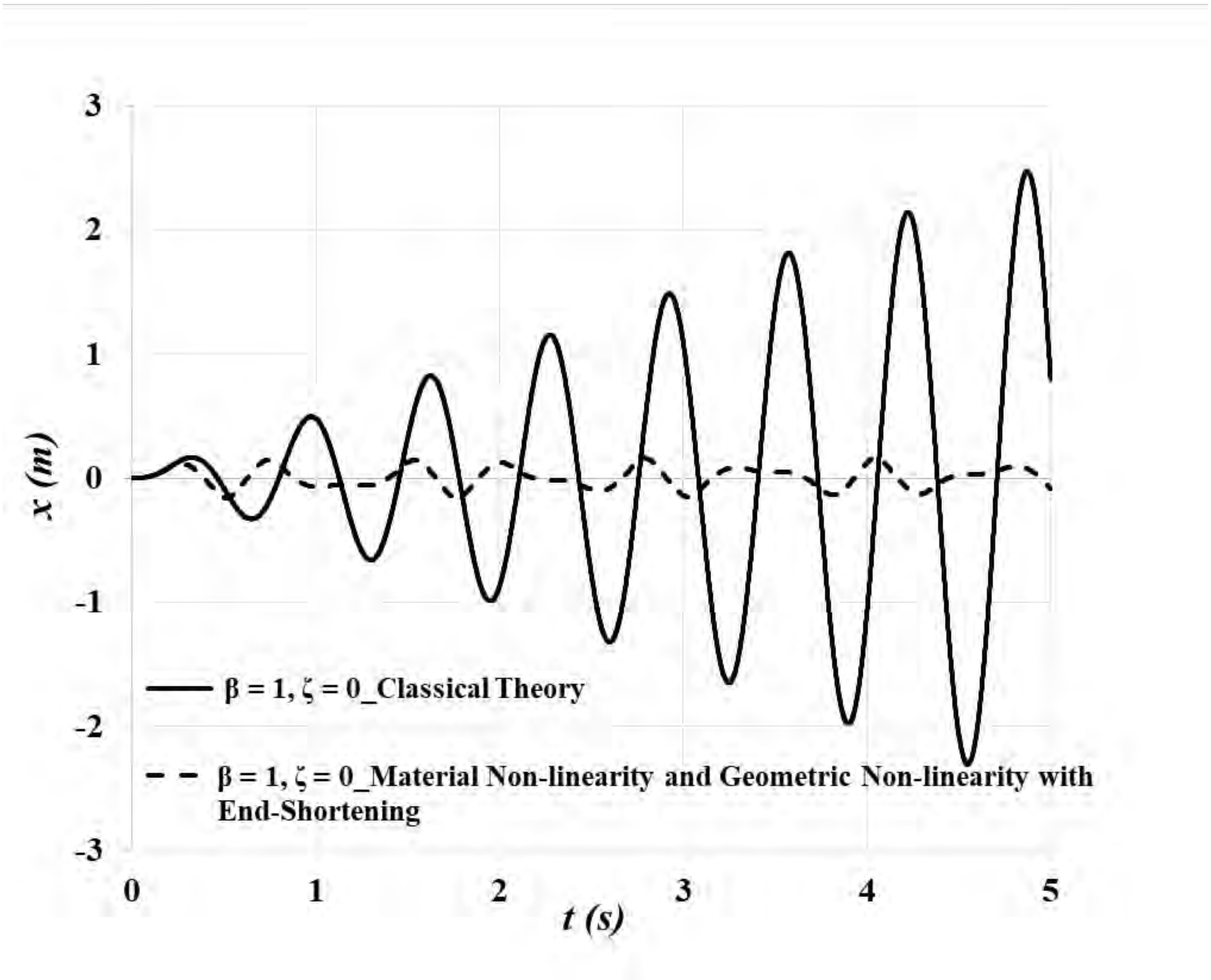

Figure 4.10.1: Displacement (m) vs time (s) curve at resonance ($\beta = 1$) when undamped ($\zeta = 0$) for classical theory and considering material non-linearity and geometric non-linearity with end-shortening.

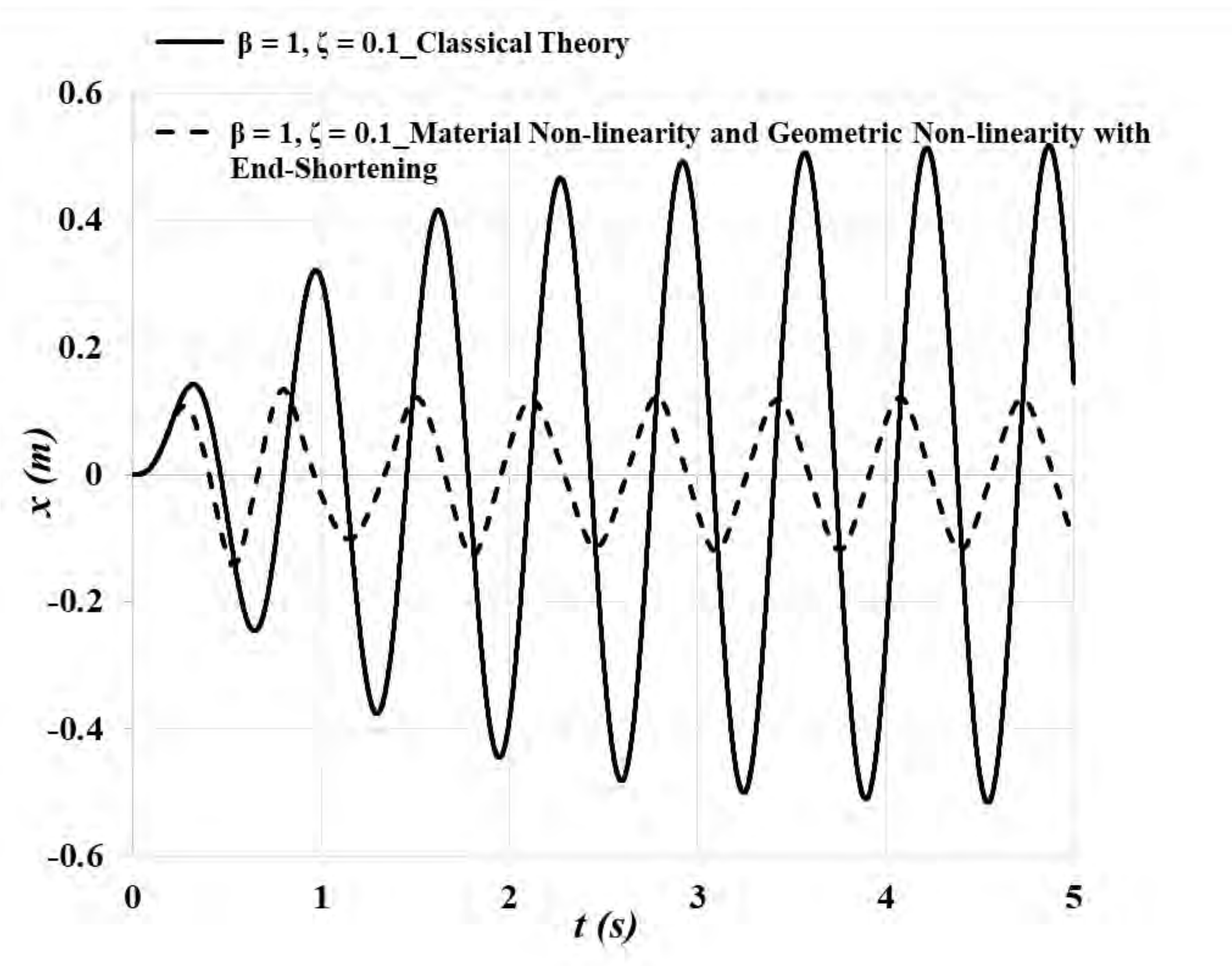

Figure 4.10.2: Displacement (m) vs time (s) curve at resonance (β = 1) for damping ratio, ζ = 0.1 for classical theory and considering material non-linearity and geometric non-linearity with end-shortening.

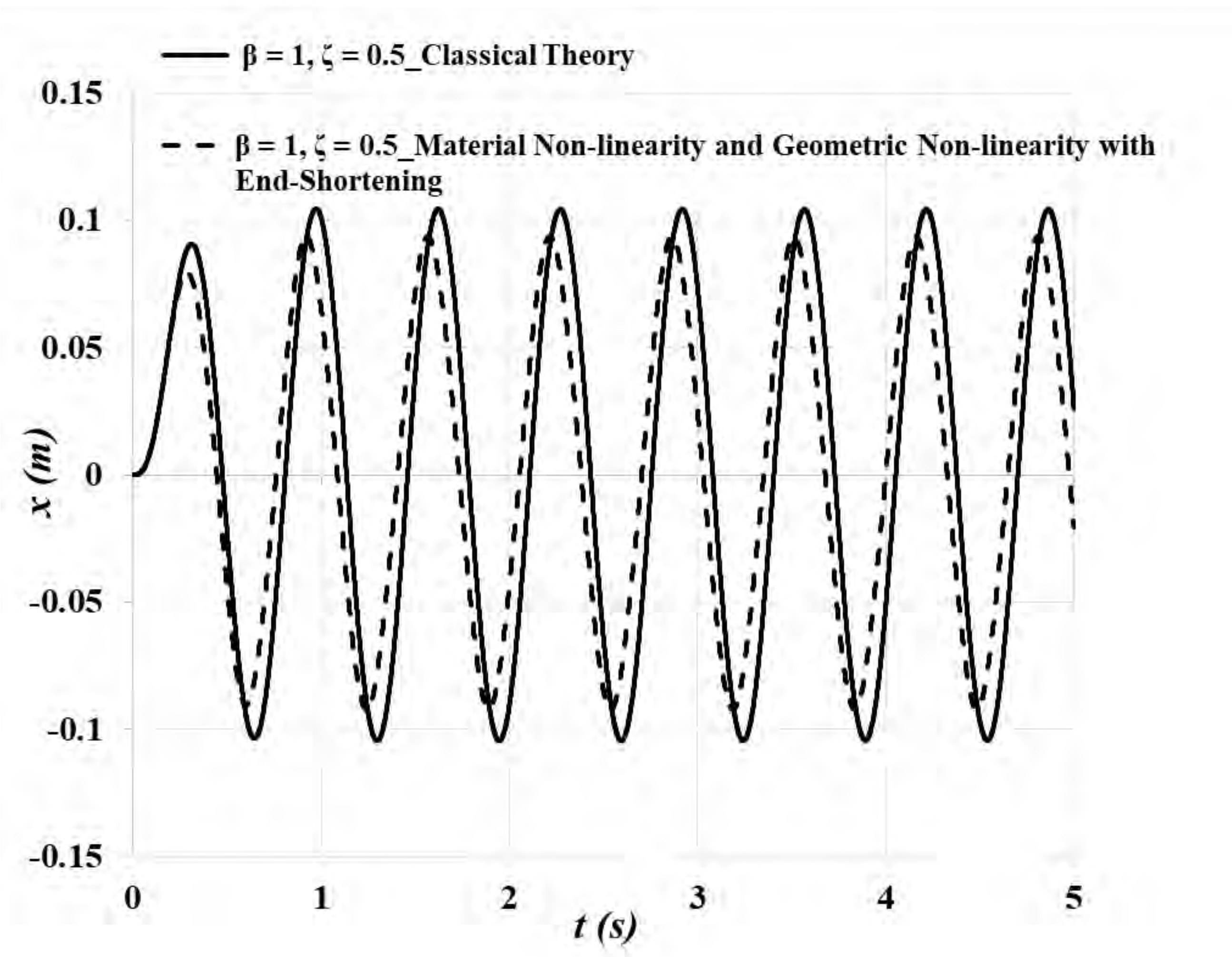

Figure 4.10.3: Displacement (m) vs time (s) curve at resonance ($\beta = 1$) for damping ratio, $\zeta = 0.5$ for classical theory and considering material non-linearity and geometric non-linearity with end-shortening.

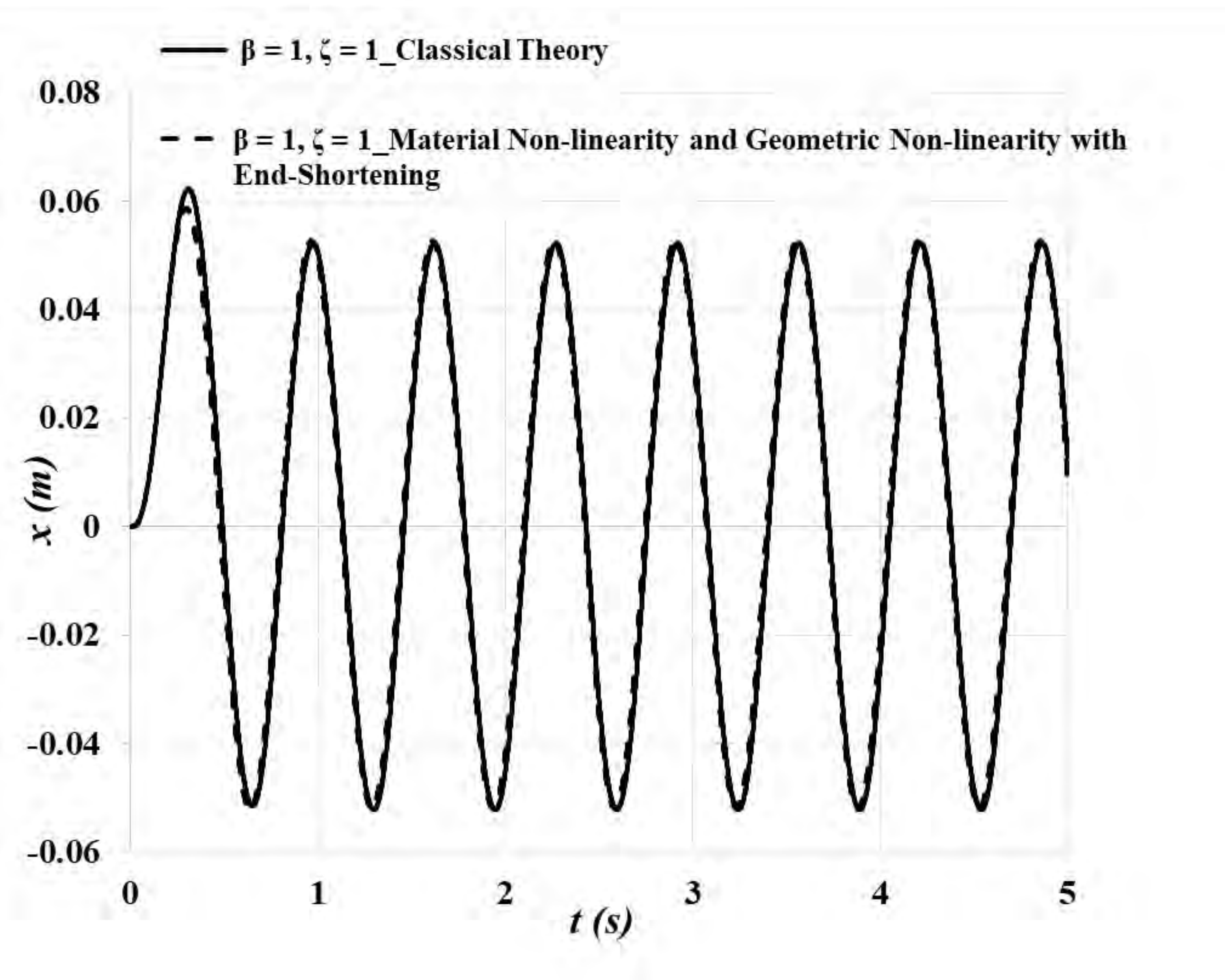

Figure 4.10.4: Displacement (m) vs time (s) curve at resonance (β = 1) for damping ratio, ζ = 1 for classical theory and considering material non-linearity and geometric non-linearity with end-shortening.

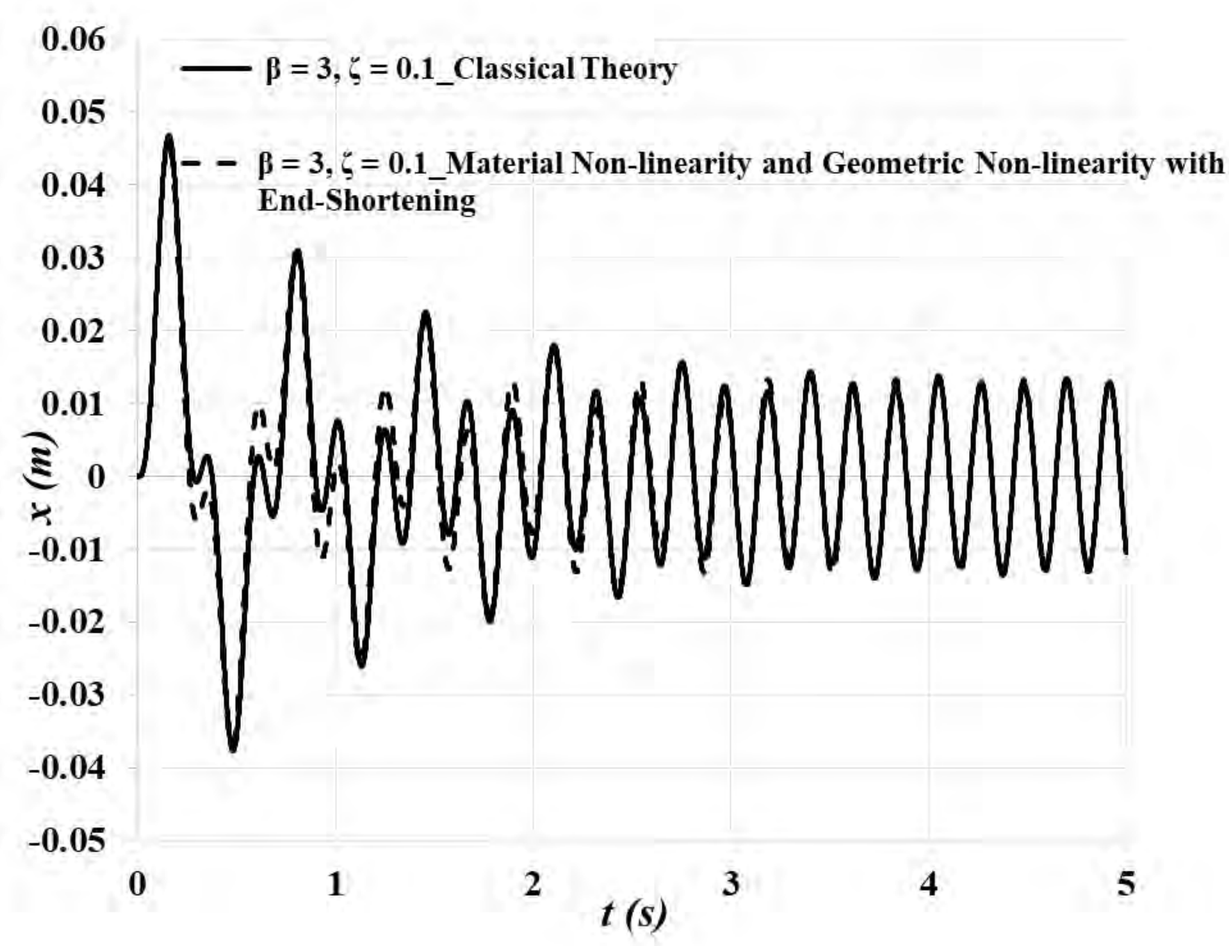

Figure 4.10.5: Displacement (m) vs time (s) curve for speed ratio, $\beta = 3$ and damping ratio, $\zeta = 0.1$ for classical theory and considering material non-linearity and geometric non-linearity with end-shortening.

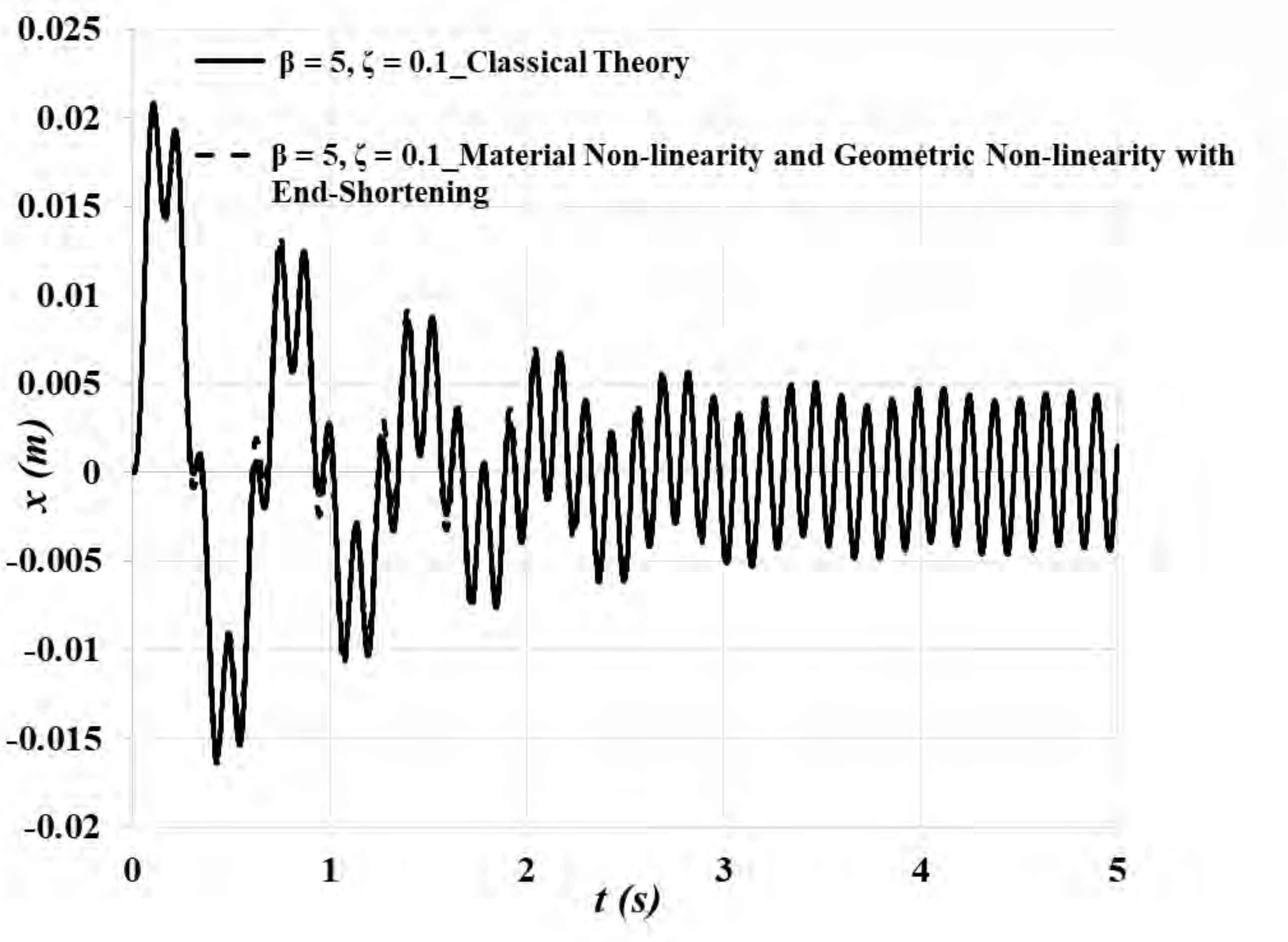

Figure 4.10.6: Displacement (m) vs time (s) curve for speed ratio, $\beta = 5$ and damping ratio, $\zeta = 0.1$ for classical theory and considering material non-linearity and geometric non-linearity with end-shortening.

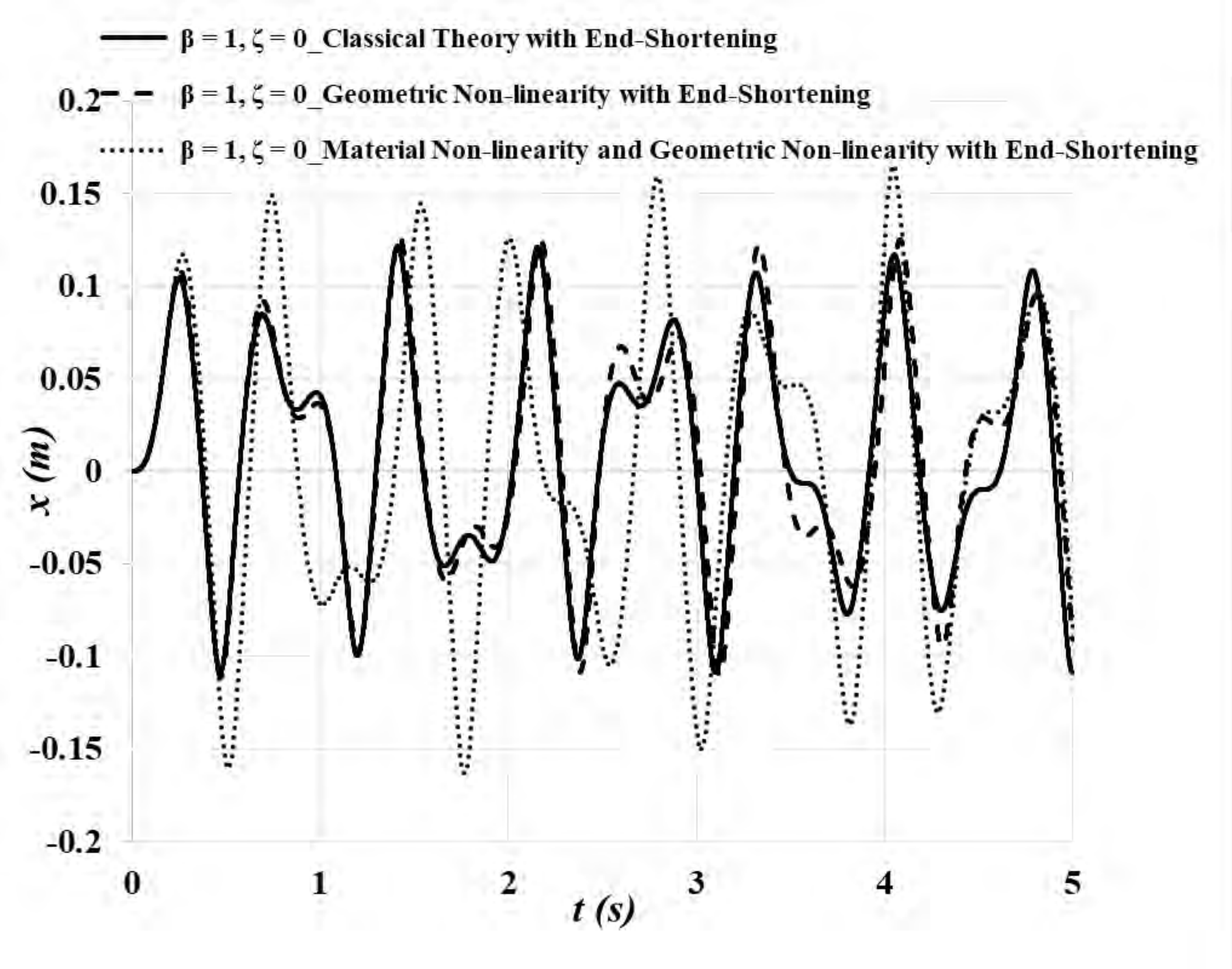

Figure 4.10.7: Displacement (m) vs time (s) curve at resonance (β = 1) when undamped (ζ = 0) for classical theory with end-shortening effect, geometric non-linearity with end-shortening and material non-linearity and geometric non-linearity with end-shortening.

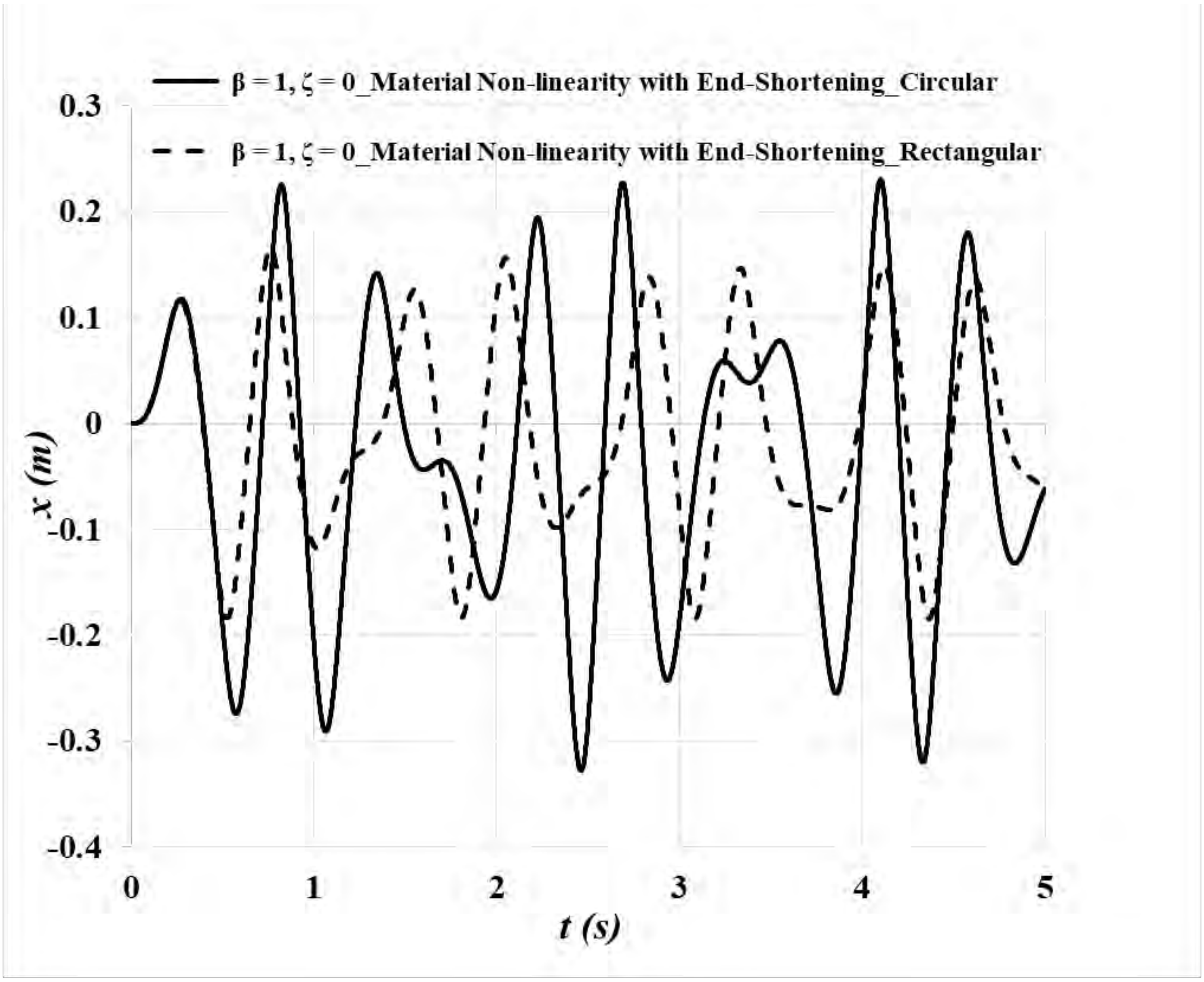

Figure 4.11.1: Displacement (m) vs time (s) curve at resonance ($\beta = 1$) when undamped ($\zeta = 0$) for circular and equivalent rectangular beam (APPENDIX-C) considering material non-linearity with end-shortening.

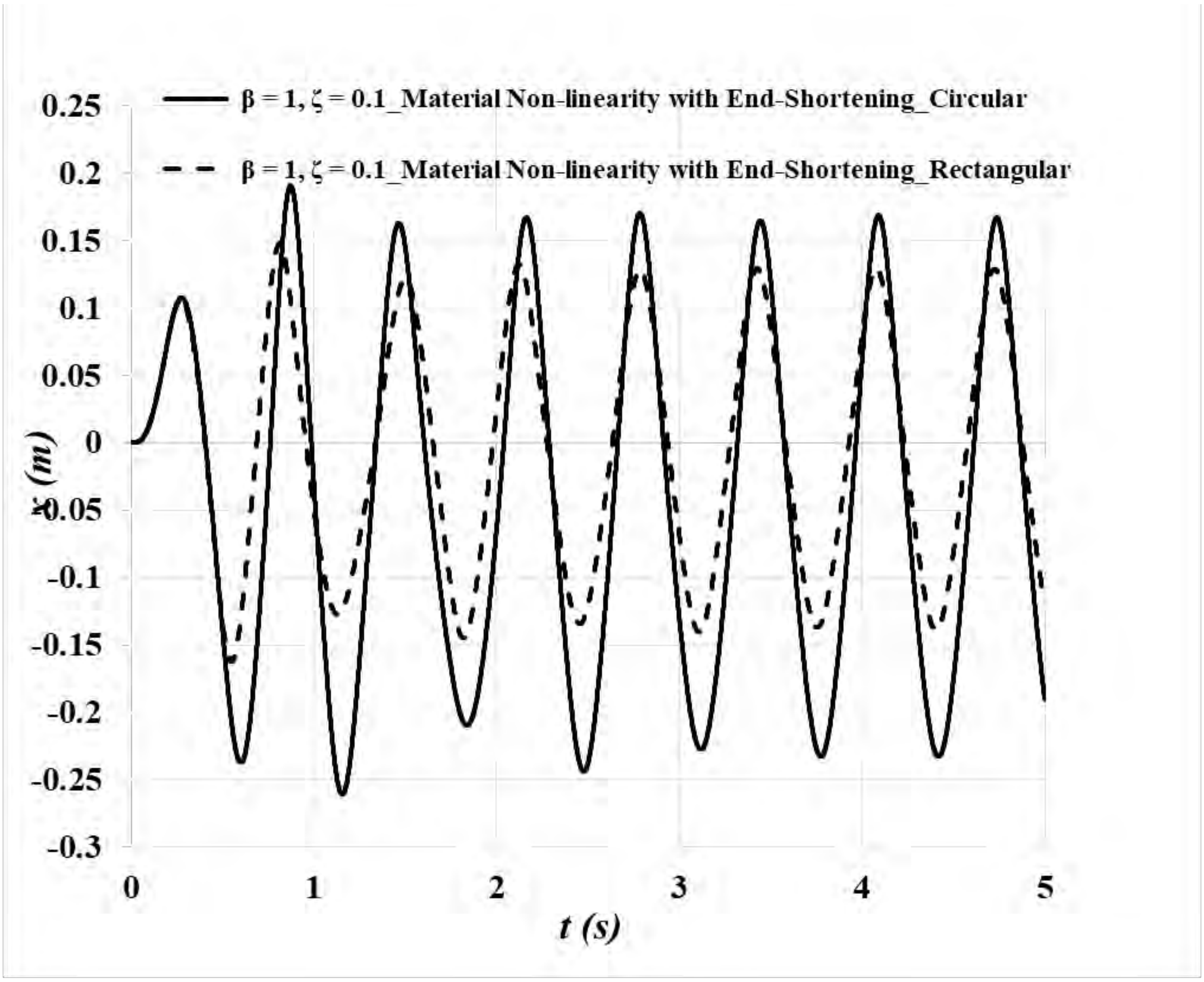

Figure 4.11.2: Displacement (m) vs time (s) curve at resonance (β = 1) for damping ratio, ζ = 0.1 for circular and equivalent rectangular beam (APPENDIX-C) considering material non-linearity with end-shortening.

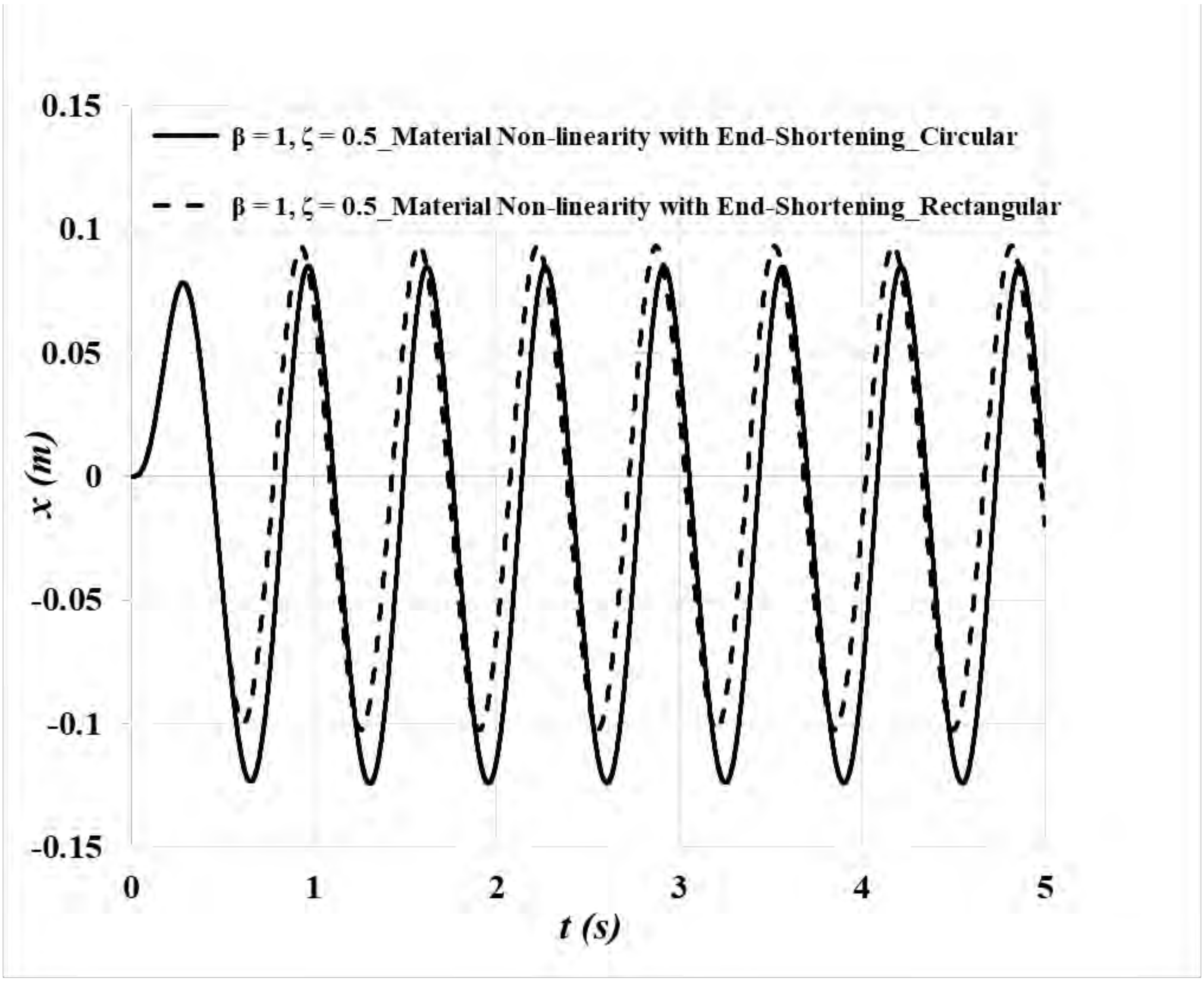

Figure 4.11.3: Displacement (m) vs time (s) curve at resonance (β = 1) for damping ratio, ζ = 0.5 for circular and equivalent rectangular beam (APPENDIX-C) considering material non-linearity with end-shortening.

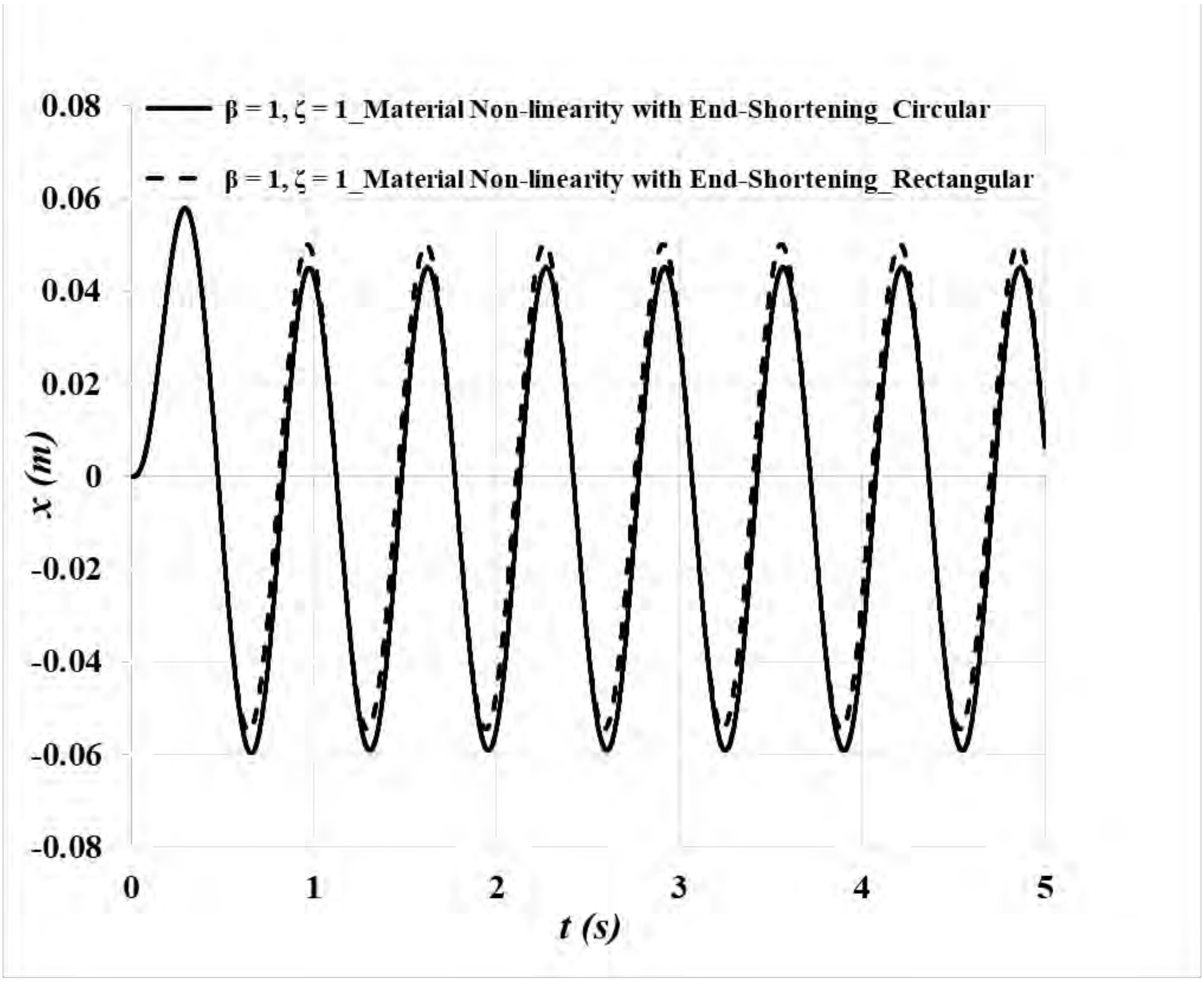

Figure 4.11.4: Displacement (m) vs time (s) curve at resonance ($\beta = 1$) for damping ratio, $\zeta = 1$ for circular and equivalent rectangular beam (APPENDIX-C) considering material non-linearity with end-shortening.

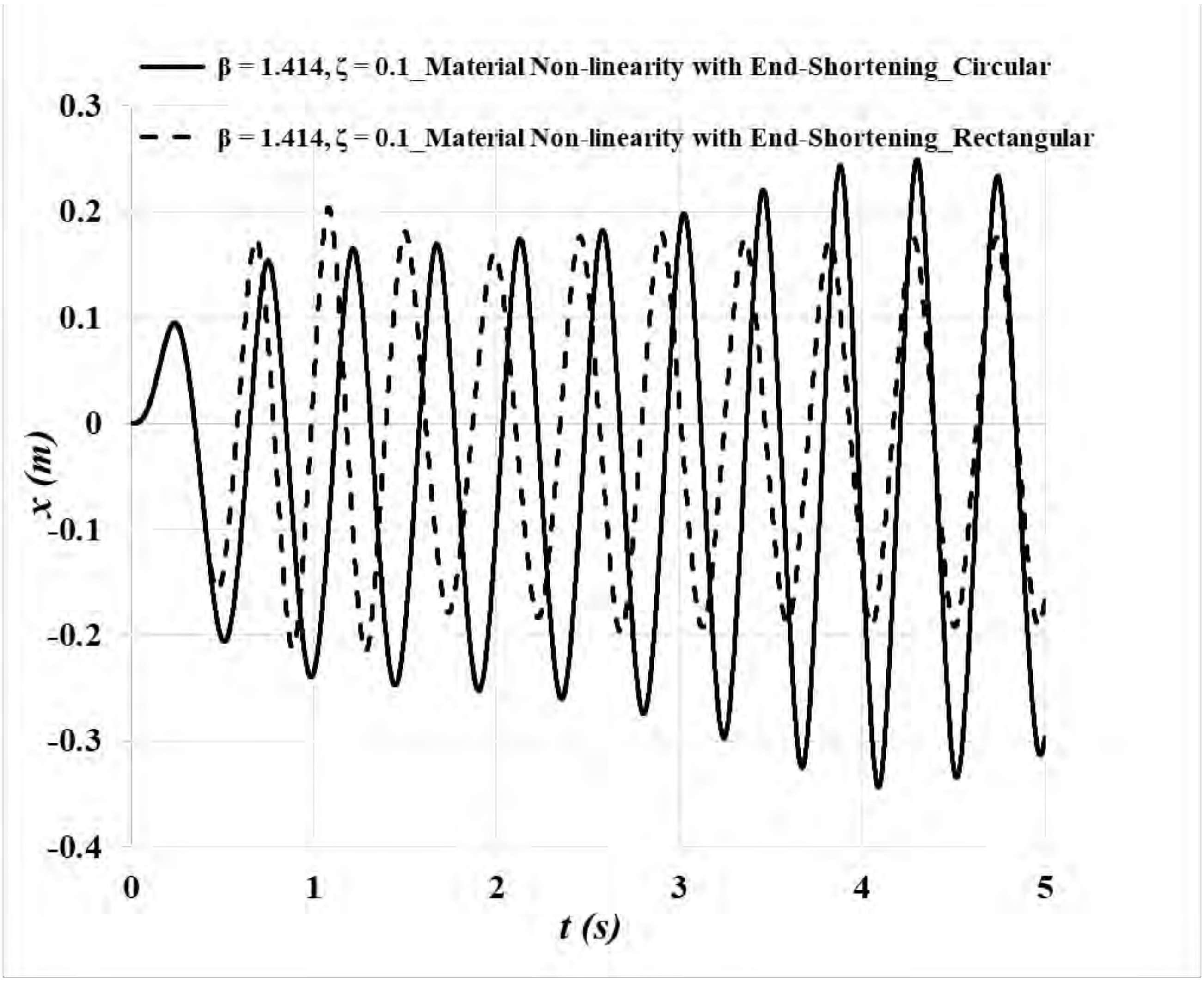

Figure 4.11.5: Displacement (m) vs time (s) curve for speed ratio, β = 1.414 and damping ratio, ζ = 0.1 for circular and equivalent rectangular beam (APPENDIX-C) considering material non-linearity with end-shortening.

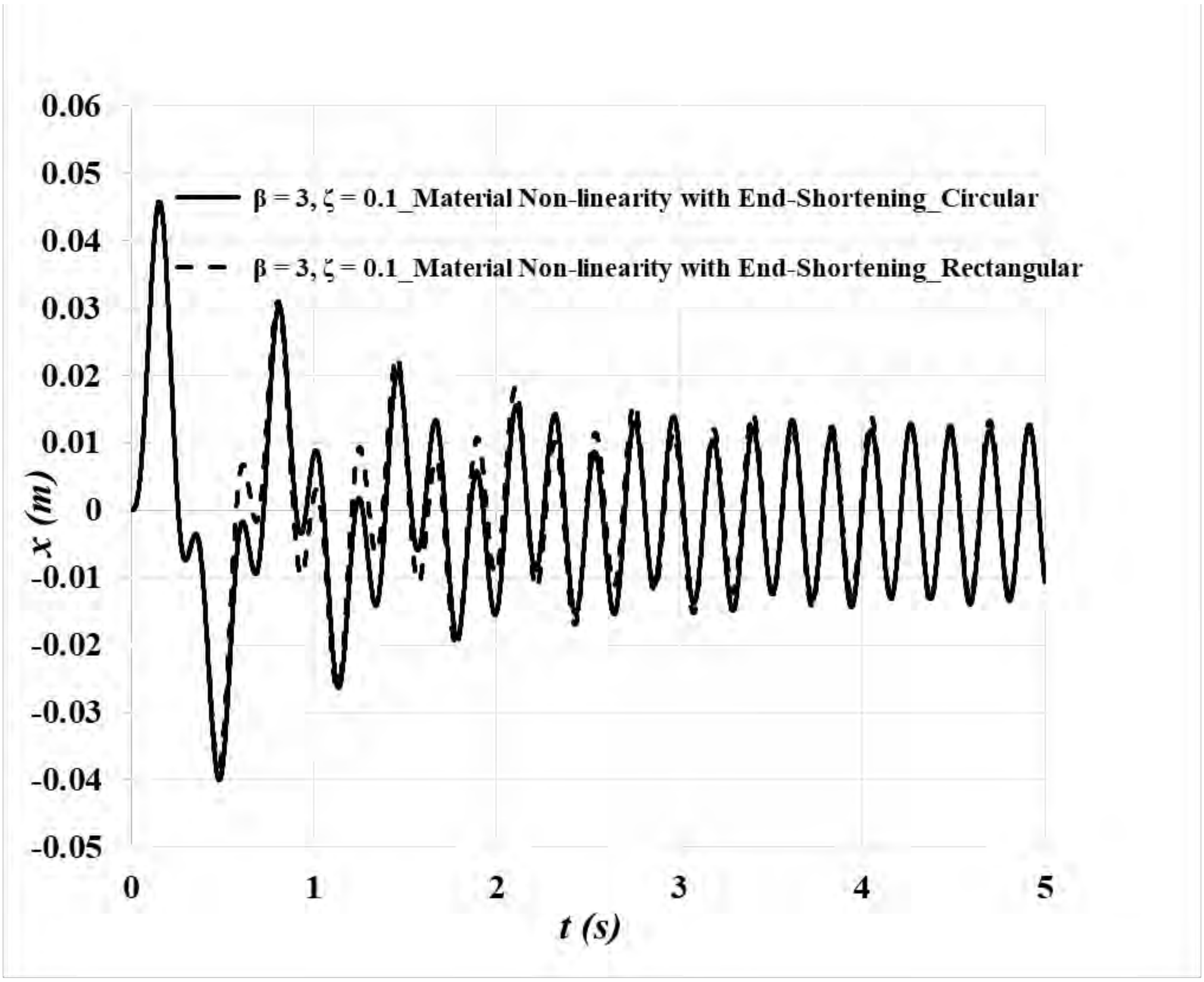

Figure 4.11.6: Displacement (m) vs time (s) curve for speed ratio, $\beta = 3$ and damping ratio, $\zeta = 0.1$ for circular and equivalent rectangular beam (APPENDIX-C) considering material non-linearity with end-shortening.

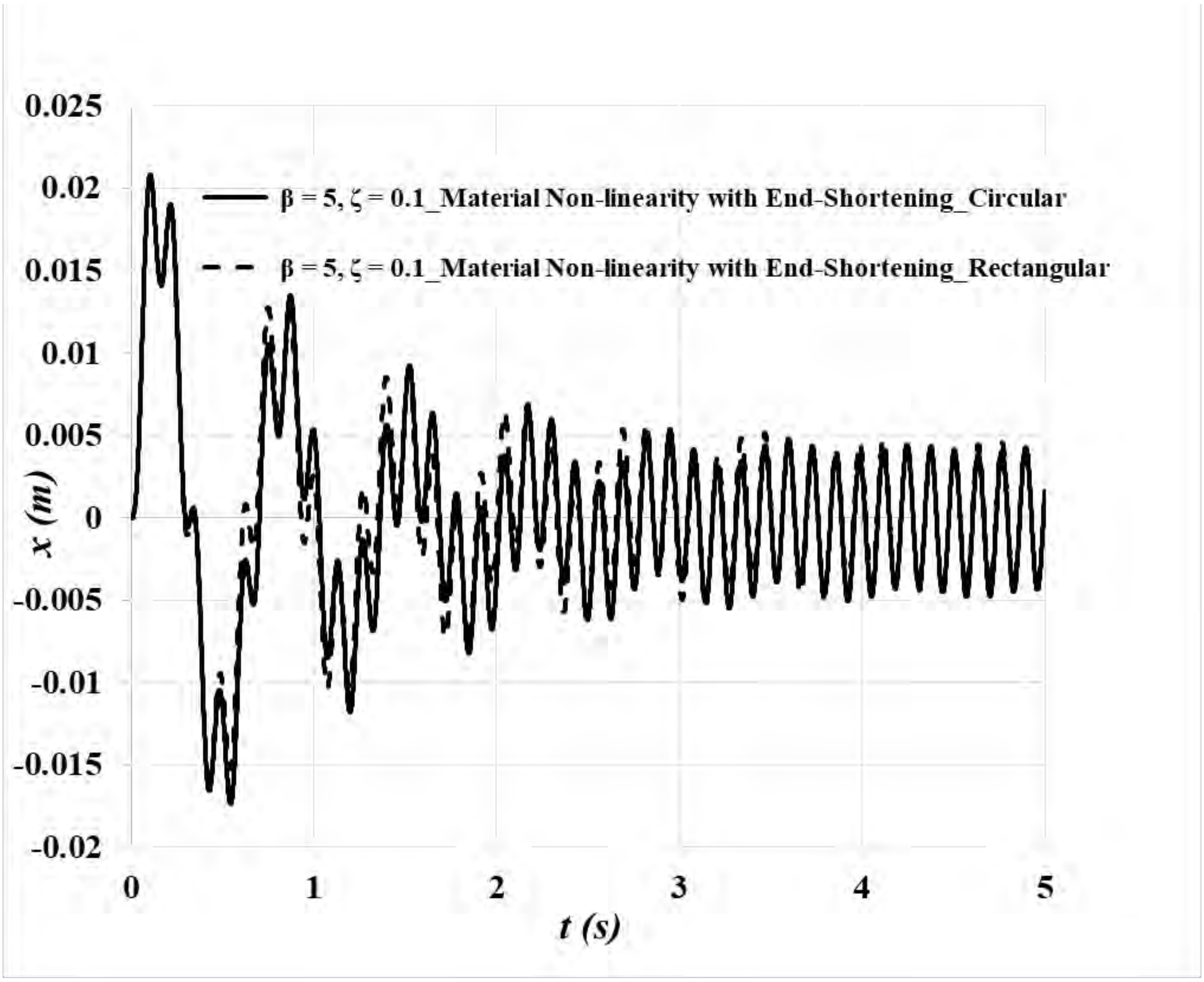

Figure 4.11.7: Displacement (m) vs time (s) curve for speed ratio, β = 5 and damping ratio, ζ = 0.1 for circular and equivalent rectangular beam (APPENDIX-C) considering material non-linearity with end-shortening.

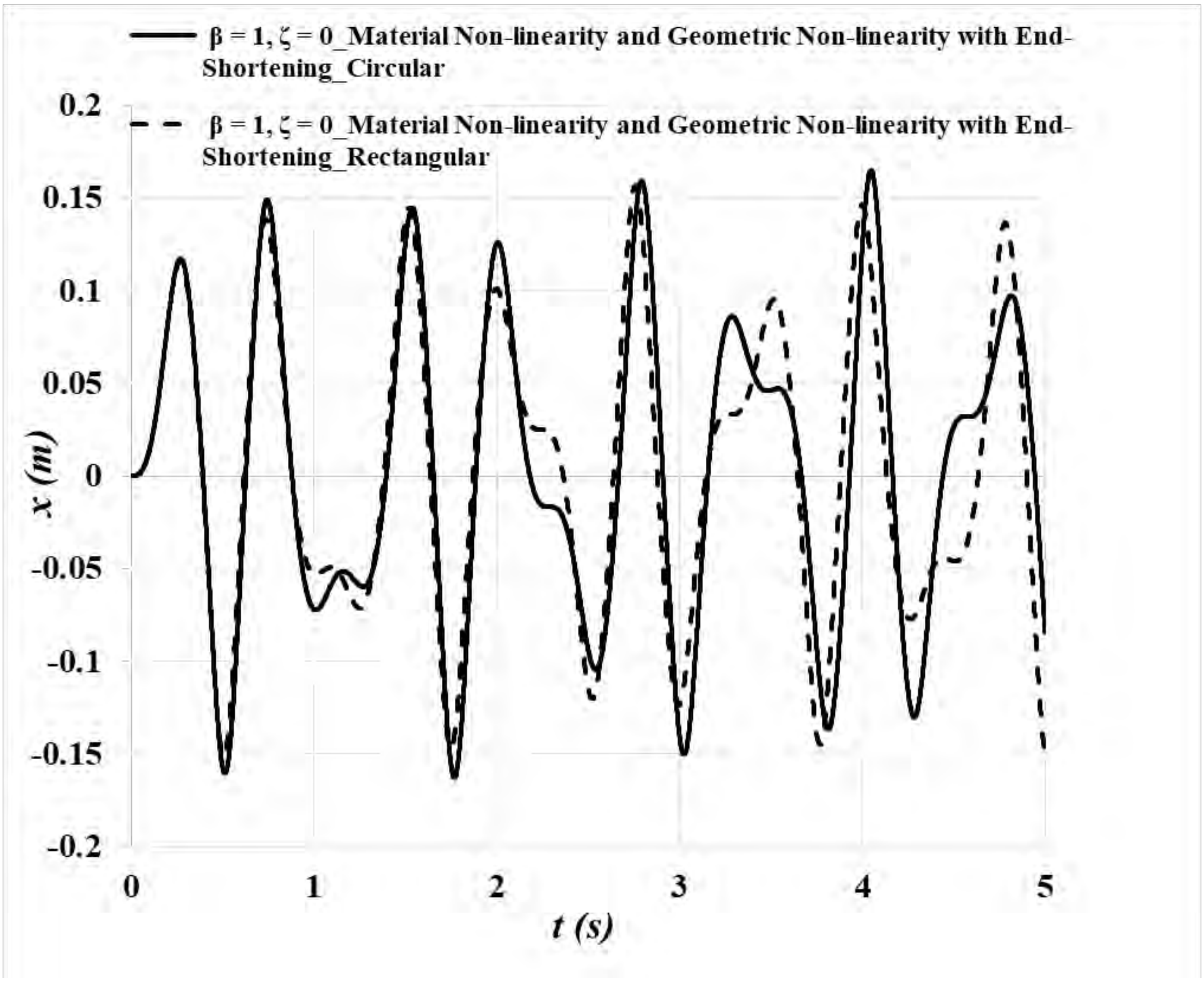

Figure 4.12.1: Displacement (m) vs time (s) curve at resonance (β = 1) when undamped (ζ = 0) for circular and equivalent rectangular beam (APPENDIX-C) considering material non-linearity and geometric non-linearity with end-shortening.

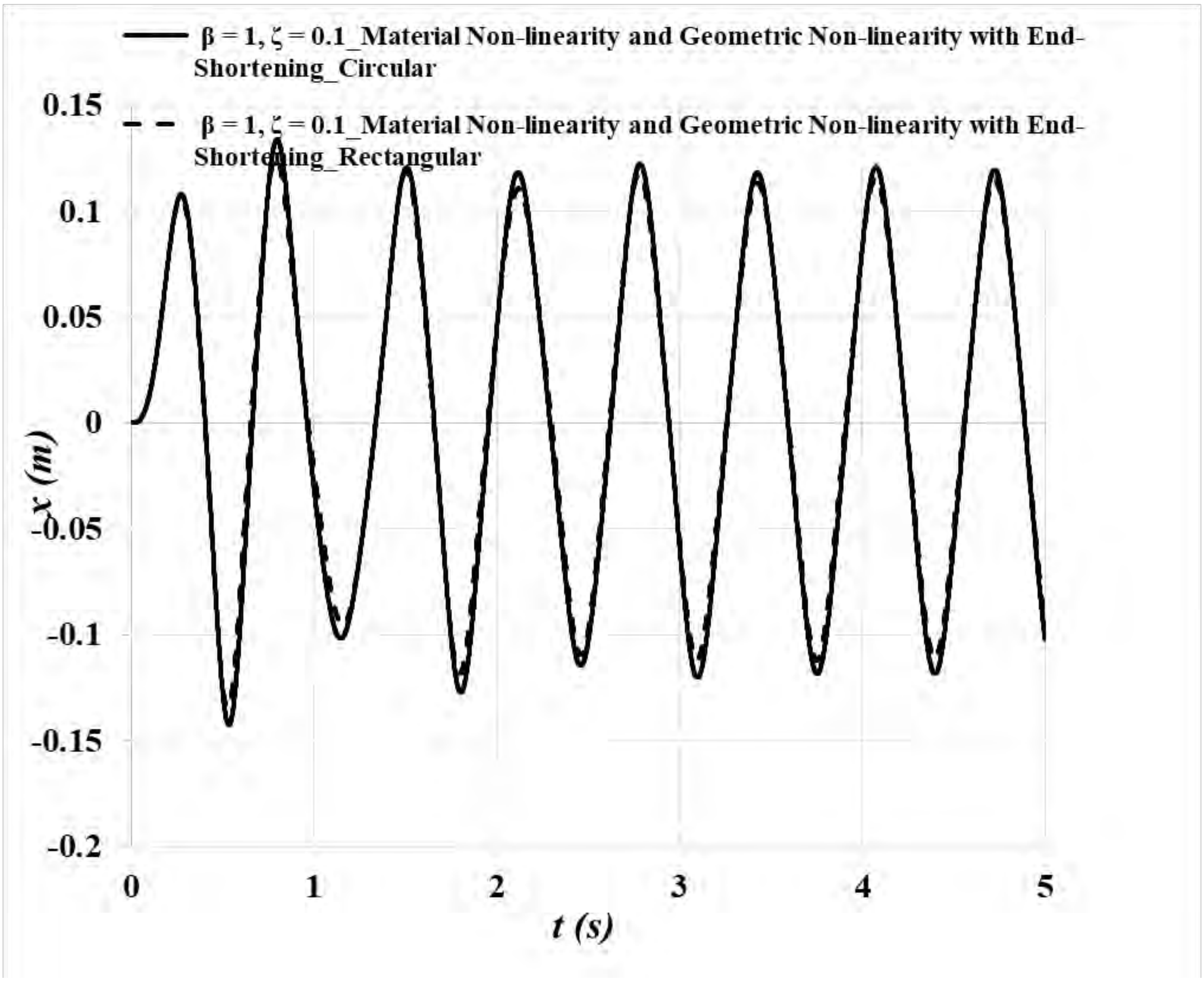

Figure 4.12.2: Displacement (m) vs time (s) curve at resonance (β = 1) for damping ratio, ζ = 0.1 for circular and equivalent rectangular beam (APPENDIX-C)) considering material non-linearity and geometric non-linearity with end-shortening.

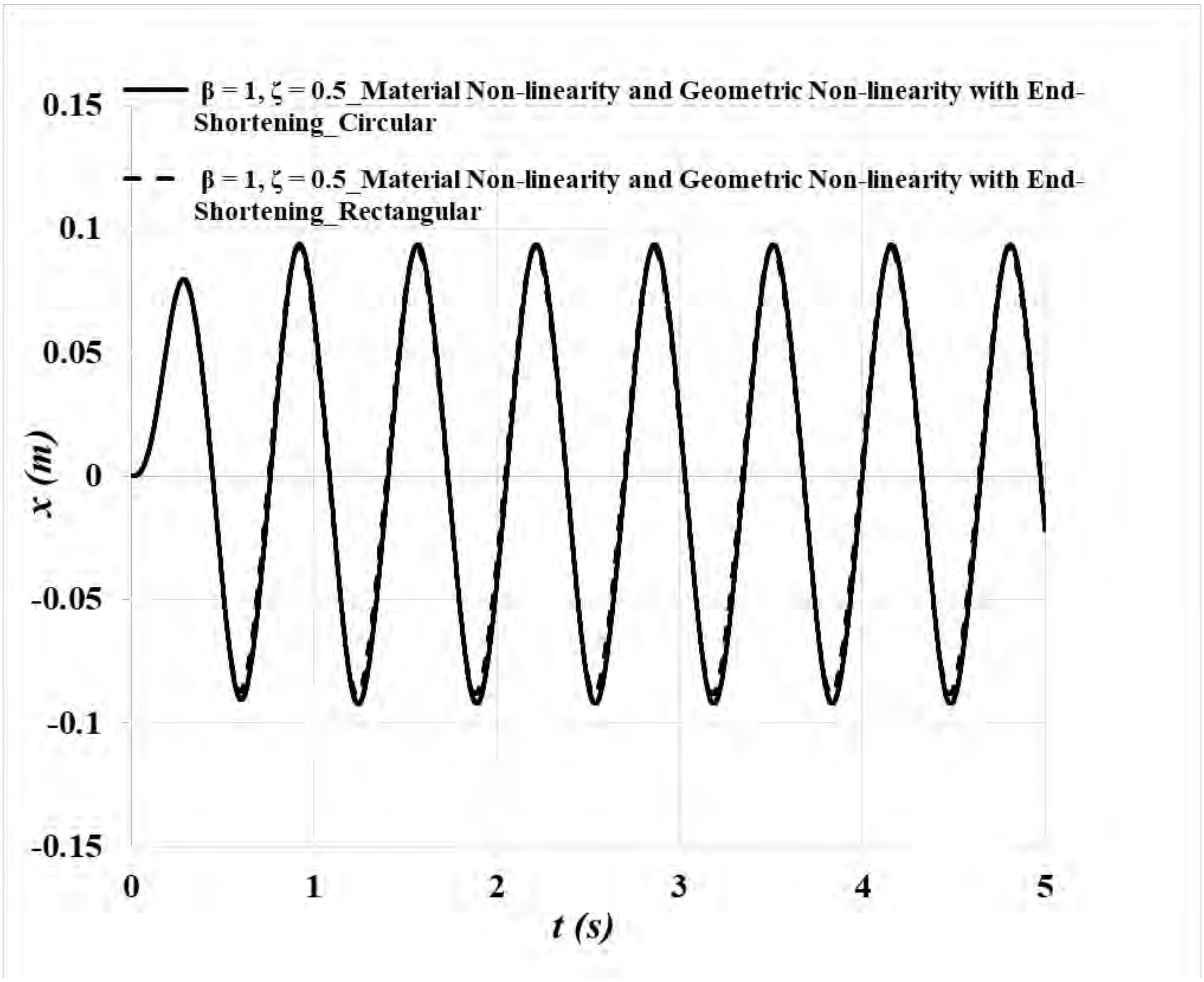

Figure 4.12.3: Displacement (m) vs time (s) curve at resonance (β = 1) for damping ratio, ζ = 0.5 for circular and equivalent rectangular beam (APPENDIX-C) considering material non-linearity and geometric non-linearity with end-shortening.

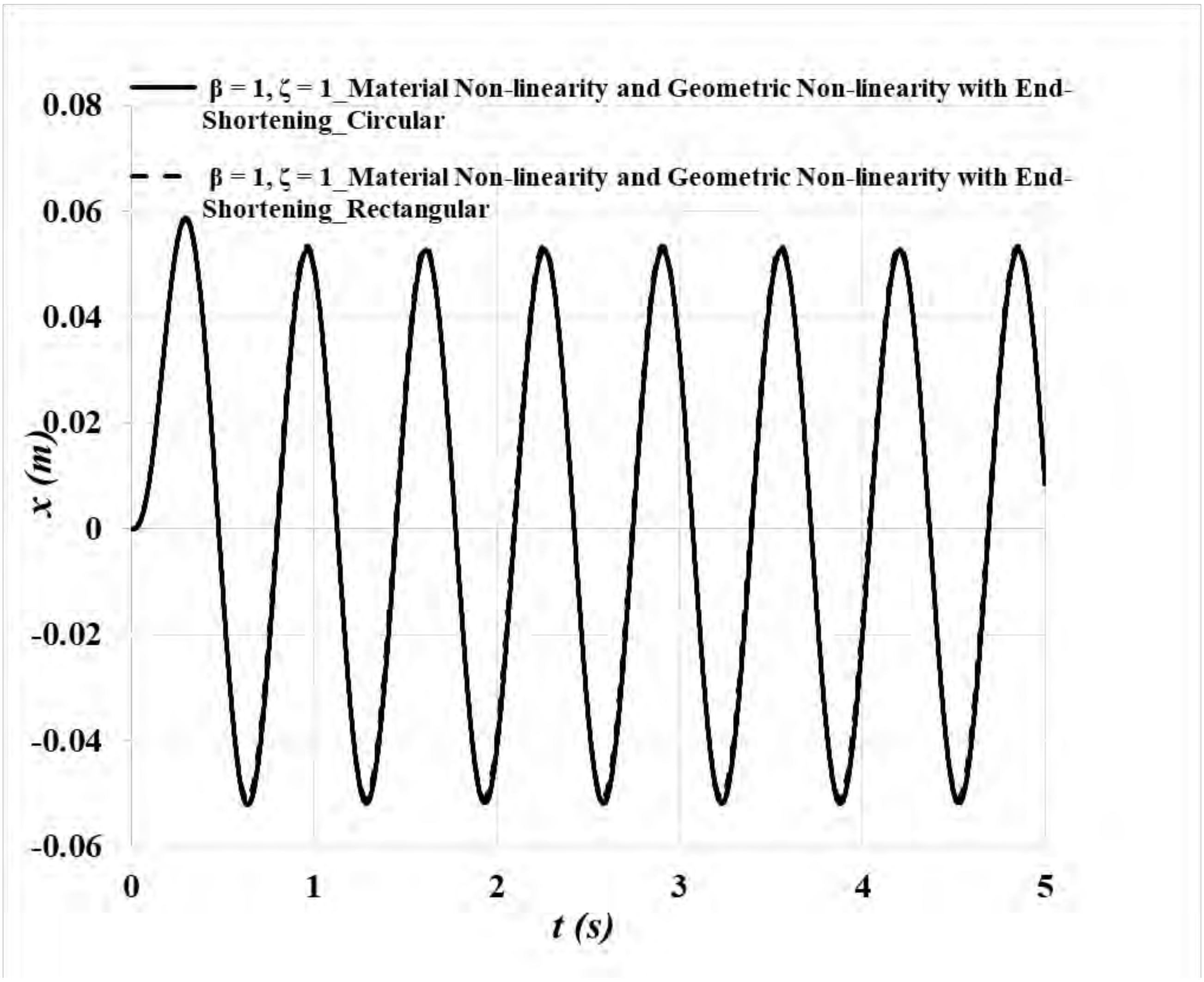

Figure 4.12.4: Displacement (m) vs time (s) curve at resonance (β = 1) for damping ratio, ζ = 1 for circular and equivalent rectangular beam (APPENDIX-C) considering material non-linearity and geometric non-linearity with end-shortening.

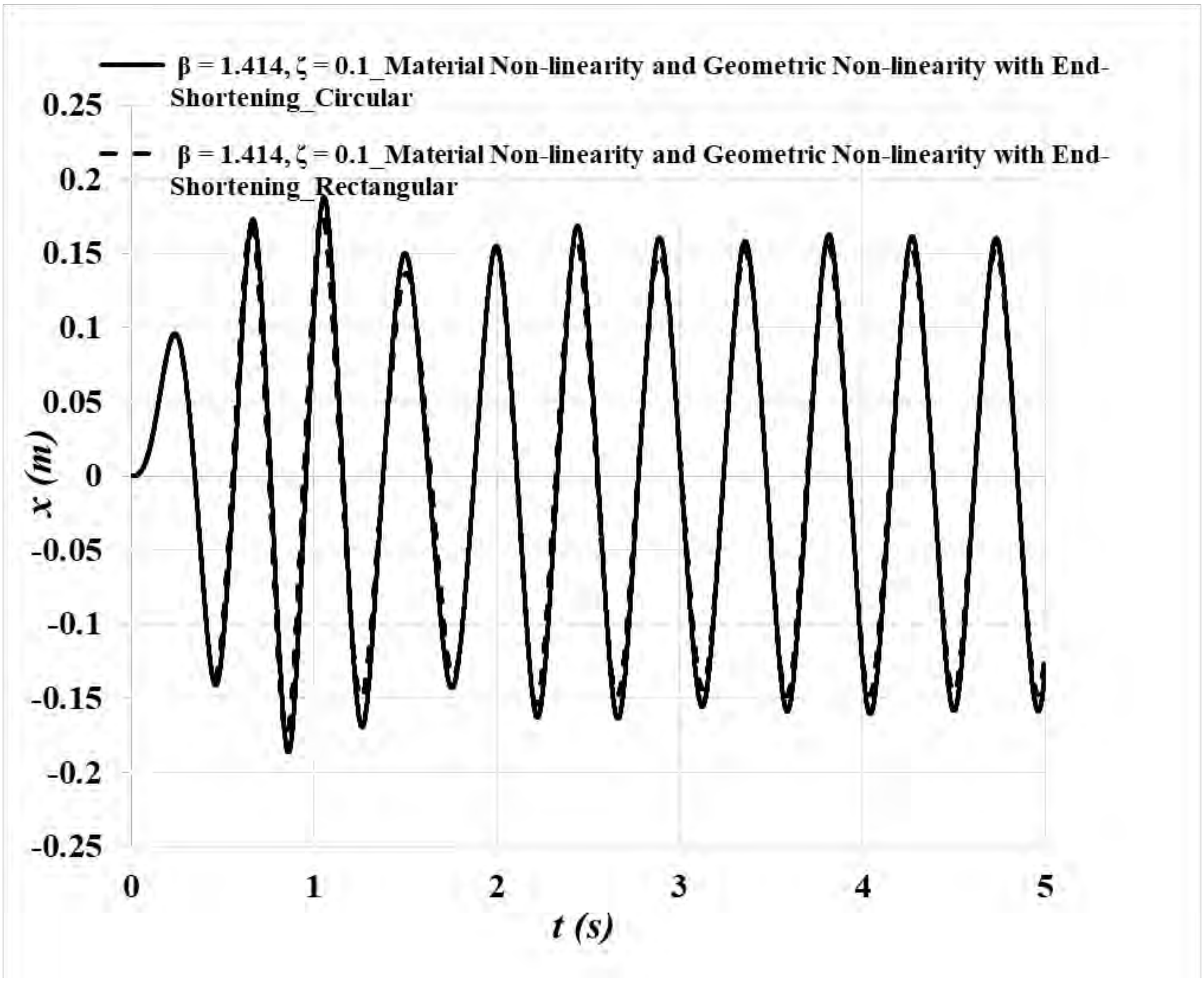

Figure 4.12.5: Displacement (m) vs time (s) curve at resonance (β = 1) when undamped for circular and equivalent rectangular beam (APPENDIX-C) considering material non-linearity and geometric non-linearity with end-shortening.

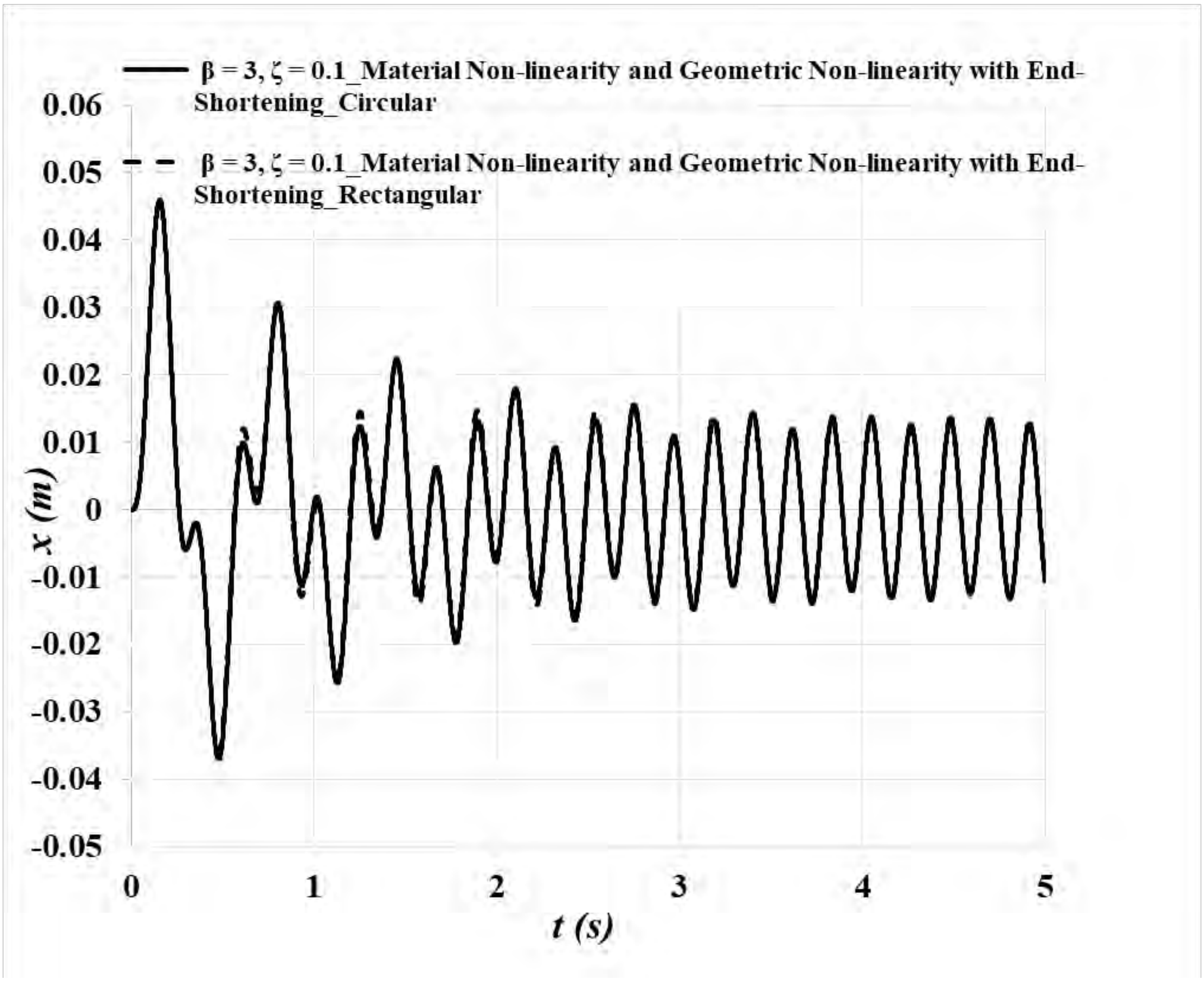

Figure 4.12.6: Displacement (m) vs time (s) curve for speed ratio, $\beta = 3$ and damping ratio, $\zeta = 0.1$ for circular and equivalent rectangular beam (APPENDIX-C) considering material non-linearity and geometric non-linearity with end-shortening.

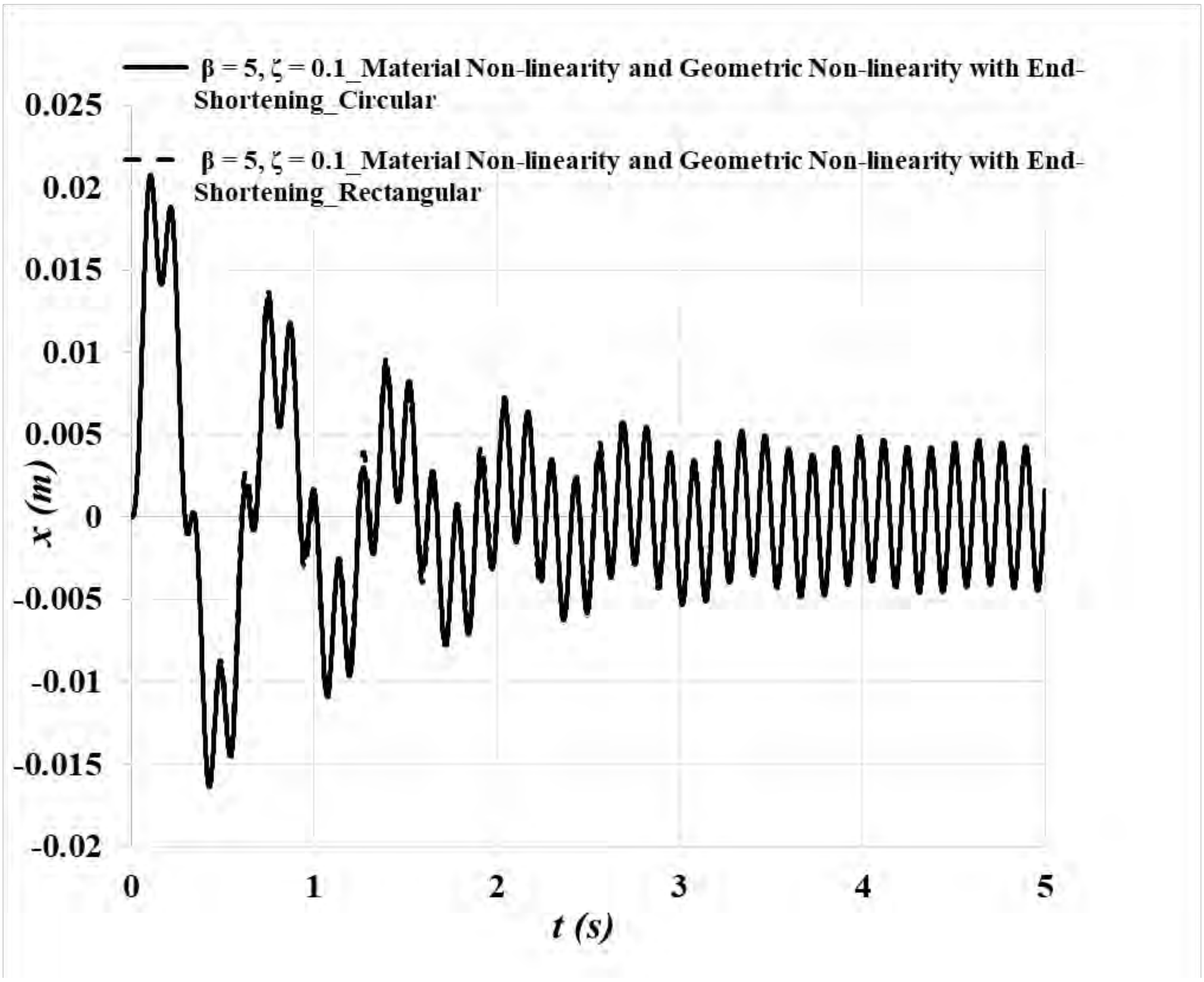

Figure 4.12.7: Displacement (m) vs time (s) curve for speed ratio, $\beta = 5$ and damping ratio, $\zeta = 0.1$ for circular and equivalent rectangular beam (APPENDIX-C) considering material non-linearity and geometric non-linearity with end-shortening.

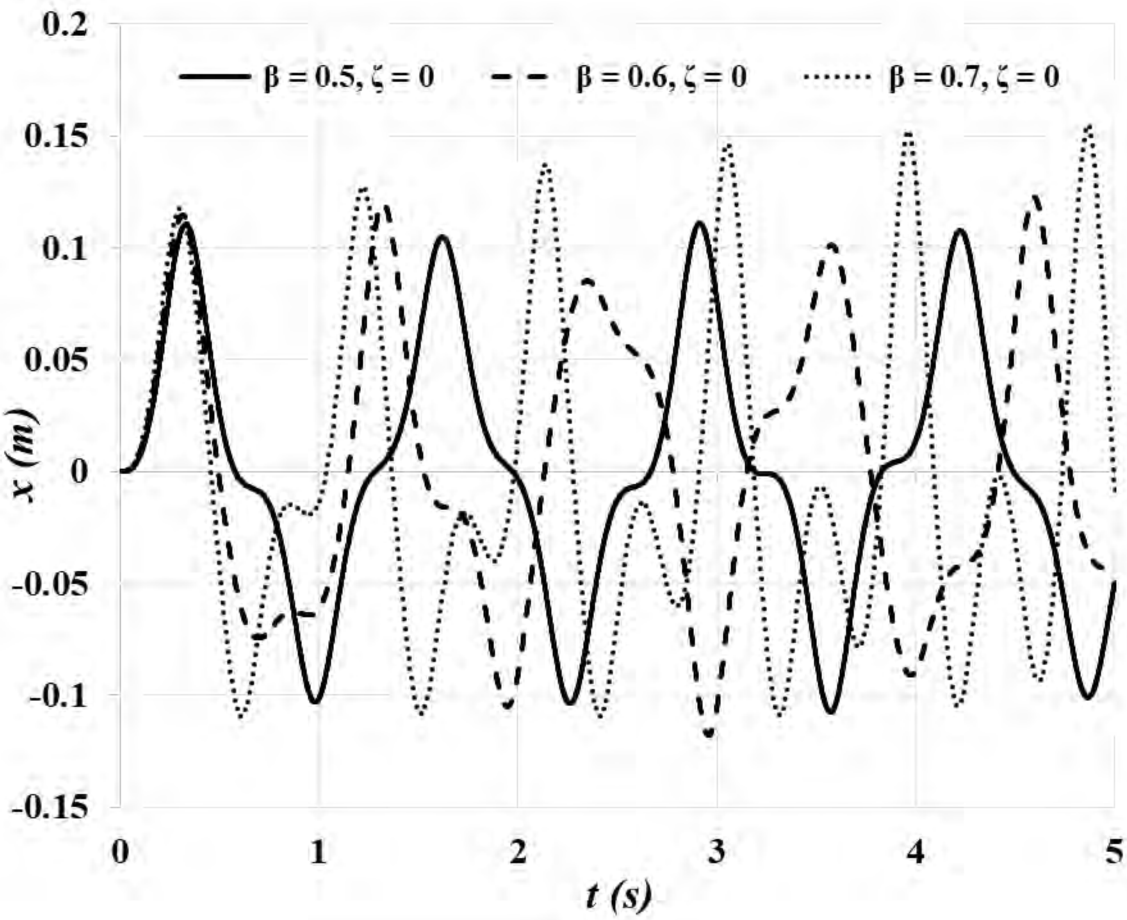

Figure 4.13.1: Displacement (m) vs time (s) curve for different speed ratio, β when undamped ($\zeta = 0$) for circular beam considering material non-linearity and geometric non-linearity with end-shortening.

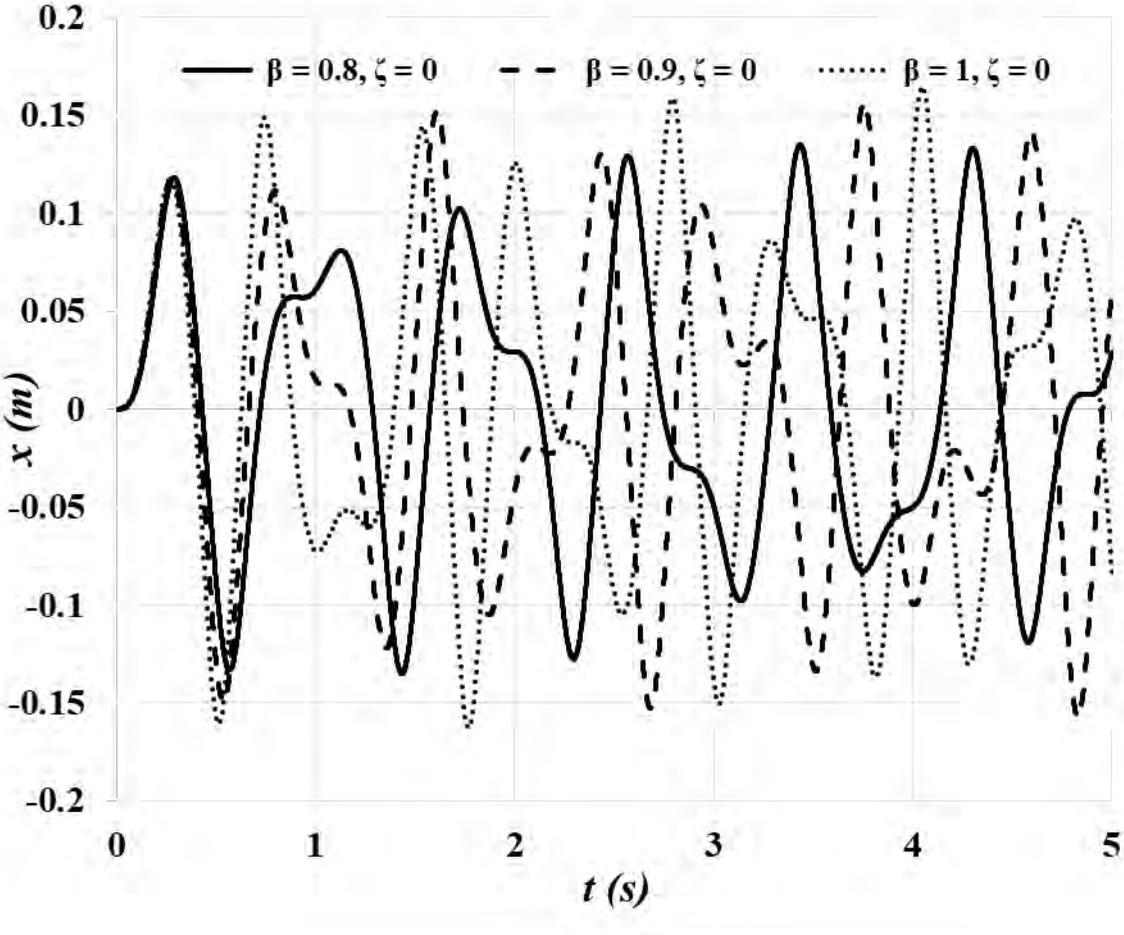

Figure 4.13.2: Displacement (m) vs time (s) curve for different speed ratio, β when undamped ($\zeta = 0$) for circular beam considering material non-linearity and geometric non-linearity with end-shortening.

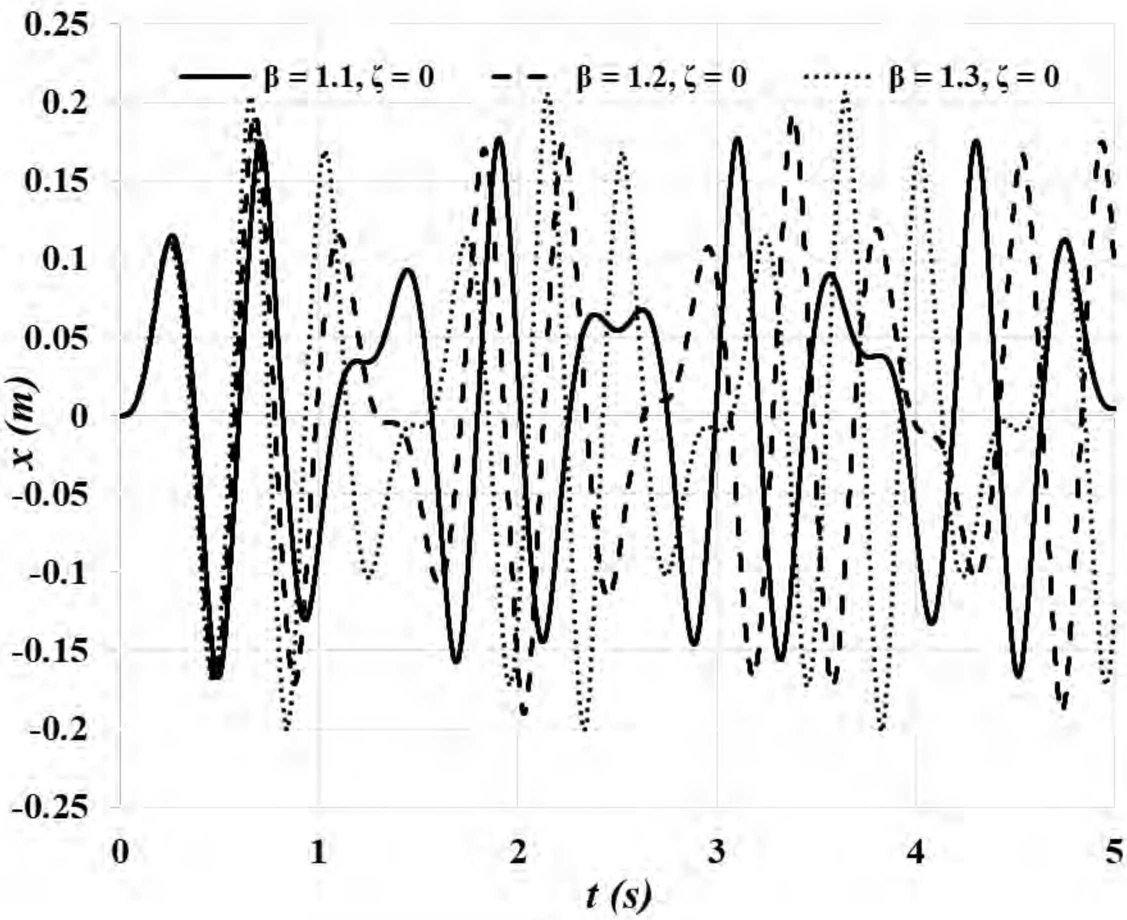

Figure 4.13.3: Displacement (m) vs time (s) curve for different speed ratio, β when undamped ($\zeta = 0$) for circular beam considering material non-linearity and geometric non-linearity with end-shortening

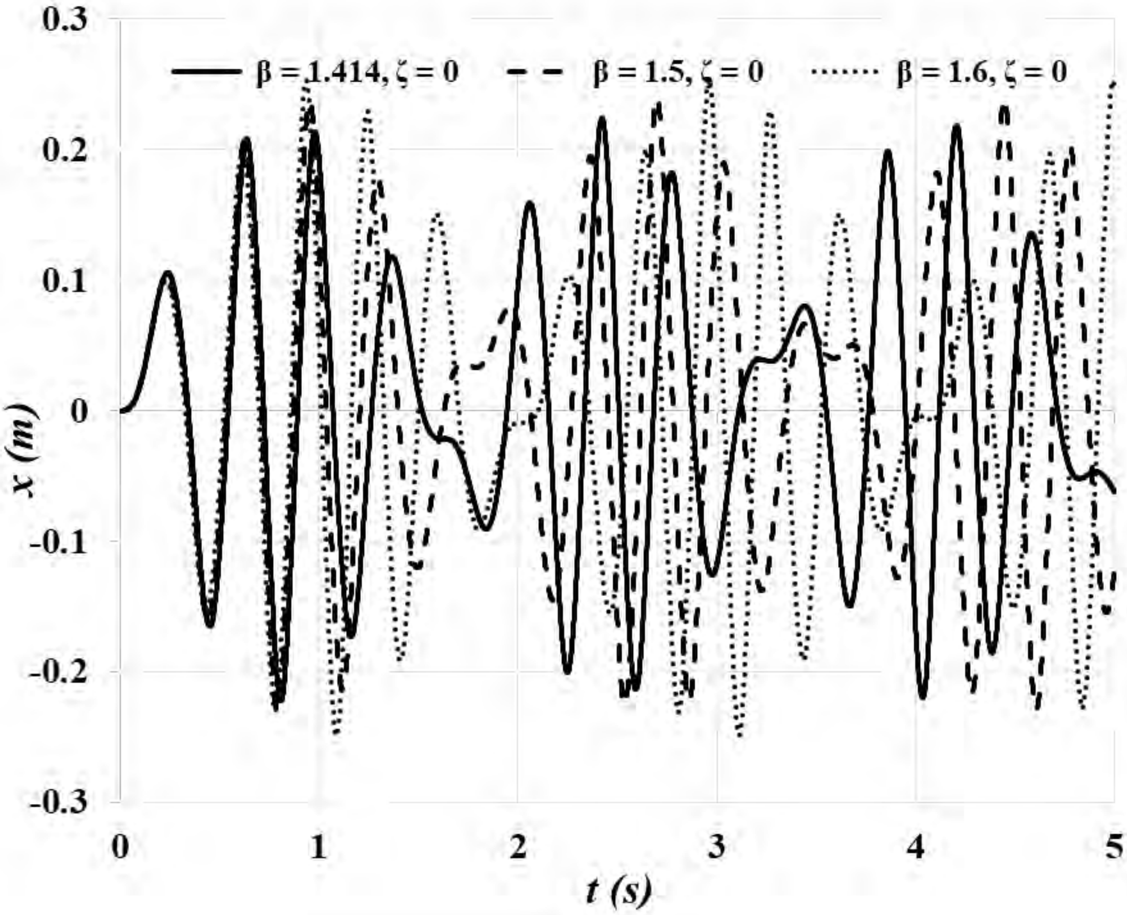

Figure 4.13.4: Displacement (m) vs time (s) curve for different speed ratio, β when undamped ($\zeta = 0$) for circular beam considering material non-linearity and geometric non-linearity with end-shortening.

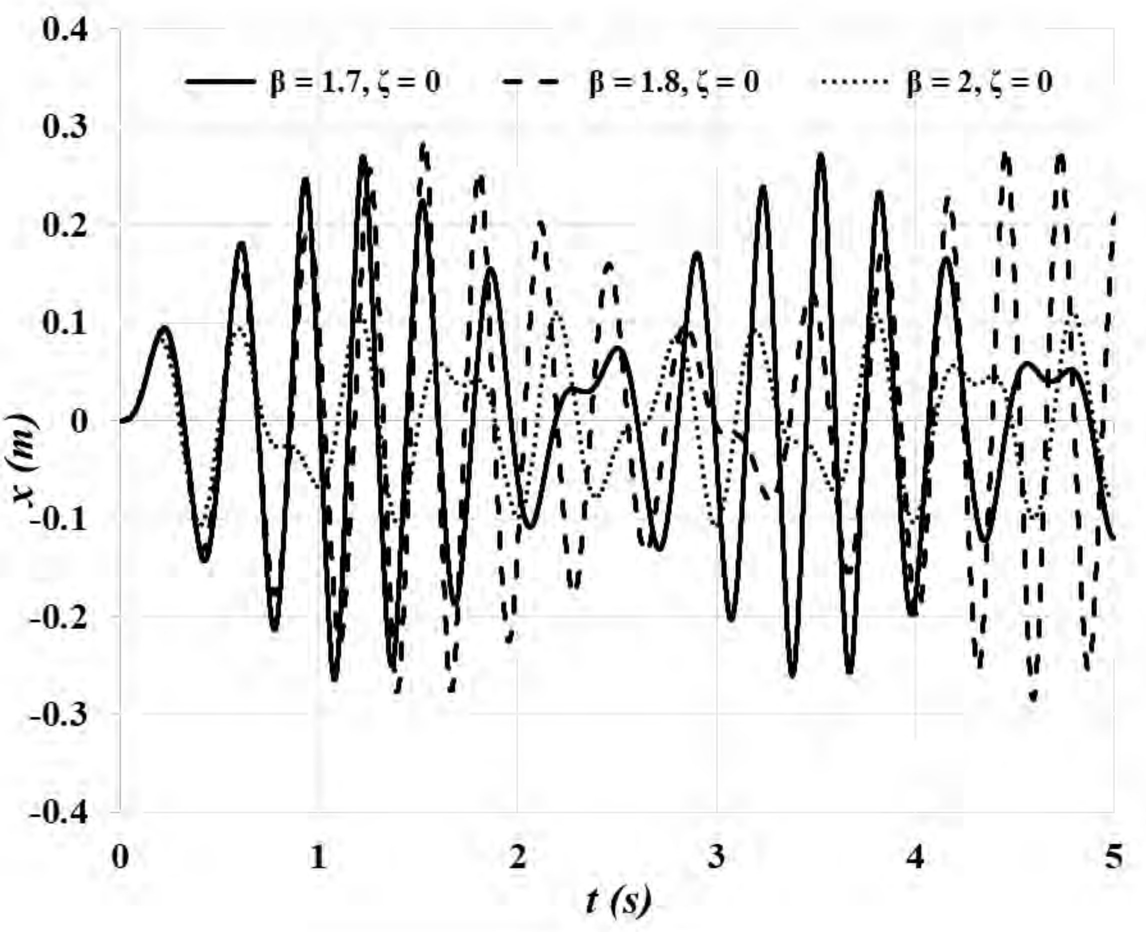

Figure 4.13.5: Displacement (m) vs time (s) curve for different speed ratio, β when undamped ($\zeta = 0$) for circular beam considering material non-linearity and geometric non-linearity with end-shortening.

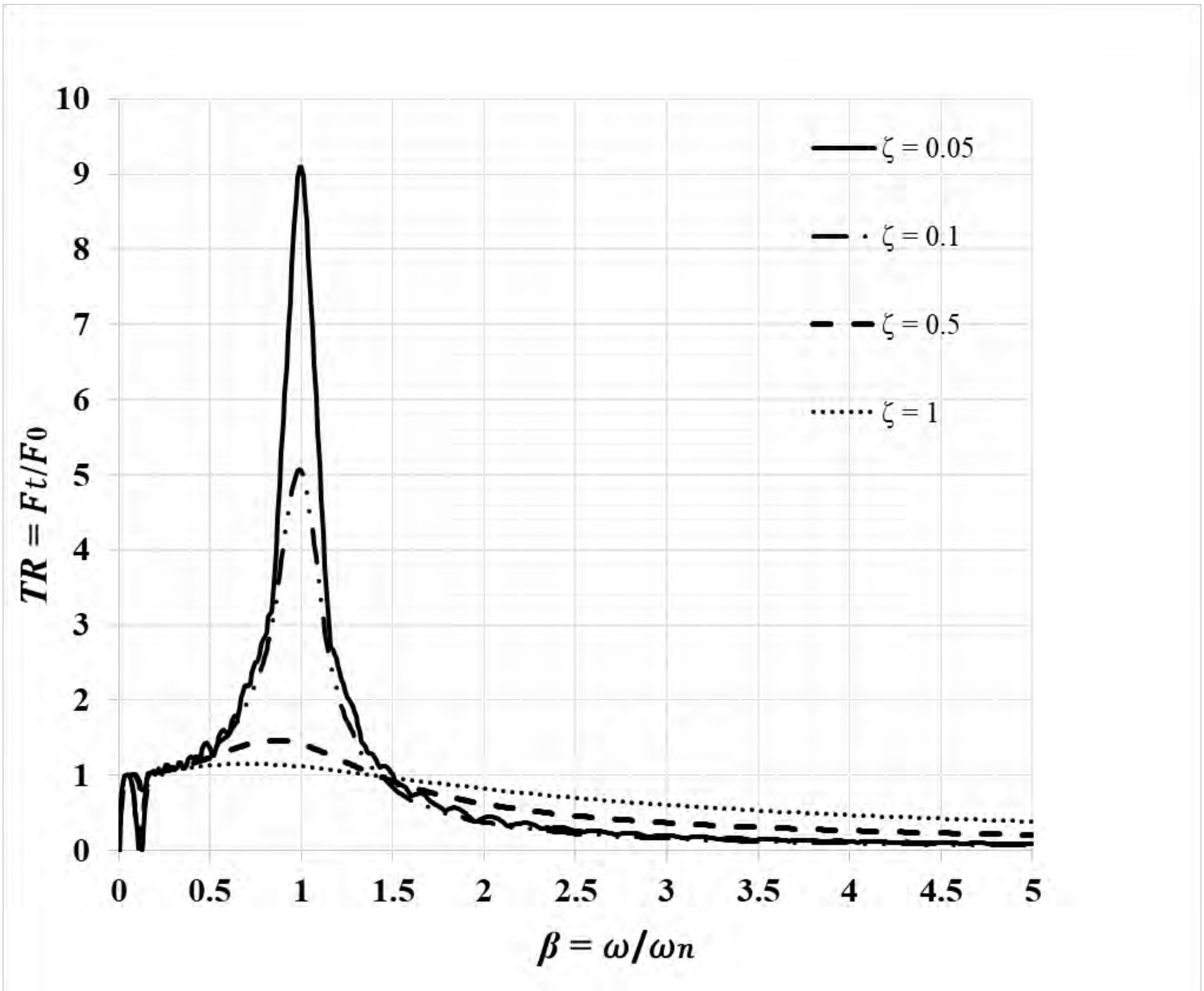

Figure 4.14.1.1: Steady-state TR vs speed ratio (β) for different damping ratio for classical theory.

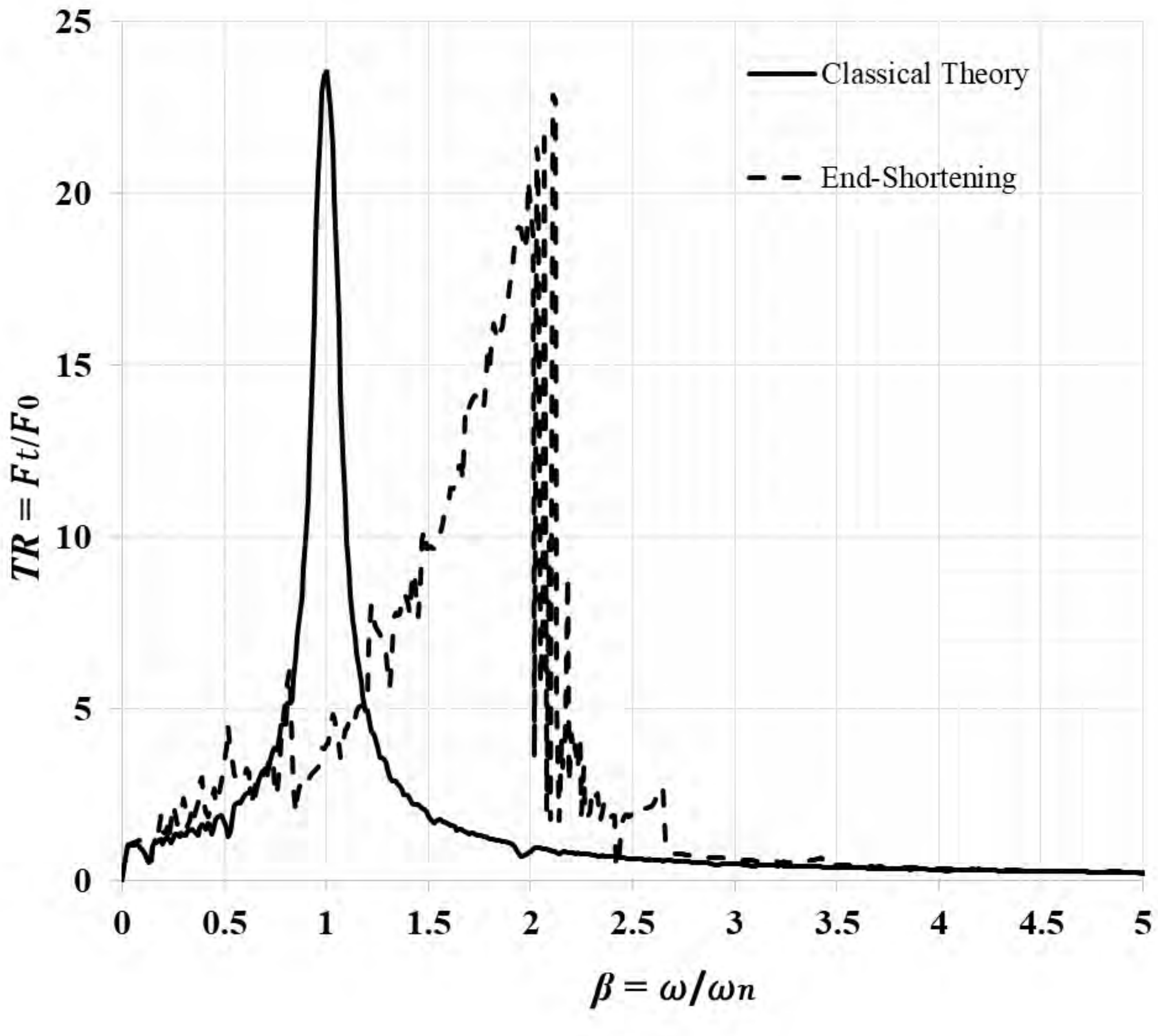

Figure 4.14.2.1: Steady-state TR vs speed ratio (β) when undamped ($\zeta = 0$) for classical theory with and without end-shortening effect.

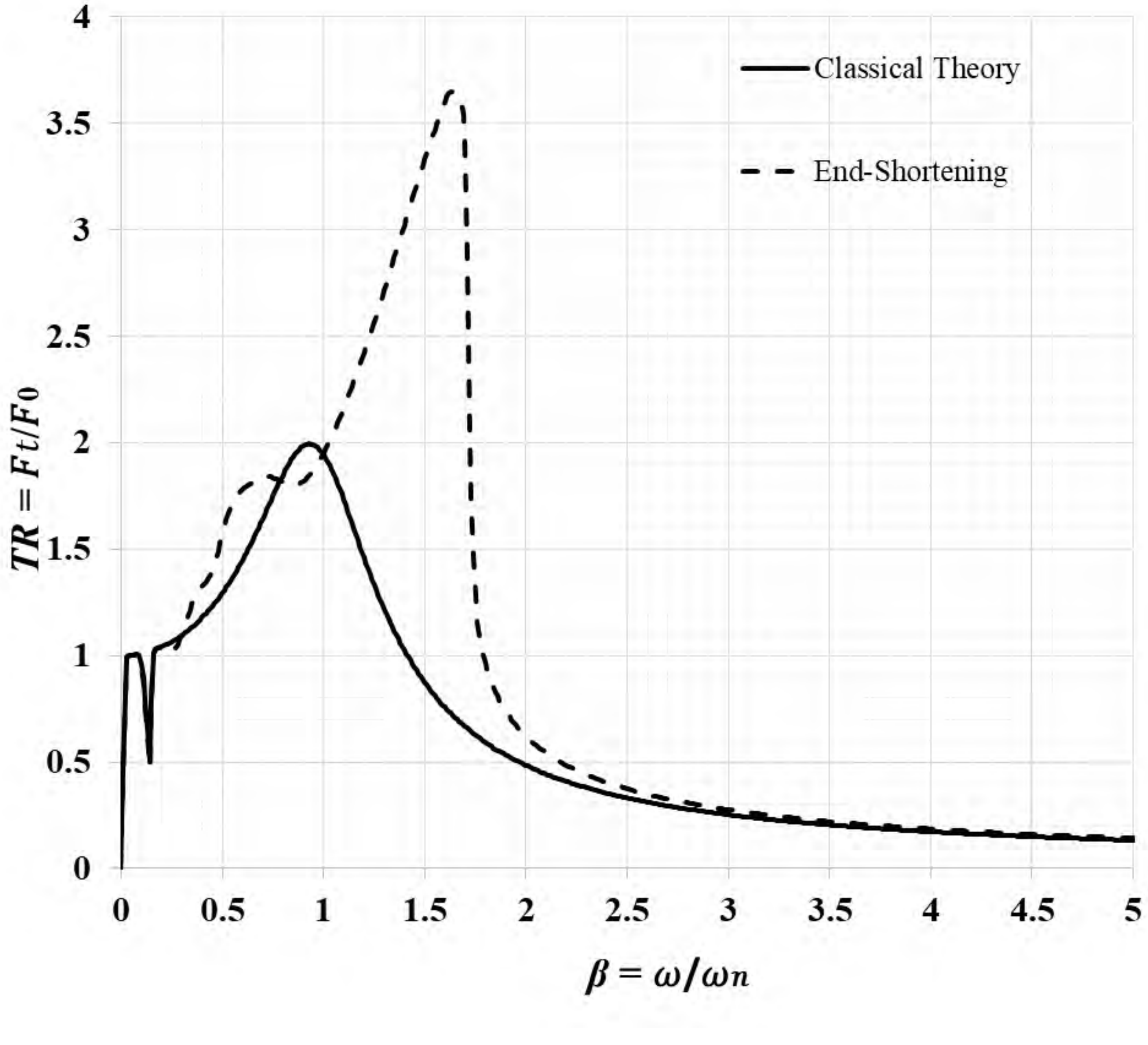

Figure 4.14.2.2: Steady-state TR vs speed ratio (β) for damping ratio $\zeta = 0.3$ for classical theory and considering end-shortening effect.

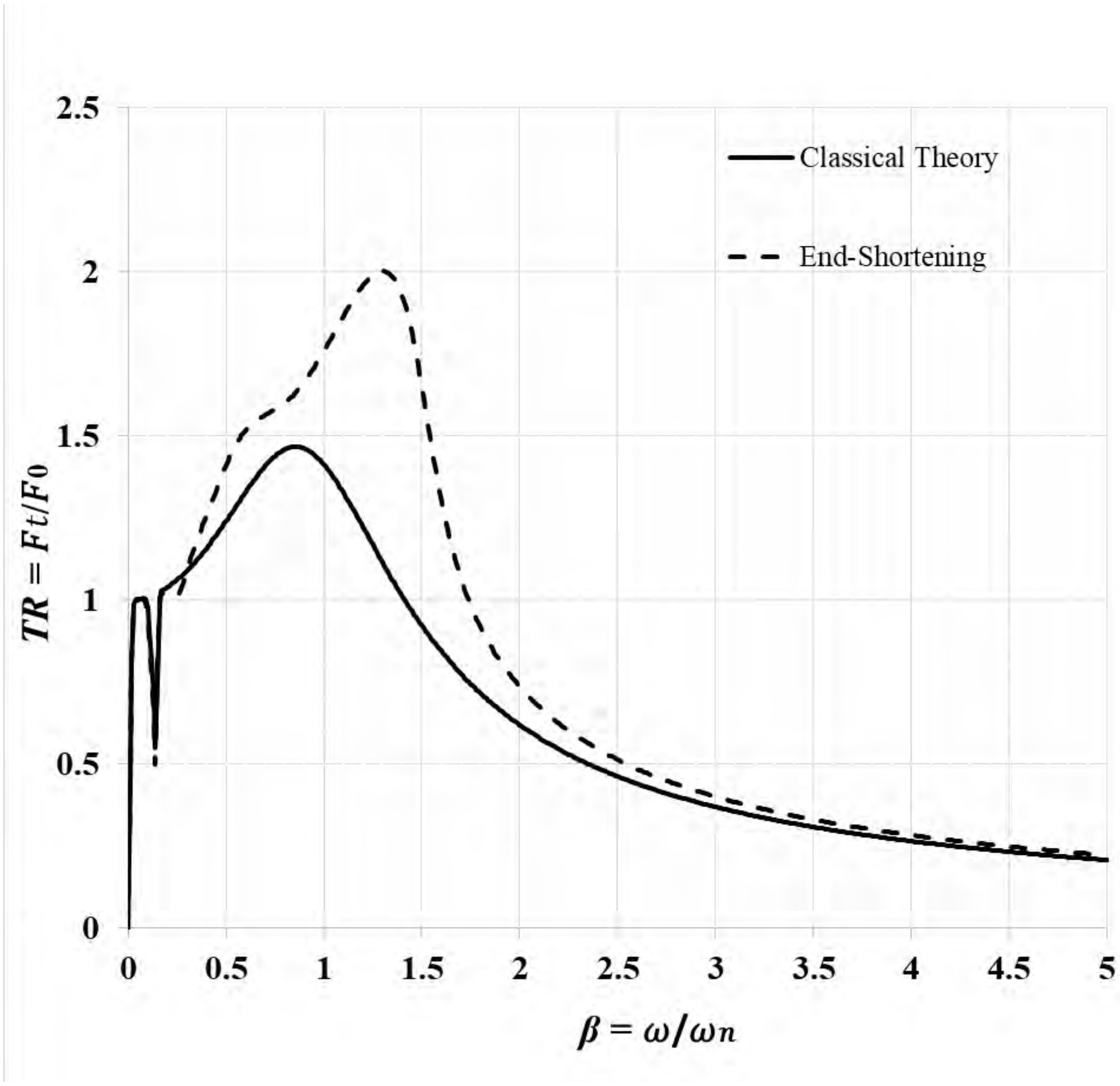

Figure 4.14.2.3: Steady-state TR vs speed ratio (β) for damping ratio $\zeta = 0.5$ for classical theory and considering end-shortening effect.

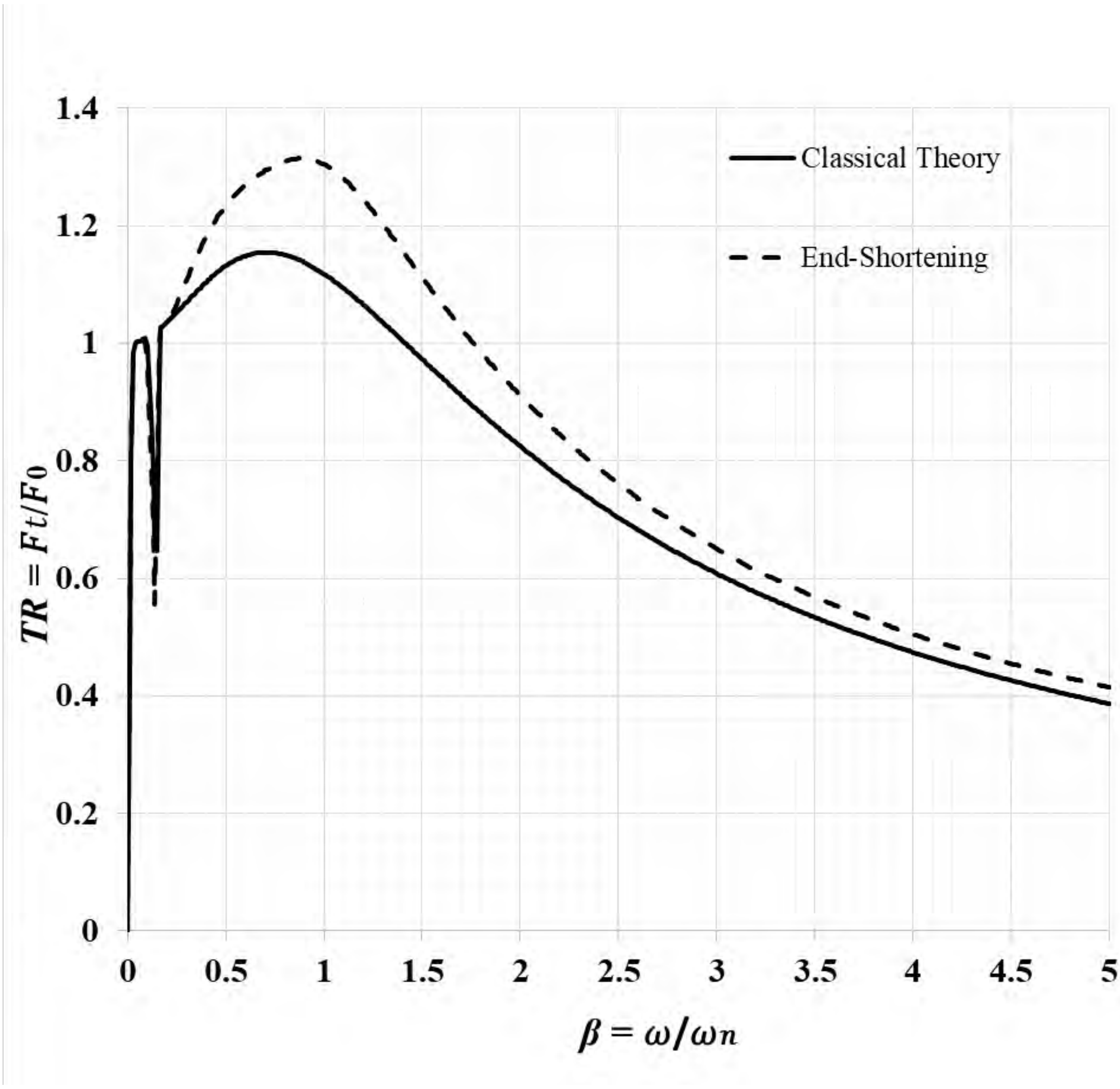

Figure 4.14.2.4: Steady-state TR vs speed ratio (β) for damping ratio $\zeta = 1$ for classical theory and considering end-shortening effect.

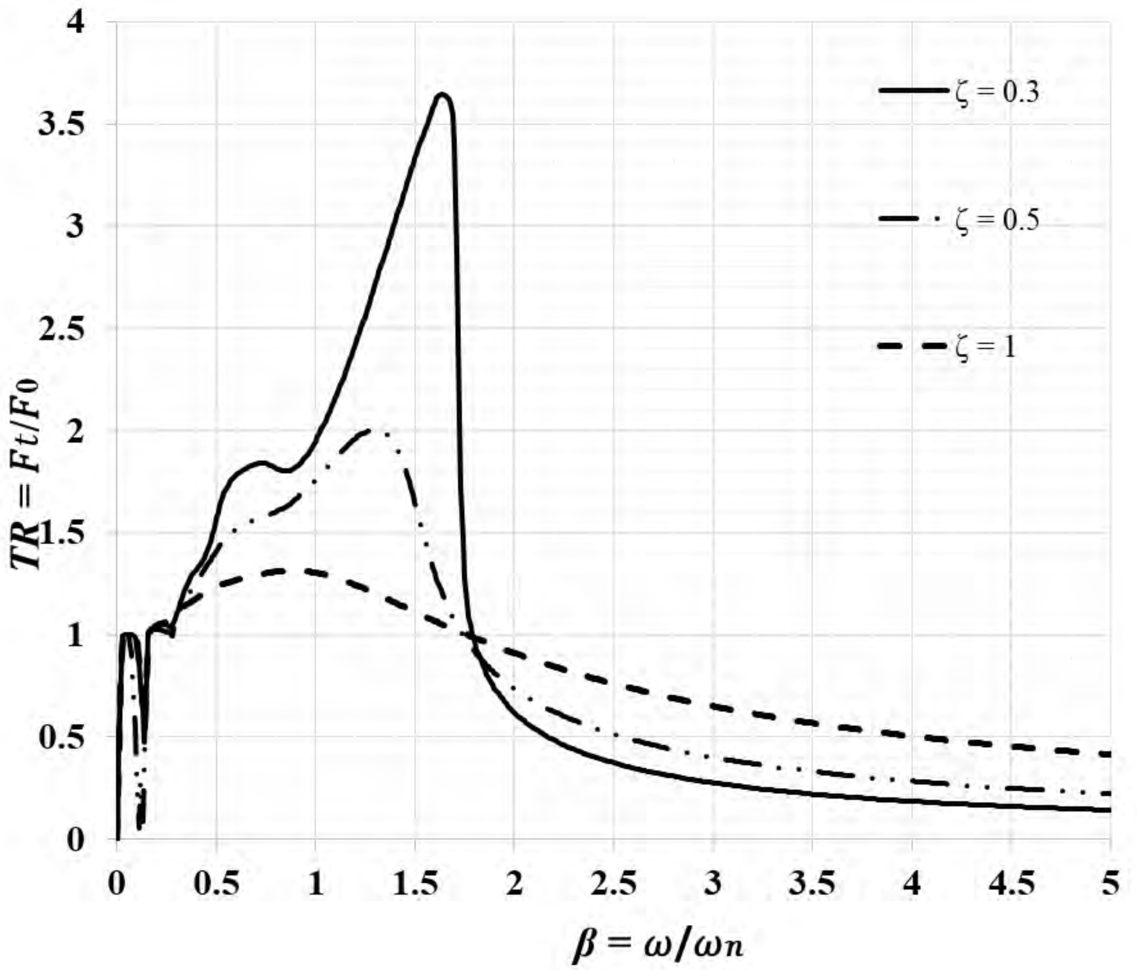

Figure 4.14.2.5: Steady-state TR vs speed ratio (β) for different damping ratio for considering end-shortening effect.

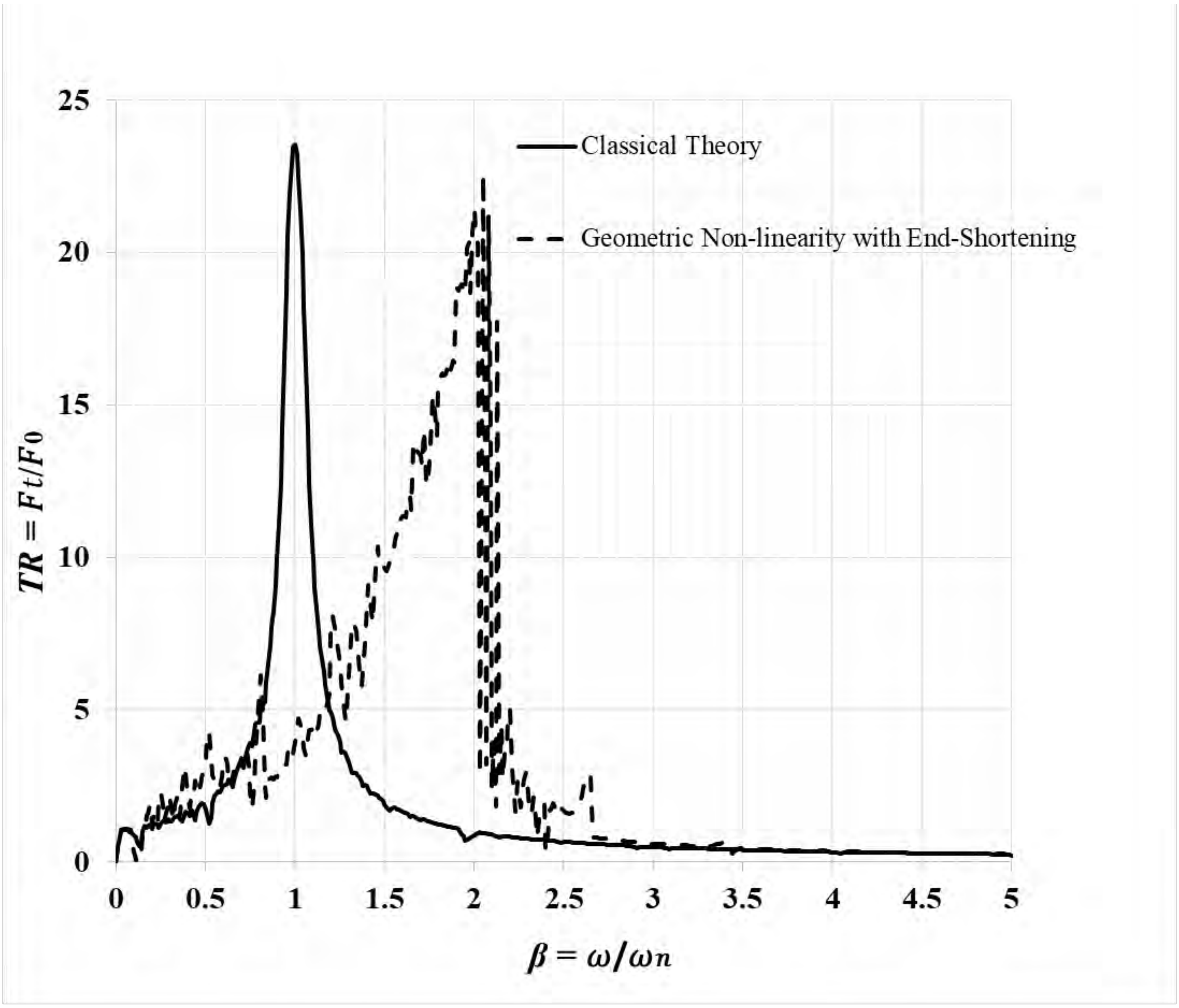

Figure 4.14.2.6: Steady-state TR vs speed ratio (β) when undamped ($\zeta = 0$) for classical theory and considering geo-metric non-linearity with end-shortening effect.

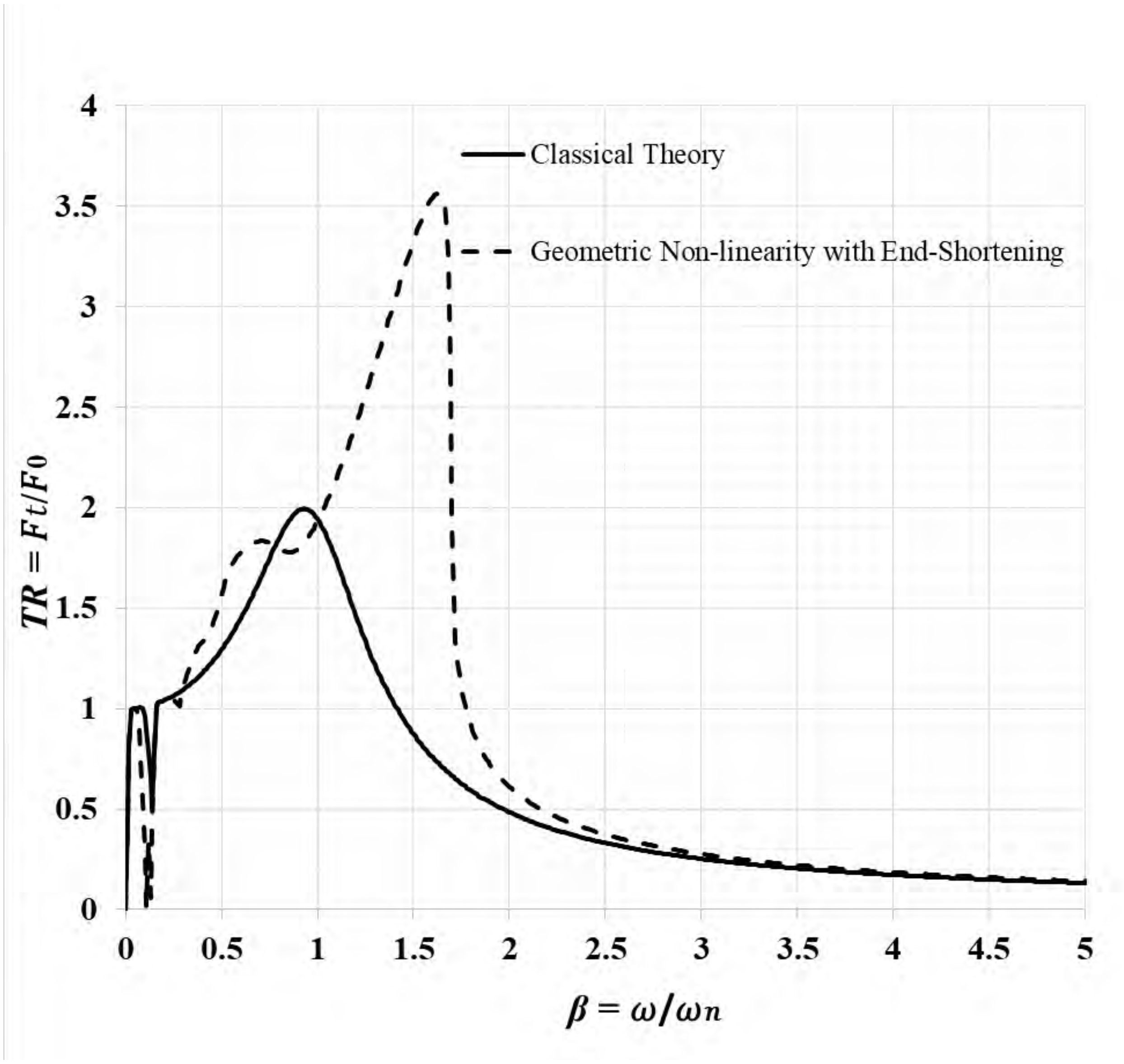

Figure 4.14.2.7: Steady-state TR vs speed ratio (β) for damping ratio $\zeta = 0.3$ for classical theory and considering geo-metric non-linearity with end-shortening effect.

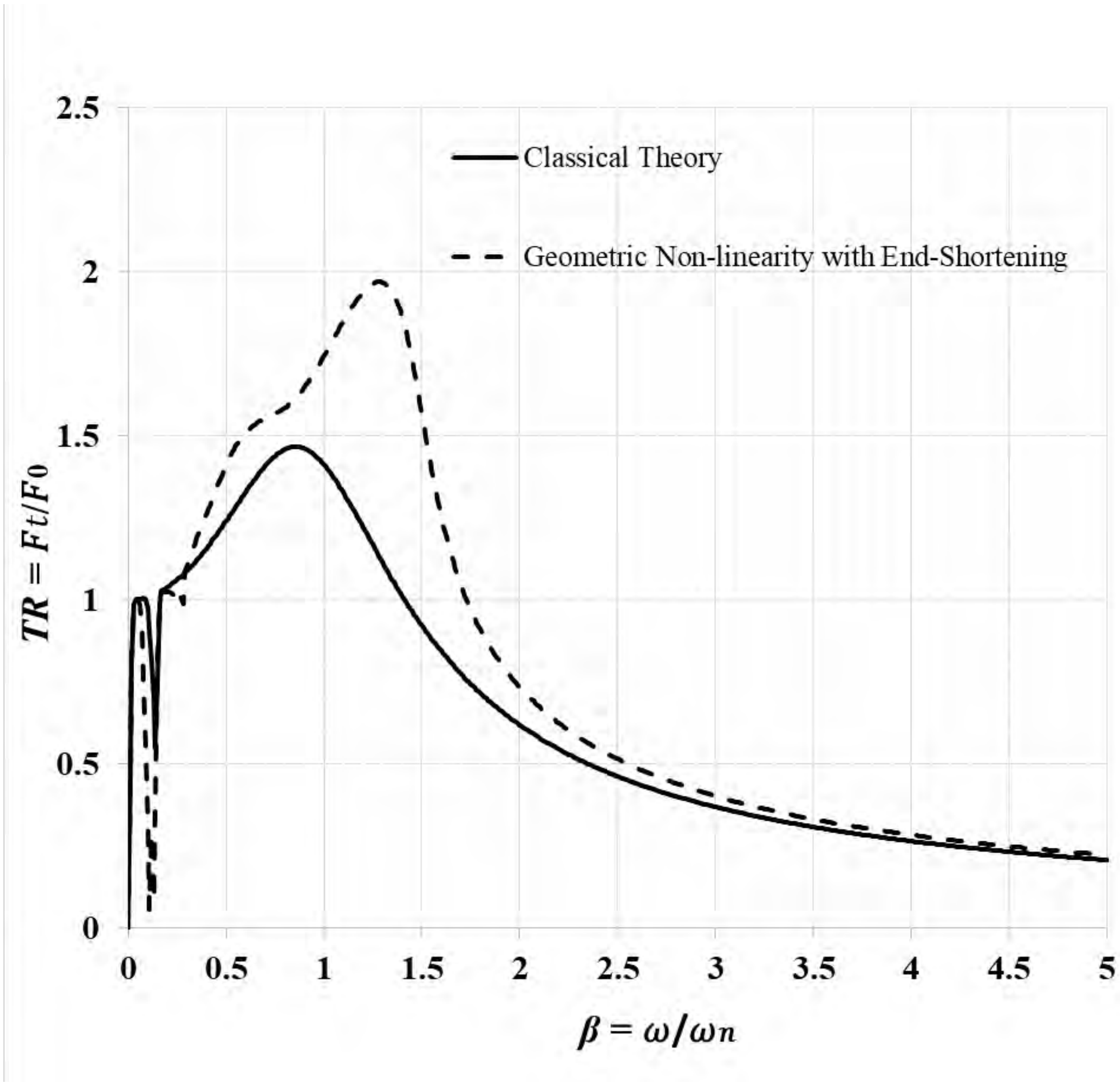

Figure 4.14.2.8: Steady-state TR vs speed ratio (β) for damping ratio $\zeta = 0.5$ for classical theory and considering geo-metric non-linearity with end-shortening effect.

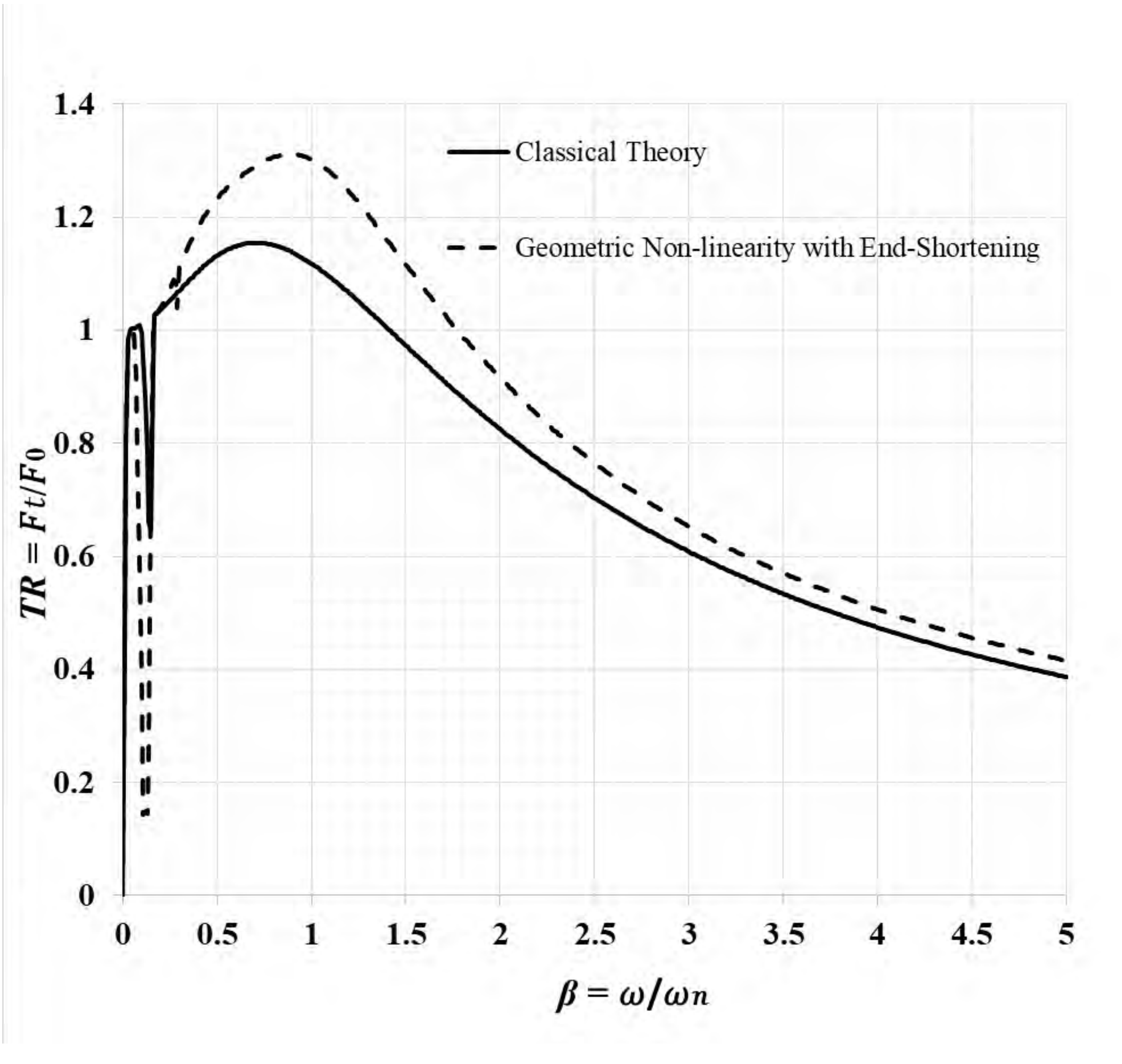

Figure 4.14.2.9: Steady-state TR vs speed ratio (β) for damping ratio $\zeta = 1$ for classical theory and considering geo-metric non-linearity with end-shortening effect

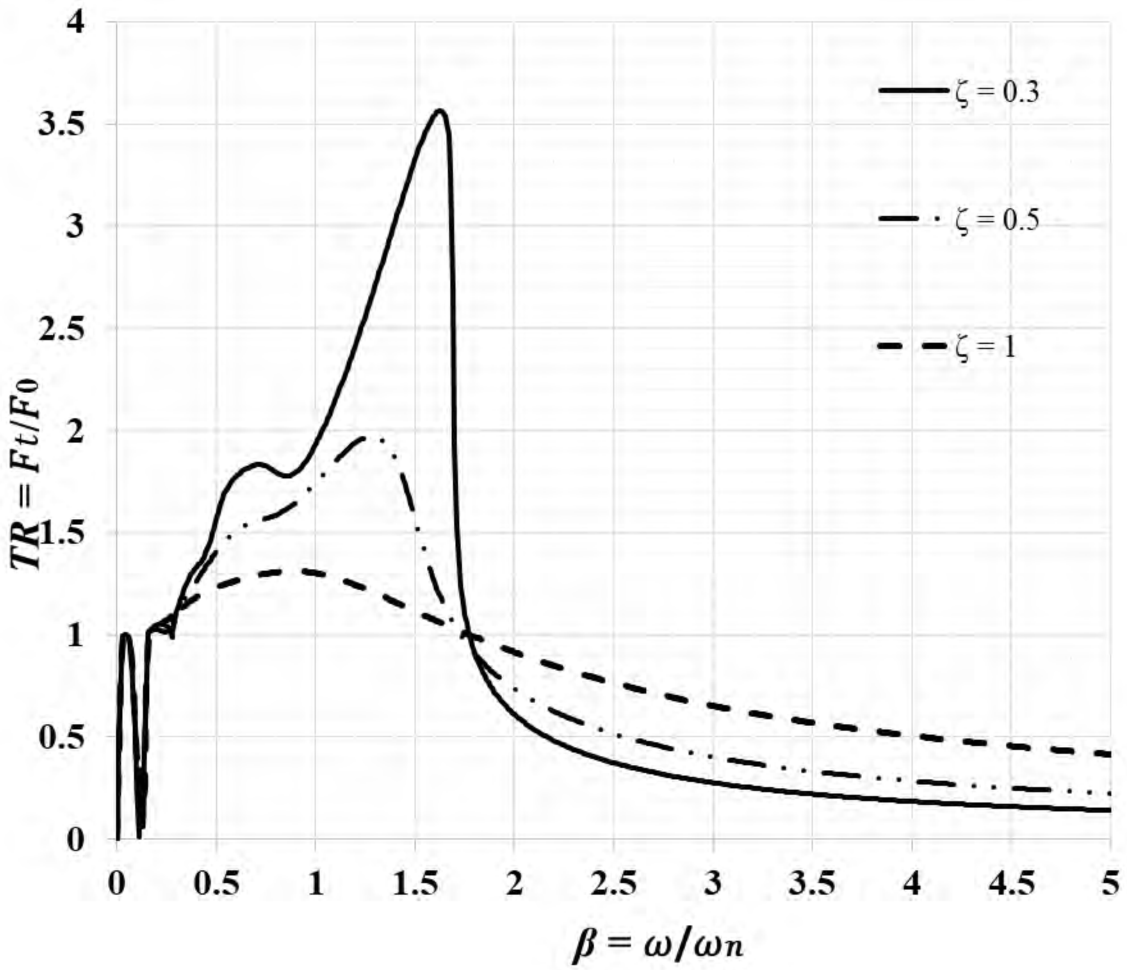

Figure 4.14.2.10: Steady-state TR vs speed ratio (β) for different damping ratio considering geo-metric non-linearity with end-shortening effect.

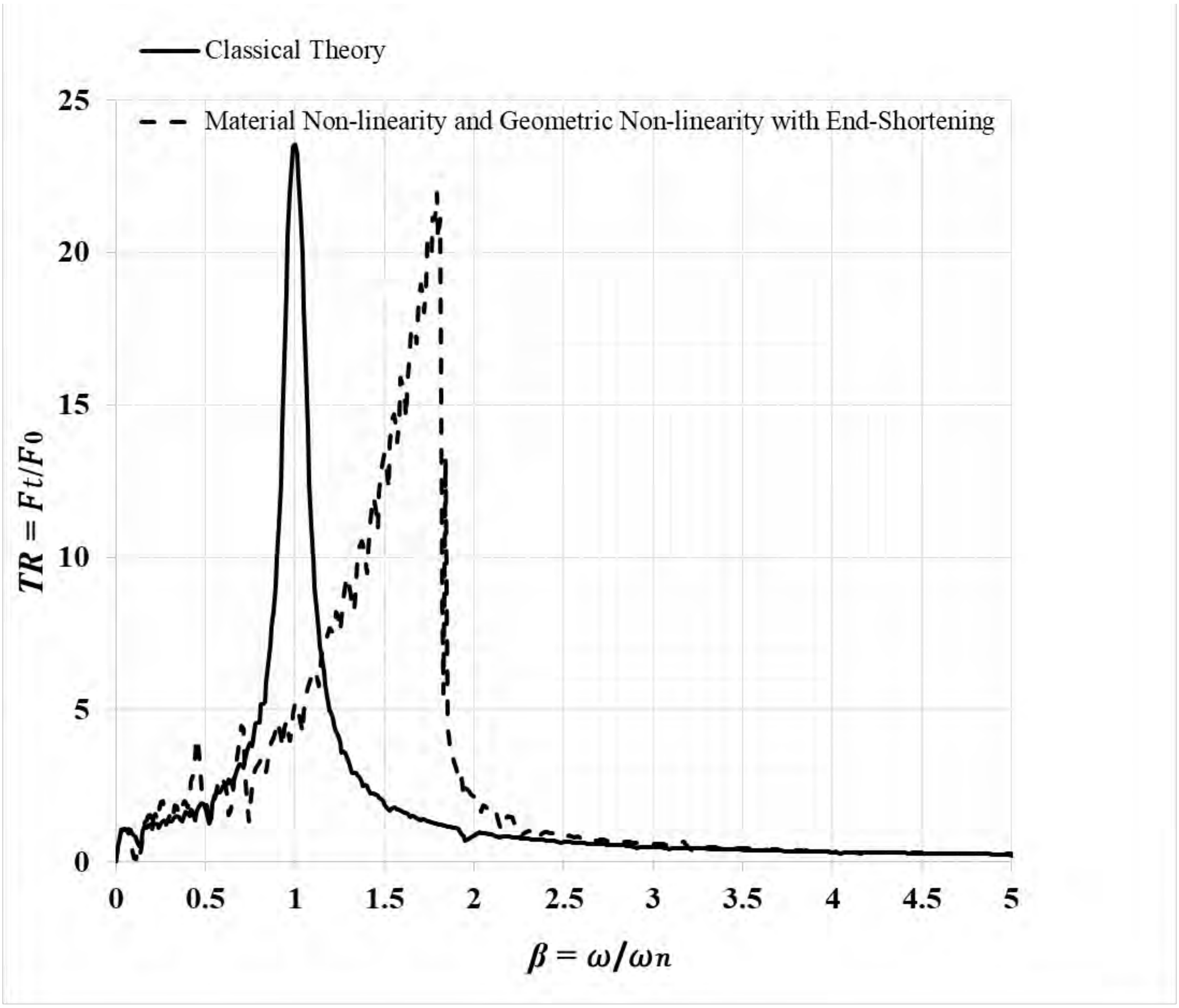

Figure 4.14.2.11: Steady-state TR vs speed ratio (β) when undamped for classical theory and considering material non-linearity and geo-metric non-linearity with end-shortening effect.

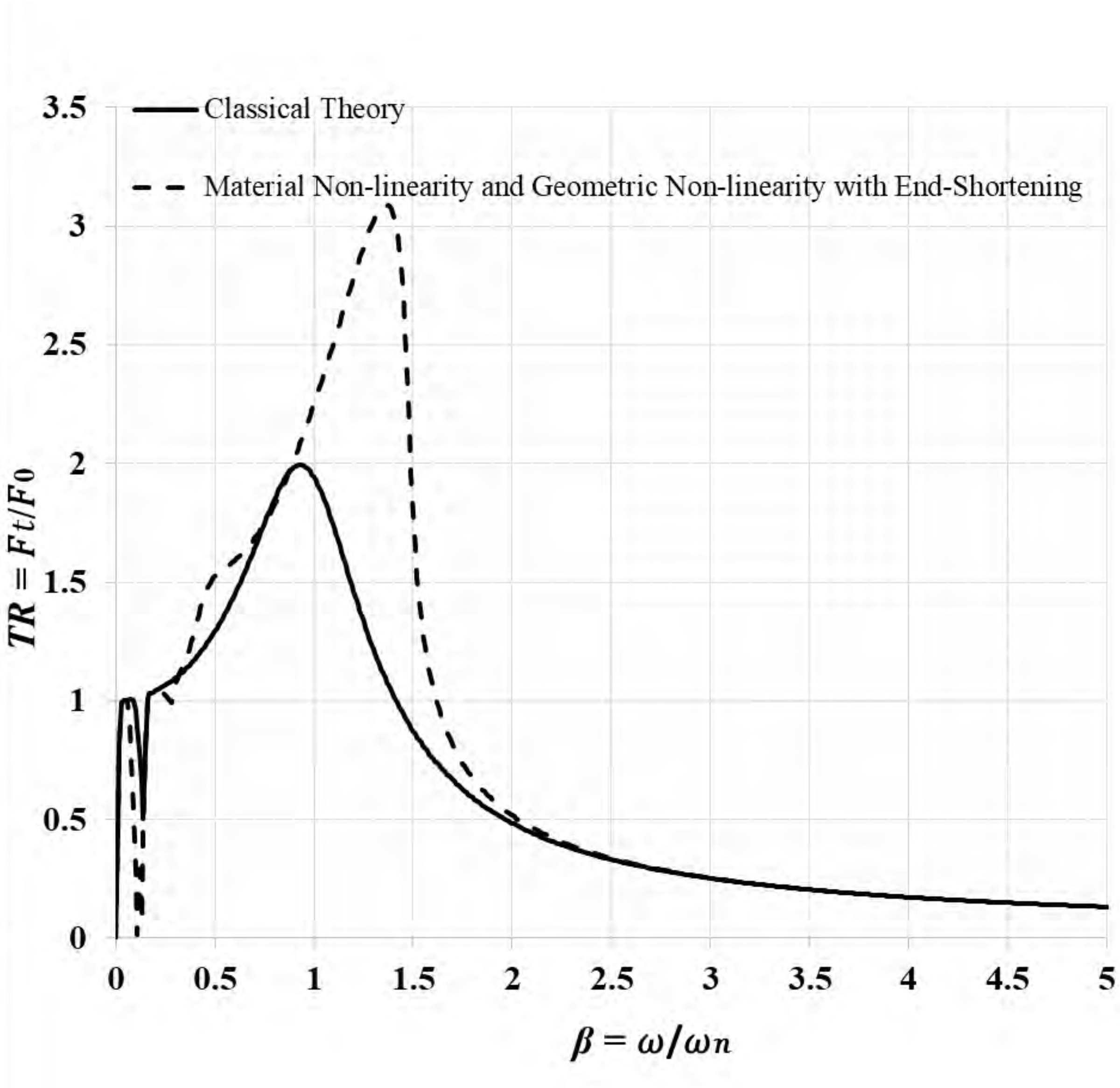

Figure 4.14.2.12: Steady-state TR vs speed ratio (β) for damping ratio $\zeta = 0.3$ for classical theory and considering material non-linearity and geo-metric non-linearity with end-shortening effect.

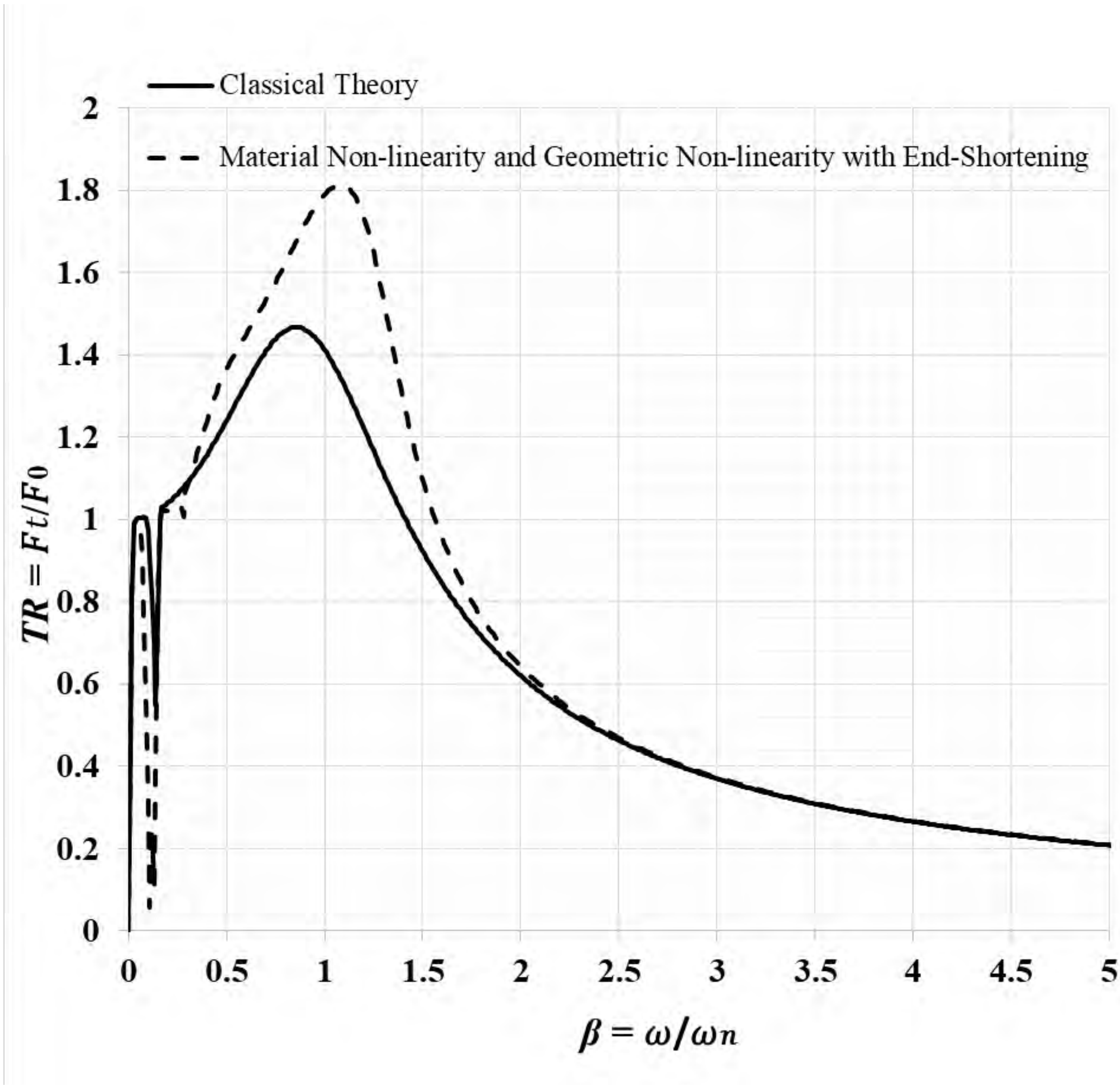

Figure 4.14.2.13: Steady-state TR vs speed ratio (β) for damping ratio $\zeta = 0.5$ for classical theory and considering material non-linearity and geo-metric non-linearity with end-shortening effect.

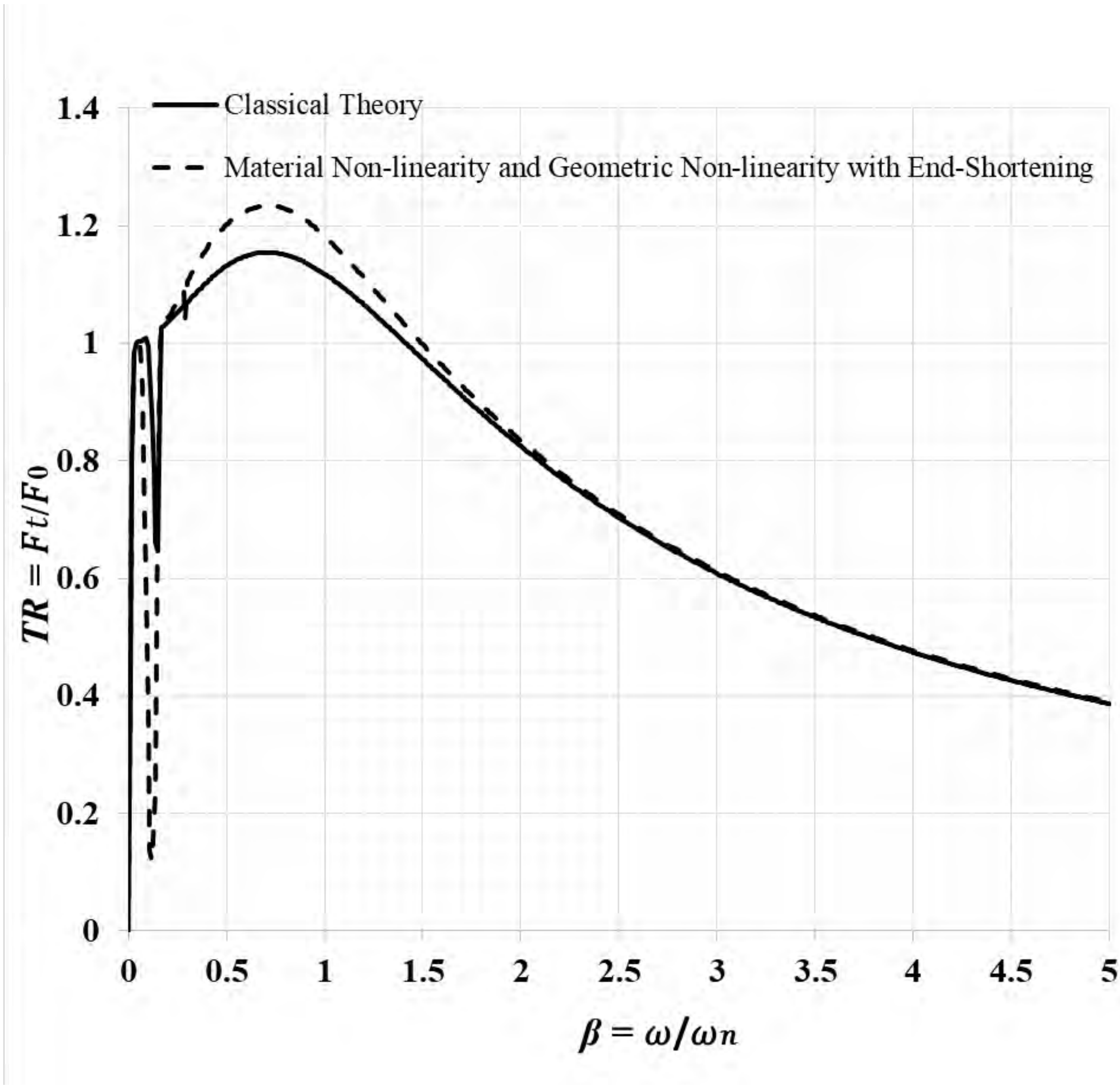

Figure 4.14.2.14: Steady-state TR vs speed ratio (β) for damping ratio $\zeta = 1$ for classical theory and considering material non-linearity and geo-metric non-linearity with end-shortening effect.

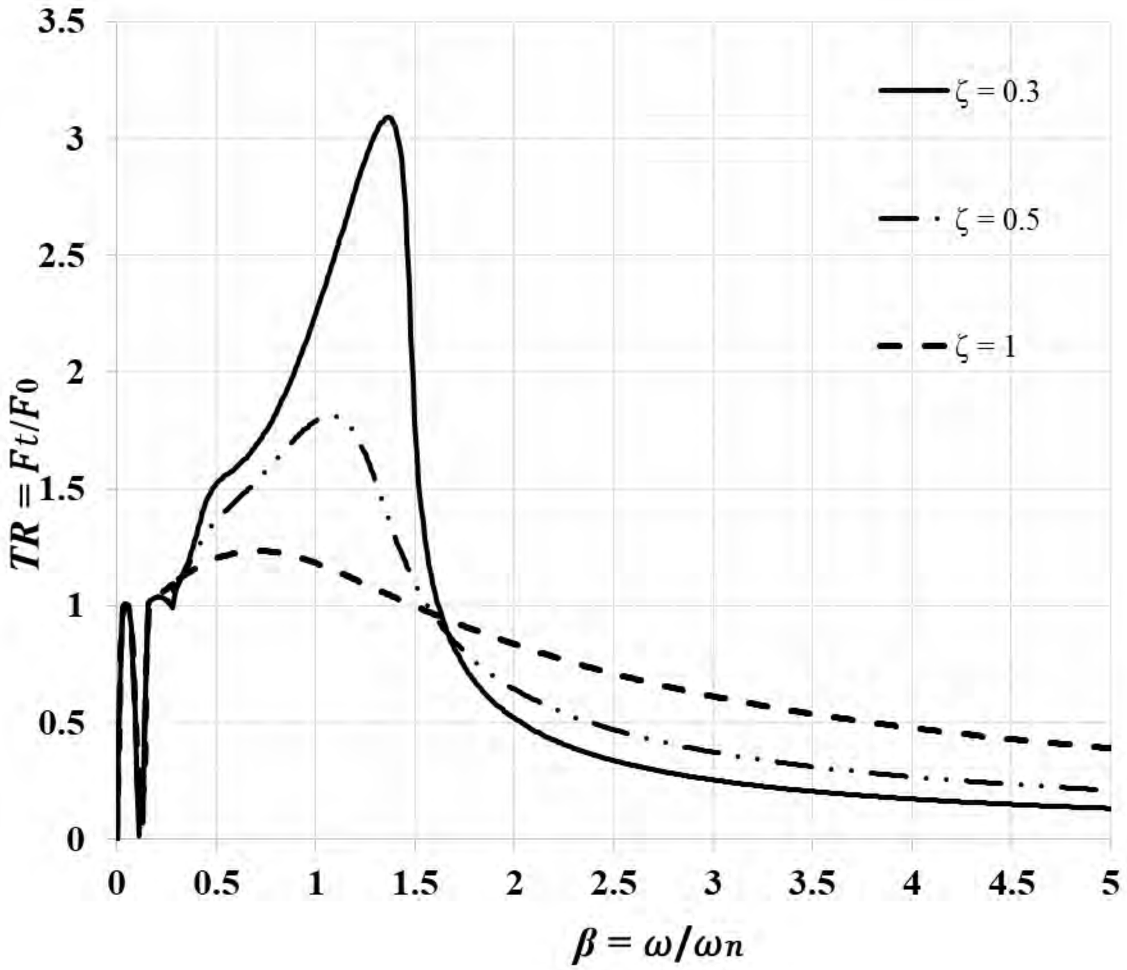

Figure 4.14.2.15: Steady-state TR vs speed ratio (β) for different damping ratio ζ considering material non-linearity and geo-metric non-linearity with end-shortening effect.

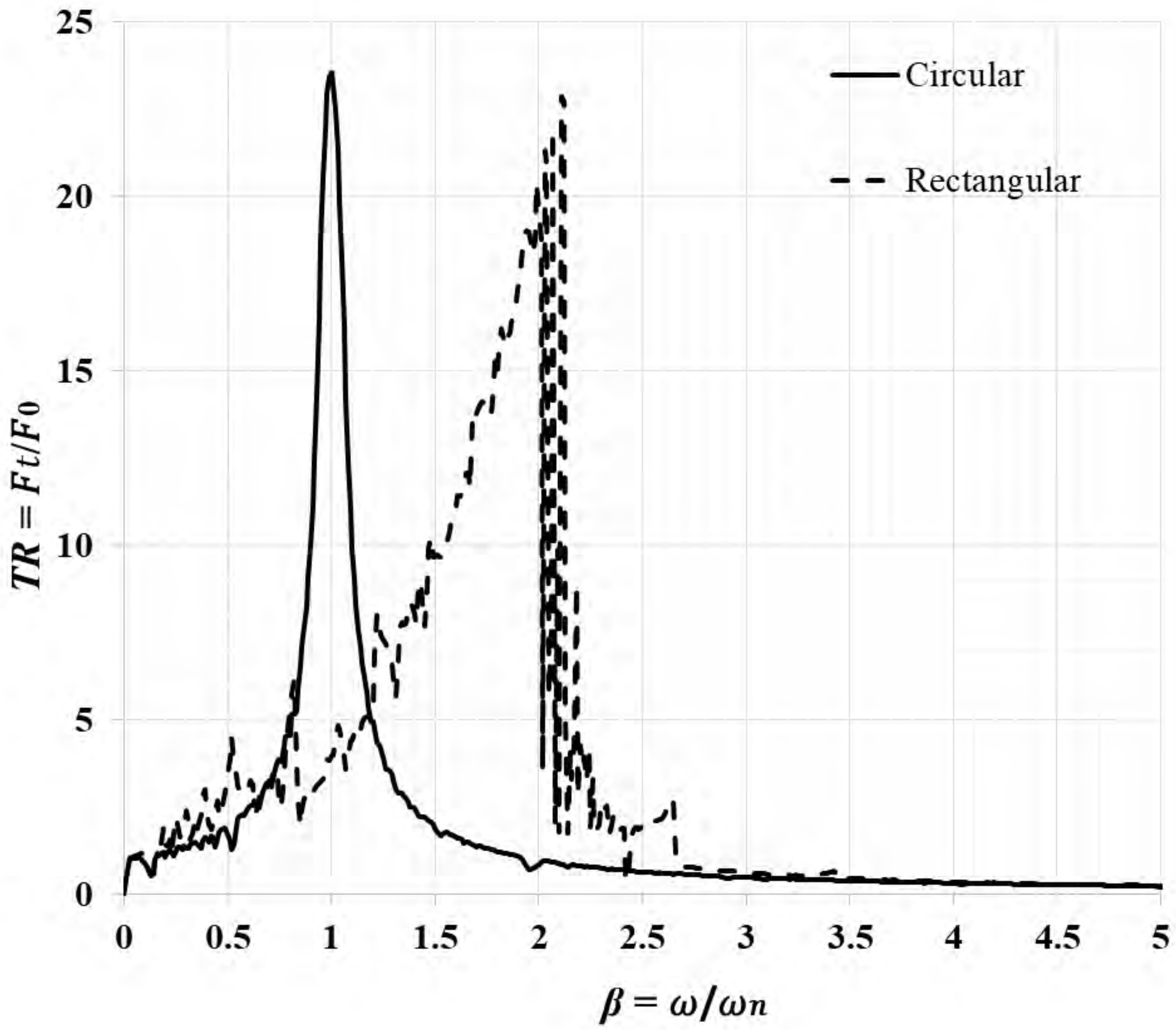

Figure 4.14.2.16: Steady-state TR vs speed ratio (β when undamped ($\zeta = 0$) for superelastic SMA circular and equivalent rectangular beam (APPENDIX-C) considering material non-linearity and geo-metric non-linearity with end-shortening.

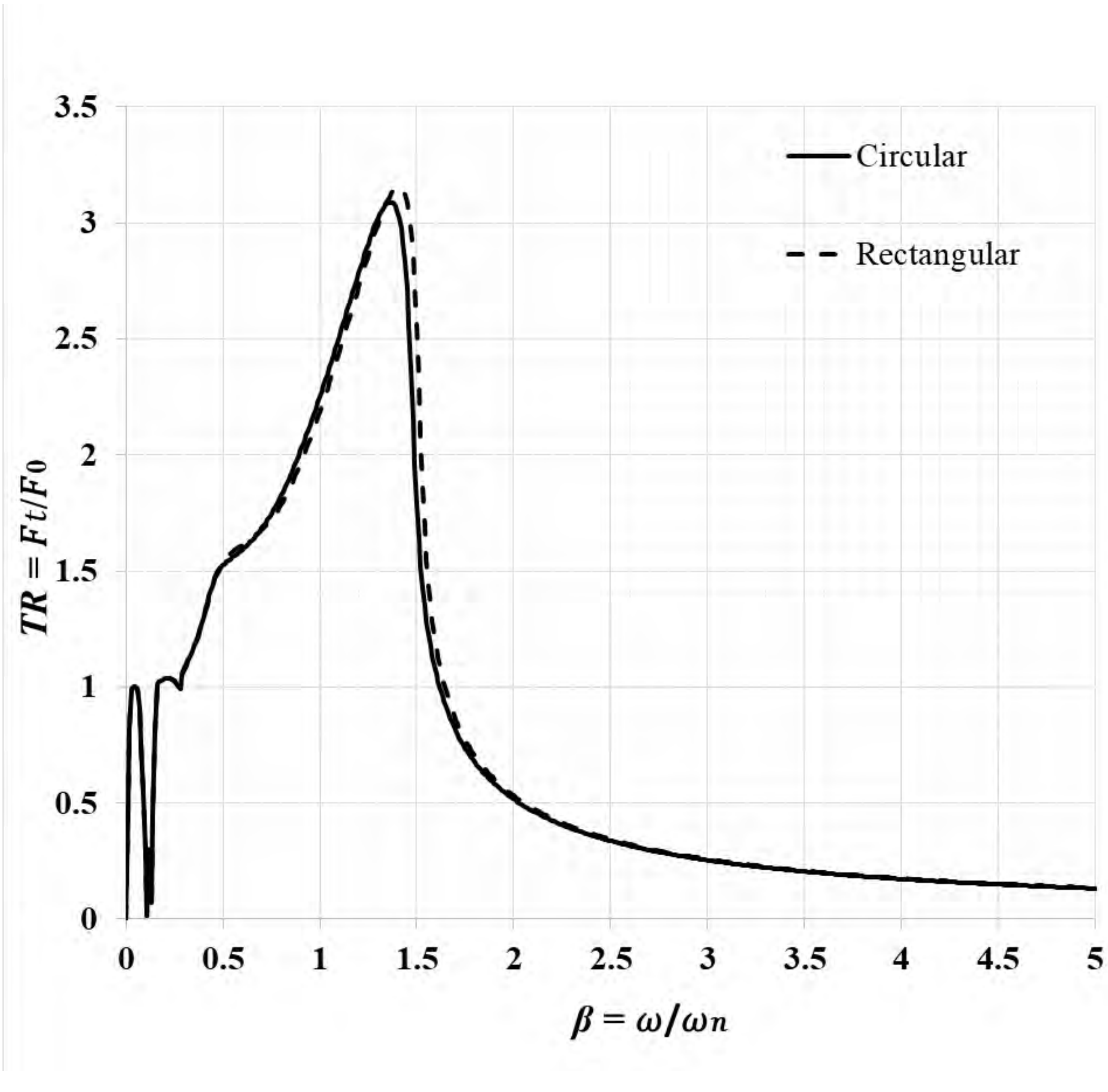

Figure 4.14.2.17: Steady-state TR vs speed ratio (β) for damping ratio $\zeta = 0.3$ for superelastic SMA circular and equivalent rectangular beam (APPENDIX-C) considering material non-linearity and geo-metric non-linearity with end-shortening.

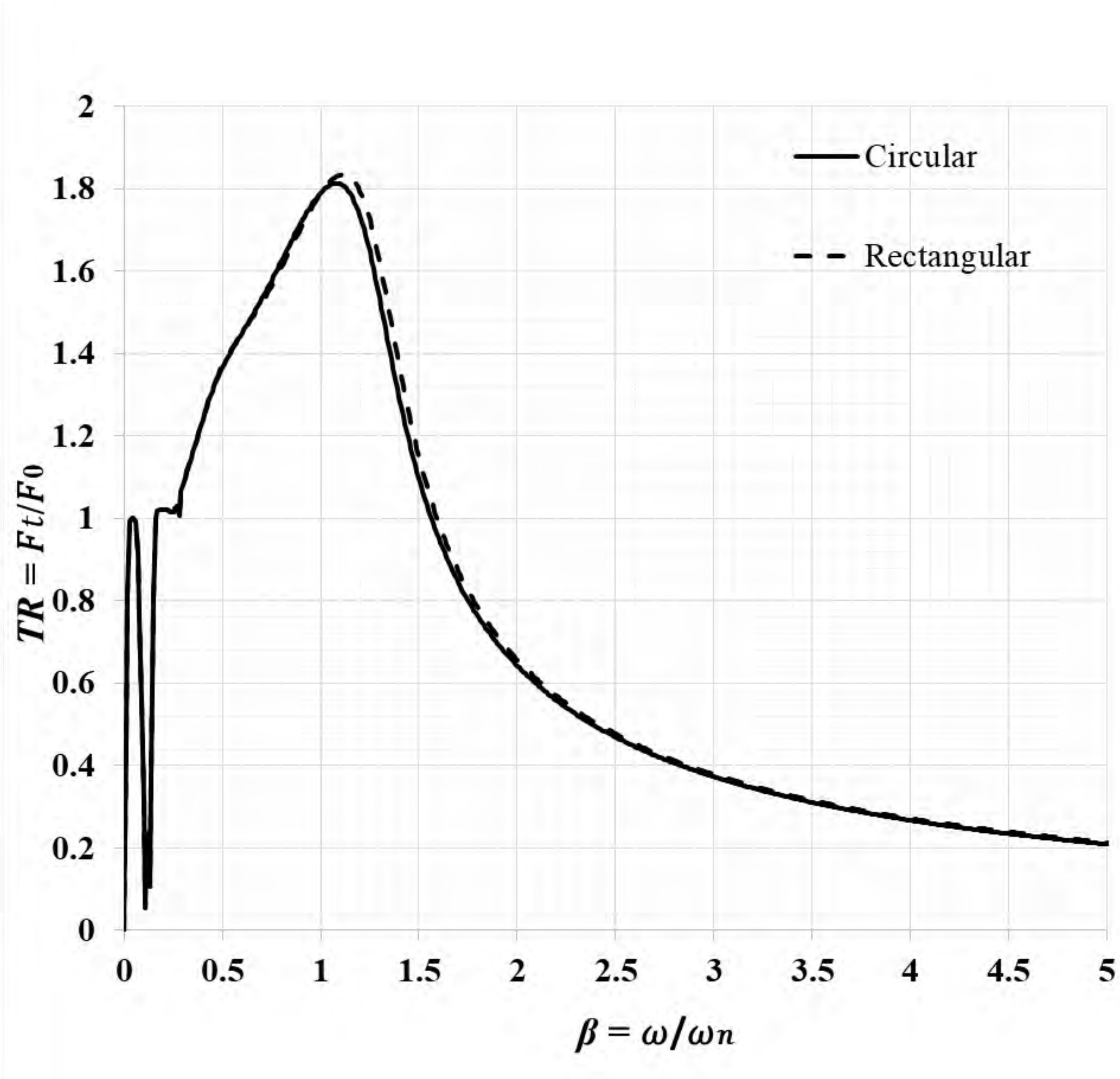

Figure 4.14.2.18: Steady-state TR vs speed ratio (β) for damping ratio $\zeta = 0.5$ for superelastic SMA circular and equivalent rectangular beam (APPENDIX-C) considering material non-linearity and geo-metric non-linearity with end-shortening.

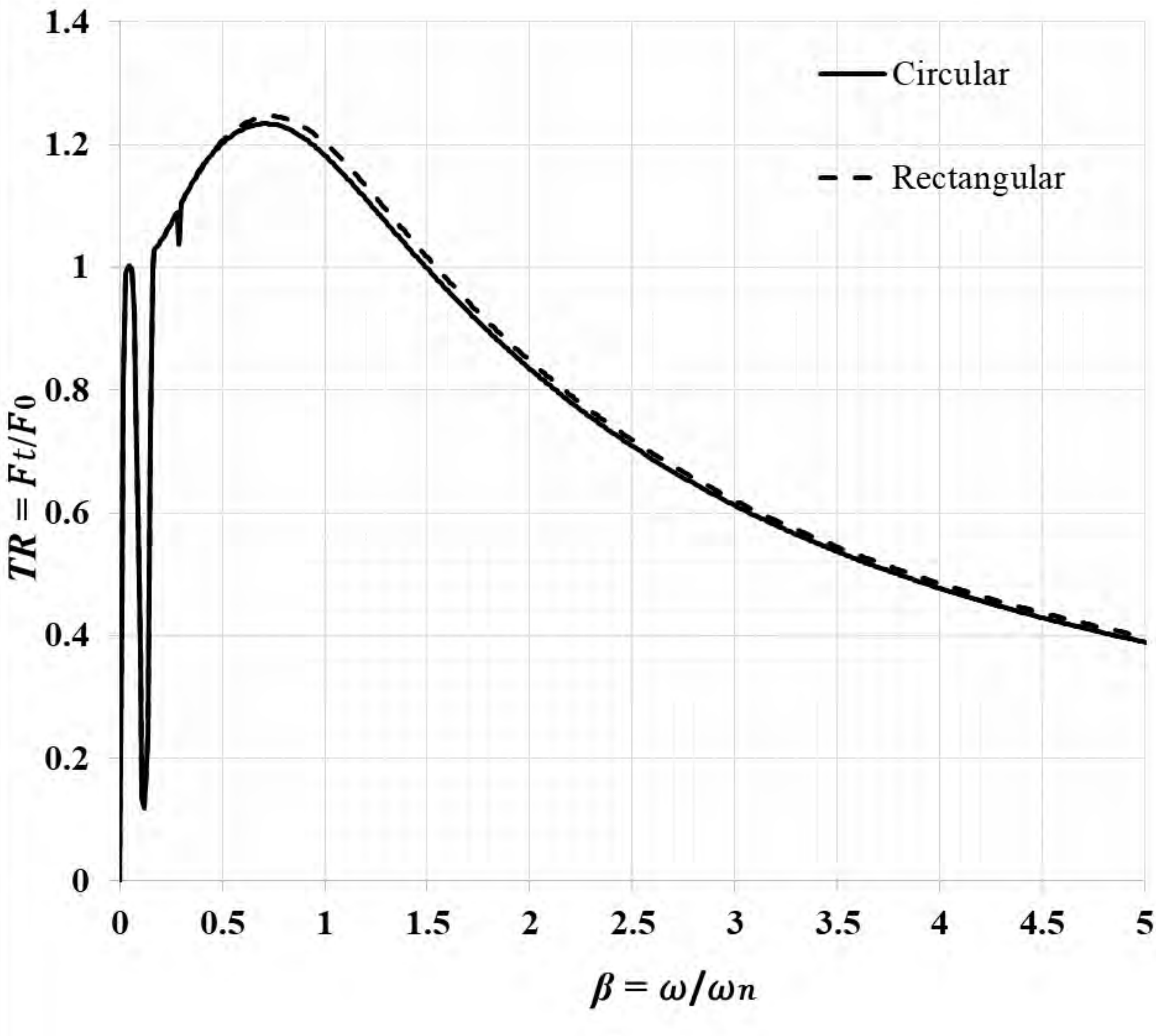

Figure 4.14.2.19: Steady-state TR vs speed ratio (β) for damping ratio $\zeta = 1$ for superelastic SMA circular and equivalent rectangular beam (APPENDIX-C) considering material non-linearity and geo-metric non-linearity with end-shortening.

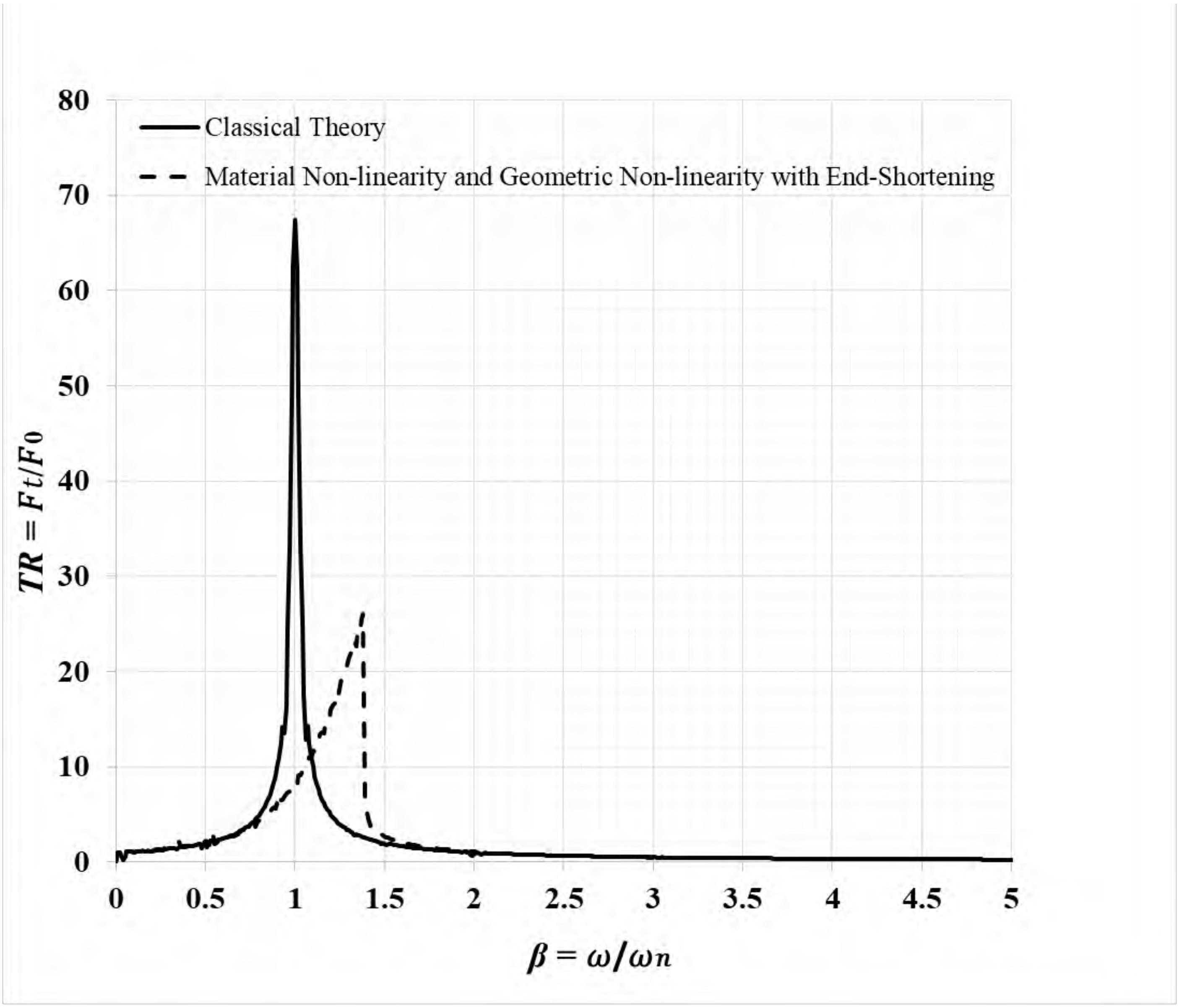

Figure 4.14.3.1: Steady-state TR vs speed ratio (β) when undamped (slenderness ratio, $\frac{L}{r}$ = 100).

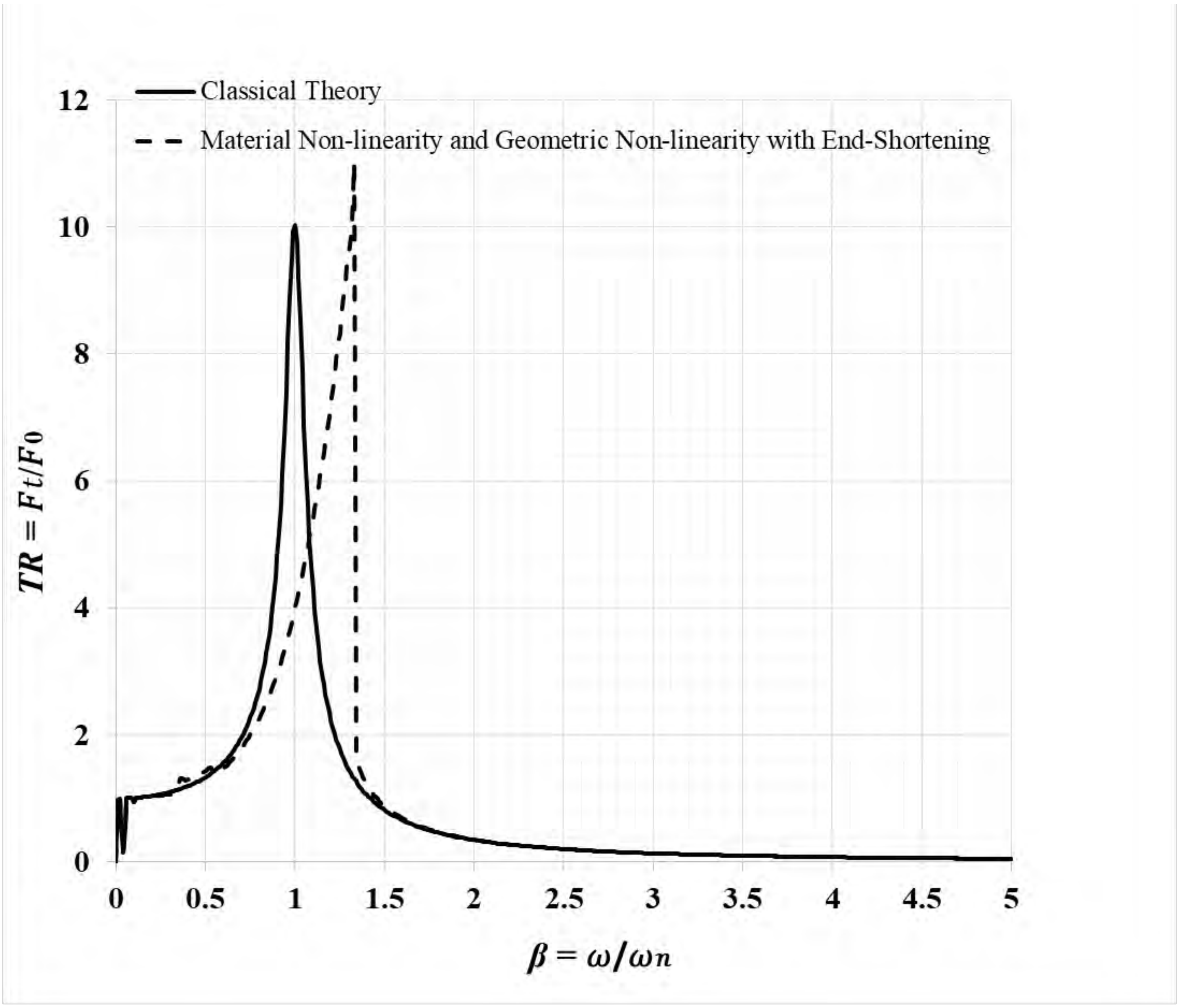

Figure 4.14.3.2: Steady-state TR vs speed ratio (β) for damping ratio ζ = 0.05 (slenderness ratio, $\frac{L}{r}$ = 100).

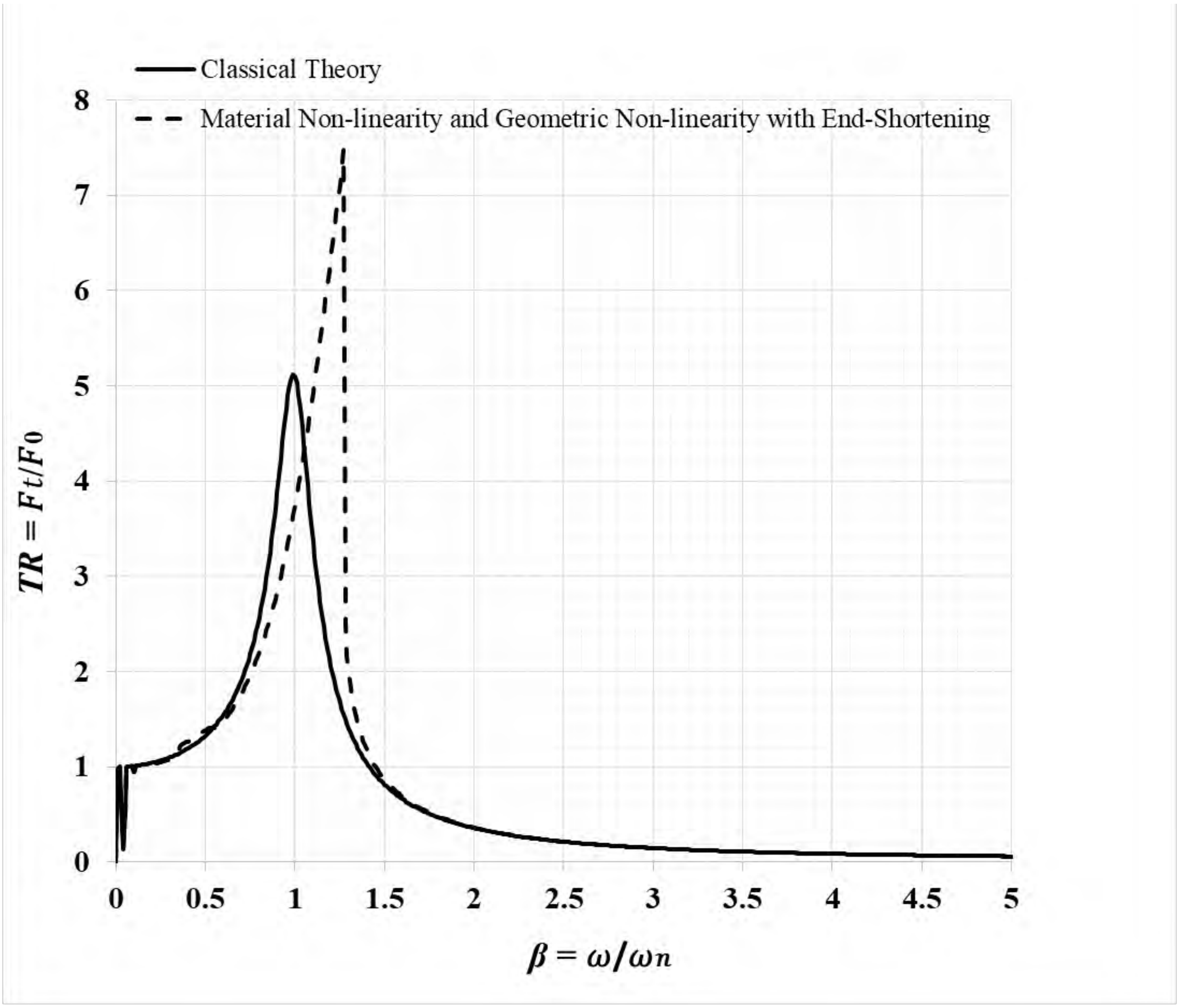

Figure 4.14.3.3: Steady-state TR vs speed ratio (β) for damping ratio $\zeta = 0.1$ (slenderness ratio, $\frac{L}{r} = 100$).

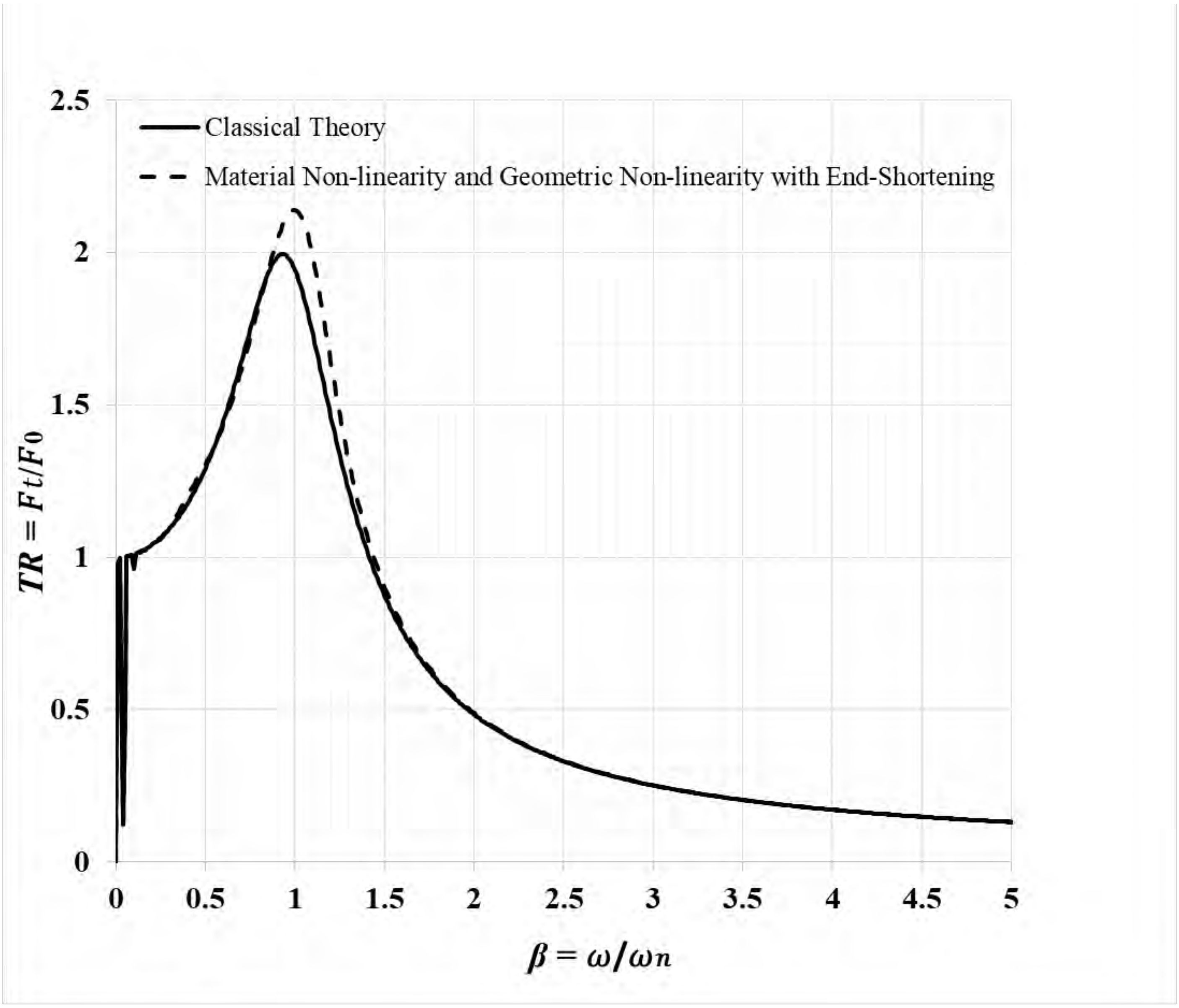

Figure 4.14.3.4: Steady-state TR vs speed ratio (β) for damping ratio $\zeta = 0.3$ (slenderness ratio, $\frac{L}{r} = 100$).

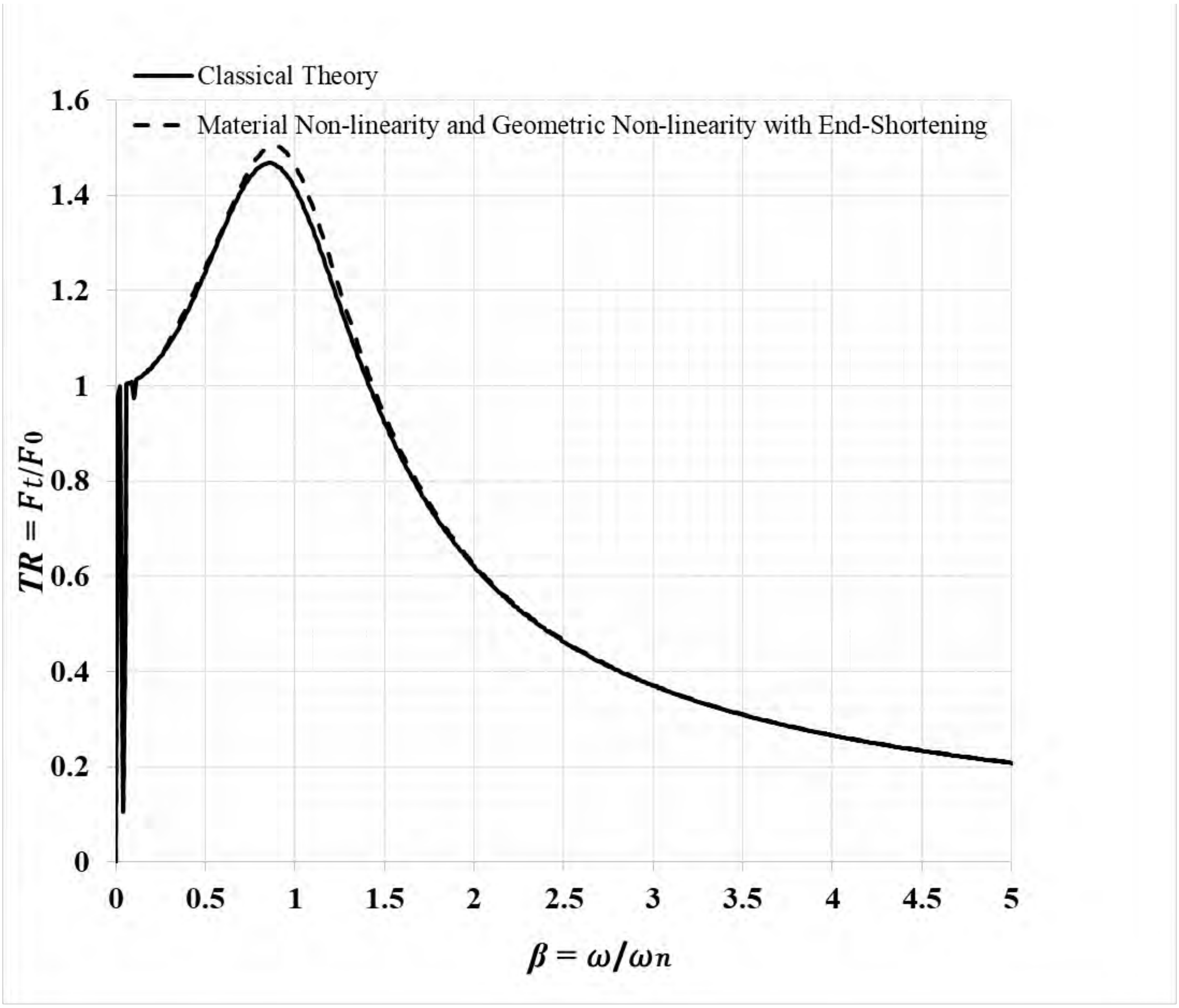

Figure 4.14.3.5: Steady-state TR vs speed ratio (β) for damping ratio ζ = 0.5 (slenderness ratio, $\frac{L}{r}$ = 100).

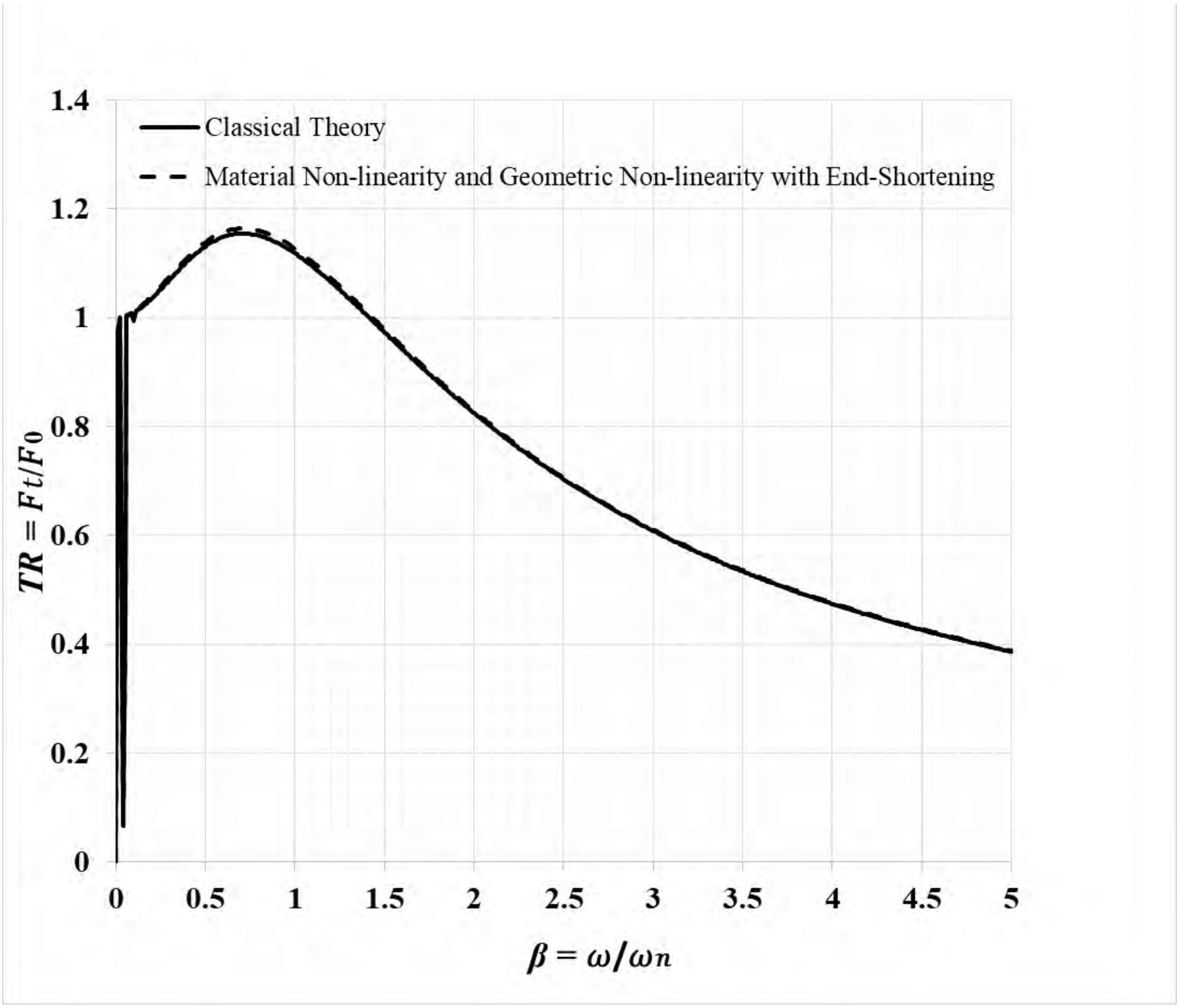

Figure 4.14.3.6: Steady-state TR vs speed ratio (β) for damping ratio ζ = 1 (slenderness ratio, $\frac{L}{r}$ = 100).

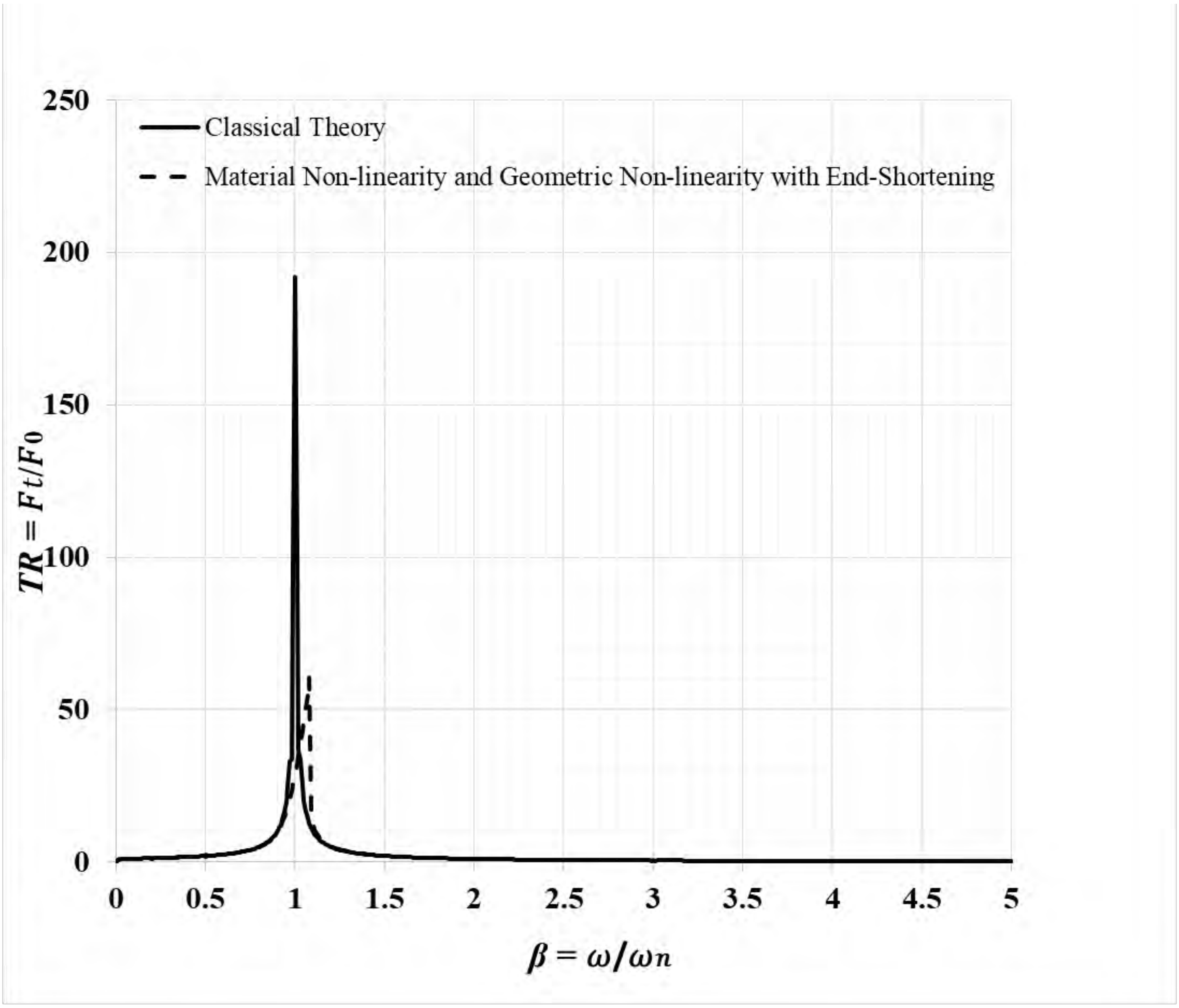

Figure 4.14.4.1: Steady-state TR vs speed ratio (β) when undamped (slenderness ratio, $\frac{L}{r}$ = 50).

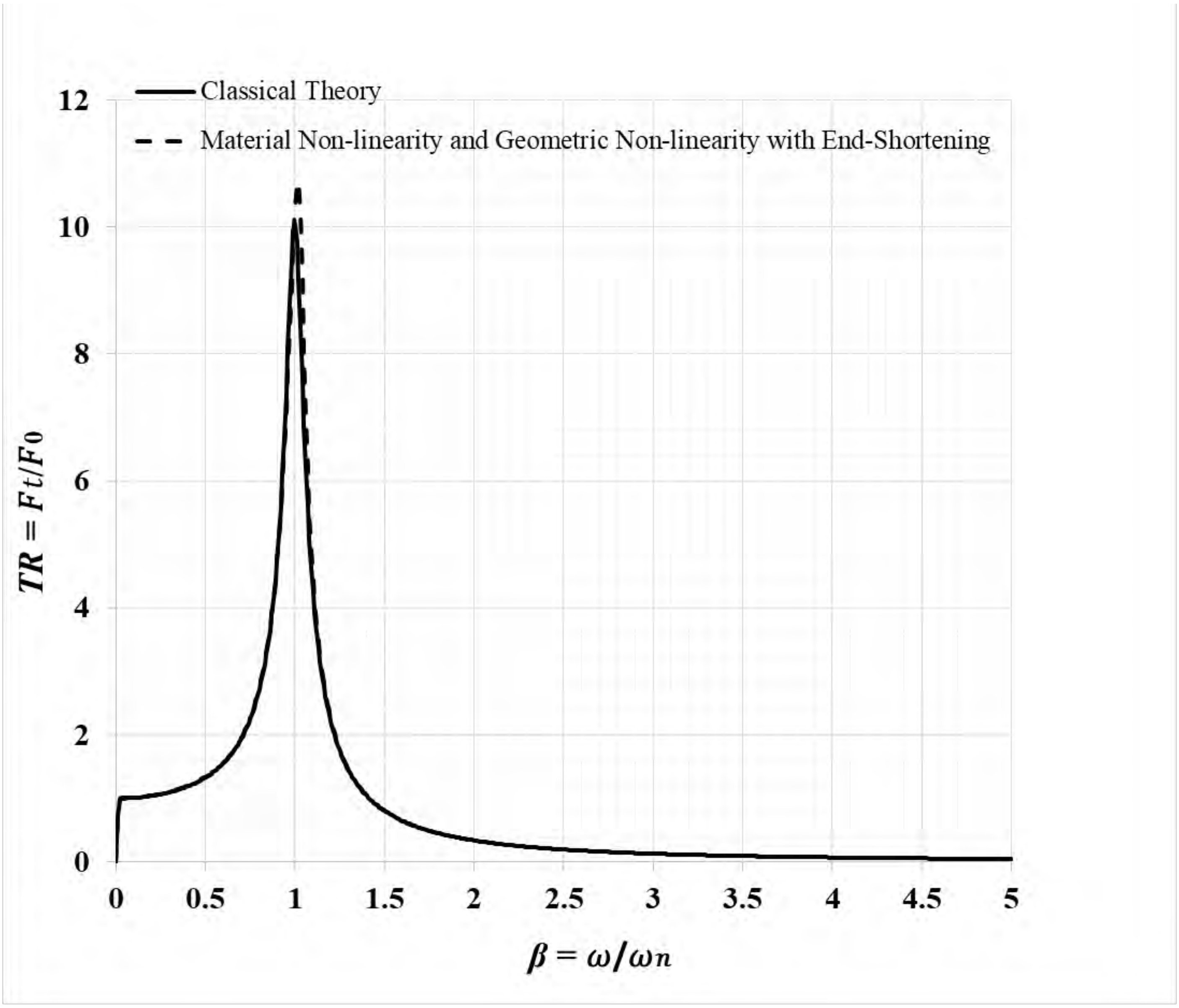

Figure 4.14.4.2: Steady-state TR vs speed ratio (β) for damping ratio $\zeta = 0.05$ (slenderness ratio, $\frac{L}{r} = 50$).

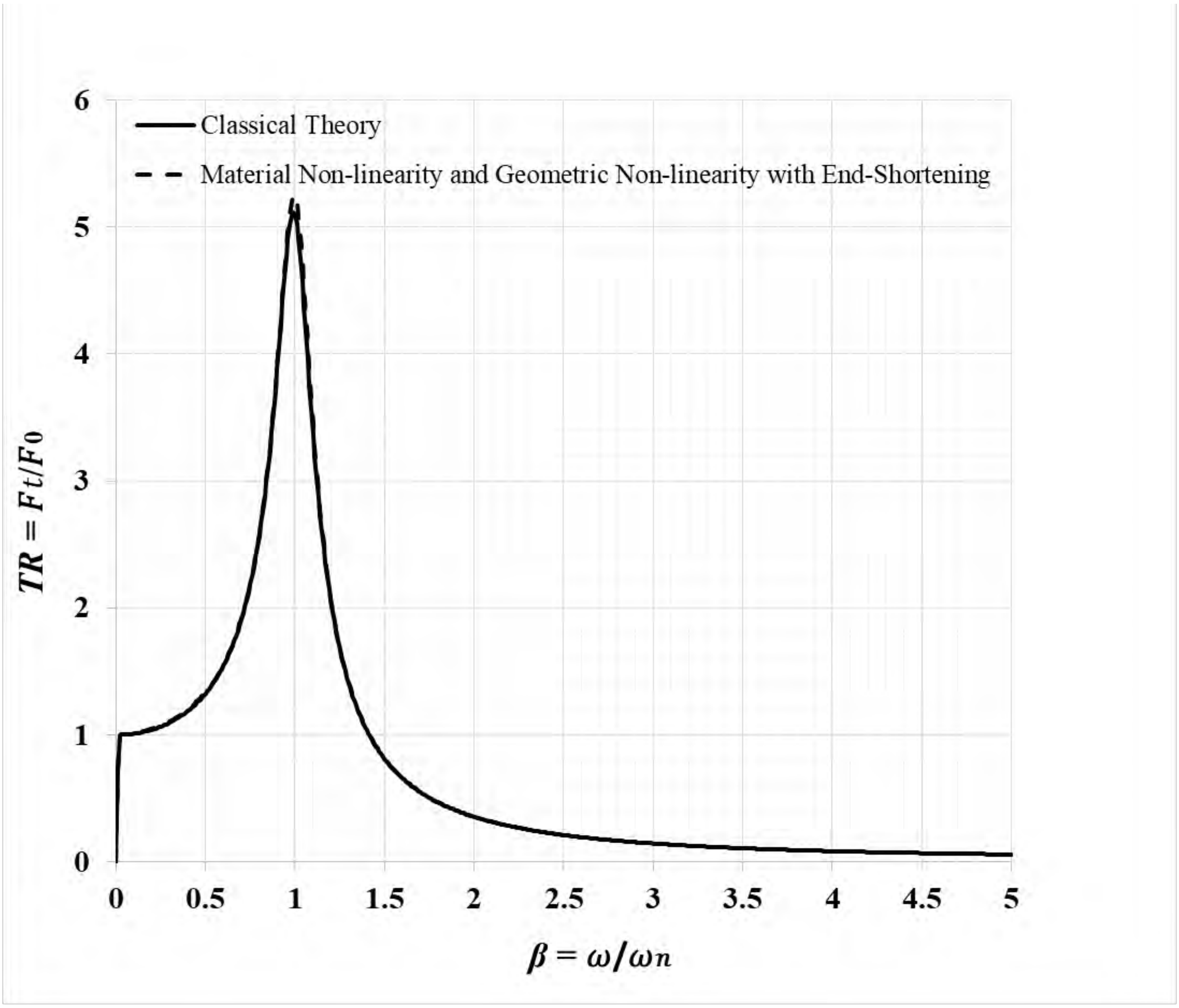

Figure 4.14.4.3: Steady-state TR vs speed ratio (β) for damping ratio $\zeta = 0.1$ (slenderness ratio, $\frac{L}{r} = 50$).

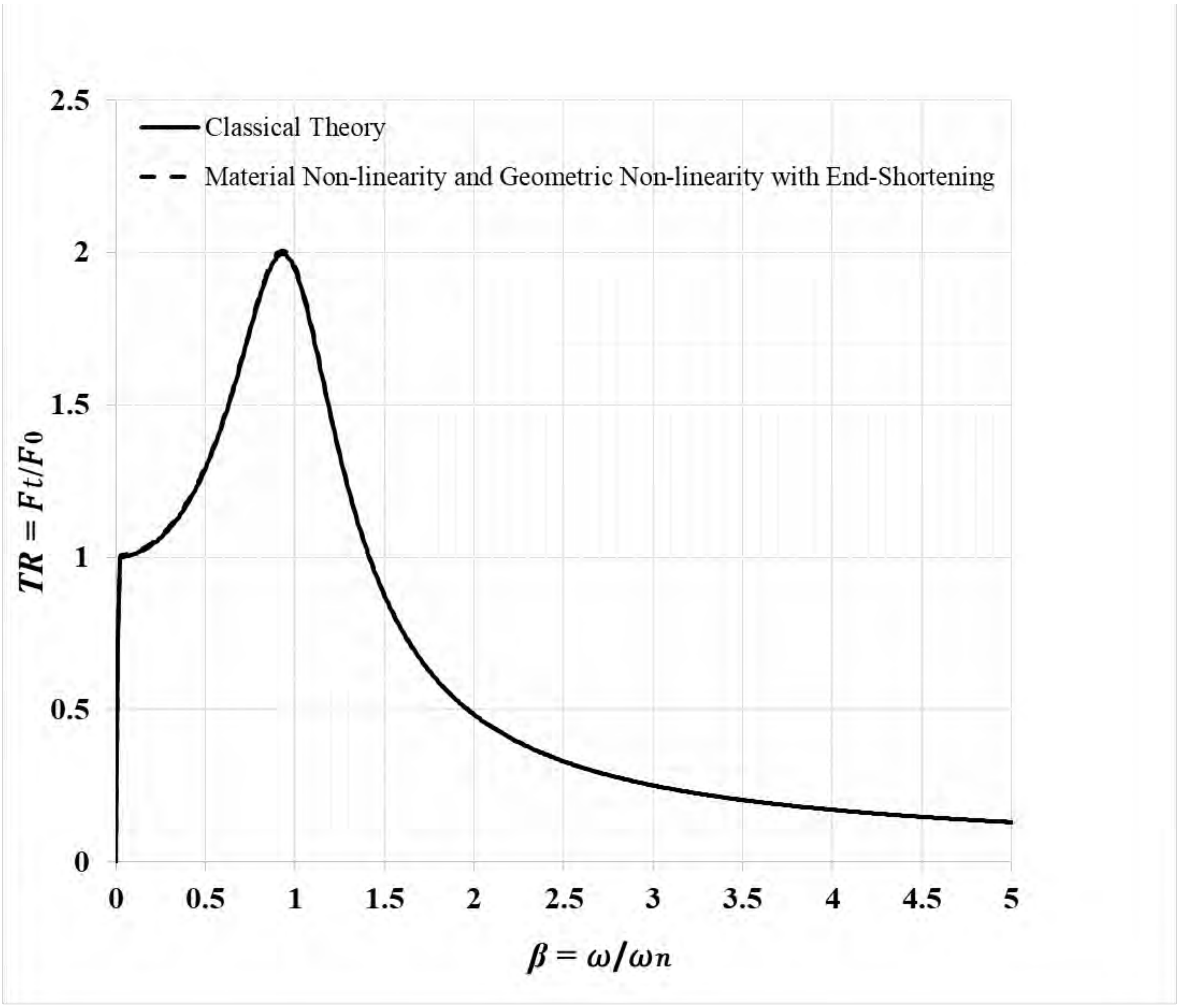

Figure 4.14.4.4: Steady-state TR vs speed ratio (β) for damping ratio $\zeta = 0.3$ (slenderness ratio, $\frac{L}{r} = 50$).

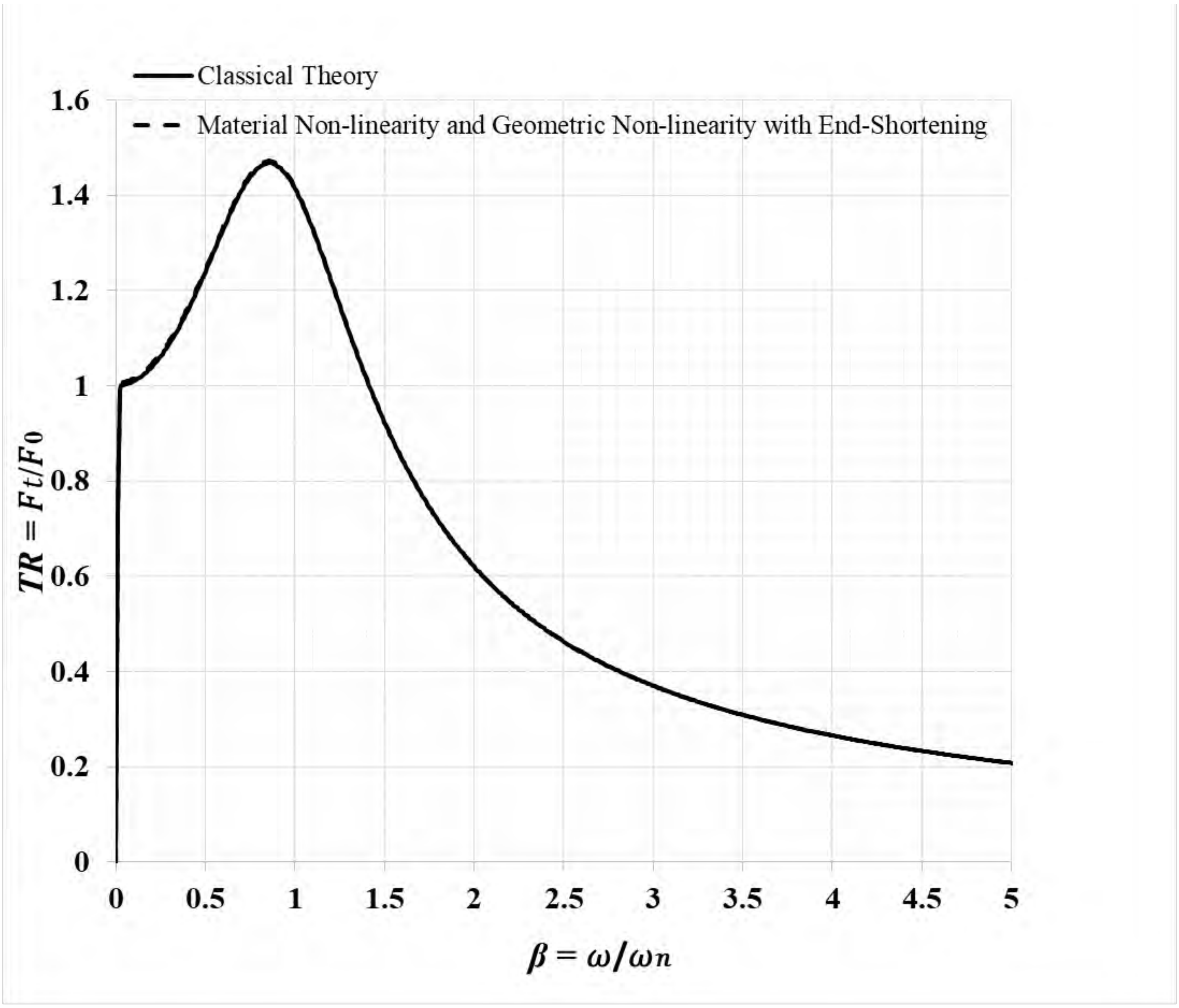

Figure 4.14.4.5: Steady-state TR vs speed ratio (β) for damping ratio $\zeta = 0.5$ (slenderness ratio, $\frac{L}{r} = 50$).

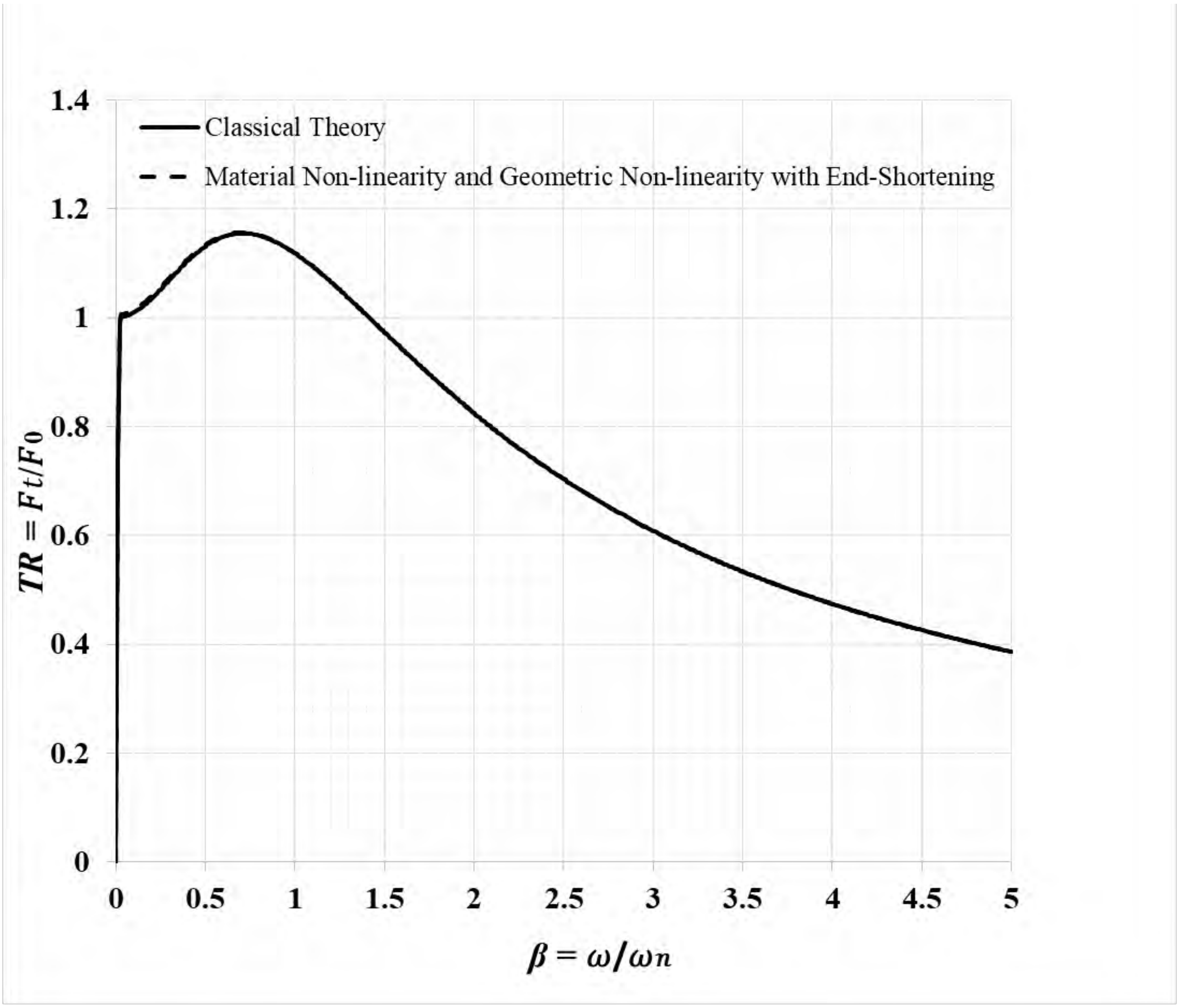

Figure 4.14.4.6: Steady-state TR vs speed ratio (β) for damping ratio $\zeta = 1$ (slenderness ratio, $\frac{L}{r} = 50$).

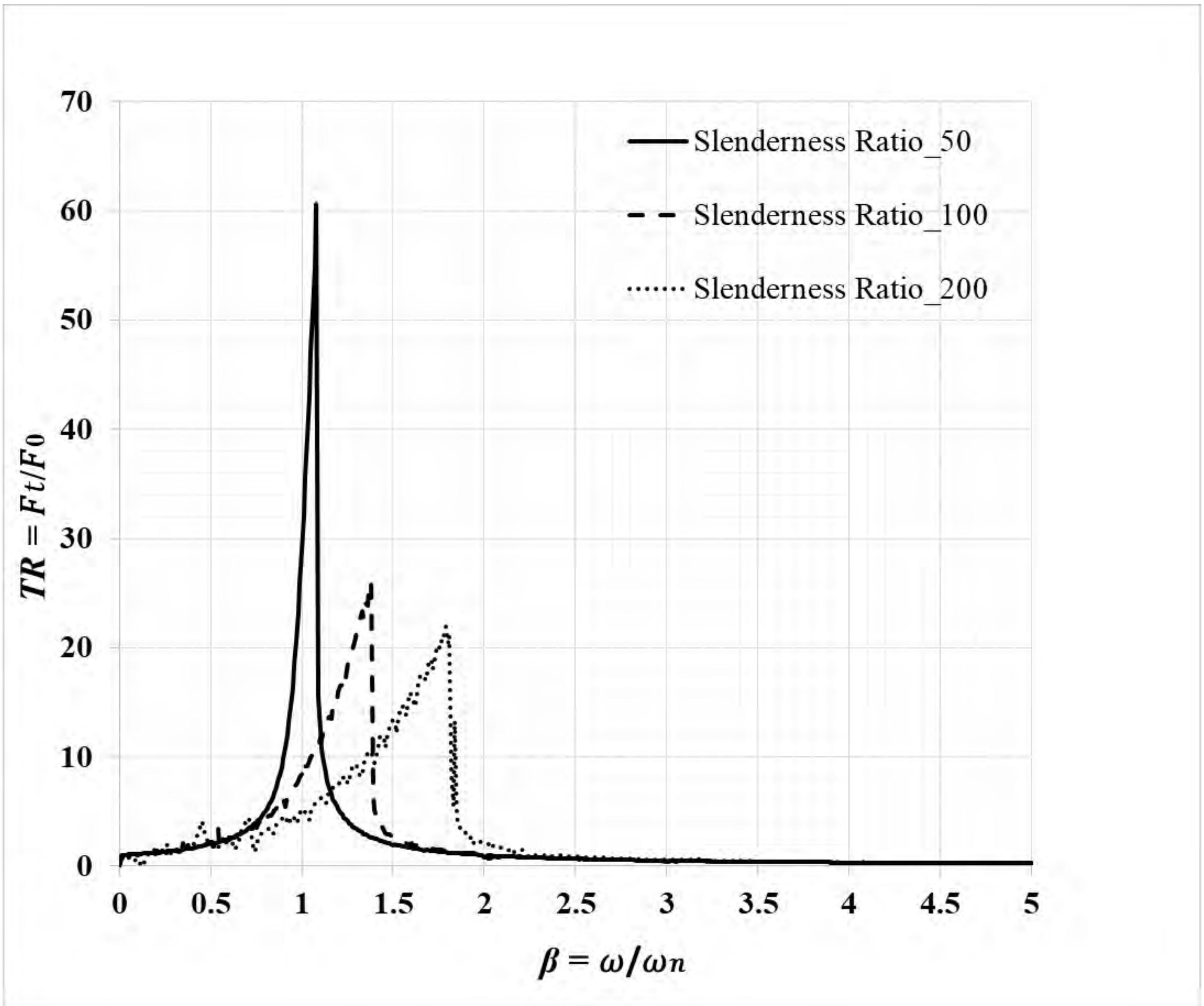

Figure 4.14.5.1: Steady-state TR vs speed ratio (β) when undamped considering material non-linearity and geometric non-linearity with end-shortening.

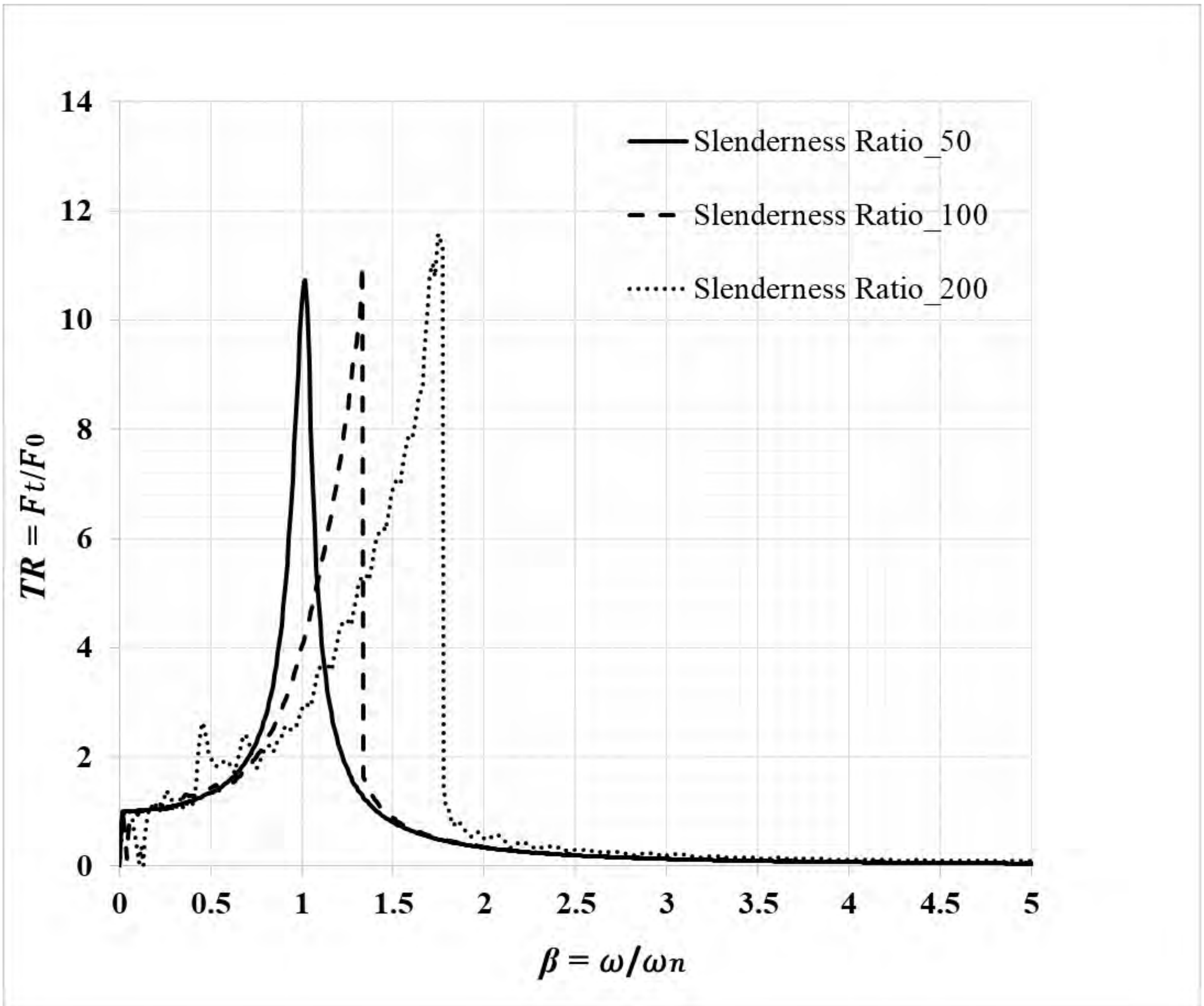

Figure 4.14.5.2: Steady-state TR vs speed ratio (β) for damping ratio, $\zeta = 0.05$ considering material non-linearity and geometric non-linearity with end-shortening.

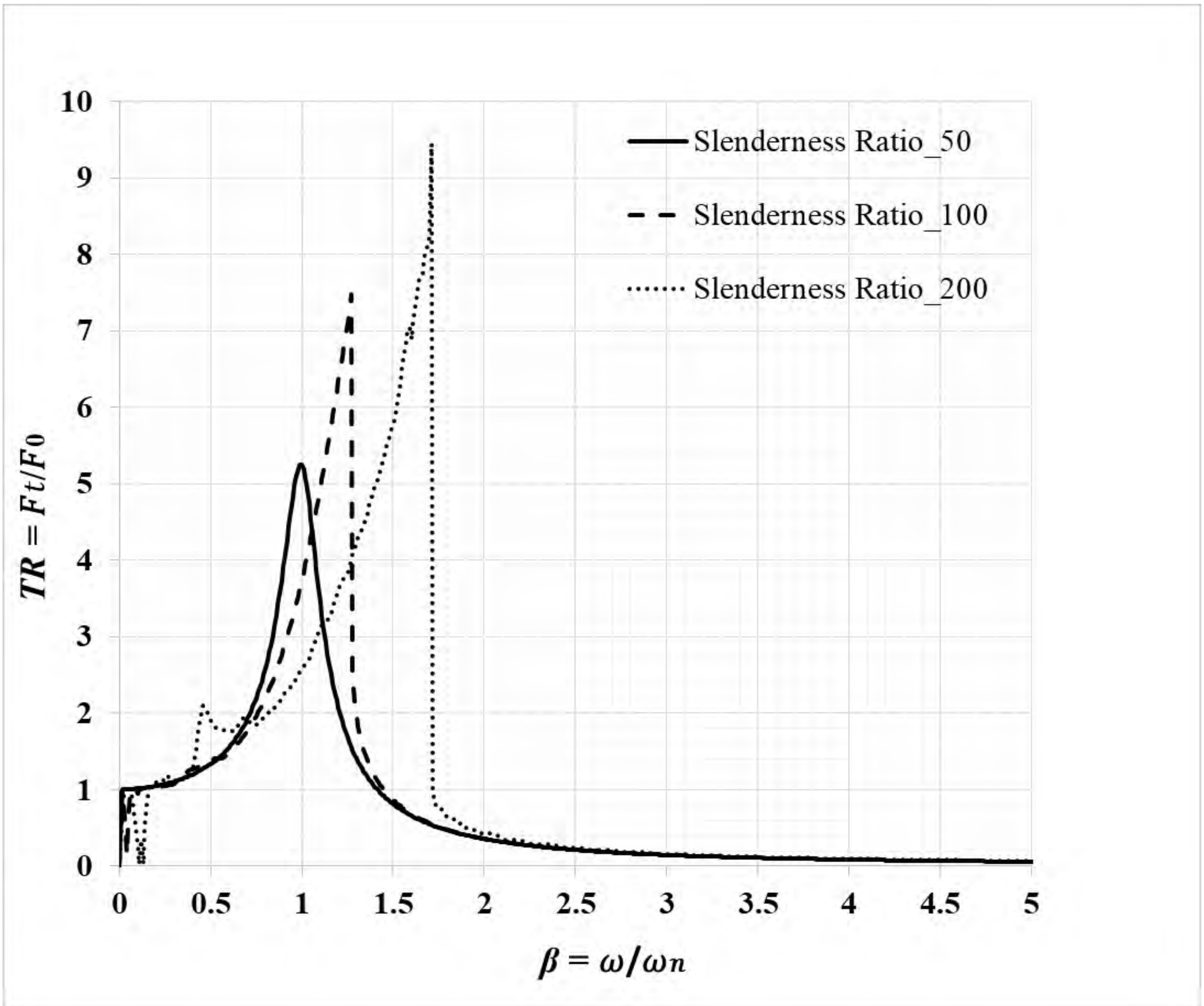

Figure 4.14.5.3: Steady-state TR vs speed ratio (β) for damping ratio, $\zeta = 0.1$ considering material non-linearity and geometric non-linearity with end-shortening.

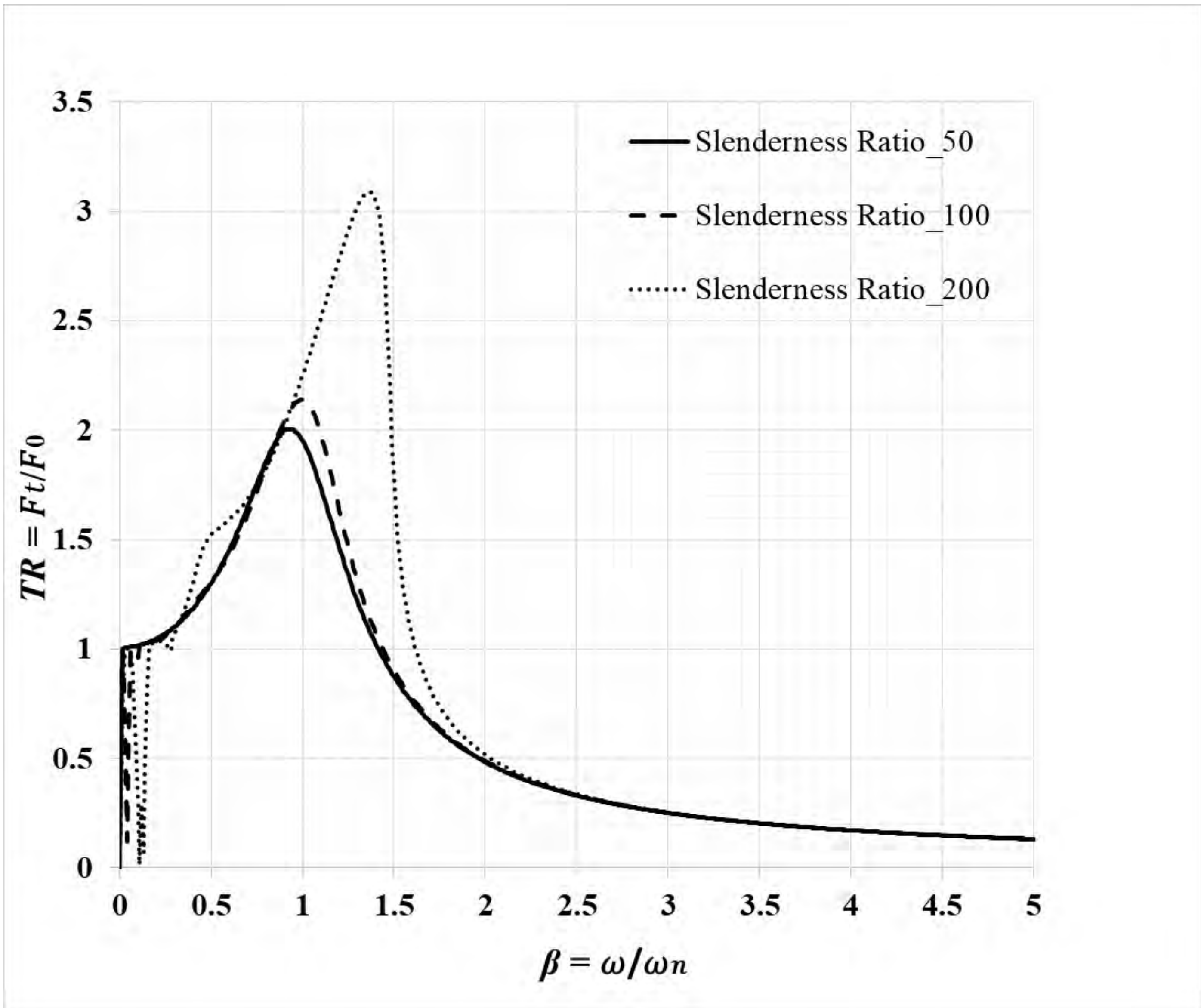

Figure 4.14.5.4: Steady-state TR vs speed ratio (β) for damping ratio, $\zeta = 0.3$ considering material non-linearity and geometric non-linearity with end-shortening.

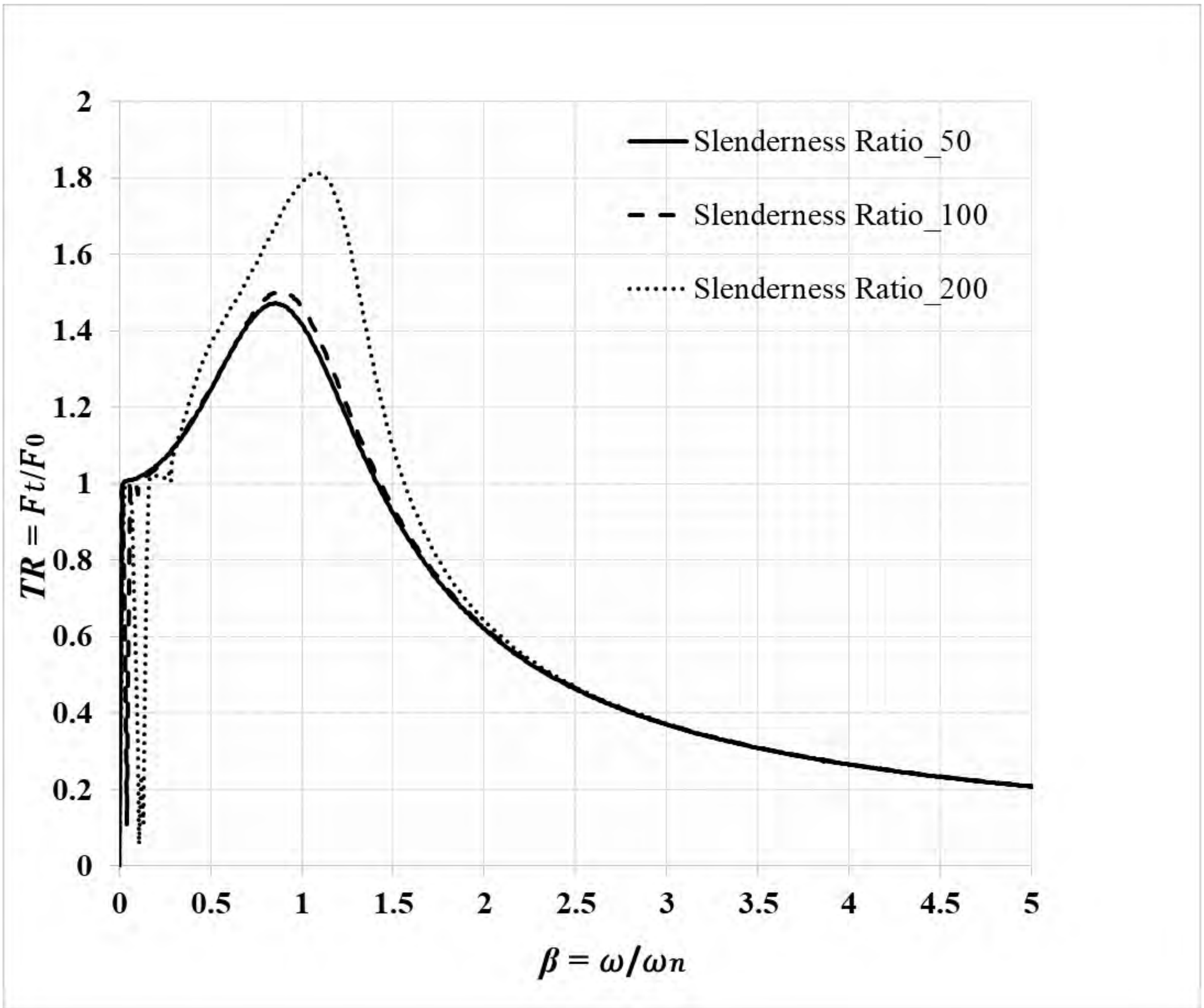

Figure 4.14.5.5: Steady-state TR vs speed ratio (β) for damping ratio, $\zeta = 0.5$ considering material non-linearity and geometric non-linearity with end-shortening.

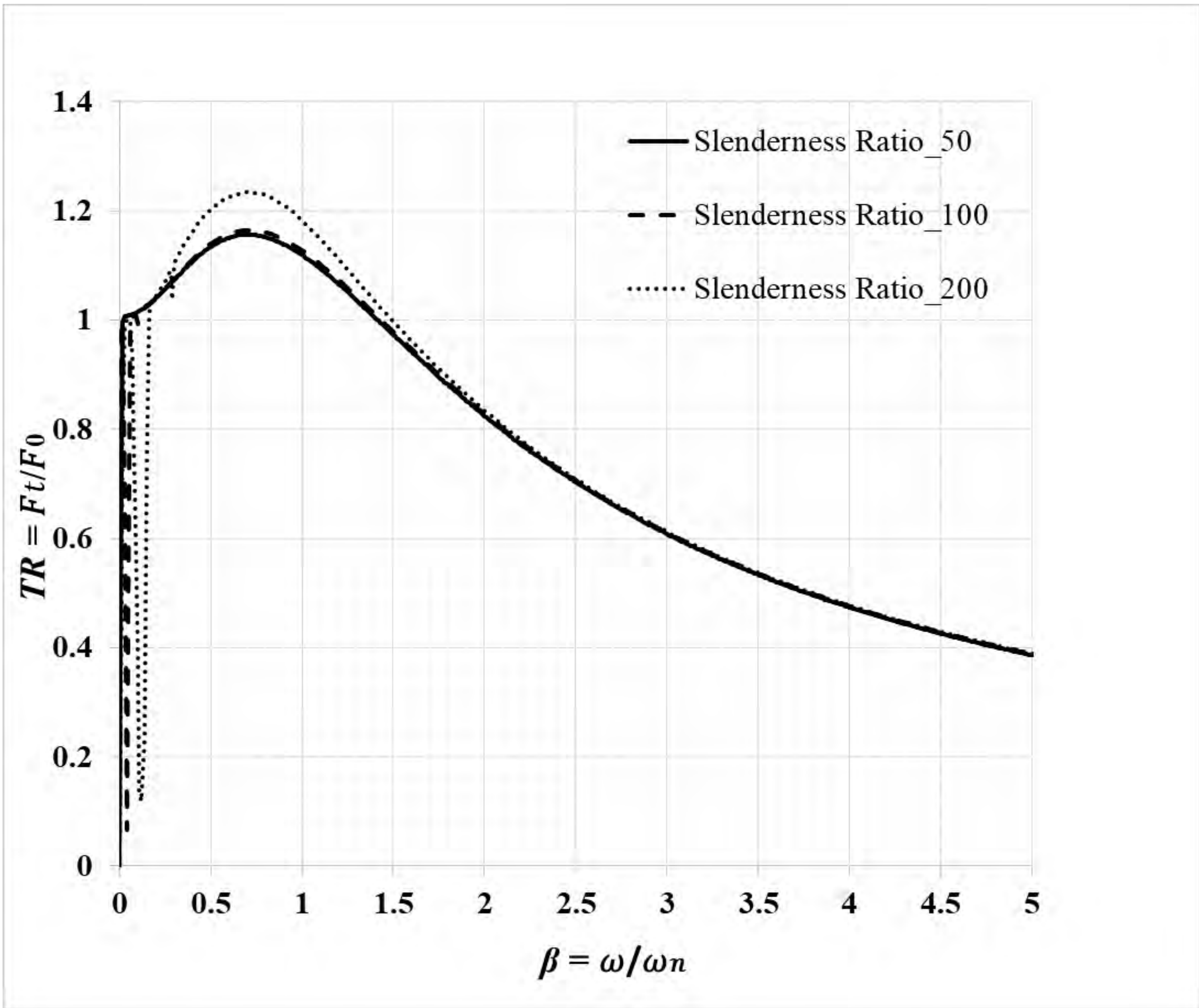

Figure 4.14.5.6: Steady-state TR vs speed ratio (β) for damping ratio, $\zeta = 1$ considering material non-linearity and geometric non-linearity with end-shortening.

APPENDIX - A

3.5: Numerical Analysis: Runge-Kutta 4th Order Method of Numerical Integration to Solve Second Order Differential Equation

The Runge-Kutta solution technique is briefly described below, as it is one of the tools of the present analysis. In this solution technique for any first order differential equation, the unknowns y_1, y_2 etcetera are successively evaluated at each grid point starting from the initial boundary as described below.

$$\frac{dy}{dx} = f(x, y)$$

$$y_{a+h} = y_a + \frac{1}{6}(k_1 + 2k_2 + 2k_3 + k_4)h$$

Where,

$$k_1 = hf(a, y_a)$$

$$k_2 = hf(a + \frac{h}{2}, y_a + \frac{k_1}{2})$$

$$k_3 = hf(a + \frac{h}{2}, y_a + \frac{k_2}{2})$$

$$k_4 = hf(a + h, y_a + k_3)$$

For an m^{th} order ordinary differential equation (ODE), it is first reduced to m number of first order ODE. Then the variables are evaluated as described below.

$$\begin{bmatrix} y_1 \\ y_1 \\ , \\ , \\ y_m \end{bmatrix}_{\boldsymbol{a+h}} = \begin{bmatrix} y_1 \\ y_1 \\ , \\ , \\ y_m \end{bmatrix}_{\boldsymbol{a}} + \frac{1}{6}\left[\begin{pmatrix} k_{11} \\ k_{12} \\ , \\ , \\ k_{1m} \end{pmatrix} + 2\begin{pmatrix} k_{21} \\ k_{22} \\ , \\ , \\ k_{2m} \end{pmatrix} + 2\begin{pmatrix} k_{31} \\ k_{32} \\ , \\ , \\ k_{3m} \end{pmatrix} + \begin{pmatrix} k_{41} \\ k_{42} \\ , \\ , \\ k_{4m} \end{pmatrix}\right]$$

Where, $$\begin{bmatrix} k_{11} \\ k_{12} \\ , \\ , \\ k_{1m} \end{bmatrix} = h \begin{bmatrix} f_1(a, y_{1a}, y_{2a}, , , , , y_{ma}) \\ f_2(a, y_{1a}, y_{2a}, , , , , y_{ma}) \\ , \\ , \\ f_m(a, y_{1a}, y_{2a}, , , , , y_{ma}) \end{bmatrix}$$

$$\begin{bmatrix} k_{21} \\ k_{22} \\ , \\ , \\ k_{2m} \end{bmatrix} = h \begin{bmatrix} f_1((a + \frac{h}{2}), (y_{1a} + \frac{k_{11}}{2}), (y_{2a} + \frac{k_{12}}{2}), , , , , (y_{ma} + \frac{k_{1m}}{2})) \\ f_2((a + \frac{h}{2}), (y_{1a} + \frac{k_{11}}{2}), (y_{2a} + \frac{k_{12}}{2}), , , , , (y_{ma} + \frac{k_{1m}}{2})) \\ , \\ , \\ f_m((a + \frac{h}{2}), (y_{1a} + \frac{k_{11}}{2}), (y_{2a} + \frac{k_{12}}{2}), , , , , (y_{ma} + \frac{k_{1m}}{2})) \end{bmatrix}$$

$$\begin{bmatrix} k_{31} \\ k_{32} \\ , \\ , \\ k_{3m} \end{bmatrix} = h \begin{bmatrix} f_1((a + \frac{h}{2}), (y_{1a} + \frac{k_{21}}{2}), (y_{2a} + \frac{k_{22}}{2}), , , , , (y_{ma} + \frac{k_{2m}}{2})) \\ f_2((a + \frac{h}{2}), (y_{1a} + \frac{k_{21}}{2}), (y_{2a} + \frac{k_{22}}{2}), , , , , (y_{ma} + \frac{k_{2m}}{2})) \\ , \\ , \\ f_m((a + \frac{h}{2}), (y_{1a} + \frac{k_{21}}{2}), (y_{2a} + \frac{k_{22}}{2}), , , , , (y_{ma} + \frac{k_{2m}}{2})) \end{bmatrix}$$

$$\begin{bmatrix} k_{41} \\ k_{42} \\ , \\ , \\ k_{4m} \end{bmatrix} = h \begin{bmatrix} f_1((a + h), (y_{1a} + k_{31}), (y_{2a} + k_{32}), , , , , (y_{ma} + k_{3m})) \\ f_2((a + h), (y_{1a} + k_{31}), (y_{2a} + k_{32}), , , , , (y_{ma} + k_{3m})) \\ , \\ , \\ f_m((a + h), (y_{1a} + k_{31}), (y_{2a} + k_{32}), , , , , (y_{ma} + k_{3m})) \end{bmatrix}$$

APPENDIX - B

3.6.2 Cantilever Beam of Equivalent Rectangular Cross-Section

For materials having non-linear stress-strain relations Timoshenko [16] derived the $M - \Delta$ and $E_r - \Delta$ relations for a rectangular beam section. He first defined the term reduced modulus, E_r for inelastic bending of beams.

Following Timoshenko [16], it is assumed that the cross-section of the beam remains plane during pure bending; hence elongations and contractions of longitudinal fibers are proportional to their distances from the neutral surface. Further assuming that during bending there exists the same relation between stress and strain as in the case of simple tension and compression, the stresses produced can be found out by a bending moment of a given magnitude. Considering the beam of rectangular cross-section in Figures 3.6.1.1 & 3.6.2.1, it is assumed that the radius of curvature of the neutral surface produced by the moments M is equal to ρ. In such a case the unit elongation of a fiber at a distance y from the neutral surface is

$$\varepsilon = \frac{y}{\rho} \quad \text{.....(3.6.2.1)}$$

Denoting h_1 and h_2 (Figure 3.6.2.1) the distances from the lower and the upper surfaces of the beam respectively to the neutral axis, we find that the elongation in the outermost fibers are

$$\varepsilon_1 = \frac{h_1}{\rho}, \varepsilon_2 = -\frac{h_2}{\rho} \quad \text{.....(3.6.2.2)}$$

It is seen that the elongation or contraction of any fiber is readily obtained provided we know the position of the neutral axis, say ratio $\frac{h_1}{h_2}$, and the radius of curvature ρ. These two quantities can be found from the two equations of static equilibrium:

$$\int \sigma dA = \int_{-h_2}^{h_1} \sigma dA = 0 \quad \text{.....(3.6.2.3)}$$

$$\int \sigma y dA = \int_{-h_2}^{h_1} \sigma y dy = M \quad \text{.....(3.6.2.4)}$$

The first of these equations states that the sum of normal forces acting on a cross-section of the beam vanishes, since those forces represent a couple. The second equation states that the moment of the same forces with respect to the neutral axis is equal to the bending moment *M*.

Equation (3.6.2.3) is now used for determining the position of the neutral axis. For finding the area *dA* at first (Figure 3.6.2.1), we consider equation of the rectangle

Here, $dA = bdy$ ……………………….…………..………...…...(3.6.2.5)

Now, employing dA in equation (3.6.2.3), we get

$$\int \sigma dA = b \int_{-h_2}^{h_1} \sigma \ dy = 0 \qquad (3.6.2.6)$$

From equation (3.6.1)

$$y = \rho \mathcal{E} \qquad (3.6.2.7)$$

$$dy = \rho d\mathcal{E} \qquad (3.6.2.8)$$

Therefore, equation (3.6.2.5) becomes

$$dA = b\rho d\mathcal{E} \qquad (3.6.2.9)$$

Employing equation (3.6.2.9) in (3.6.2.3), we get,

$$\int \sigma dA = b \int_{-h_2}^{h_1} \sigma \, dy = b\rho \int_{\varepsilon_2}^{\varepsilon_1} \sigma \, d\varepsilon = 0 \qquad (3.6.2.10)$$

Hence the position of the neutral axis is such that the integral $\int_{\varepsilon_2}^{\varepsilon_1} \sigma \, d\varepsilon$ vanishes.

Therefore, $\int_{\varepsilon_2}^{\varepsilon_1} \sigma \, d\varepsilon = 0$……………………………………………(3.6.2.11)

Equation (3.6.2.11) is rewritten as

$$\int_{\varepsilon_2}^{0} \sigma \, d\varepsilon = \int_{0}^{\varepsilon_1} \sigma \, d\varepsilon \quad \text{...(3.6.2.12)}$$

Integral on the left hand side of the equation (3.6.2.12) represents normal forces acting on the compression region of the beam and right hand side of the equation represents normal forces acting on the tension region of the beam.

To determine the neutral axis position, we use the curve AOB (Figure 3.6.1.3a) which represents the ($\sigma - \varepsilon$) diagrams in tension and compression for the material of the beam, and we denote Δ, the sum of the absolute values of the maximum elongation and the maximum contraction, which is

$$\Delta = |\varepsilon_1| + |\varepsilon_2| = \left|\frac{h_1}{\rho}\right| + \left|\frac{h_2}{\rho}\right| = \frac{h}{\rho} \quad \text{..............................(3.6.2.13)}$$

$$\rho = \frac{h}{\Delta} \quad \text{...(3.6.2.14)}$$

$$\rho = \frac{h}{|\varepsilon_1| + |\varepsilon_2|} \quad \text{...(3.6.2.15)}$$

Since, integral of equation (3.6.2.11) has no closed form solution, numerical solution technique has been used. As stress-strain curve of superelastic SMA is asymmetric in tension and compression beyond proportional limit,

Therefore, $|\varepsilon_1| \neq |\varepsilon_2|$

Therefore, from the stress-strain curve $|\varepsilon_2|$ is chosen. And for any chosen values of $|\varepsilon_2|$, by applying numerical integration method, $|\varepsilon_1|$ is found out which can make the integral zero. In this manner we obtain strain ε_2 and ε_1 in the outermost fibers; Equation 3.5.2 then gives

$$\frac{h_1}{h_2} = \left|\frac{\varepsilon_1}{\varepsilon_2}\right| \quad \text{...(3.6.2.16)}$$

This determines the position of neutral axis. Observing that elongations ε are proportional to the distance from the neutral axis, we conclude that the curve AOB (Figure 3.6.1.3a) also represents the distribution of bending stresses along the depth of the beam, if h is substituted for Δ.

Therefore, the equation of moment at any of the point on the beam is,

$$M = \int \sigma y dA = b\rho^2 \int_{\varepsilon_2}^{\varepsilon_1} \sigma \varepsilon \, d\mathcal{E} \quad \text{……………………………..…(3.6.2.17)}$$

Applying numerical integration method to equation (3.6.2.17), moments are known. Value of stress in equation (3.6.2.17) is taken from corresponding value of strain from stress-strain curve.

If the stress-strain curve is known for a specific material, then considering the value of strain (piece-wise linear) from the diagram, value of corresponding stress can be found out.

Equation of straight line for $(x - y)$ coordinate,

$$y = vx + z \quad \text{……………..…..(3.6.2.18)}$$

Here, v is the gradient of the straight line.
Similarly for $(\sigma - \varepsilon)$ curve,

$$\sigma_{i+1} = v\mathcal{E}_{i+1} + \sigma_i \quad \text{....……………………..(3.6.2.19)}$$

Equations (3.6.2.17) and (3.6.2.19) give,

$$M = b\rho^2 \int_{\mathcal{E}_2}^{\mathcal{E}_1} [(v\mathcal{E}_{i+1} + \sigma_i)] \, \mathcal{E} d\mathcal{E} \quad \text{…………………………..…..(3.6.2.20)}$$

Incorporating moment of inertia (I) in Equation (3.6.2.20), we get,

$$M = \frac{I}{\rho} \times \frac{12}{\Delta^3} \int_{\mathcal{E}_2}^{\mathcal{E}_1} [(v\mathcal{E}_{i+1} + \sigma_i)] \mathcal{E} \, d\mathcal{E} \quad \text{…………………………………..………(3.6.2.21)}$$

Let, moment of inertia,

$$I = \frac{\pi d^4}{64} \quad \ldots\ldots\ldots\ldots\ldots\ldots\ldots\ldots\ldots\ldots\ldots\ldots\ldots\ldots\ldots (3.6.2.22)$$

Linear moment-curvature relation,

$$M = \frac{EI}{\rho} \ldots\ldots\ldots\ldots\ldots\ldots\ldots\ldots\ldots\ldots\ldots\ldots\ldots\ldots (3.6.23)$$

If equations (3.6.21) and (3.6.23) are compared, then for bending of beam following , we conclude that beyond the proportional limit, the curvature produced by a moment *M* can be calculated from the equation,

$$M = \frac{E_r I}{\rho} \ldots\ldots\ldots\ldots\ldots\ldots\ldots\ldots\ldots\ldots\ldots\ldots\ldots\ldots (3.6.24)$$

Here E_r is the reduced modulus. Now comparing equations (3.6.21) and (3.5.24), the value of E_r (reduced value) can be obtained as follows.

$$E_r = \frac{12}{\Delta^3} \int_{\varepsilon_2}^{\varepsilon_1} [(v + \sigma_i)] \varepsilon \, d\varepsilon \ldots\ldots\ldots\ldots\ldots\ldots\ldots\ldots\ldots\ldots\ldots (3.6.25)$$

The integral in this expression represents the moment with respect to the vertical (σ) axis through the origin *O* of the shaded area shown in Figure 3.6.1.3a. Since the ordinate of the curve in the figure represents stresses, and the abscissas, strain, the integral and also E_r have the dimension of GPa, i.e., the same dimension as the modulus *E*. The magnitude of E_r for a given material is a function of Δ or of h/ρ. Taking several values of Δ and using each time the curve in Figure 3.6.1.3a as was previously explained, we determine for each value of Δ the corresponding outermost elongations ε_1 and ε_2, and from equation (3.6.25) the corresponding value of E_r as a function of ($\Delta = h/\rho$) is obtained.

Equations (3.6.20) and (3.6.25) can be solved by applying numerical method to obtain values of bending moment and reduced modulus for different values of Δ.

From the actual true stress-strain diagram (Figure 3.6.1.3b) random values of strain ε_2 from the compression region is chosen like that from Figure 3.6.1.3a and by using equation (3.6.21) and by applying trial and error method, values of strain ε_1 at tension region is found out for which result of the integral of equation (3.6.11) becomes zero each time. This determines the position of neutral axis and, value of total strain Δ as well. Numerical method used to solve this problem in Matlab.

Using values of ε_1 and ε_2 in equation (3.6.2.13), value of Δ and corresponding ρ is found out from equation (3.6.2.14) as well. Now, taking several values of Δ and using equations (3.6.2.20) and (3.6.2.25), values of corresponding bending moment and reduced modulus are obtained. Again numerical method is used in Matlab to solve equations (3.6.2.20) and (3.6.2.25). Finally, Figures of $E_r - \Delta$ and M –   are obtained for superelastic SMA beam.

APPENDIX - C

Calculations of Circular Beam and Equivalent Rectangular Cross-section

Circular Beam: Beam length (L) = 200 mm, beam dia (d) = 2 mm

Area (A) = $\frac{\pi d^2}{4}$ = 3.1416 mm^2 ……………………………………….(C1)

And the area moment of inertia (I) = $\frac{\pi d^4}{64}$ = 0.7854 mm^4……………….(C2)

Modulus of elasticity (E) = 65 GPa, linearly elastic bending stiffness of the beam ($k = 3EI/L^3$) = 19.14 N/m, exciting force (F_0) = 2 N, mass (m) = 0.204 kg, natural frequency (ω_n) = $\sqrt{\frac{k}{m}}$ = 9.69 rad/s, critical damping of the beam (c_c) = 3.9535 Ns/m.

Equivalent Rectangular Beam: Beam length (L) = 200 mm

Now equivalent area (A) = beam width (b) × beam height (h) = $\frac{\pi d^2}{4}$ = 3.1416 mm^2 ….(C3)

And the area moment of inertia (I) = $\frac{bh^3}{12} = \frac{\pi d^4}{64}$ = 0.7854 mm^4……………………….(C2)

Solving equations (C3) and (C4), It is found that beam width (b) = 1.8138 mm and beam height (h) = 1.7321 mm. Other properties are as same as circular cross-section.

APPENDIX- D Matlab Codes

D1: Matlab Codes to Determine the Load-Deflection Curve Considering Geometric Non-linearity

```
clc;
close all;
clear all;

P=2                     % Load (N)
dh=0.001:0.001:0.100;   % End Shortening_dh(m)
L=0.200;                % Length (m)
r=0.001;                % Radius (m)
d=0.002;                % Diameter (m)
E=65000000000;          % Modulus (Pa)
def=zeros(1,length(P));
iter=zeros(1,length(P));
I=(pi/64)*d^4;          % Inertia (m^4)
for i=1:1:length(P)
    for j=1:length(dh)
        xh=L-dh(j);
        Q=(P*xh)/(E*I);
        R=P/(2*E*I);
        slp =(Q*xh-R*xh.^2)./(sqrt(1-(Q*xh-R*xh.^2).^2));
        s=sqrt(1+slp.^2)*xh;
        if L>=s>=(0.995*L)
             break;

        end

    end
     def(i)=(P(i)/(3*E*I))*xh^3;
     iter(i)=j;
     fprintf('%f',xh)
```

```
end
End_Short =L-xh
New_Length =xh
plot( def,P,'k')
xlabel('Tip Deflection (m)')
ylabel('Load (N)')
hold on
```

D2: Matlab Codes to Solve the Vibration Equation by R-K 4th Order Integration Method

```
clc;
close all;
clear all;
%Constant
m=0.204;
Wn=1.414*9.69;
c=0.1*3.9535;  %Cc=3.9535
w=1*Wn;
F=2;
f1=@(t,x,z) z;
f2=@(t,x,z) ((F*sin(w*t))-c*z-(-119.62*x(1)^3-
13.88*x(1)^2+20.273*x(1)-0.0075607))/m;

t(1)=0;
x(1)=0;
z(1)=0;
h=0.001;
tfinal=5;
N=ceil(tfinal/h);
for i=1:N
    t(i+1)=t(i)+h;
```

```
    k1=h*f1(t(i)          ,x(i)          ,z(i));
    p1=h*f2(t(i)          ,x(i)          ,z(i));

    k2=h*f1(t(i)+0.5*h    ,x(i)+0.5*k1  ,z(i)+0.5*p1);
    p2=h*f2(t(i)+0.5*h    ,x(i)+0.5*k1  ,z(i)+0.5*p1);

    k3=h*f1(t(i)+0.5*h    ,x(i)+0.5*k2  ,z(i)+0.5*p2);
    p3=h*f2(t(i)+0.5*h    ,x(i)+0.5*k2  ,z(i)+0.5*p2);

    k4=h*f1(t(i)+h        ,x(i)+k3      ,z(i)+p3);
    p4=h*f2(t(i)+h        ,x(i)+k3      ,z(i)+p3);

    x(i+1)=x(i)+(1/6)*(k1 +2*k2 +2*k3 +k4);
    z(i+1)=z(i)+(1/6)*(p1 +2*p2 +2*p3 +p4);


end

plot (t,x,'r')
xlabel('Time (s)')
ylabel('Displacement (m)')
title('Displacement Vs Time Curve')
axis tight
grid on
t'
x
```

D3: Matlab Codes to Plot *M – Δ and Er – Δ* Curves

D31: Step 1

```
 clc;
close all;
clear all;

x=[0:0.004:0.2];

p1 = 3.2831e+16;
p2 = -2.5104e+16;
p3 = 7.7402e+15;
p4 = -1.2205e+15;
p5 = 1.0246e+14;
p6 = -4.304e+12;
p7 = 8.2048e+10;
p8 = -1.7487e+07;

y = @(x)p1*x.^7 + p2*x.^6 + p3*x.^5 + p4*x.^4 + p5*x.^3 +
p6*x.^2 + p7*x + p8;

 a=integral(y,0,0.007)
```

D32: Step 2

```
clc;
close all;
clear all;
C  = dlmread('Compression.txt');
x1 = C(:,1);
y  = C(:,2);
z1 = cumtrapz(x1,y);
plot(x1,z1)
```

D33: Step 3

```
clc;
close all;
clear all;

x=[0:-0.004:-0.2];

p1 = 2.8564e+16;
p2 = 2.1928e+16;
p3 = 6.7256e+15;
p4 = 1.0424e+15;
p5 = 8.4704e+13;
p6 = 3.4088e+12;
p7 = 7.6321e+10;
p8 = 6.7009e+06;

y =@(x) p1*x.^7 + p2*x.^6 + p3*x.^5 + p4*x.^4 + p5*x.^3 +
p6*x.^2 + p7*x + p8;
b=integral(y,0,-0.00693)
```

D34: Step 4

```
clc;
close all;
clear all;
format short;
x1=-0.00693;
x2= 0.007;
syms x;
b=0.0018138;
h=0.00173205;
delta=x2-x1;
Rho=h/delta;
```

```
inertia = (1/12)*b*h.^3;

%Compression
 p1 = 2.8564e+16;
 p2 = 2.1928e+16;
 p3 = 6.7256e+15;
 p4 = 1.0424e+15;
 p5 = 8.4704e+13;
 p6 = 3.4088e+12;
 p7 = 7.6321e+10;
 p8 = 6.7009e+06;

%y=@(x) p1*x.^7 + p2*x.^6 + p3*x.^5 + p4*x.^4 + p5*x.^3 +
p6*x.^2 +p7*x + p8

 % I1=@(x) sqrt(abs((r/Rho)^2 - x.^2))*5.30e+10.*x.^2;
 % I2=@(x) sqrt(abs((r/Rho)^2 - x.^2))*4.58e+8.*x;

s1=@(x) p1.*x.^8;
s2=@(x) p2.*x.^7;
s3=@(x) p3.*x.^6;
s4=@(x) p4.*x.^5;
s5=@(x) p5.*x.^4;
s6=@(x) p6.*x.^3;
s7=@(x) p7.*x.^2;
s8=@(x) p8.*x;

y1= integral(s1,x1,0);
y2= integral(s2,x1,0);
y3= integral(s3,x1,0);
y4= integral(s4,x1,0);
y5= integral(s5,x1,0);
y6= integral(s6,x1,0);
y7= integral(s7,x1,0);
```

```
 y8= integral(s8,x1,0);

 Y1=y1+y2+y3+y4+y5+y6+y7+y8;



  %Tension
  p10 = 3.2831e+16;
  p20 = -2.5104e+16;
  p30 = 7.7402e+15;
  p40 = -1.2205e+15;
  p50 = 1.0246e+14;
  p60 = -4.304e+12;
  p70 = 8.2048e+10;
  p80 = -1.7487e+07;


%y =@(x) p1*x.^7 + p2*x.^6 +  p3*x.^5 + p4*x.^4 +  p5*x.^3
+p6*x.^2 +   p7*x + p8


s10=@(x) p10.*x.^8;
s20=@(x) p20.*x.^7;
s30=@(x) p30.*x.^6;
s40=@(x) p40.*x.^5;
s50=@(x) p50.*x.^4;
s60=@(x) p60.*x.^3;
s70=@(x) p70.*x.^2;
s80=@(x) p80.*x;
```

```
y10= integral(s10,0,x2);
y20= integral(s20,0,x2);
y30= integral(s30,0,x2);
y40= integral(s40,0,x2);
y50= integral(s50,0,x2);
y60= integral(s60,0,x2);
y70= integral(s70,0,x2);
y80= integral(s80,0,x2);

Y10=y10+y20+y30+y40+y50+y60+y70+y80;

Y=Y10+Y1;
%Y=y1+y2+y3+y4+y5+y6+y7+y8+y9;
M1=b*Rho.^2*Y
%M2=(inertia*128)./(pi*d*delta.^3)*Y
Er1= (M1*Rho)/(inertia*1e+9)
%C=128/(pi*delta.^4);
%Er2= Y*C*(1/1e9)
```